JOHANNES GUTENBERG UNIVERSITÄT MAINZ

Stimuli-Responsive Behavior of Supramolecular Cyclic Peptide Assemblies and Peptide-Polymer Conjugates for Biomedical Applications

Dissertation

Zur Erlangung des Grades

„Doktor der Naturwissenschaften“

im Promotionsfach Chemie

am Fachbereich Chemie, Pharmazie, Geografie und Geowissenschaften

der Johannes Gutenberg-Universität Mainz

Nicole Martina Hutter

geboren in [redacted]

Mainz, Mai 2025

Dekanin: Prof. Dr. EVA RENTSCHLER

Erster Berichterstatter: [redacted]

Zweiter Berichterstatter: [redacted]

Tag der Disputation: [redacted]

Preamble

This thesis was started in May 2020 and completed in March 2025 in the research group of [redacted] at the Department of Chemistry of Johannes Gutenberg University Mainz. Partial sections of the thesis have been published in international scientific journals or are in preparation for submission.

D77 – Dissertation Johannes Gutenberg University Mainz

Für meine Familie

Danksagung

[redacted]

[redacted]

DANKE.

Kurzzusammenfassung

Diese Arbeit untersucht die gezielte Selbstassemblierung supramolekularer zyklischer Peptide und Peptid-Polymer-Konjugate, um adaptive Materialien mit stimuli-responsiven Eigenschaften für biomedizinische Anwendungen zu entwickeln.

Oxidationssensitive zyklische Peptide wurden synthetisiert, die sich zu supramolekularen Nanoröhren organisieren und durch oxidative Stimuli gezielt destabilisiert werden können. Die Oxidation führte zu einer nahezu vollständigen Auflösung der Nanoröhrenstruktur, was eine kontrollierte Wirkstofffreisetzung ermöglichen könnte. Aufgrund der eingeschränkten Wasserlöslichkeit der Peptide in biologischen Medien sind jedoch strukturelle Anpassungen erforderlich, um ihre Anwendung zu verbessern.

Ein weiteres System umfasst Hydrogel bildende zyklische Peptide, die sich zu mechanisch stabilen supramolekularen Netzwerken organisieren. Die Integration telecheler PEG-Vernetzer ermöglichte eine gezielte Steuerung der Gelstärke, wobei die PEG-Kettenlänge einen entscheidenden Einfluss hatte. Während die strukturelle Stabilität umfassend untersucht wurde, sind weitere Studien zur biologischen Stabilität erforderlich.

Das entwickelte Peptid-Polymer-Copolymersystem für die Nukleinsäure-Transfektion zeigte eine effiziente siRNA-Komplexierung ab einem N:P-Verhältnis von 8:1 sowie eine pH-abhängige Disassemblierung des Copolymersystems im sauren Bereich. Zellstudien belegten eine erfolgreiche Aufnahme der Polyplexe sowie eine sehr hohe Zellviabilität. Zudem führte die Transfektion von CpG ODN zur Immunstimulation in dendritischen Zellen. Zukünftige Untersuchungen zur Assemblierung unter biologisch relevanten Bedingungen könnten weitere Erkenntnisse über Stabilität und Wechselwirkungen dieses Systems liefern.

Die entwickelten supramolekularen Peptid- und Peptid-Polymer-Systeme demonstrieren das Potenzial, durch kontrollierte Selbstassemblierung und gezielte Strukturauflösung funktionale Biomaterialien bereitzustellen. Während die oxidationssensitiven Nanoröhren stimuli-responsive Destabilisierung ermöglichen, bieten die Hydrogele eine flexible Plattform für regenerative Medizin und depotbasierte Wirkstofffreisetzung. Das supramolekulare Polyplexsystem erweitert die Anwendungsmöglichkeiten supramolekularer Peptidchemie in der gezielten Genmodulation und immunologischen Forschung.

Abstract

This work explores the targeted self-assembly of supramolecular cyclic peptides and peptide-polymer conjugates to develop adaptive materials with stimuli-responsive properties for biomedical applications.

Oxidation-sensitive cyclic peptides were synthesized, forming supramolecular nanotubes that undergo controlled destabilization upon oxidative stimuli. Oxidation led to a nearly complete disassembly of the nanotube structure, demonstrating potential for drug release applications under oxidative stress. However, due to limited water solubility in biological media, structural modifications are necessary to improve applicability.

Another system involved hydrogel-forming cyclic peptides, which assemble into mechanically stable supramolecular networks. The incorporation of telechelic PEG cross-linkers enabled precise control over gel strength, with PEG chain length playing a crucial role. While structural stability was well characterized, further studies on biological stability are needed.

The peptide-polymer copolymer system for nucleic acid transfection demonstrated efficient siRNA complexation at a charge ratio of 8:1 (N:P) and pH-sensitive copolymer disassembly under acidic conditions to regulate intracellular release pathways. Cell studies confirmed successful polyplex uptake and excellent cell viability. Additionally, the transfection of CpG ODN induced immunostimulation in dendritic cells. Further investigations into the assembly behavior under biologically relevant conditions could provide insights into the system's stability and interactions.

The developed supramolecular peptide and peptide-polymer systems highlight the potential of controlled self-assembly and targeted structural disassembly for functional biomaterials. While oxidation-sensitive nanotubes enable stimuli-responsive destabilization, the hydrogels provide a versatile platform for regenerative medicine and depot-based drug release. The supramolecular polyplex system further expands the application of supramolecular peptide chemistry in targeted gene modulation and immunological research.

Table of Contents

1 INTRODUCTION

1.1 Peptide Synthesis

1.1.1 The amide bond

A peptide bond represents a specific type of amide bond utilized for the linkage of amino acids in peptides and proteins. The carboxyl group of one amino acid is connected to the α-amino group of a second amino acid.[1] The formation of this bond under neutral conditions entails the condensation of water, which results in creation of an amide group (figure 1.1A).[1] The formation of a peptide bond necessitates a significant input of energy. In living organisms, this process occurs with the assistance of enzymes and energy-rich molecules such as ATP.[2] As illustrated in figure 1.1B, peptide bond is typically highly rigid due to the planar configuration of the participating atoms. The hydrogen atom of the amino group is in the trans position relative to the oxygen atom of the carbonyl group. The length of the C-N bond in a peptide bond is 1.32 Å, which is shorter than that of a typical single bond with 1.47 Å.[3] The shortening is attributed to the delocalization of the π-electrons, which imparts a degree of double-bond character to the C-N bond (figure 1.1C).[3] This prevents both hydrolytic cleavage and free rotation around the peptide bond. In contrast, the bonds on either side of the peptide bond exhibit a high degree of rotational freedom. The rigidity of the peptide unit is essential for the structure and stability of proteins in their native form, while the rotational ability of the neighboring bonds enables the multitude of possible secondary structures in protein folding.[2]

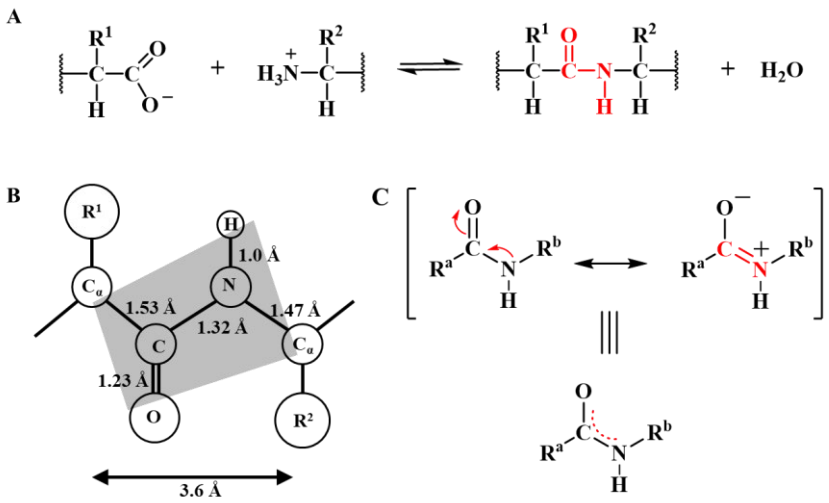

Figure 1.1: ***A*** *Formation of a peptide bond; the right amino acid residue of the dipeptide contains a free amino group (in the protonated form NH_3^+) and thus forms the amino terminus; the left amino acid residue with the free carboxyl group forms the carboxyl terminus;* ***B*** *Dimensions of the peptide bond;* ***C*** *Double-bond character of a peptide bond.*[1,2]

Given that peptide synthesis *in vivo* is enzymatic and occurs under strictly controlled conditions, *in vitro* synthesis presents several significant challenges. The most significant of these are the energy requirements and the necessity for selective reactions. To address these issues, solid phase peptide synthesis has been developed. This method provides a systematic and efficient approach to the artificial production of peptides, whereby the controlled and stepwise formation of peptide bonds on a solid support is employed.

1.1.2 Solid-phase peptide synthesis (SPPS)

Solid-phase peptide synthesis (SPPS) is a widely utilized methodology to produce peptides in laboratory settings. It was initially developed by ROBERT MERRIFIELD in 1963.[4] The principal

advantage of SPPS is that the peptide chain is constructed in a stepwise manner on a solid support, known as a resin. In his initial experiments, MERRIFIELD employed a cross-linked polystyrene resin, which remains a prevalent choice in solid-phase peptide synthesis to this day.[4]Synthesis on a resin greatly simplifies the purification and handling of the reaction steps, as excess reagents and by-products can be readily removed through repeated washing steps.

Figure 1.2 shows the fundamental methodology for peptide synthesis. The synthesis commences with the attachment of the C-terminal residue of the initial amino acid to a resin. To prevent unwanted polymerization of amino acids, the α-amino group is temporarily protected by a suitable protecting group. Subsequently, filtration and washing are conducted to eliminate any residual reagents and by-products that may have accumulated during the binding process. The N-terminal protecting group is then subjected to a deprotection step. This is followed by further washing to ensure that no interfering substances remain. The following step is to attach the next sequential amino acid to the one already attached. This process, which comprises coupling, deprotection, and washing, is repeated sequentially until the desired peptide sequence is fully synthesized. The peptide synthesis occurs in a direction opposite to that of natural peptide and protein synthesis, proceeding from the C-terminus to the N-terminus. Once the synthesis process is complete, all protective groups are removed, and the resulting peptide is cleaved from the resin. As side chains of many amino acids are reactive, it is necessary to stabilize them with suitable protecting groups during synthesis to prevent the formation of unwanted side products. It is imperative that side chain protecting groups remain intact throughout the synthesis process, despite the repeated N-terminal deprotection steps. An optimal system would be one in which the side chain and N-terminal protecting groups can be selectively removed under different conditions, a principle known as "orthogonal protection".[5,6]

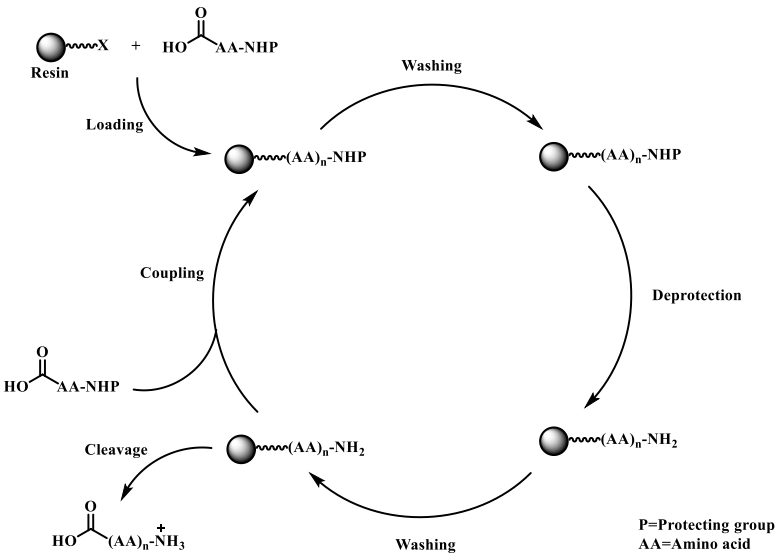

Figure 1.2: *General solid phase peptide synthesis cycle.[5]*

Synthesizing a peptide chain on a resin simplifies purification, as intermediates can be separated from excess reagents and solvents by filtration and washing, which significantly reduces the time and labor required compared to synthesis in solution. A further advantage is that physical losses, such as those caused by the transfer of reaction solutions or the removal of solvents, can be reduced as the peptide remains bound to the resin throughout the synthesis. Nevertheless, resin synthesis is not without limitations. Side products, resulting from incomplete, side, or impure reactions, accumulate on the resin during chain assembly and contaminate the final product. The impact of achieving less than 100% conversion in each step on product purity can be significant, with an overall yield of only 35% after 10 coupling cycles if the coupling efficiency per coupling was only 90%. [5]

In terms of protecting group chemistry, two systems have proven successful over time in solid phase peptide synthesis. The Boc/Bzl protection scheme developed by MERRIFIELD uses Boc protecting

groups to temporarily protect the α-amine group of amino acids, while benzyl-based protecting groups provide permanent side-chain protection.[7] Both protecting groups are acid labile, so this scheme cannot be considered orthogonal. However, the Boc group offers practical advantages, as it can be removed under moderate conditions, such as 50% trifluoroacetic acid (TFA) in dichloromethane (DCM), whereas benzyl-based protecting groups require stronger acids, such as hydrofluoric acid (HF) or trifluoromethanesulfonic acid (TFMSA), for cleavage. The second established protecting system is the Fmoc/tBu system. Here, the α-amine group of the amino acids is protected by the base-sensitive fluorenylmethoxycarbonyl (Fmoc) group, while the side chains are protected by acid-labile protecting groups such as *tert*-butyl esters or triphenylmethyl (trityl) group. This scheme is orthogonal, which means that the side chain protecting groups can be removed without affecting the N-terminal protection and vice versa. This is particularly advantageous when selective modification of the side chains is required, for example in targeted labelling or cyclisation of a peptide. It should also be noted that the Fmoc/tBu system is now increasingly preferred because it offers milder conditions and greater flexibility in the synthesis of complex peptides.[8,9]

In this work, the Fmoc/tBu protecting group system is employed. The Fmoc protecting group is removed by abstraction of an acidic proton from the fluorenyl group by a base, such as piperidine. This process results in an E_{1cB} elimination and the generation of a free amine, leading to the formation of dibenzofulvene and carbon dioxide (figure 1.3). Dibenzofulvene is a highly reactive electrophile that can irreversibly bond to the exposed amine, resulting in the reblocking of the N-terminus. To prevent this issue, the use of large excess of base (e.g. secondary amines) to intercept the dibenzofulvene have to be employed. The deprotection reagent piperidine, can be an effective option in this instance.[10]

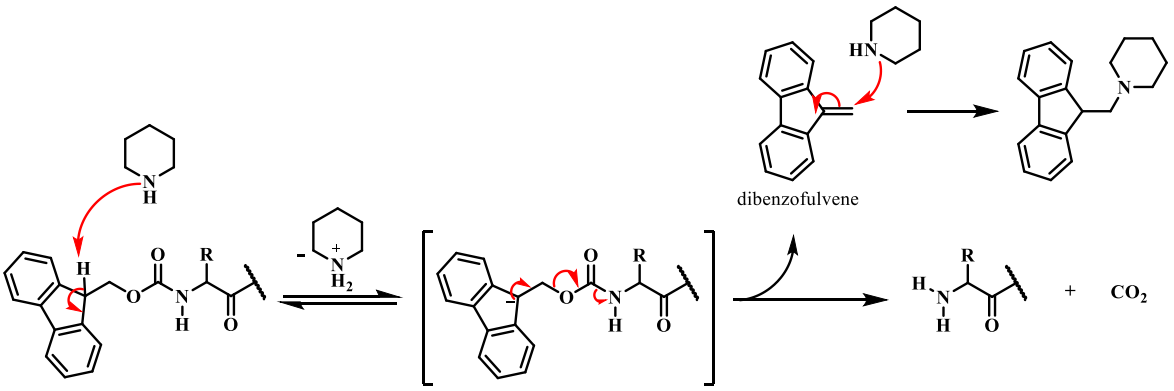

Figure 1.3: *Fmoc-deprotection mechanism.*[10]

The time required to remove the Fmoc group varies depending on the length of the peptide. A deprotection time of 20 to 30 minutes was found to be sufficient for the first five alanine residues of a polyalanine peptide. But for longer residues Ala6 to Ala10, longer deprotection times of 100 to 170 minutes were observed for complete removal of the Fmoc protecting group.[11] This effect is probably due to aggregation of longer peptide chains.[11] Accordingly, the duration of Fmoc deprotection has to be monitored regularly as the peptide length increases, and the reaction time adjusted as needed. An alternative reagent for more rapid removal of the Fmoc protecting group is 1,8-diazabicyclo[5,4,0]undec-7-ene (DBU). DBU has been observed to remove the Fmoc group at a significantly faster rate than piperidine.[12] As DBU does not undergo a nucleophilic reaction with dibenzofulvene, piperidine is still added to react with this reactive side product.[13]

Another crucial aspect of protecting group chemistry in the context of SPPS is the selection and subsequent removal of side chain protecting groups. More than half of the amino acids commonly found in peptides possess side chains with reactive functional groups. In solid phase synthesis it is standard practice to mask all these potentially reactive groups to prevent side group reactions. In the case of the Fmoc/tBu system, protective groups are usually removed with TFA. This approach allows simultaneous global deprotection of the peptide and cleavage or release from the resin at the same time. During the deprotection process, highly reactive cationic species are formed from the protecting groups and resin linkers. In the absence of capture, these species can react with and alter amino acids containing electron-rich functional groups. Amino acids such as tyrosine, tryptophan, methionine, and cysteine, are particularly vulnerable to such side reactions. To address this issue, various nucleophilic reagents, known as scavengers, are added to the TFA solution to intercept these ions. Examples of scavengers include triisopropylsilane (TIPS) and water, which effectively scavenge the resulting alkyl cations. [14] Mechanistically (figure 1.4), TFA protonates the nitrogen of the carbamate in the Boc protected amino group. This produces the free amine and releases carbon dioxide (CO_2), which drives the reaction. Concurrently, the isobutyl cation is formed and subsequently reduced to isobutane by the hydrogenating TIPS. The addition of water serves to hydrolyze the resulting triisopropylsilyl trifluoroacetate, thereby forming TFA and triisopropylsilanol as byproducts.

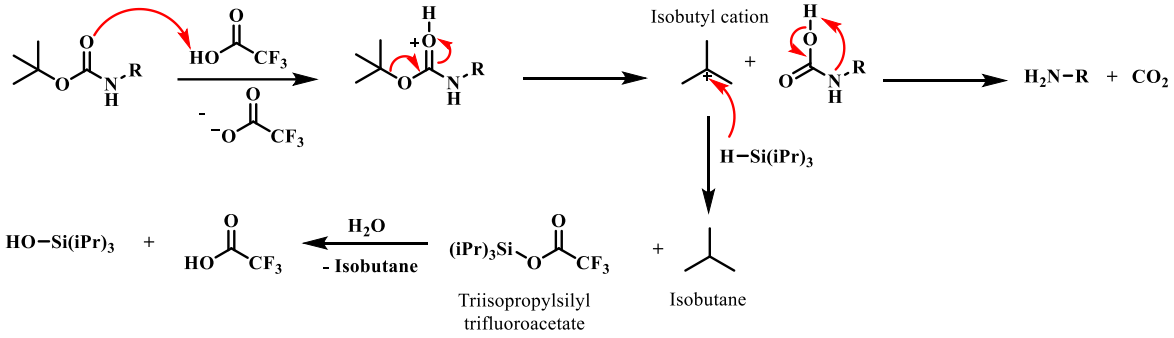

Figure 1.4: *Boc deprotection mechanism.*

In contrast to TIPS, which functions as a general scavenger for the cleavage of protecting groups, 1,2-ethanedithiol (EDT) is employed specifically to protect sensitive amino acids, such as cysteine, methionine, and tryptophan, during acidic deprotection. EDT's function is to prevent oxidative damage through its reducing properties and to capture reactive intermediates, such as carbocations, which are formed during the cleavage of protective groups. Consequently, it prevents unwanted alkylation or modifications to amino acid side chains.[15]

In addition to the protecting groups, the linker to which the peptide is attached to the resin during synthesis can also be cleaved by acids to release the peptide. Several linkers have been developed for this purpose, including Wang, Rink-amide, and trityl linkers. Trityl linkers are characterized by their high acid instability, so that cleavage takes place even in the presence of relatively weak acids such as acetic acid or trifluoroethanol (TFE).[16] This make them particularly useful in situations where it is necessary to maintain the integrity of specific protecting groups after the synthesis process. The bulky structure of the triphenylmethyl group also prevents unwanted side reactions or cyclization that could otherwise lead to premature cleavage.[16] A variant of trityl resins is the 2-chlorotrityl chloride resin, which is used when sensitive amino acids such as tryptophan, methionine, or proline are used at the C-terminus.[17] These resins do not require activation to load the first C-terminal amino

acid, which makes them less prone to side reactions such as enantiomerization or dipeptide formation. This increases their efficiency in the synthesis of complex peptide structures.[17]

Despite options for optimizing solid phase peptide synthesis, there are still challenges that can reduce the yield and purity of the synthesized peptides. The main challenge today, despite improvements in linkers, protective groups and cleavage techniques, is peptide aggregation. As peptide chains grow on a resin matrix, they tend to form secondary structures or aggregates, either with other peptide chains or with the polymer support itself.[18] The aggregation process results in a reduction in the reaction rate for the amidation, which in turn leads to a decline in the coupling yields. One of the indications of aggregation is the shrinkage of the resin matrix that occurs during the synthesis stage. This is caused by the formation of hydrogen bonds and hydrophobic interactions between and within the chains, which can be observed after several coupling step.[19] To reduce aggregation, a resin with lower substitution (0.1 to 0.4 mmol/g) is often used.[19] Another significant challenge is the epimerization of the amino acids that occurs during the coupling process. Except for glycine, all 20 proteinogenic amino acids possess a stereogenic center at the α-carbon atom. It is of great importance to maintain the correct configuration at these asymmetric centers, as this is fundamental to the secondary structure. The integrity of these centers is particularly vulnerable during the coupling process. The use of strong or an excess of bases can facilitate racemization or epimerization. This tendency is further enhanced by electron-withdrawing groups on the α-amino group. The primary mechanism of base-catalyzed racemization (figure 1.5A, pathway 1) involves the formation of a 5-membered oxazolone via deprotection of the activated amino acid. The rate-determining step is the abstraction of the amide proton, followed by ring closure. Subsequently, a resonance-stabilized carbanion is formed by abstraction of the α-proton. Re-protonation of this carbanion finally leads to the racemic mixture. Alternatively, if the α-proton is abstracted directly (figure 1.5A, pathway 2), an enolate intermediate is formed, which can subsequently be re-protonated on both sides, resulting in a racemic mixture.[20]

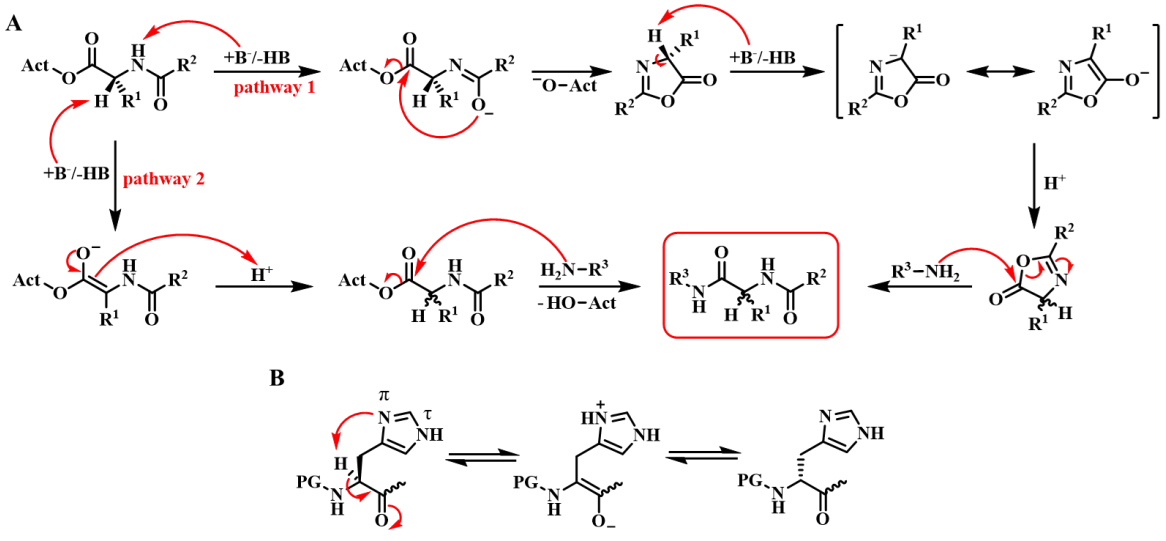

***Figure 1.5: A** Base-catalyzed racemization of amino acids during peptide synthesis;[20] **B** Epimerization mechanism of histidine.[21]*

Histidine derivatives are particularly prone to epimerization, as the basic π-nitrogen of the imidazole side chain can intramolecularly abstract the α-proton, thereby facilitating racemization (figure 1.5B).[21] The likelihood of epimerization is further increased when an electron-withdrawing

group is present at the C-terminus, such as during activation with a coupling reagent. This increases the acidity of the Cα proton at the stereocenter, facilitating its abstraction and subsequent racemization. While this is generally not a problem when using Fmoc-His(Trt) derivatives, it can occur in slow coupling reaction times with aggregated peptide sequences.[22] Furthermore, the thioether side chain of methionine is prone to undesired oxidation reactions, resulting in methionine sulfoxide (Met(O)), which can occur during synthesis or during storage in the presence of oxygen. To overcome this challenge, the incorporation of effective scavenging agents, such as EDT, is imperative to minimize the incidence of undesirable side reactions.[23] In addition, uronium or guanidinium coupling reagents have the potential to react with the free N-terminus of the peptide chain, leading to guanidinylation and subsequent irreversible inactivation of chain growth.[24] To prevent this reaction, the amino acids should be preactivated with a stoichiometric amount of coupling reagent prior to addition to the peptide resin, and excessive amount of coupling reagent should not be used.[5]

1.1.3 Coupling methods

The formation of an amide bond by the reaction of a carboxylic acid with an amine is difficult due to the competing acid-base reaction. This results in the formation of an inactive ammonium and carboxylate salt before nucleophilic substitution can occur.[25] To make this reaction efficient, a coupling reagent is added. This activates the carboxyl group by converting the hydroxyl group of the carboxylic acid to a more favorable leaving group. Consequently, the carboxy group becomes more accessible to nucleophilic attack by the amino group of another amino acid, thereby facilitating formation of the amide and reducing unwanted side reactions. A variety of coupling reagents are available for use in this reaction. Carbodiimides, such as diisopropylcarbodiimide (DIC), were among the first coupling reagents[26] used and are now being replaced in many solid phase peptide syntheses by uronium/guanidinium salts, such as O-(7-aza-1H-benzotriazol-1-yl)-*N*,*N*,*N*',*N*'-tetramethyluronium hexafluorophosphate (HATU), or O-(benzotriazol-1-yl)-*N*,*N*,*N*',*N*'-tetramethyluronium hexafluorophosphate (HBTU). Another class of compounds are phosphonium salts, such as benzotriazol-1-yloxytripyrrolidinophosphonium hexafluorophosphate (PyBOP), which are preferred for amidation reactions in solutions. An alternative approach to forming amide bonds is to convert the C-terminus into a stable activated ester, such as *N*-hydroxysuccinimide (NHS) derivatives or phenols with electron-withdrawing groups, including pentafluorophenol (OPfp). Nevertheless, this approach has the disadvantage of being less selective and prone to the formation of unwanted side products.[27]

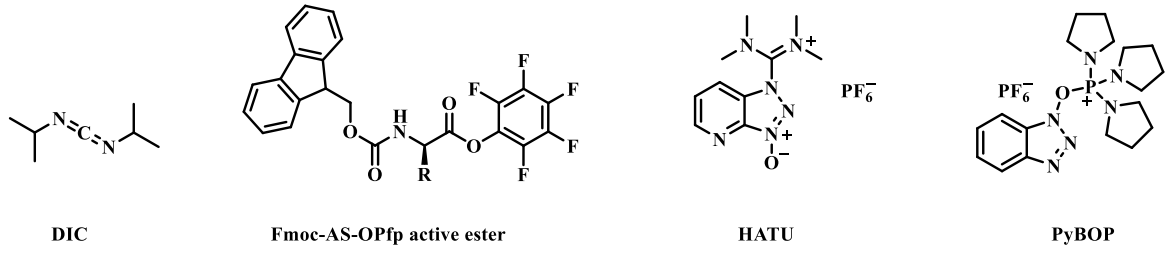

Figure 1.6: *Chemical structure of different coupling reagents active esters.*

The efficacy of the various coupling methodologies exhibits variability, with the following hierarchy of performance: OPfp ester < DIC < PyBOP < HATU.[28] Nevertheless, the selection of the optimal coupling reagent remains a crucial aspect in each synthesis.

In peptide synthesis, particularly solid-phase peptide synthesis, there is a tendency for racemization, whereby the stereochemistry of the amino acids can be altered during coupling, resulting in the formation of undesirable side products (figure 1.5). The use of additives (figure 1.7), including 1-hydroxybenzotriazole (HOBt), 1-hydroxy-7-azabenzotriazole (HOAt), hydroxyiminocyanoic acid ethyl ester (Oxyma) and 2-hydroxypyridine-N-oxide (HOPO) prevent racemization of the amino acid during activation.[29] The coupling efficiency of the active esters formed is slightly reduced but remains high enough to ensure rapid amide bond formation. In particular HOAt-based reagents are more reactive than HOBt. The additional nitrogen in the benzotriazole core of HOAt increases the acidity of the molecule, rendering it a superior leaving group. Moreover, the nitrogen in position 7 enables a neighboring group effect, which increases the efficiency of the coupling reaction and further suppresses the formation of unwanted side products.[30]

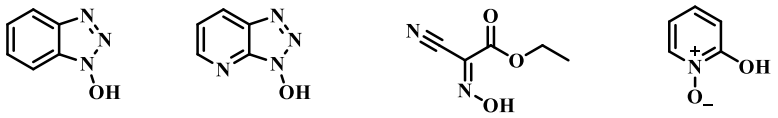

Figure 1.7: *Chemical structure of additives for amide coupling.*

Carbodiimides, including dicyclohexylcarbodiimide (DCC) and DIC, are commonly used reagents in the synthesis of amides. They can also convert primary amides to nitriles, which is useful in organic synthesis, but can be an undesirable side reaction in peptide synthesis with asparagine and glutamine residues.[31] DCC leads to the formation of dicyclohexylurea as a byproduct, which exhibits poor solubility in the majority of organic solvents and precipitates during the reaction.[32] For this reason, DCC is the optimal choice for reactions in solution, as the byproduct can be filtered off as a precipitated solid for purification, it is less suitable for solid-phase synthesis. In contrast, DIC is the preferred option for solid-phase synthesis, given that its byproduct, diisopropylurea, exhibits enhanced stability and solubility in solution. One challenge associated with carbodiimide activation in peptide synthesis is the potential for racemization of the activated amino acids. This effect can be mitigated through the addition of additives. The reaction of an Fmoc-protected amino acid with DIC and HOBt results in the formation of an OBt ester, which proceeds rapidly, particularly in non-polar solvents such as DCM. The reaction also functions effectively in DMF if the mixture is pre-activated prior to addition to the resin. Nevertheless, racemization persists as a challenge with specific residues, such as histidine.[5] To address these limitations, 1-*tert*-butyl-3-ethylcarbodiimide (TBEC) has emerged as an alternative to DIC in peptide synthesis.[33] TBEC exhibits higher reactivity, enabling faster coupling reactions while reducing the formation of side products such as urea derivatives. Furthermore, it demonstrates a lower propensity for racemization, thereby improving the stereochemical integrity of peptides.[33,34]

To minimize unwanted racemization that often occur when using carbodiimide reagents, alternative reagents such as HATU and HBTU have been devised to generate OBt esters *in situ*.[35] These uronium derivatives are widely used due to their high reactivity and rapid coupling efficiency. They allow the formation of peptide bonds in a few minutes and exhibit a low tendency to racemization.[36] Racemization process can be further reduced by the addition of additives such as HOBt, making these reagents particularly suitable for challenging syntheses. The mechanism of HATU-mediated coupling (figure 1.8) commences with the activation of the carboxyl group by a base such as *N*,*N*-diisopropylethylamine (DIPEA), which increases the nucleophilicity of the carboxyl group. The

carboxyl group initiates a nucleophilic attack on the sp^2-hybridized carbon atom of HATU, resulting in the formation of the activated ester via the *O*-acyl(tetramethyl)isouronium intermediate. This reacts with the amino group of a second amino acid to form the peptide bond.[35] HATU exists in two structural forms, the *N*-shape (guanidinium form) and the *O*-shape (uronium form). The *O*-shape is described as the more reactive isomer, as it activates the carboxyl group with greater efficiency, thereby facilitating the formation of the activated OBt ester.[37] But the *O*-shape is unstable and readily converts to the *N*-shape, which is more stable but slightly less reactive.[37]

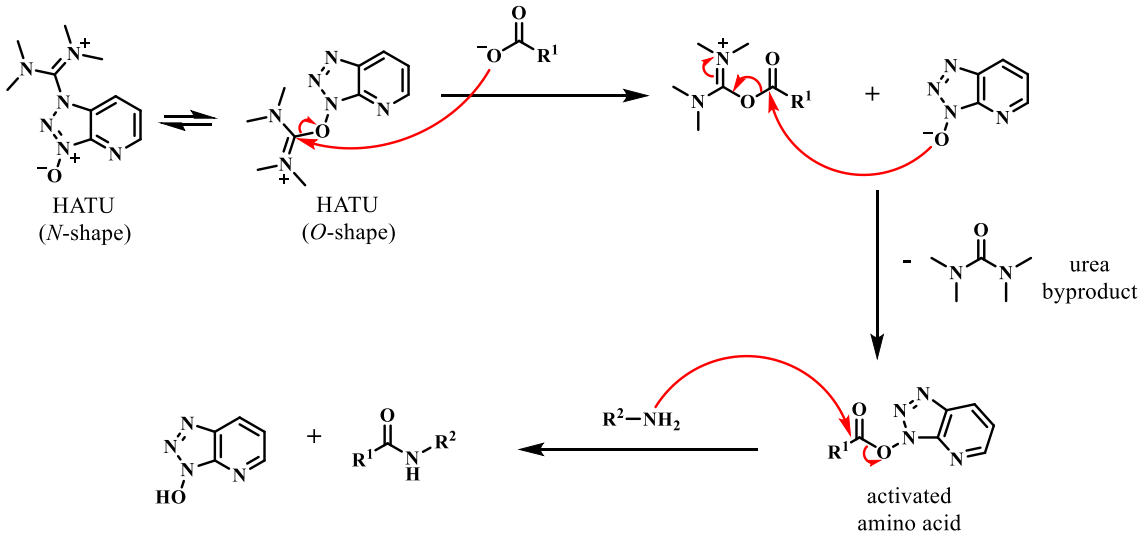

Figure 1.8: *Mechanism of the HATU and HOBt mediated peptide coupling.*[35]

While uronium-based reagents offer several advantages, they can also lead to unwanted reactions, such as N-terminal guanidination of peptides into truncated sequences. Newer reagents, such as PyBOP, have been developed to circumvent this issue. However, they are less commonly utilized in solid-phase peptide synthesis due to their inherent instability, which renders them less suitable for extended synthesis processes.[38] A particular advantage of PyBOP over other reagents, such as DIC, HATU, or HBTU, is the oxophilicity of the phosphorus atom, which is absent in the last mentioned reagents.[35] This makes this class of coupling reagents interesting for the cyclization of peptides in solution. Preactivation of the C-terminus by e.g. uronium/guanidinium salts is not possible during cyclization, as both ends of the peptide are protected. This means that the coupling reagent can also block the N-terminus. In such cases, PyBOP is particularly suitable as it reacts preferentially with the carboxyl group due to its oxophilicity. The mechanism of PyBOP-mediated amidation (figure 1.9) commences with the attack of the carboxylate anion of the peptide on the phosphonium ion of the reagent, resulting in the release of the oxybenzotriazolyl anion. The positive polarization and oxophilicity of the phosphorus atom drive this reaction. Next, the oxybenzotriazolyl anion attacks the carbonyl group, forming a benzotriazolyl active ester and releasing tripyrrolidine phosphine oxide. The peptide bond is formed by aminolysis of the active ester with the elimination of HOBt.[35]

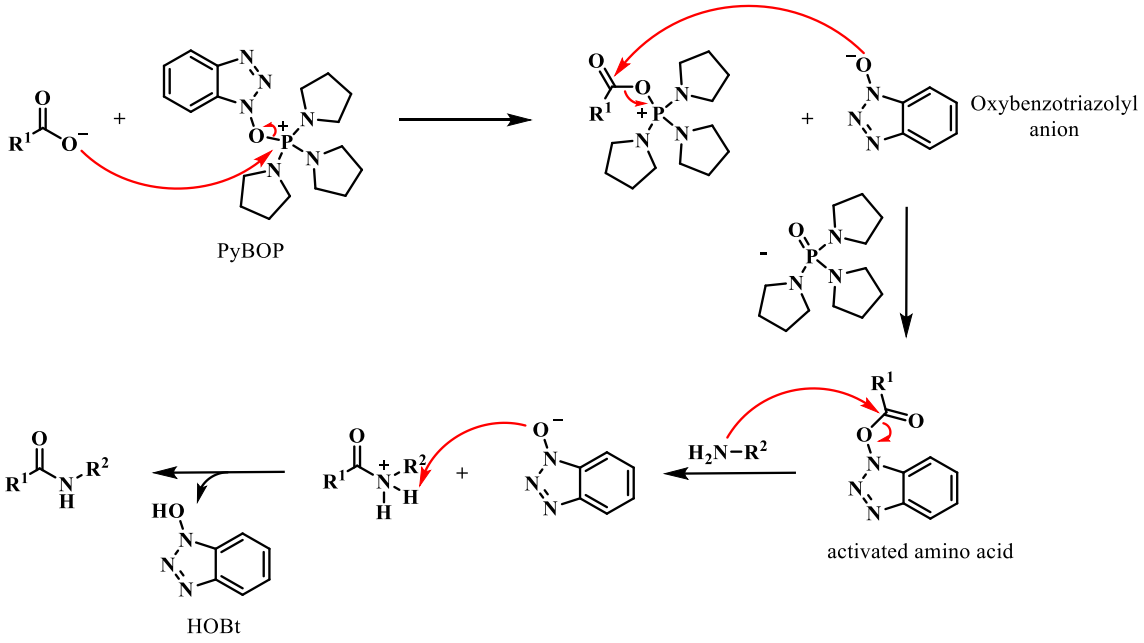

Figure 1.9: *Mechanism of the PyBOP mediated peptide coupling.*[39]

In addition to the established coupling reagents such as DIC, HATU, or PyBOP, this study employed less common reagents that offer specific advantages. These include 4-(4,6-dimethoxy-[1,3,5]-triazin-2-yl)-4-methylmorpholinium tetrafluoroborate (DMTMM·BF_4) and diethylphosphoryl cyanide (DEBPT).

DMTMM·BF_4 is a remarkable coupling reagent that exhibits notable efficacy in cyclization of peptides. [40,41] In comparison to its chloride salt derivative, it exhibits several significant advantages. The BF_4 anion exhibits a high degree of resistance against hydrolysis and is less nucleophilic due to delocalization of its negative charge over highly electronegative fluorine atoms. This prevents undesirable side reactions that could otherwise be initiated by the more reactive and strongly nucleophilic chloride ion.[42] It also exhibits excellent solubility in both organic and aqueous solvents, rendering the reaction conditions flexible and versatile.[43] In contrast to numerous conventional coupling reagents, DMTMM·BF_4 does not necessitate the addition of a base, as the electron acceptor capacity of the triazine and quaternary amonium effectively facilitates the activation of the carboxy group.[42] This reduces potential side reactions that could be triggered by bases. Furthermore, it can be used efficiently even under physiological conditions. The mechanism of DMTMM·BF_4-mediated coupling (figure 1.10) is based on the activation of the carboxy group of the peptide. A nucleophilic attack of the carboxylic acid group on DMTMM·BF_4 leads to the formation of an active ester with the release of BF_4^- and *N*-methylmorpholinium (NMM). Subsequently, the active ester is nucleophilically attaced by an amino group.[44]

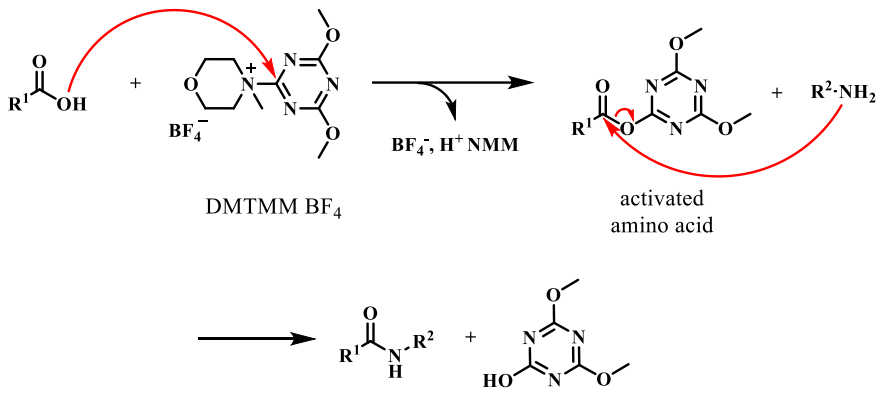

Figure 1.10: *Mechanism of DMTMM·BF_4 mediated peptide coupling.*[44]

DEPBT is a coupling reagent that offers the advantage of epimerization-free synthesis.[45] The intermediate active ester's high stability significantly reduces the formation of undesirable racemic side products.[46] The mechanism of DEPBT (figure 1.11) is based on the activation of the carboxy group through the formation of a stable active ester, similar to the phosphonium reagent PyBOP. This process involves the nucleophilic attack of the deprotonated carboxy group on the reagent, which leads to the formation of a reactive intermediate and the cleavage of diethyl phosphite as a byproduct. This activation of the carboxy group is fast and reliable, minimizing reaction times and reducing the need for excess reagents. The active ester formed is then attacked nucleophilically by the amino group, leading to the formation of an amide bond. The stability of the active ester plays a pivotal role in the suppression of undesirable side reactions and epimerization.[45]

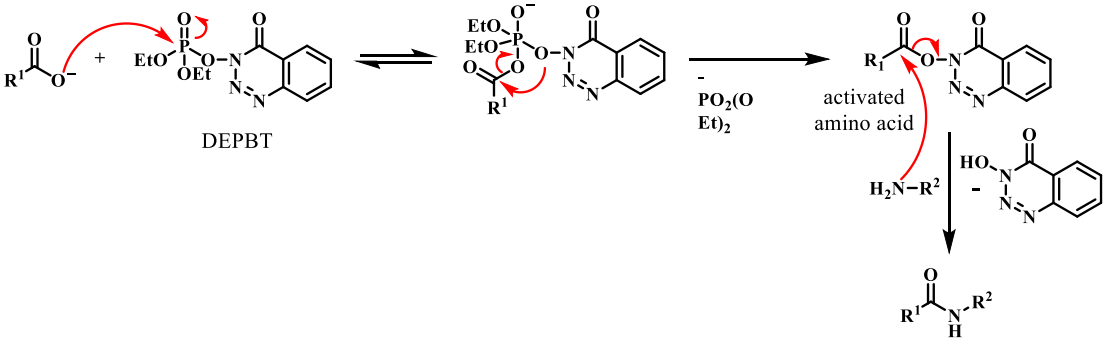

Figure 1.11: *Mechanism of DEPT mediated peptide coupling.*[45]

The selection of a suitable coupling reagent is imperative for the efficiency and selectivity of the reaction, as well as the avoidance of undesirable side reactions such as racemization. While established reagents such as HBTU, HATU, and PyBOP are widely employed in peptide synthesis due to their reliability and versatility, newer alternatives such as DMTMM·BF_4 and DEPBT offer additional advantages. These reagents enable targeted application in specific contexts, such as the gentle activation or cyclization of peptides, thereby expanding the scope of contemporary peptide synthesis.

1.2 Supramolecular Chemistry - A short Overview

Supramolecular chemistry, referred to by Nobel Laureate JEAN-MARIE LEHN (1987) as "chemistry beyond the [individual] molecule"[47], is a field of research concerned with the study of chemical systems in which molecules are spatially organized by non-covalent interactions. The most important

of these interactions include metal coordination, solvophobic effects, van der Waals forces, π-π interactions, electrostatic interactions and hydrogen bonding.[48] The last is the most widely used in supramolecular chemistry. It is based on the electrostatic attraction between an electronegative atom with a lone pair and a hydrogen atom covalently bonded to another electronegative atom such as nitrogen, oxygen or sulfur.[49] Although a single hydrogen bond is too weak to form stable supramolecular structures (10^1 to 10^3 M^{-1})[50], the arrangement of several of these bonds in the form of hydrogen bond arrays leads to a significant increase in stability and direction, resulting in association constants in the range of 10^3 M^{-1} to 10^9 M^{-1}.[51] The use of such arrays is very common in synthetic supramolecular systems, but there are numerous natural models in which they are used for self-assembly.[6,52] The secondary structures of proteins, such as the α-helix or β-sheet, are stabilized by hydrogen bonding between the carbonyl oxygen of one peptide bond and the amide hydrogen of another, following specific patterns along the peptide backbone.[2] Similarly, the stability of the DNA double helix is based on complementary hydrogen bonds between the nucleotides (figure 1.12).[2]

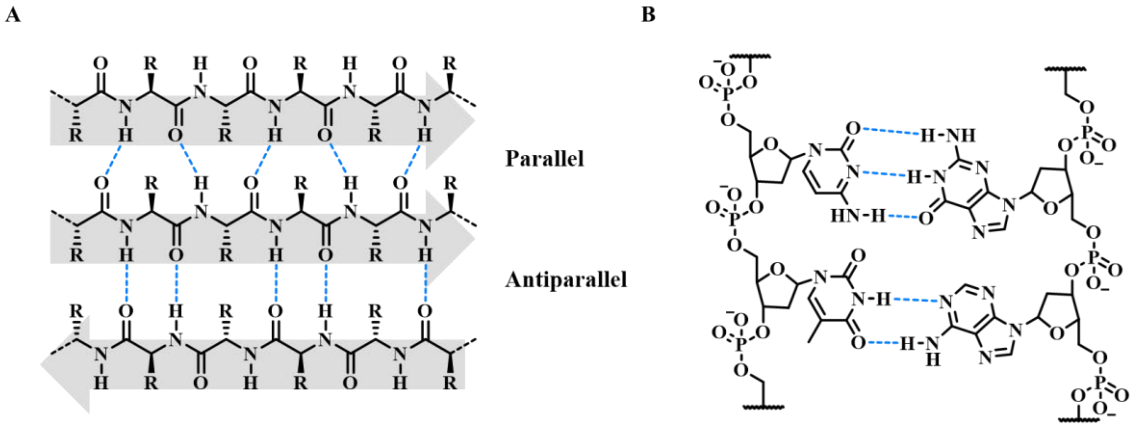

Figure 1.12: *Examples of multiple-hydrogen-bonding in nature.* ***A*** *Parallel and antiparallel β-sheet structure of a protein;* ***B*** *double helix structure of DNA.*

An important concept in supramolecular chemistry is the formation of supramolecular polymers through self-assembly.[53] In contrast to their classical covalent counterparts, macromolecules that are traditionally linked by covalent bonds[54], supramolecular polymers consist of repeating subunits, but are held together by supramolecular interactions, allowing them to form larger morphologies such as nanofibers[55], nanoribbons[56], nanorods[57] and nanotubes[58]. Another special feature is the reversibility of polymerization through non-covalent interactions that can respond to different stimuli. These stimuli can be of chemical, physical or biochemical nature.[59] An elegant way to incorporate these stimuli for biological applications is via amino acids, which also contribute to the formation of supramolecular structures. There is a wide range of natural and synthetic amino acids that can be incorporated to control supramolecular polymerization and make the system biocompatible. One example is a supramolecular polymer developed by the BESENIUS group that exhibits both RedOx and thermoresponsive properties (figure 1.13).[60] The monomers consist of C_3-symmetric units containing a peptide sequence that stabilizes a β-sheet structure by hydrogen bonding and leads to the formation of nanorods in aqueous media. This peptide sequence provides the system with multiple levels of stimuli responsiveness: glutamic acid can be reversibly protonated, and methionine can be oxidized either by the enzyme glucose oxidase through in situ production of gluconic acid from glucose and generation of H_2O_2, or by direct external addition of H_2O_2.

Furthermore, the incorporation of triethylene glycol units into the supramolecular polymer not only enhances its water solubility but also introduces temperature-dependent properties. These properties result in the physical cross-linking of the polymer chains at a temperature above 35 °C.[60]

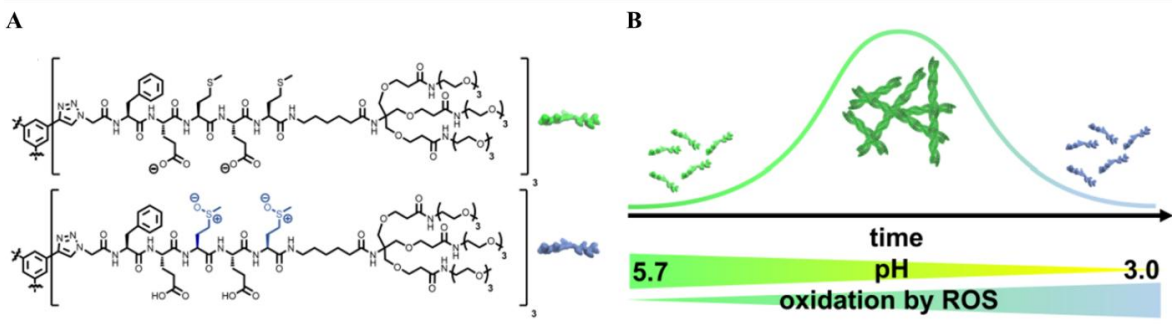

Figure 1.13: *A Chemical structure of the β-sheet encoded dendritic peptide amphiphile (green) and its oxidized form (blue);* ***B*** *Chemical representation of pH switchable supramolecular polymerization and oxidation-induced degradation.[60] Reproduced with permission from John Wiley and Sons.*

1.3 Cyclopeptides - A Supramolecular Building block

Cyclic peptides (CPs, cyclopeptides) are a class of nature-inspired supramolecular structures in which oligopeptide chains are cyclized via covalent linkages. This ring formation gives cyclopeptides special structural and functional properties. For example, they are often more resistant to enzymatic degradation by exopeptidases, which leads to a longer biological half-life and they exhibit increased thermostability. These properties have to lead to great interest, particularly in drug discovery.[61] In biology a distinction is made between homodetic and heterodetic cyclopeptides, depending on the type of bond leading to the cyclization of the peptide.[62] Homodetic cyclopeptides consist exclusively of amide bonds between the amino acids, as in the case of cyclosporin A[63] (figure 1.14A). Cyclosporin A is a natural product found in the Norwegian fungus *Tolypocladium inflatum*[63] and is used in transplantation medicine to prevent graft rejection due to its immunosuppressive effects.[64] Heterodetic cyclopeptides, on the other hand, contain other covalent bonds in addition to peptide bonds, such as isopeptide, ester or disulfide bridges in the backbone of the cyclopeptide. A prominent example of this is oxytocin, shown in figure 1.14B, commonly referred to as the "cuddle hormone".[65] Oxytocin is released during positive social interactions and lactation and plays a key role in mother-infant bonding and the regulation of social behavior.[65] In oxytocin, oxidation of two cysteine residues leads to the formation of a disulfide bridge which stabilizes the ring closure of the molecule[66] as shown in red in the figure.

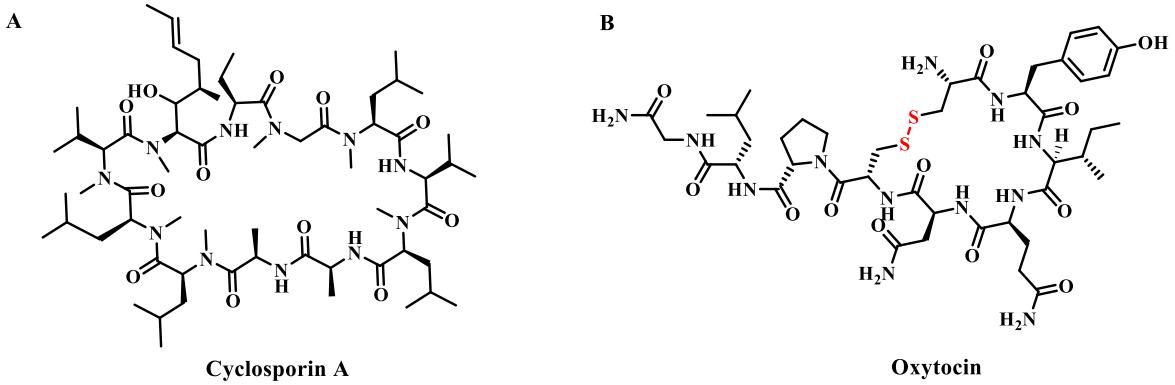

Figure 1.14: *Chemical structure of* ***A*** *cyclosporin A and* ***B*** *oxytocin.*

One class of synthetic supramolecular building blocks are self-assembling cyclic peptides, inspired by the aforementioned biological CPs. These synthetic peptides tend to stack into supramolecular cyclic peptide nanotubes (SCPNs), with multiple β-sheet-like hydrogen bonds of the peptide backbone acting as the driving force. To date, several types of cyclic peptides have been developed that can be stacked into SCPNs. They are mainly classified into cyclic α-*alt*(D,L) peptides, cyclic β-peptides, cyclic α,γ-peptides, and cyclic peptides with δ- or ε-amino acids (figure 1.15).[67]

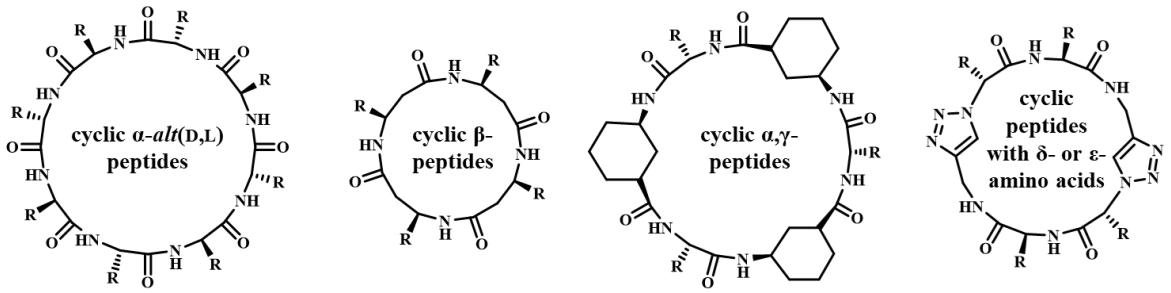

Figure 1.15: *Classes of cyclic peptides.*

Despite their different compositions, they all adopt a nearly flat conformation in which the amide bonds of the peptide backbone are orientated vertically to the plane of the ring, while the amino acid side chains point outwards in a pseudo-equatorial position. This special arrangement allows the formation of β-sheet-like hydrogen bonds between neighboring peptide ring units and makes the resulting nanotubes very stable. [67]

Cyclic α-*alt*(D,L) peptides hold a distinctive position among cyclic peptides and will be discussed in detail in the following chapter.

1.3.1 Cyclic α-*alt*(D,L) peptides

Cyclic α-*alt*(D,L) peptides are the closest to naturally occurring cyclopeptides. In his 1974 study, DE SANTIS postulated the formation of SCPNs based on mathematical calculations. His results showed that cyclic peptides with an even number of alternating D- and L-amino acids can adopt a flat, ring-shaped structure. [68] The CO and NH groups of the amide bond are oriented in opposite directions, almost parallel to the axis of symmetry, while the side groups are pseudo-equatorial.[69] These calculations led to the prediction that such cyclic peptides could form cylindrical structures by stacking, stabilized by both van der Waals forces and hydrogen bonds (figure 1.16). Almost two decades later, in 1993, GHADIRI and his colleagues were first to demonstrate the formation of such a cyclic peptide nanotube, trough successful synthesis of Cyclo-[(L-Gln-D-Ala-L-Glu-D-Ala)$_2$-] including glutamic acid served to prevent the peptide units from associating by electrostatic repulsion in a basic aqueous solution.[58] Targeted acidification of this solution led to the formation of rod-shaped crystals, as confirmed by transmission electron microscopy (TEM) (figure 1.17).[58]

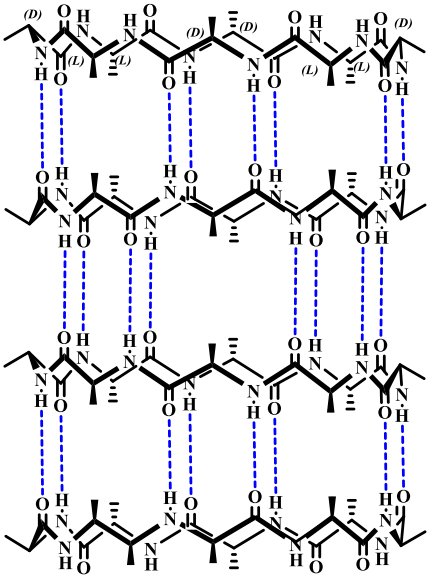

Figure 1.16: *Schematic representation of the SCPN emphasizing the antiparallel stacking and the extensive network of intermolecular hydrogen-bonding interactions.*

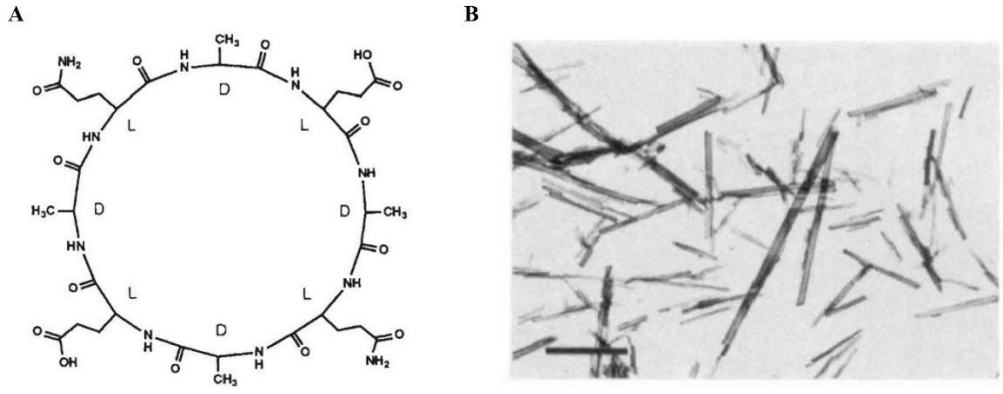

***Figure 1.17: A** Chemical structure of the cyclic α-alt(D,L)-peptide; **B** Low-magnification image of nanotube suspension adsorbed on carbon support film (scale bar, 1 µm).[58] Reproduced with permission from Springer Nature.*

To date, much more insight has been gained about structure and self-assembly behavior of α-*alt*(D,L) peptides. Investigations by X-ray crystallography, electron diffraction and mathematical modelling were used to determine the distance between two cyclic octapeptides to approximately 4.5 Å[70], which roughly corresponds to the distance between two peptide chains in a β-sheet structure with 4.8 Å[71]. Cyclic α-*alt*(D,L) peptides with ten or twelve residues have also been successfully synthesized and form nanotubes, but these are less stable compared to their smaller eight amino acids long CPs.[72,73] Enlarging the ring leads to slacker rings that no longer have the optimal planar conformation and therefore cannot be stacked as efficiently.[69] It was also possible to determine the inner diameter of the cyclic peptides, which is identical for a fixed number of amino acids. All peptides with eight amino acids have an inner diameter of 7.5 Å[58], while peptides with ten and twelve amino acids have nanotubes with an inner diameter of 10 Å and 13 Å, respectively.[74] Investigations into the interior of an octacyclopeptide tube also showed that there are on average 32.8 water molecules inside, indicating the hydrophilic nature of the cavity.[75] Despite the presence of water, water molecules do not interfere with the hydrogen bonds between the peptide rings. In addition, analysis of the movement of water molecules within the peptide channel structure revealed a diffusion constant of 4.4 10^{-6} cm²/s, which is significantly higher than the diffusion rates in comparable biological channels of the cell membrane, such as the gramicidin A transmembrane channel.[75]

Like in natural proteins, the self-assembly behavior of cyclopeptides is based on the assumption that the side groups of the amino acids play different roles in controlling and assembling superstructures through non-covalent interactions. To better understand this mechanism, GHADIRI and colleagues carried out studies on four cyclic peptides, each consisting of cyclo-[(L-Gln-D-Xxx)$_4$-], replaceing the Xxx-position through alanine, valine, leucine or phenylalanine.[76] Under suitable conditions all four peptides crystallized into needle-shaped microcrystals which were analyzed using cryogenic TEM and molecular modelling. This showed that all four peptide ensembles can not only arrange along the tube axis to form nanotubes, but also exhibit lateral aggregation of the tubes, which varies significantly depending on the residue of the variable amino acid. Cyclopeptides with leucine and phenylalanine showed denser packing than alanine and valine analogues, which showed less ordered lateral structures. This suggests that the side chains of amino acids, in particular the zipper structures of leucine and the π-π interactions of phenylalanine, promote the lateral packing of the nanotubes, while they have little effect on the axial stacking of the nanotubes.[76]

The hierarchical self-assembly of cyclic α-*alt*(D,L) peptides into nanotubes can also lead to the formation of fibrils, which exhibit impressive chemical and mechanical stability. In 2015, JOSHI and colleagues first investigated the mechanical properties of nanotubes formed by cyclo-[(D-Leu-L-Gln)$_4$-] in the solid state using electron microscopy, nanomechanical characterization and molecular modelling (figure 1.18).[77] They found an average modulus of elasticity of 11.3 ± 3.3 GPa and a hardness of 387 ± 136 MPa, comparable to amyloid fibrils, which are among the stiffest biological materials.[77] These unique mechanical properties of cyclic peptides and their potential as structural components in composite materials remain largely unexplored.

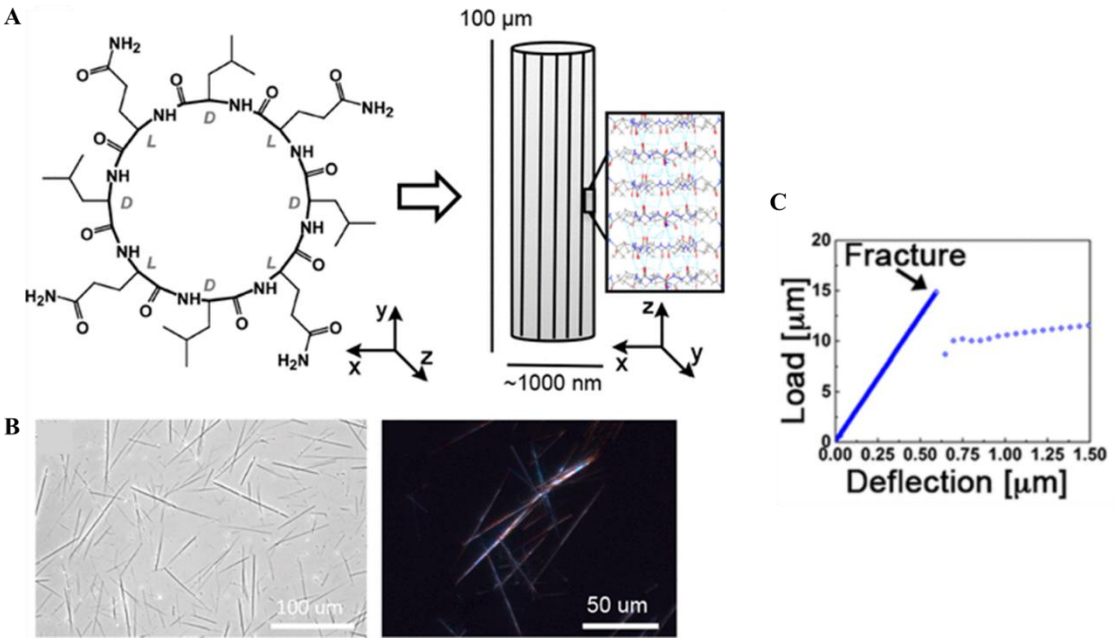

Figure 1.18: ***A*** *Chemical structure of cyclo-[(D-Leu-L-Gln)$_4$-] and schematic illustration of fibers;* ***B*** *Optical micrograph of fibers and polarized light micrograph;* ***C*** *Bending data of a linear elastic region followed by a series of a fracture point.[77] Reproduced with permission from American Chemical Society.*

In summary, the assembly of cyclic peptides into SCPNs can be achieved with a sequence containing an even number of alternating D- and L-amino acid residues. Self-assembly relies on strong, multiple hydrogen bonds between the cyclic peptide backbone, which have a flat, ring-shaped conformation. At the same time, the lateral aggregation of the nanotubes is mainly influenced by the interactions between the side chains of the amino acids. With these properties, predominantly one-dimensional fibers can be represented in the crystalline state. A particularly interesting aspect of supramolecular chemistry is the analysis of these structures in aqueous solution, as this highlights their potential for various biomedical applications. Due to their hydrophobic character and strong tendency to aggregate, these structures have very poor solubility in water. Through targeted peptide design and conjugation with water-soluble polymers, initial studies on water-soluble SCPNs have been carried out and will be discussed in more detail in the following chapter.

1.3.2 Supramolecular properties of CP in an aqueous medium

Due to the self-assembly processes of cyclic peptides and the lateral aggregation of SCPNs, these structures have very poor solubility in most solvents. Only in TFA, HFIP, DMSO and DMF most structures can be dissolved, which on the one hand facilitates purification by precipitation compared to their linear counterparts. [58,78] On the other hand, their insolubility in water makes their biological application almost impossible, despite the natural origin of the subunit amino acids. Nevertheless,

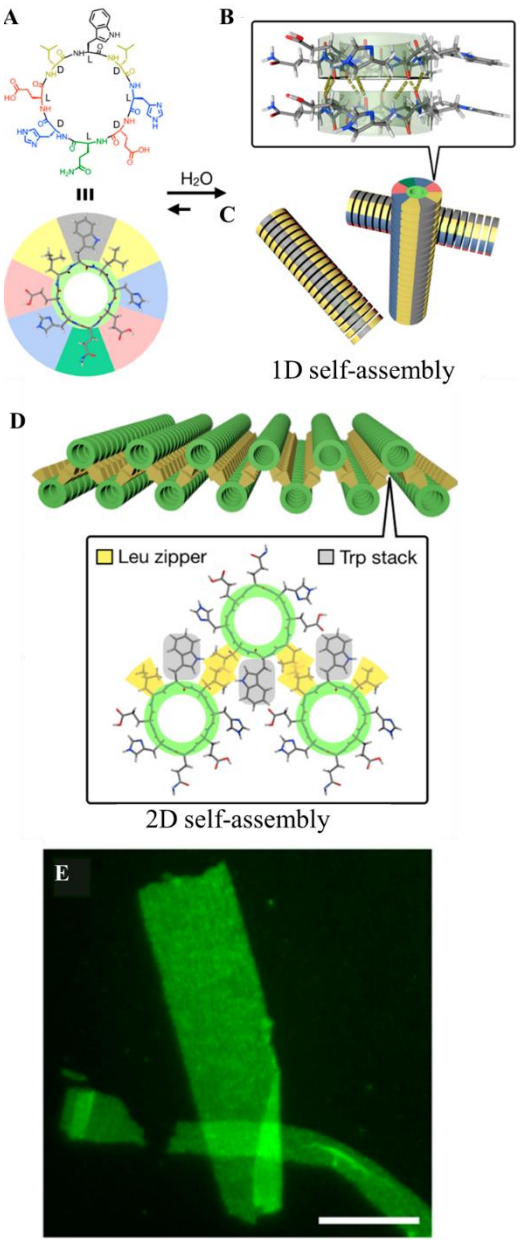

Figure 1.19: ***A-C*** *Proposed model for the sequential 1D-to-2D self-assembly of cyclic peptide;* ***A*** *Chemical structure cyclopeptide with color coding;* ***B*** *Secondary parallel β-sheet conformation between cyclopeptide backbones within nanotubes stabilized via eight hydrogen bonds (dashed lines);* ***C*** *Tertiary 1D self-assembly of cyclopeptide as amphiphilic peptide nanotubes with hydrophobic (Leu−Trp−Leu in yellow-gray) and hydrophilic (Glu−His−Gln in red-blue-green) surfaces;* ***D*** *2D self-assembly of cyclopeptide into nanosheets comprising nanotube bilayers with hydrophobic cores, composed of Leu zippers (yellow) and Trp stacks (gray), and polar residues on their surface;* ***E*** *Microscopic characterization of cyclopeptide supramolecular nanosheets by epifluorescence micrographs of nanosheets (100 µM, pH 7.4).*[79] *Reproduced with permission from American Chemical Society.*

water-soluble SCPNs can be generated by integrating suitable amino acids and targeted use of hydrophilic and hydrophobic domains in the cyclopeptide sequence. A simple approach is to incorporate ionizable amino acids such as Glu, His or Lys so that cyclopeptide molecules behave similarly to surfactants in aqueous media due to the hydrophobic nature of the peptide backbone and the rest of the sequence. The directed, hydrogen-bonding β-sheet motifs of the peptides allow for an ordered nanotube conformation.

For example, MONTENEGRO and coworkers reported a cyclic peptide capable of sequential 1D-2D self-assembly in an aqueous medium.[79] As shown in figure 1.19A, an asymmetric cyclic peptide with the sequence cyclo-[D-Leu-L-Trp-D-Leu-L-His-D-Glu-L-Gln-D-His-L-Glu-] was designed to have four different domains: A hydrophobic tripeptide domain of Leu-Trp-Leu (yellow-grey-yellow), two hydrophilic pH-sensitive domains of His-Glu (red) on either side of the peptide ring, and a neutral hydrophilic domain of Gln (green) opposite the hydrophobic domain. In aqueous solution, the multitude of hydrogen bonds facilitate the stacking of the peptide rings (figure 1.19B), thereby enabling the formation of amphiphilic one-dimensional nanotubes (figure 1.19C). These subsequently assemble into a two-dimensional nanotubular bilayer, which serves to protect the hydrophobic side from the aqueous environment (figure 1.19D). At physiological pH, the surface of the tubular ensemble is strongly anionic due to the deprotonated glutamic acids (pKa ≈ 4.2) and neutral histidine residues (pKa ≈ 6.0), which prevents the aggregation of the individual layers, leading to the formation of large and flat nanosheets with lateral dimensions in the high micrometer range, as shown in figure 1.19E by epifluorescence microphotographs at pH=7.4. The formed nanosheets are highly dynamic and can reversibly transform into 1D nanotubes under the influence of pH or temperature.[79] A follow-up study underlined the necessity of the four domains mentioned above.[80]

Fibrillation of cyclic α-*alt*(D,L) peptides can also be observed not only in the crystalline state but also in aqueous solutions, where it leads to physically cross-linked networks that can lead to hydrogel formation.

PELTIER, PERRIER and co-workers developed a series of gelators based on cyclic peptides and investigated the effects of structure and environmental conditions on the gelation of these compounds.[81] pH-responsive hydrogels were formed from cyclic peptides containing two charged residues, either lysine or glutamic acid residues (figure 1.20B). It has been shown that these hydrogels are formed by a hierarchical self-assembly process in which cyclic peptides first stack vertically to form nanotubes, this process is shown schematically in figure 1.20A. These nanotubes aggregate into larger fibers, forming a dense network that can trap solvent molecules, resulting in hydrogel formation with a gel strength of 200 Pa, which can also be demonstrated by rheological studies (figure 1.20D). The driving force behind fibrillation is also the choice of amino acids. Leucine, with its hydrophobic side chain, promotes the formation of a leucine zipper, thereby facilitating hydrophobic interactions and stabilizing lateral aggregation. Tryptophan, on the other hand, contributes to π-π stacking interactions through its aromatic side chain, which stabilizes the nanotubular bilayer by promoting ordered stacking of the cyclic peptide units, leading to extended 2D assemblies. The observation of hydrogels was only possible under conditions of acidic or basic pH, as precipitates were formed in the neutral pH range. To address the solubility of the cyclopeptide structures, ionizable amino acids such as lysine and glutamic acid were incorporated, as their charges cause electrostatic repulsions at acidic or basic pH values. Within the neutral and physiological pH range, these side chains undergo a loss in charge, thereby favoring hydrophobic interactions and leading to the aggregation of the cyclopeptides.[81]

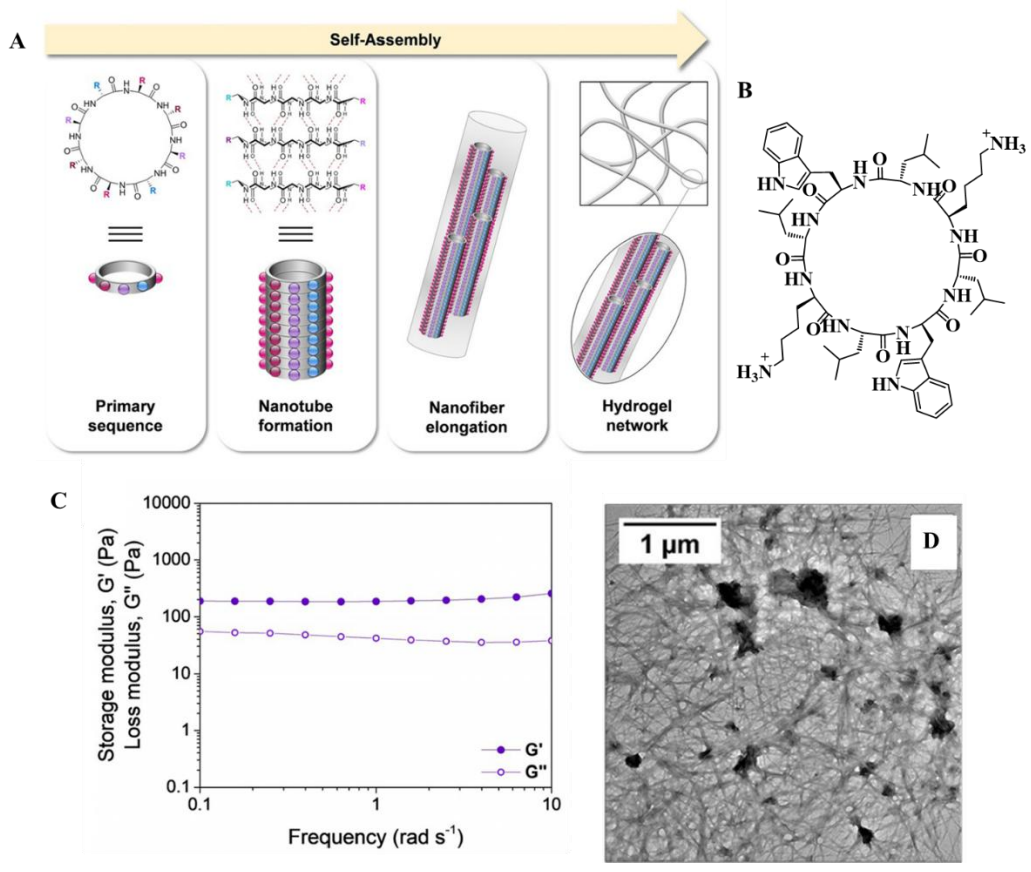

Figure 1.20: ***A*** *Hierarchical self-assembly process involved in hydrogel formation from D, L alternating cyclopeptides;* ***B*** *Chemical structure of cyclopeptide;* ***C*** *Rheology of cyclic peptide hydrogel(frequency sweep 3 wt %, water, pH 3) carried out at a temperature of 22 °C and 0.5 % strain;* ***D*** *TEM images and fiber size distribution for a solution of cyclopeptide at 0.3 wt % in water (pH 3).[81] Reproduced with permission from John Wiley and Sons.*

In addition, GRANJA, MONTENEGRO and co-workers studied the hydrogelation of a cyclic peptide with pH-sensitive His and Lys residues, where one Lys group is substituted with a pyrene fluorophore to visualize the nanotube structure microscopically (figure 1.21A).[82]

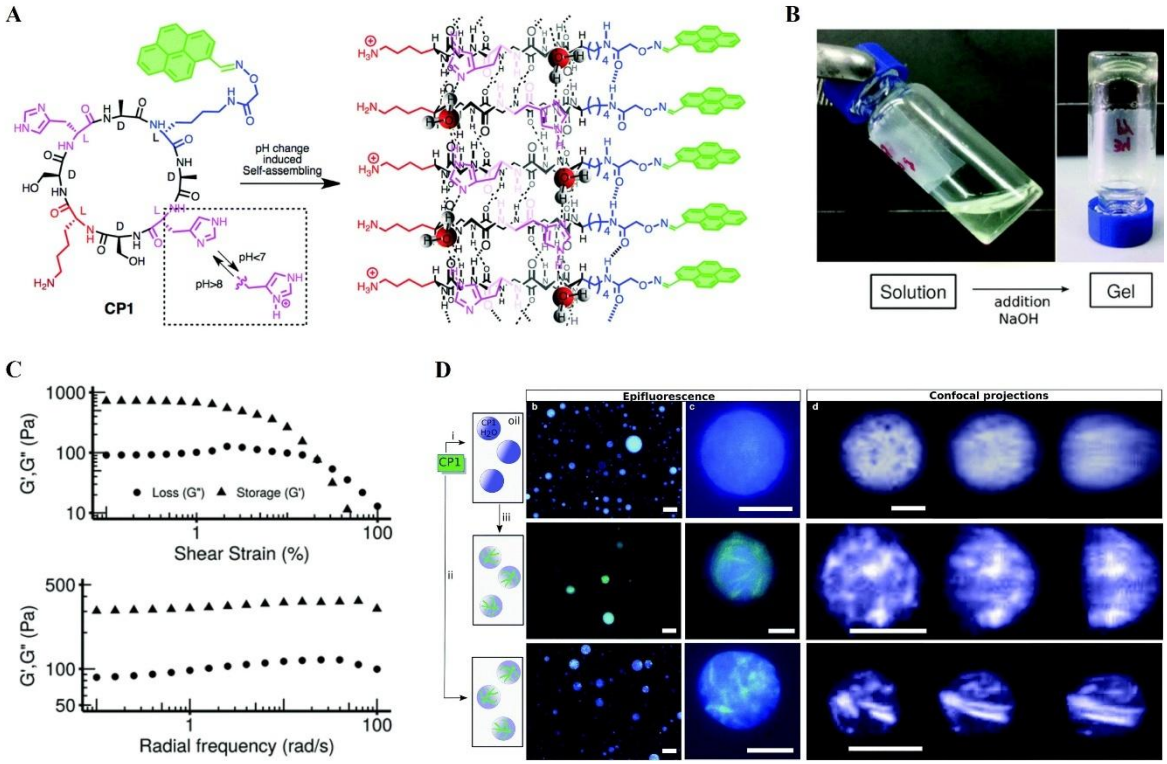

Figure 1.21: ***A*** *Structure and self-assembly of cyclic peptide in single peptide nanotubes;* ***B*** *2% w/w solution of cyclic peptide in milliQ water before (left) and after (right) addition of NaOH (0.1 M) to pH ~8–9;* ***C*** *Rheology measurements for gels of cyclic peptide (2% w/w) strain test and frequency sweep at constant strain of 5%;* ***D*** *Scheme of the procedure for the formation of fibers within water-in-oil droplets: (i) cyclic peptide in water (1–2% w/w); (ii) cyclic peptide (1–2% w/w) in HEPES 30 mM at pH 8; (iii) addition of propylamine (b) epifluorescence images of droplets at low magnification. (c) Epifluorescence images of individual droplets at high magnification. (d) Confocal microscopy projections of individual droplets. Scale bars are 20 µm for (b) 5 µm for (c) and 10 µm for (d).[82] Reproduced with permission from Royal Society of Chemistry.*

This amphiphilic architecture allowed the generation of self-assembled nanotubes that can further interact through the formation of histidine-histidine hydrogen bonds and cation-π interactions, as well as hydrophobic π-π interactions. The samples were dissolved in an acidic aqueous medium. Neutralization of the aqueous medium resulted in deprotonation of the histidine side chains, which triggered supramolecular processes and led to hydrogel formation (figure 1.21B). To visualize the possible superstructures formed, the peptide self-assembly was studied in water microdroplets containing the cyclic peptide in an oil emulsion at a pH of 4 to analyze the polymerization in a confined space. Epifluorescence and confocal microscopy images of the acidic droplet suspensions showed uniform pyrene blue fluorescence, indicating that the cyclic peptide entrapped in the droplets remains in a non-aggregated state and homogeneously distributed in the aqueous phase (figure 1.10Da-i). Two strategies were used to study nanotube formation and fibrillation in these aqueous droplets. In the first method, 2-[4-(2-Hydroxyethyl)piperazin-1-yl]ethane-1-sulfonic acid (HEPES) buffer was used to adjust the pH to 8. In the second, propylamine, which is soluble in both water and oil, was used for basification. The addition of the cyclic peptide with HEPES led to a bathochromic shift in the fluorescence of the droplets and to the formation of confined fibril-like structures several micrometers in length (figure 1.21Dii). Addition of propylamine to the suspensions of acidic droplets also induced the formation of 1D fibril-like structures of the peptides. In both cases, no precipitation

of aggregates was observed, and the fibrillation took place in solution. Furthermore, the hydrogel character was confirmed via rheological measurements through a higher storage modulus G' than loss modulus G'' and a gel strength of 200-800 Pa (figure 1.21C).[82]

An alternative method for facilitating CP water solubility while maintaining the capacity for supramolecular polymerization is through conjugation with water-soluble polymers, such as polyethylene glycol (PEG). This approach will be elaborated upon in greater detail in chapter 1.4.

1.3.3 Cyclic peptide synthesis strategies

Solid phase peptide synthesis is often used to produce linear peptides with a desired sequence (chapter 1.1). The peptide chain is synthesized *via* standardized coupling methods in conjunction with orthogonal protecting group chemistry, which facilitates a stepwise and accurate assembly of amino acids to a solid-phase bound resin. The cyclization of the linear peptide to a cyclic α-*alt*(D,L)-peptide is achieved through *head-to-tail* cyclization, which involves the formation of a covalent amide bond between the N-terminal amino group and the C-terminal carboxyl group.[83,84] As this process necessitates specific conditions, it differs from standard amidation reactions. Two principal methodologies are available for cyclization: resin-bound cyclization (figure 1.22A) and cyclization in solution (figure 1.22B). Resin-bound cyclization represents a powerful method for the generation of cyclic peptides with diverse sequences.[85] Initially, a specific amino acid, such as Asp or Glu (*via* the side chain carboxyl group) or Lys (*via* the amino group) is attached to the resin through use of a cleavable linker.[86] Standard coupling and deprotection procedures are utilized for the synthesis of linear peptide precursor, which remains attached to the resin. Following the targeted removal of the terminal protecting groups, the peptide is cyclized while still attached to the resin by addition of coupling reagents. Subsequently, the cyclic peptide is obtained by cleaving the linker and removing protecting groups from amino acid side chains. This method entails a reduction in the oligomerization of the linear peptide through a process of pseudo-dilution, whereby the peptide is bound to a solid support.

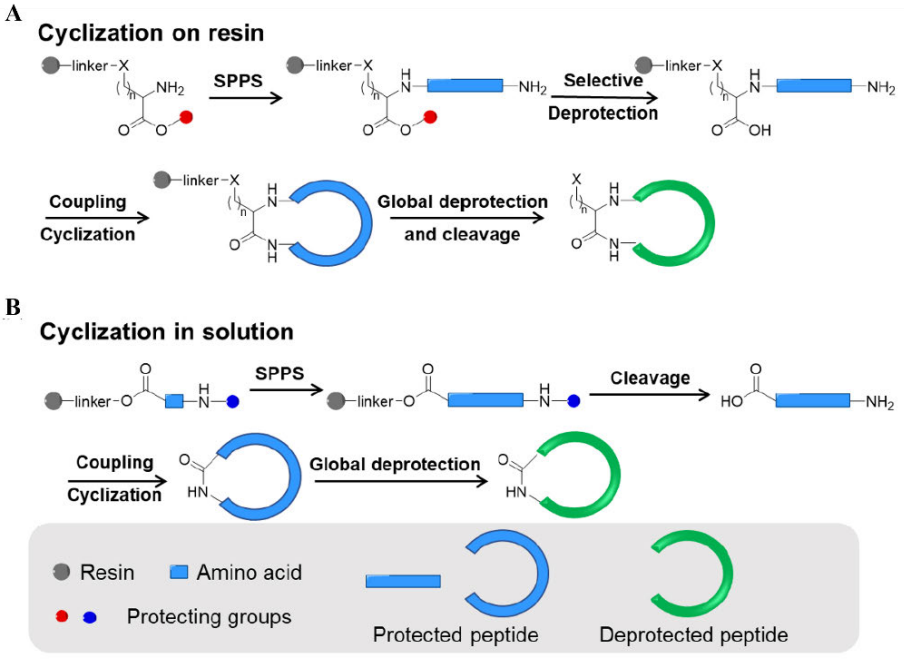

Figure 1.22: *Schematic representation showing the synthesis of cyclic peptides via **A** cyclization on resin and **B** cyclization in solution methods.[69] Reproduced with permission from American Chemical Society.*

Nevertheless, two significant limitations exist with regard to resin-bound cyclization. Firstly, the peptide sequence must contain an amino acid with a carboxyl or amino functionalized side chain, which serves as a point of attachment to the resin. Secondly, the use of multiple orthogonal protecting groups is necessary for the selective removal of terminal protecting groups, as well as those of the peptide side chains and linker. Consequently, solution cyclization is frequently preferred as it circumvents these structural and synthetic limitations.

In the solutions method, the linear peptide with free terminal carboxyl and amino groups is synthesized via solid phase peptide sequencing and subsequently cleaved from the resin. Cyclization is then performed by dissolving the peptide in a highly diluted solution (typically 1 mg/mL DMF) and adding coupling reagents.[87] The cyclic peptide is obtained by separating it from reaction solution (e.g., by precipitation) and removing any remaining protecting groups. This method is theoretically applicable to the synthesis of any cyclic peptide. Although the propensity to form oligomers is a common challenge, this intermolecular reaction is significantly attenuated in self-assembling cyclic peptides due to the pseudocyclic conformation of the linear precursor by the D,L alternating sequence of amino acids. Moreover, this method necessitates the use of fewer orthogonal protecting groups, thereby facilitating the modification of cyclic peptides with functional units or polymer chains. A disadvantage of solution cyclization is that it is a slower process in dilute solutions and necessitates additional isolation and purification steps compared to resin cyclization. Furthermore, the limited solubility of fully protected linear peptide precursors in organic solvents and water may impact the efficacy of the cyclization process.[69]

The utilization of enzymes may be proposed as an alternative methodology for the cyclisation of linear peptides in conjunction with coupling reagents. In their study, ANDERSON *et al.* demonstrated the enzymatic cyclisation of linear peptides using the enzyme asparaginyl endopeptidase (OaAEP1b).[88] The asparagine residue at the C-terminus of the peptide sequence plays a pivotal role. OaAEP1b has been observed to catalyze the cleavage at this position, thereby linking the C-terminus with the N-terminus to form a cyclic peptide. Regarding the size of the ring formed, the enzyme displays a certain flexibility, although this is contingent upon the sequence and conformation of the substrate. However, the efficiency of this method is reduced in cases where the sequence is either very short or very long.

The choice of cyclization method is dependent on the specific synthesis of the cyclopeptide in question. Each method has its own set of advantages and disadvantages, and it is therefore essential to select the most appropriate method for the synthesis in question.

1.4 Supramolecular Polymer-Conjugates

Polymer conjugates are hybrid materials that combine the versatile properties of polymers with the specific functionalities of a secondary component, such as peptides or other supramolecular units. The polymer typically functions as a structural backbone, providing mechanical stability, enhanced solubility, and tunable physical properties. In contrast, the secondary component contributes to functionality, including biological activity, molecular recognition, and the ability to form ordered supramolecular structures. The combination of these elements enables the production of materials with highly customizable and responsive properties.[89]

A prominent example of these systems are polymer-peptide conjugates. The combination of peptides and polymers into conjugates allows the mitigation of the respective weaknesses of two substance classes while simultaneously capitalizing on their respective strengths in a targeted manner. This

results in the generation of properties that are adaptable and optimal for utilization as a supramolecular building block. Each of both classes possesses particular advantages with regard to the synthesis and application of conjugates. Polymers afford a multitude of possibilities regarding variation, contingent upon the selection of monomers and the type of polymerization employed. For instance, hydrophilicity, solubility, functional groups, and polymer architecture can be modified with a high degree of flexibility. A disadvantage is their polydispersity, which presents a challenge for the formation of ordered supramolecular morphologies as it leads to irregularities in supramolecular structures, which in turn makes it difficult to predict the material features that will result.[90] In contrast, peptides possess a clearly defined amino acid sequence, rendering them monodisperse and conferring well-defined properties, with poor water solubility.[2] In polymer-peptide conjugates, the peptide plays the essential role in self-assembly, whereby ordered supramolecular structures are formed through the creation of secondary structures, such as β-sheets or α-helices. The polymer component can facilitate enhanced water solubility through the selection of an appropriate polymer and through the incorporation of functional groups that impart a degree of responsiveness.[91] Despite the polydispersity of the polymer part, the structure formation remains primarily controlled by the monodisperse peptide, resulting in the formation of stable and ordered supramolecular structures.

The BESENIUS group provided an illustrative example of the properties exhibited by such conjugates. Triblock peptide-polymer-peptide conjugates were synthesized by coupling pentapeptide sequences with alternating phenylalanine and histidine residues to hydrophilic polysarcosine (PSar) to enhance water solubility (figure 1.23A).[92] These heterotelechelic conjugates encode the formation of an antiparallel β-sheet, with the histidine moieties introducing a reversible pH trigger into the oligopeptide sequence, thereby forming supramolecular nanorods, as shown in figure 1.23B. Circular dichroism (CD) and fluorescence spectroscopy revealed a transition from an ordered to a disordered structure at pH = 6, which is likely due to intramolecular folding of the peptide end groups. TEM images (figure 1.23C) demonstrated formation of anisotropic nanorods in neutral aqueous solutions as a consequence of intramolecular folding and subsequent supramolecular self-assembly. Furthermore, this peptide PSar conjugate was compared with telechelic peptide polyethylene glycol (PEG) and peptide PSar conjugates that also contain the pentapeptide strands in contrast encoding parallel β-sheet assembly. TEM images once more confirmed the formation of pH-dependent nanorods in neutral buffers exhibiting anisotropic morphologies of comparable thickness. At a concentration of 1.5% (*w*/*v*), PEG- or PSar-based parallel β-sheet encoded peptide conjugates led to the formation of hydrogels with a storage modulus G' of 90 Pa at room temperature. In contrast, the antiparallel β-sheet encoded peptide-PSar conjugate did not form a stable hydrogel and only reached storage modulus of 1 Pa (figure 1.23D). This illustrates how minor alterations in supramolecular interactions can have considerable repercussions on macroscopic material properties.

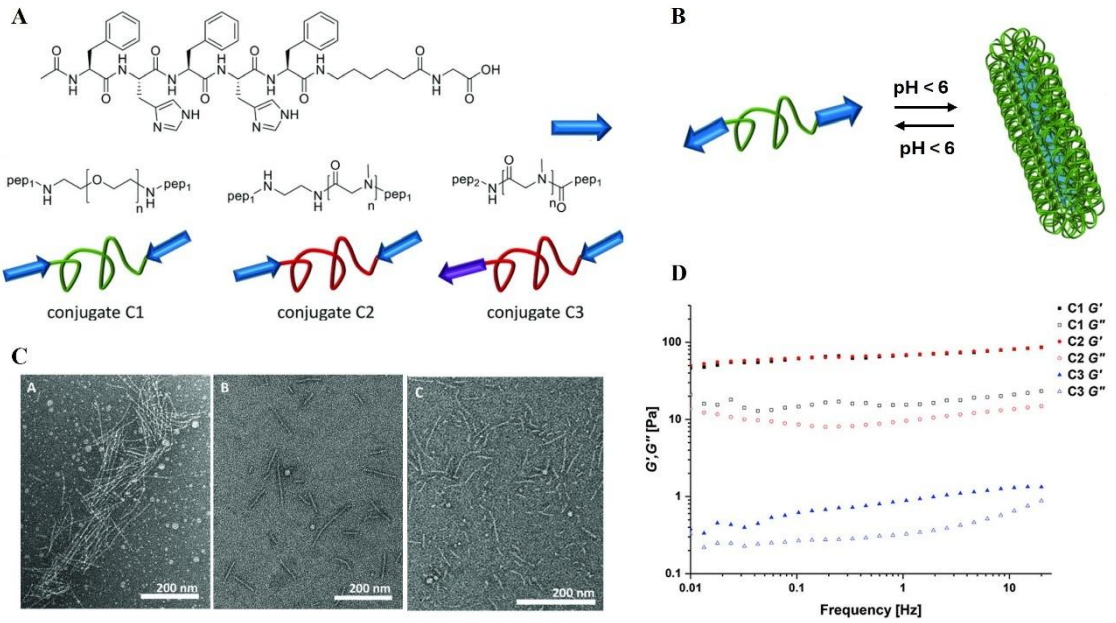

Figure 1.23: ***A*** *Chemical structures of the deprotected peptide strands used for the PEG and PSar polymer functionalization and chemical structures and schematic representation of the synthesized polymer–peptide conjugates C1, C2 and C3;* ***B*** *Schematic representation of pH-dependent 1D supramolecular nanorod formation;* ***C*** *Negatively stained TEM Images: C1 (50 µm) in Tris buffer (20 mm, pH = 8.8), C2 (50 µm) in Tris buffer (20 µm, pH = 7.3) and C3 (50 µm) in Tris buffer (20 mm, pH = 8.0);* ***D*** *Oscillatory shear rheology, frequency sweep measurements (1% strain, 0.01–20 rad·s^{-1}) of C1 (pH = 7.7, 1.5% w/v), C2 (pH = 7.5, 1.5% w/v), and C3 (pH = 7.4, 1.5% w/v) with storage (G') and loss moduli (G") at constant 20 °C and aqueous phosphate buffer (10 mm).*[92] *Reproduced with permission from John Wiley and Sons.*

Conjugation to polymers has also been demonstrated to enhance the water solubility of cyclic peptides. In a study conducted by PERRIER and colleagues, the effects of graft density and polymer architecture on the self-assembly process as well as the influence of solvent on the length of the supramolecular nanotubes of cyclopeptide-polymer conjugates in water under neutral pH conditions were investigated.[93] Cyclopeptides were conjugated with one, two, or three PEG2000 chains and two bottlebrush polyPEG acrylate brush chains (pPEGA) (figure 1.24A). The steric repulsion of the polymers, which influences the hydrogen bond-mediated stacking of the cyclopeptides, was identified as a critical factor in determining the size of the structure. Furthermore, the impact of the number of polymers per peptide in diverse solvents was examined to ascertain the influence of polarity and hydrogen bonding capacity on nanotube formation. The findings indicate that the selection of solvent and the number of polymer arms have a considerable impact on the extent of aggregation (N_{agg}). It was determined that an increased number of polymer arms or more sterically demanding polymers result in a reduction in the degree of aggregation (Figure 1.24B). In particular, the use of a pPEGA brush resulted in a notable reduction in the degree of aggregation. Additionally, contour plots indicated that the polarity and hydrogen bond acceptor ability of a solvent exert a considerable influence on self-assembly.

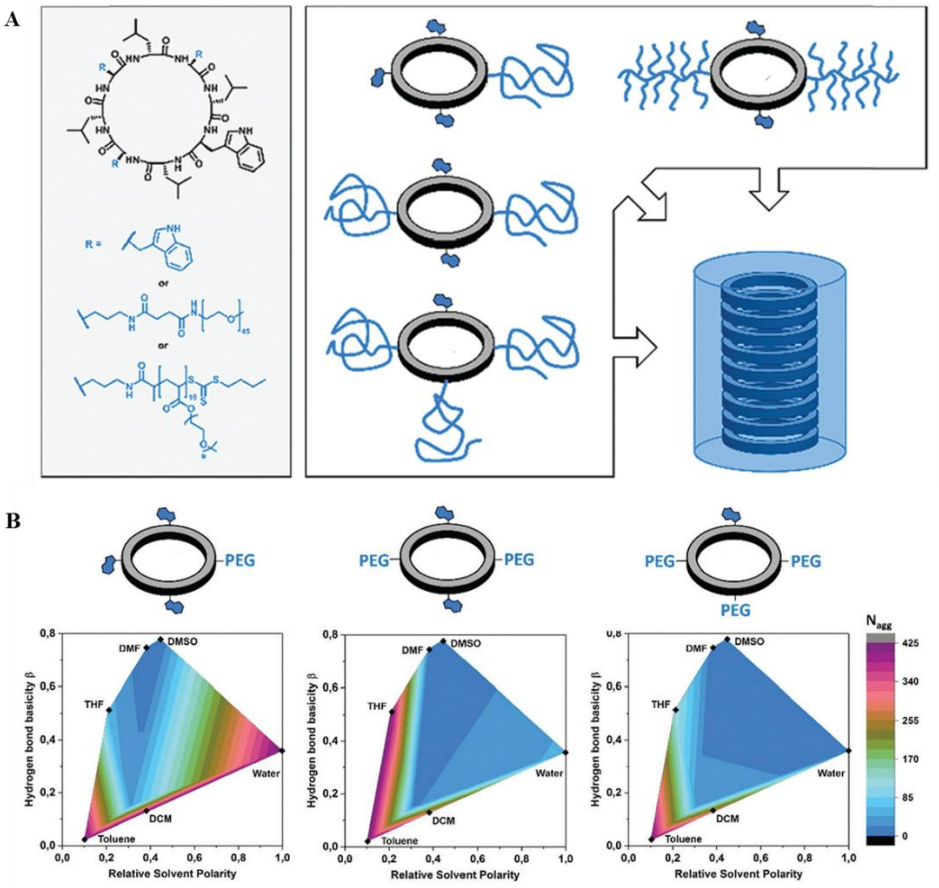

Figure 1.24: A *Summary of the different CP–polymer conjugates used in this study;* ***B*** *Contour plots of the degree of aggregation as a function of solvent polarity and the hydrogen bond acceptor capacity for one-arm, two-arm, and three-arm cyclic peptide polymer conjugates.*[93] *Reproduced with permission from Royal Society of Chemistry.*

The peptide sequence can be also replaced by alternative structural building blocks for other supramolecular polymer-conjugates, such as ureidopyrimidinone (UPy). MEIJER *et al.* presented a multicomponent self-assembly strategy in which polymer conjugates serve as crosslinkers to specifically control the mechanical properties of supramolecular hydrogels.[94] In this study, monofunctional UPy-PEG was investigated by mixing it with the bifunctional crosslinking UPy-PEG, in different ratios (figure 1.25B). This approach allows for substantial alteration of the mechanical properties of the resulting hydrogels. The two components were initially combined in the solid state at varying proportions, up to a total concentration of 5 wt%. It is assumed that mixing in the solid state is essential to prevent the formation of supramolecular homopolymers upon dissolution and instead promote the formation of a supramolecular copolymer system comprising both components. The solid mixture was then dissolved under basic conditions to increase the exchange dynamics between the two fibrillar species (Figure 1.25A). Notably, neither the monofunctional nor the bifunctional fibrils are molecularly dissolved, which enables partial self-sorting of the individual components within the final architecture. Upon subsequent acidification of the mixture, the supramolecular groups reorganize into heterosupramolecular structures, leading to the formation of strong and stable hydrogels even when only small amounts of the crosslinker are combined with the monofunctional UPy-PEG (Figure 1.25B). These properties surpass those of the individual components, as structural modifications allow for precise tuning of non-covalent interactions, which in turn enables the adjustment of macroscopic properties. It has been proposed that the varying

exchange rates of the supramolecular units play a pivotal role in shaping the formation and characteristics of these materials.

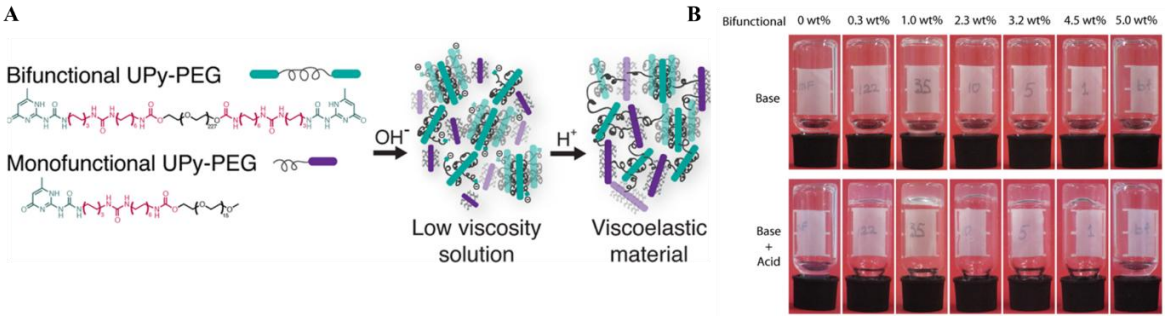

Figure 1.25: A *Scheme representing cross-linking of monofunctional UPy-PEG (purple) and bifunctional UPy-PEG (green) to prepare a mixed supramolecular viscoelastic material. First, basic conditions (pH ~12) permit dissolution of the fibers increasing their exchange, followed by acidic conditions (pH ~3) locking in the hierarchical aggregate structure;* ***B*** *Mixing supramolecules, on a total of ~5 wt%, yields a low viscosity liquid under basic (0.1 M NaOH, pH ~12) conditions (top) and subsequently, viscoelastic materials of varied elastic modulus after 90 min after acidification (0.1 M HCl, pH ~3) (bottom).[94] Reproduced with permission from American Chemical Society.*

2 OBJECTIVES

Supramolecular chemistry utilizes non-covalent interactions to create highly ordered molecular architectures. Peptides have emerged as versatile building blocks for supramolecular systems, as their ability to form hydrogen bonds, hydrophobic interactions, and π-π stacking enables precisely controlled self-assembly progress.[95] Due to their structural variability, peptides can be tailored for functional applications in materials science and biomedicine. A key aspect in the development of supramolecular peptide systems is the choice between linear and cyclic peptides. While linear peptides often exhibit high structural flexibility, which can hinder their assembly into well-defined superstructures, cyclic peptides offer increased structural stability and more precise control over intermolecular interactions due to their constrained conformation. Cyclization reduces enzymatic degradation and enables fine-tuned supramolecular organization, making cyclic peptides particularly attractive platforms for functional materials.[69,96]

This work aims to develop and characterize supramolecular peptide and peptide-polymer systems that self-assemble into well-defined nanostructured architectures. The focus lies on controlling these self-assembly processes to create adaptive and functional materials for biomedical applications.

A major part of this work investigates supramolecular structures based on cyclic peptides that assemble into highly ordered nanotubes via non-covalent interactions. Compared to linear peptides, cyclic peptides provide more precise control over intermolecular hydrogen bonding, leading to more stable and predictable structures. These systems are designed to respond to oxidative stimuli, allowing for controlled depolymerization. By incorporating oxidative sensitive amino acids into the peptide sequence, supramolecular assembly can be selectively disrupted by oxidative stress, enabling precise control over molecular disassembly. The combination of structural stability and stimuli-responsiveness makes these cyclic peptide-based systems particularly promising for applications in controlled drug release and diagnostic platforms.

Beyond redox-sensitive nanotubes, this work explores the development of supramolecular hydrogels based on cyclic peptides. These networks are stabilized by hydrogen bonds and π-π interactions and exhibit high water retention capacity. By strategically modifying the peptide sequences, the network formation can be fine-tuned, allowing for precise control over mechanical stability and structural dynamics. For this purpose, besides cyclopeptides bifunctional telechelic cyclopeptide-PEG conjugates will be used as crosslinkers to support the formation of supramolecular networks into hydrogels. The resulting hydrogels are highly adaptive to external conditions, making them particularly attractive for biomedical applications, such as scaffolds for regenerative medicine or carriers for bioactive molecules.

Another focus of this work is the development of supramolecular peptide-polymer copolymer systems for nucleic acid transfection. The combination of peptide and polymer components enables the design of functional carrier systems that engage in specific molecular interactions with nucleic acids while also providing enhanced stability in biological environments. For these two pH-responsive multi-domain peptide-polymer conjugates ware used. In these systems, one polymer component is cationic and mediates electrostatic interactions with nucleic acids, while the other, a PEG-chain, forms a protective shell around the nucleic acid-loaded complex to enhance stability and biocompatibility for biomedical applications. A peptide component governs supramolecular self-assembly. This architecture not only ensures precise control over the assembly process but also enables pH-responsive disassembly in the acidic endosomal environment, facilitating efficient nucleic acid release. To evaluate the biological efficacy of these carrier systems, cell assays are conducted to analyze cellular uptake and transfection efficiency. The insights gained contribute to

optimizing the structure-function relationships of these systems and expanding their potential applications in gene therapy.

The supramolecular systems developed in this work encompass both the synthesis and comprehensive characterization of their structural and functional properties. By harnessing non-covalent interactions in a controlled manner, a deeper understanding of self-assembly mechanisms in supramolecular peptide systems is achieved, advancing their potential for biomedical and materials science applications.

This work provides new insights into the controlled assembly and functionalization of supramolecular peptide and peptide-polymer systems. The findings contribute to the advancement of intelligent biomolecular materials and enable precise control of supramolecular processes, opening new perspectives for applications in diagnostics, therapy, and materials development.

3 OXIDATION-RESPONSIVE CYCLOPEPTIDES: NANOTUBE ASSEMBLY AND DISASSEMBLY UNDER OXIDATIVE STRESS

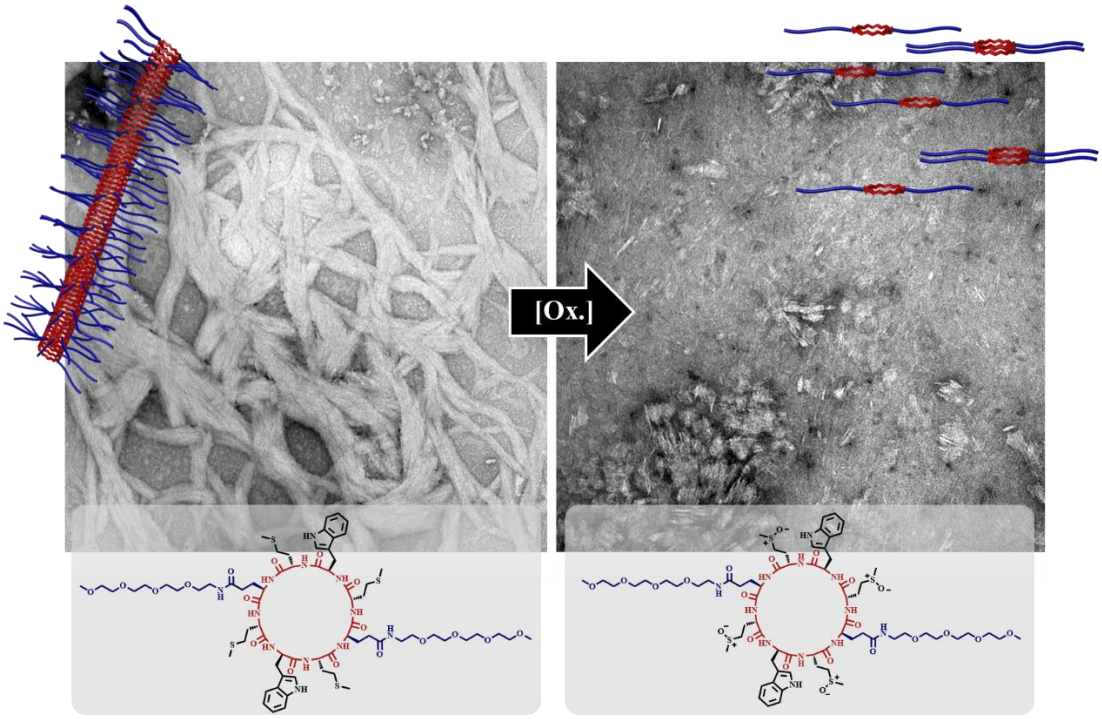

3.1 Motivation and Concept

The formation of β-sheets from self-assembling cyclic peptides provides an extremely versatile scaffold for supramolecular chemistry, particularly for the design and alignment of hydrogen-bonded nanotube arrangements. The β-sheet structures along the amide bonds in the backbone of the cyclopeptides provide the basis for these ordered superstructures. However, there are special cyclopeptides that can respond to external stimuli. These stimuli-responsive properties can be introduced through targeted modifications, particularly to the side chains of the amino acids. These extensions enable targeted adaptation to chemical triggers such as pH changes, redox reactions, metal ions, or specific gases.[59,97] While the pH reactivity of such cyclic peptide-based nanotubes has already been extensively studied,[98] the effect of oxidation processes as a stimulus has not been sufficiently investigated so far.

The strategic incorporation of methionine, a naturally occurring proteogenic amino acid, into the peptide sequence can facilitate the regulated disassembly of nanotubes through oxidation.[99] Methionine contains a thioether that can be oxidized by reactive oxygen species (ROS), such as hydrogen peroxide (H_2O_2). This process leads to the formation of hydrophilic sulfoxide, which disrupts the balance between hydrophobic and hydrophilic forces within the nanotubes. This change has been shown to destabilize the supramolecular structure of the peptides, leading to the dissolution of the nanotubes into their individual components.[100,101] Studies by the BESENIUS group have demonstrated the efficiency of such redox-sensitive processes in peptide systems, for instance in C_3-symmetric amphiphiles[102,103] and peptide-polymer conjugates[104]. These systems utilize β-sheet-encoded peptide sequences with methionine, enabling controlled supramolecular polymerization through pH- and redox-controlled mechanisms.

These systems are of particular interest for biomedical applications. In living organisms, the concentrations of ROS are strictly regulated, given the close association between oxidative processes and inflammatory reactions, as well as oxidative stress.[105] This phenomenon presents a compelling prospect for the development of diagnostic and therapeutic systems, as well as the regulated release of active pharmaceutical agents.[100]

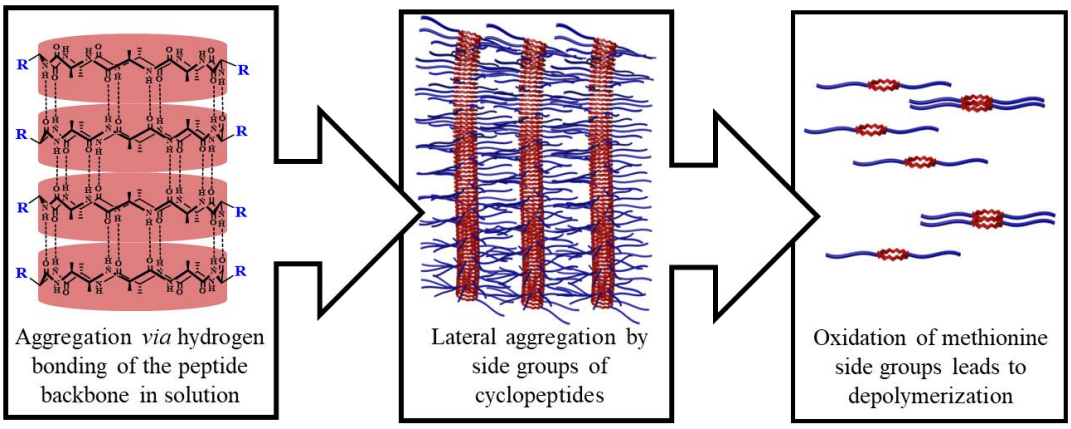

Figure 3.1: *Concept of oxidation responsive cyclopeptides.*

The aim of this project is to develop a cyclic octapeptide able to form nanotubes in an aqueous medium and to be depolymerized into its monomers under oxidative stress (figure 3.1). The alternating D,L configuration was chosen to facilitate uniform and stable stacking of individual CPs,

enabling the formation of β-sheet-like structures through hydrogen bonding between the amide bonds. Furthermore, the insertion of tetraethyleneglycol monomethyl ether units in the side chains of the peptide sequence improves the system's solubility in water and contributes to lateral aggregation of nanotubes by promoting intermolecular interactions. The oxidation sensitive function group is provided by methionine, which has been incorporated into the peptide sequence. The oxidation-triggered increase in hydrophilicity and charge repulsion destabilize the ordered structure of the nanotubes and leads to their depolymerization. The dynamics of this process were investigated using circular dichroism spectroscopy (CD) and transmission electron microscopy (TEM), with hydrogen peroxide being used as a model of ROS.

3.2 Results and Discussion

3.2.1 Ester conjugation of tetraethyleneglycol to cyclopeptides

To investigate cyclopeptides with the above mentioned properties, the cyclic peptide Cyclo-[(L-Met-D-Glu(-COO-TEGOMe))$_4$-] (**CP1**) was synthesized. The amide backbone of the D,L-alternating octapeptide allows the formation of nanotubes by hydrogen bonding. **CP1** consists of only two different amino acids in a symmetrical structure, which also facilitates the stacking of the individual rings to form nanotubes. The four D-methionine units incorporated enable oxidation of the system. In addition, the synthetic amino acid D-Glu(COO-TEGOMe) (**III-4**), which has ethylene glycol units that increase the hydrophilicity of cyclic peptides, is incorporated four times.

Two synthetic routes were pursued for the synthesis of cyclopeptide **CP1** (Figure 3.2). Route A is based on a linear synthesis strategy, whereby cyclopeptide **III-3** is synthesized initially from the commercially available amino acids L-methionine and D-glutamic acid. This is followed by the conversion of the resulting compound to **CP1** through the acidic esterification of the free glutamic acid side groups with tetraethyleneglycol monomethyl ether. Cyclopeptide **III-3** functions as a modular basic building block. The free glutamic acid side chains provide a variety of modifications, as they can be conjugated with different ethers or amines. However, this subsequent modification of the glutamic acid side groups of cyclopeptide **III-3** increases the probability of incomplete functionalization, and impurities include mono-, di-, and tri-substituted cyclopeptides.The multitude of potential products makes purification difficult and requires a complex separation of the desired product from the sideproducts. Synthesis route B circumvents the issues associated with multiple substitutions, as tetraethyleneglycol monomethyl ether is already integrated into the synthetic amino acid **III-5**. This approach enables an optimized and more effective synthesis of the desired **CP1** cyclopeptide, as the challenges associated with route A are mitigated. By incorporating the ether directly into the peptide sequence, the cyclopeptide synthesis loses its modularity, which limits the scope for subsequent modifications, but it is less prone to the efects and impurities associated with side-chain modification.

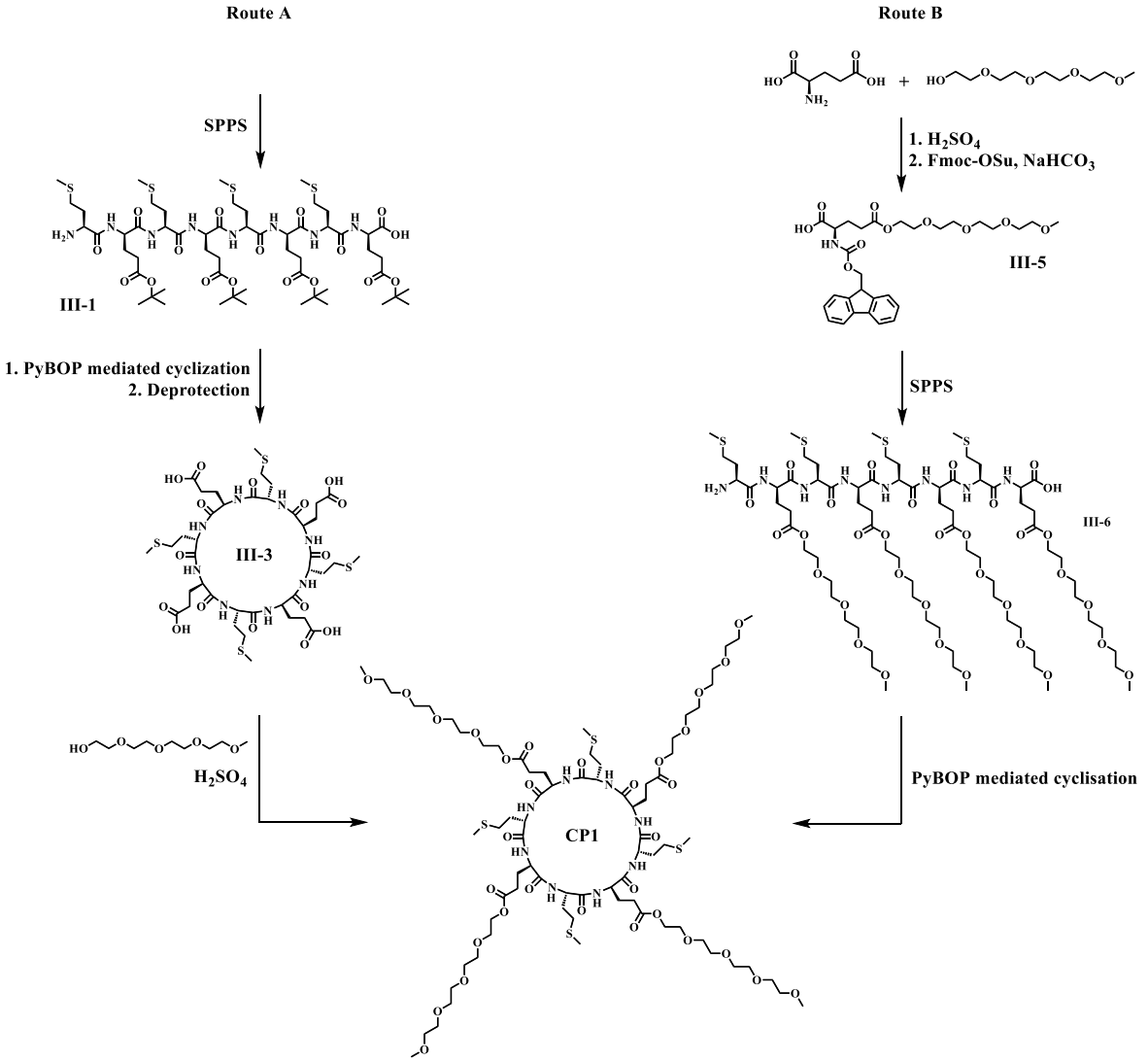

Figure 3.2: *Synthetic strategy of route A and B for* ***CP1****.*

The initial approach was to follow synthesis route A (figure 3.3). Linear peptide **III-1** was synthesized *via* automated solid-phase peptide synthesis, employing the Fmoc protocol. HATU/HOBt was selected as coupling reagent and a polystyrene resin modified with a 2-chlorotrityl linker was utilized for the synthesis. This allows the peptide to be cleaved from the resin under milder conditions, such as a 30% TFE solution in DCM, without the loss of protecting groups. It was of high importance that the *tert*-butyl ester protecting groups on the glutamic acid side chains be retained for the subsequent cyclization process; otherwise, oligomerization of peptide chains may occur *via* the carboxylic acid of the free glutamic acid residues. The cyclization method was chosen under highly diluted conditions to reduce side reactions, preventing peptide oligomerization, and favoring intramolecular ring closure. PyBOP was selected as the coupling reagent for the cyclization of the linear peptide chain, as no pre-activation of the N-terminus is required in this case. Nevertheless, the required reaction times, which may span several days, are necessary to ensure complete cyclization. To prevent oxidation of the thioethers present in the methionine side chains, the reaction is conducted in an internal nitrogen atmosphere. Afterwards, the *tert*-butyl protecting groups are removed from the glutamic acid side chains using TFA/TIPS/H_2O/EDT (reagent L)[5]. The resulting acid groups were esterified in a final step using acidic esterification with tetraethylene glycol monomethyl ether.

To prevent the undesired oxidation of methionine to its corresponding sulfoxide during deprotection, EDT was added as a reducing agent.

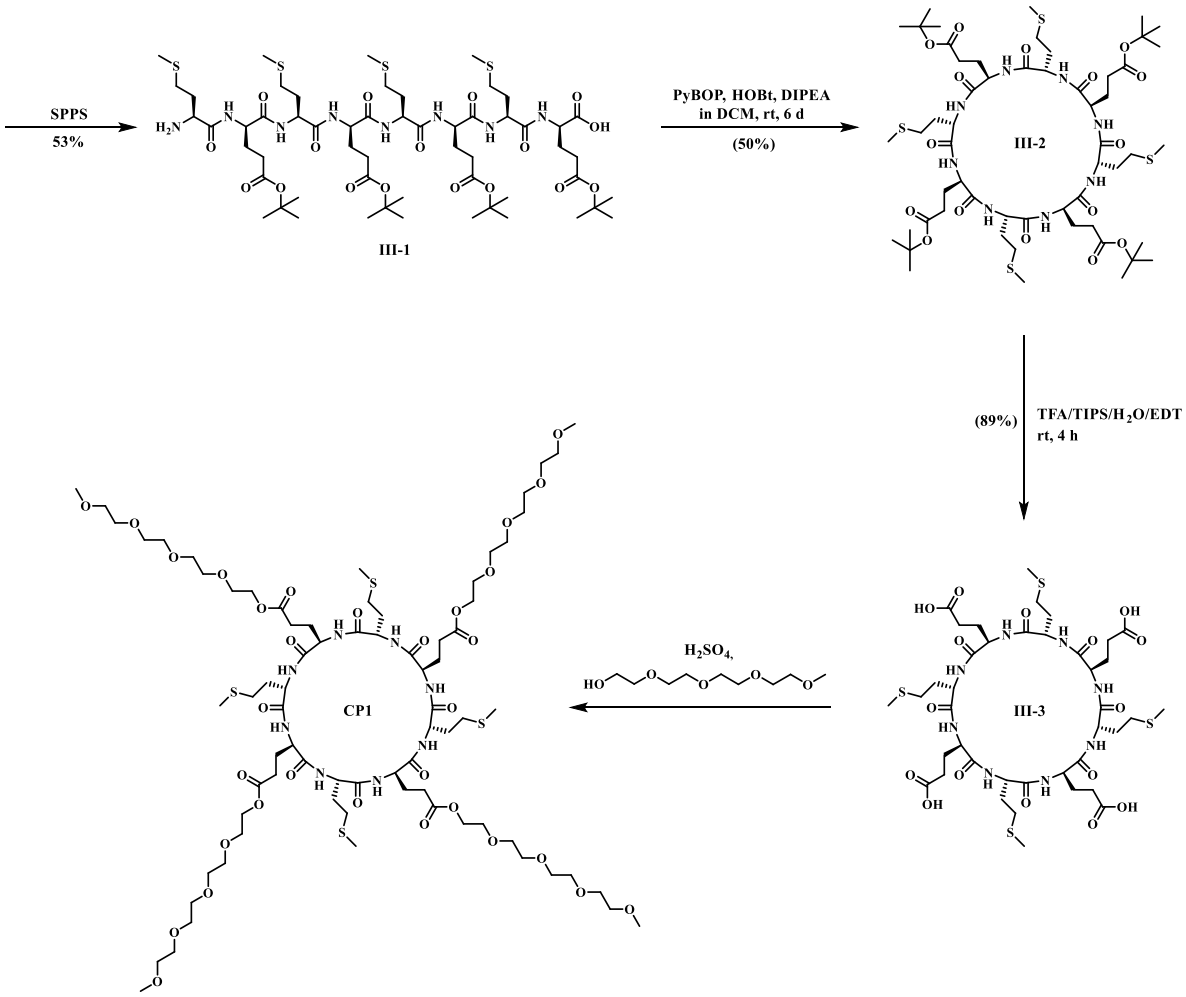

Figure 3.3: *Synthesis of* ***CP1*** *based on route A.*

Linear peptide **III-1** was synthesized *via* solid-phase peptide synthesis, resulting in a yield of 53%. The cyclisation process proved to be challenging, as the linear peptide obtained showed poor solubility in the common polar protic and aprotic solvents, including H_2O, DMF, DCM, DMSO, ACN, and the apolar solvents dioxane and THF. Nevertheless, an attempt was made to carry out the cyclization reaction to **III-2** in DCM at a concentration of 1 mg/mL. Due to the insufficient solubility of the peptide, it was not possible to

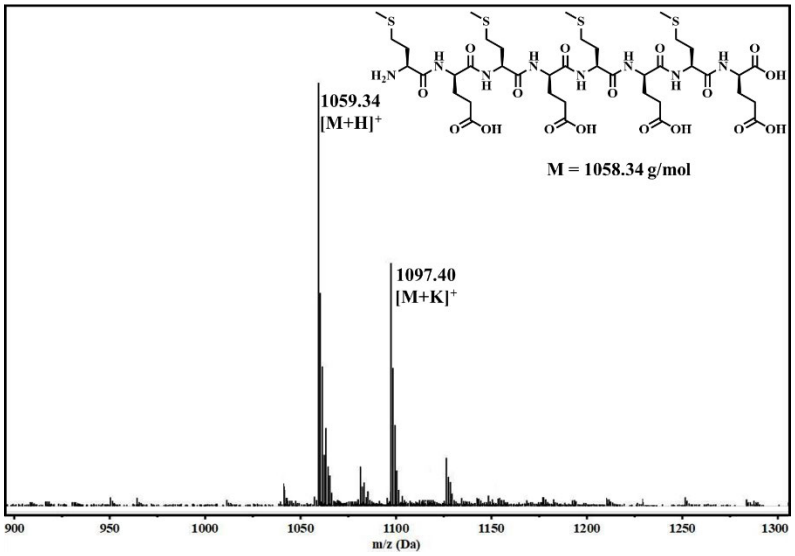

Figure 3.4: *ESI-MS spectrum (pos.) of* ***III-3*** *after cyclization attempt and deprotection.*

monitor the reaction progress. Consequently, the cyclization process was stopped after six days. The product was precipitated in cold diethyl ether and deprotected directly with TFA/TIPS/H_2O/EDT without further analysis, yielding **III-3**. Due to its low solubility, it was not possible to identify the protected cyclopeptide **III-2**. Following the deprotection of **III-3**, the solubility of the compound increased sufficiently to allow analysis by NMR-spectroscopy, mass spectrometry, and analytical RP-HPLC. After the deprotection process, the ESI-MS spectrum of the resulting product (figure 3.4) showed the fully deprotected linear peptide, indicating that cyclization did not occur. It was not possible to determine whether the unsuccessful cyclization was due to the poor solubility of the compound or of the chosen coupling reagents were unsuitable.

Considering these challenges, the initial decision was made to drop synthesis route A and to pursue synthesis route B instead. In order to produce linear peptide **III-6** with esterified glutamic acid side groups, it is first necessary to synthesize the Fmoc-protected amino acid **III-5** in two steps from D-glutamic acid for solid-phase peptide synthesis (figure 3.5).

In the initial step, D-glutamic acid is reacted at the carboxylic acid group in the γ-position with tetraethyleneglycol monomethyl ether to form ester **III-4** in an acidic esterification using concentrated sulfuric acid.[106] The protonation of the amino group (p*K*a (NH_3^+)=9.96[107]) under acidic conditions enables regioselective esterification.

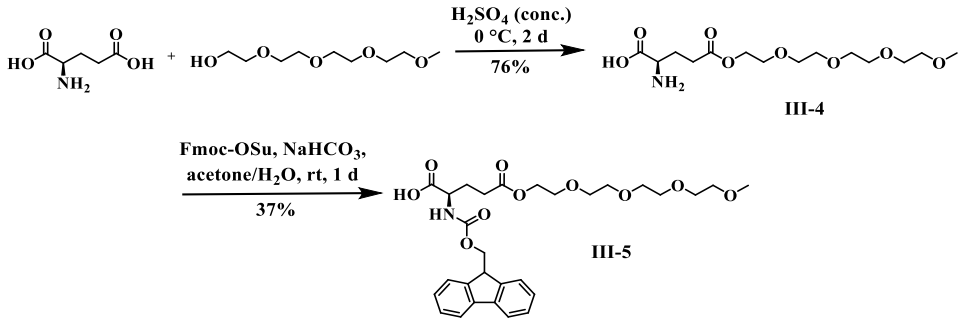

Figure 3.5: *Synthesis of* ***III-5****.*

On the one hand, this results in electrostatic repulsion between the attacking nucleophilic hydroxyl group and the ammonium ion. On the other hand, the carbonyl oxygen in γ-position is more easily protonated, as there is no -I-effect of the amine, and therefore can be attacked more easily.[108] In this acidic esterification process, as described by E. FISCHER[109], a yield of 76% of compound **III-4** was observed. To utilize amino acid **III-4** in SPPS according to the Fmoc protocol, it is necessary to protect the N-terminus with a base-labile Fmoc protecting group. In the second step, **III-4** is converted to target molecule **III-5** *via* active ester Fmoc-OSu in a slightly basic environment. Following purification by column chromatography, the amino acid was obtained in high purity in a yield of 37%.

Synthesis of linear peptide **III-6** was carried out using a polystyrene resin with a 2-chlorotrityl linker in the Fmoc protocol, utilizing HBTU/HOBt as previously described. In this instance, the selection of the acid-labile linker is of primary importance for the efficient release of the peptide from the resin, as it allows cleavage under mild conditions, minimizing the risk of ester bond hydrolysis. Linear peptide **III-6** was obtained in a yield of 26% using this method after purification by column chromatography.

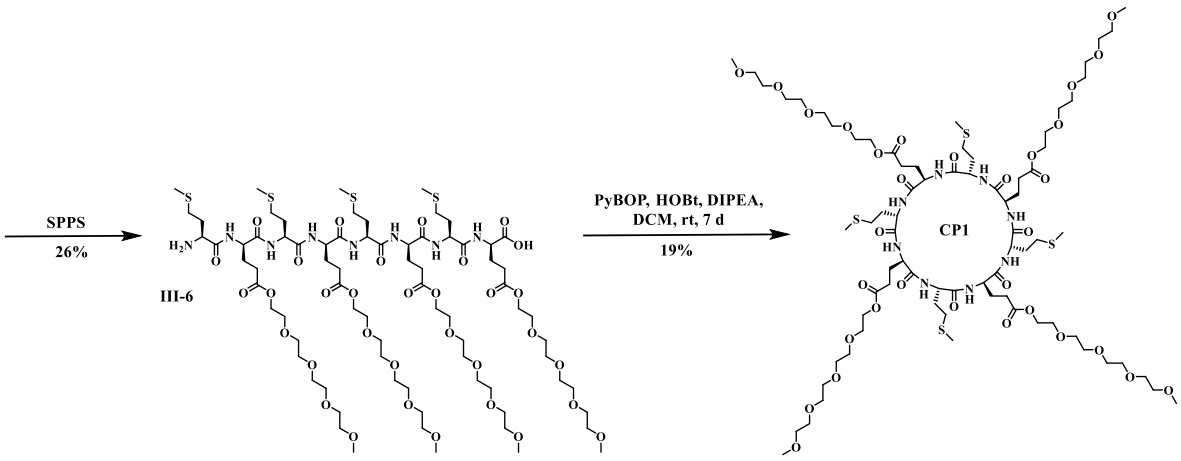

Figure 3.6: *Cyclization of* ***CP1****.*

III-6 exhibits improved solubility compared to **III-1**, which is particularly important for monitoring the progress of the cyclization reaction. PyBOP-mediated amide coupling in DCM under a nitrogen atmosphere was also used for the cyclization of **CP1**, and the reaction progress was monitored by RP-HPLC. After seven days, the RP-HPLC analysis shows full conversion to the cyclic product. Purification of **CP1** proved to be a challenge due to its insolubility in conventional solvents. The compound was only soluble in DMSO under highly diluted conditions. **CP1** was obtained with a yield of 19%. As shown in figure 3.7A, the ^{1}H-NMR spectrum of **CP1** reveals a broadening of the most proton signals, a phenomenon commonly observed in cyclic peptides that exhibit pronounced aggregation behavior in a majority of solvents, including DMSO.[110,111] Mass spectrometry provides a more effective identification method compared to NMR analysis, as **CP1** can be detected as a sodium and potassium salt, as shown in Figure 3.7B.

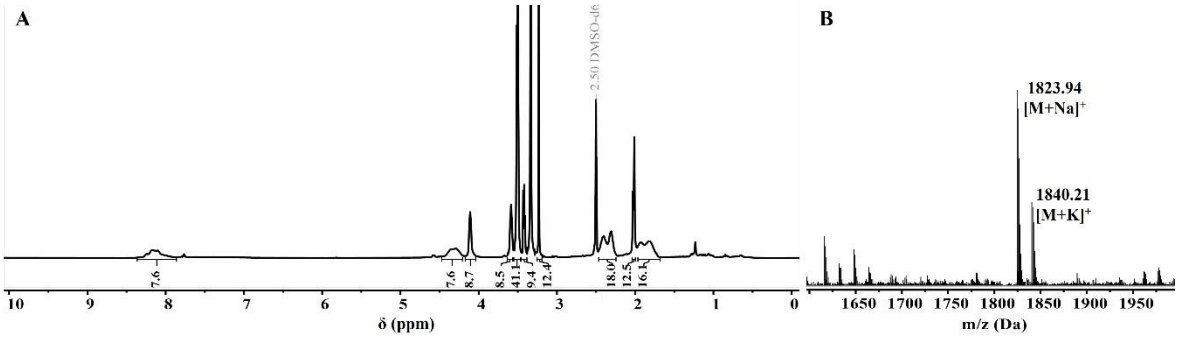

Figure 3.7: ***A*** *^{1}H-NMR spectrum and* ***B*** *ESI-MS spectrum (pos.) of* ***CP1****.*

Following successful isolation of **CP1**, an investigation was carried out to examine the assembly behavior in aqueous solution. To investigate the formation of nanotubes and the morphology of potential aggregates, transmission electron microscopy (TEM) was used to visualize structures in the nanometer range.[112]

Two solutions of **CP1** with a concentration of 200 µM and 300 µM were prepared using negative staining and subsequently analyzed. Both samples were subjected to an ultrasonic bath treatment for a period of three hours, followed by an overnight incubation period at room temperature. The 200 µM sample was observed to be completely soluble. However, the TEM images did not show any ordered structures at this concentration. As shown in Figure 3.8B and C, aggregates are visible, but these do not correspond to the defined nanotubes. In contrast, the 300 µM sample was cloudy, indicating that

CP1 is not completely dissolved. TEM images show the presence of superstructures indicating a lateral and two-dimensional organization imposed by the tetraethyleneglycol chains. Figure 3.8D illustrates the presence of fiber-like structures in bundles. Similarly, bundles to sheets of a similar nature can be observed in figure 3.8E. It is important to note, however, that these ordered superstructures were observed only in a limited number of TEM samples, suggesting that their formation is not very consistent under these conditions. The behavior of CP1, which is soluble at 200 µM but does not form superstructures, but aggregates into supramolecular nanotubes at 300 µM, can be explained by the critical aggregation concentration (CAC).[113] Below the CAC, the cyclopeptide molecules are predominantly present as monomers in solution, whereas above the CAC, spontaneous aggregation into ordered structures such as nanotubes is promoted. In this case, the CAC of **CP1** seems to be between 200 µM and 300 µM. This behavior is characteristic of supramolecular systems in which aggregation is strongly dependent on monomer concentration.[114]

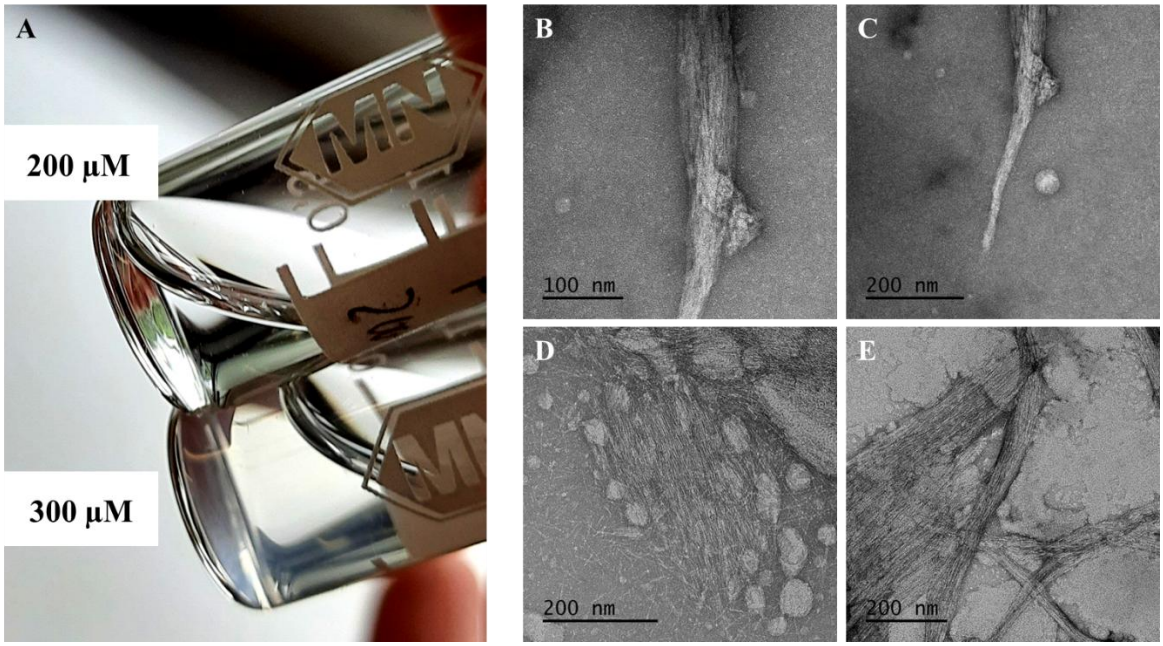

Figure 3.8: *Solubility and assembly behavior of **CP1** in water; **A** 200 µM and 300 µM solutions; **B-C** TEM images of a 200 µM solution in water (negative stain); **D-E** TEM images of 300 µM solution in water (negative stain).*

To address limitations observed in the previous design and improve the assembly properties, tryptophane was introducted in the peptide sequence. The incorporation of aromatic groups into the peptide can facilitate assembly by interacting with each other *via* π-π interactions to promote lateral aggregation. Tryptophan is a naturally occurring, highly hydrophobic amino acid that contains an indole group in its side chain and can therefore carry out such interactions. This will be exploited in the following by modifying the peptide sequence of the cyclopeptide (figure 3.9). The replacement of two synthetic amino acids (**III-5**) with two tryptophanes in the peptide sequence to form cyclo-[(L-Met-D-Trp-L-Met-D-Glu(-COO-TEGOMe))$_2$-] (**CP2**) has the additional effect of increasing hydrophobicity. The hydrophilic ethyleneglycol chains extend outward, interacting with water molecules to enhance solubility and create favorable conditions for controlled self-assembly in water, while preventing excessive aggregation that could lead to precipitation.

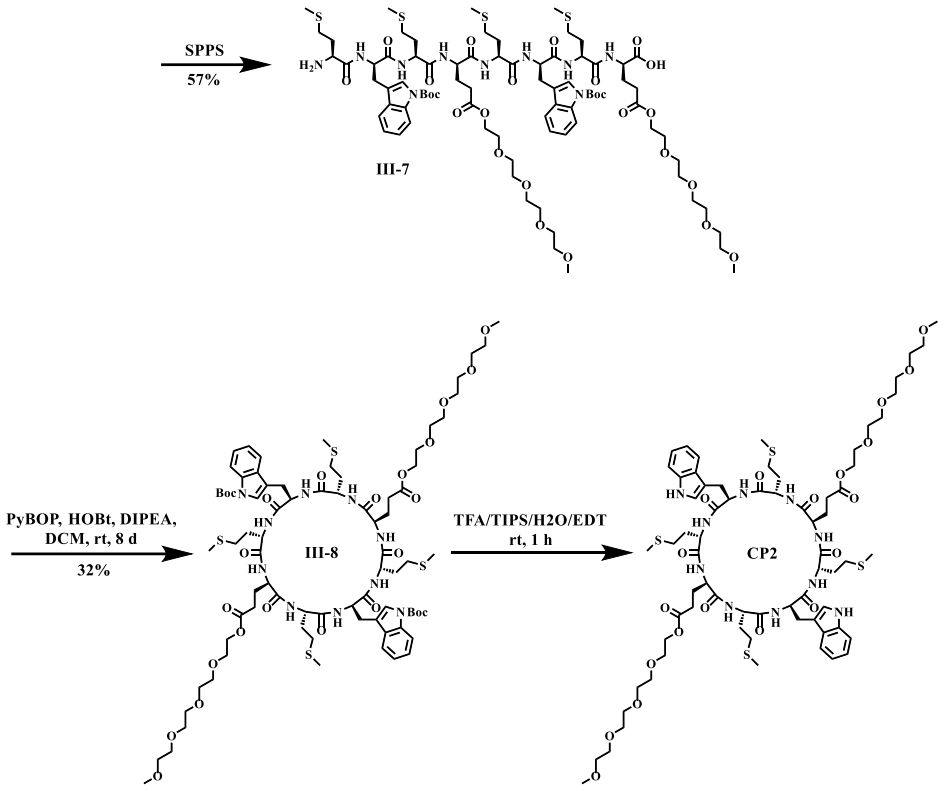

Figure 3.9: *Synthesis of* ***CP2****.*

Linear peptide **III-7** was synthesized *via* SPPS following the previously described methodology. Cleavage of the peptide from the resin was achieved using a TFE/DCM mixture, yielding 57% of the desired product. Cyclization of the resulting peptide **III-8** was performed over a period of eight days using PyBOP as the coupling reagent. Following cyclization, Boc protecting groups on the tryptophan residues were removed *via* treatment with TFA/TIPS/H_2O/EDT. This deprotection step also resulted in simultaneous cleavage of the glutamic acid ester groups. MALDI-TOF-MS measurements of the product (see appendix figure 10.7) confirmed the successful deprotection and the presence of double-, single-, and unesterified cyclic peptide species, highlighting the impact of ester cleavage during TFA treatment. The ester groups in the glutamic acidic residues were hydrolyzed under these acid conditions, making this synthetic route unsuitable for the preparation of **CP2**.

3.2.2 Amide conjugation of tetraethyleneglycol to cyclopeptides

As an alternative to the labile ester bond, an amide bond was introduced for conjugation between glutamic acid and tetraethyleneglycol to form the L-amino acid **III-13**. This compound exhibits properties nearly identical to those of the previously used amino acid **III-5**. The additional amide bond introduces another hydrogen donor and acceptor, potentially influencing the assembly of supramolecular nanotubes. Since the starting material for **III-13** synthesis is only commercially available in the L-configuration, we opted for a design where both **III-13** and tryptophan retain this configuration, while methionine in the peptide sequence has the D-configuration, to ensure the D,L-alternating structural motif. The subsequent peptide synthesis and cyclization to cyclopeptide **CP3** follow the same method previously described for **CP2** (figure 3.10).

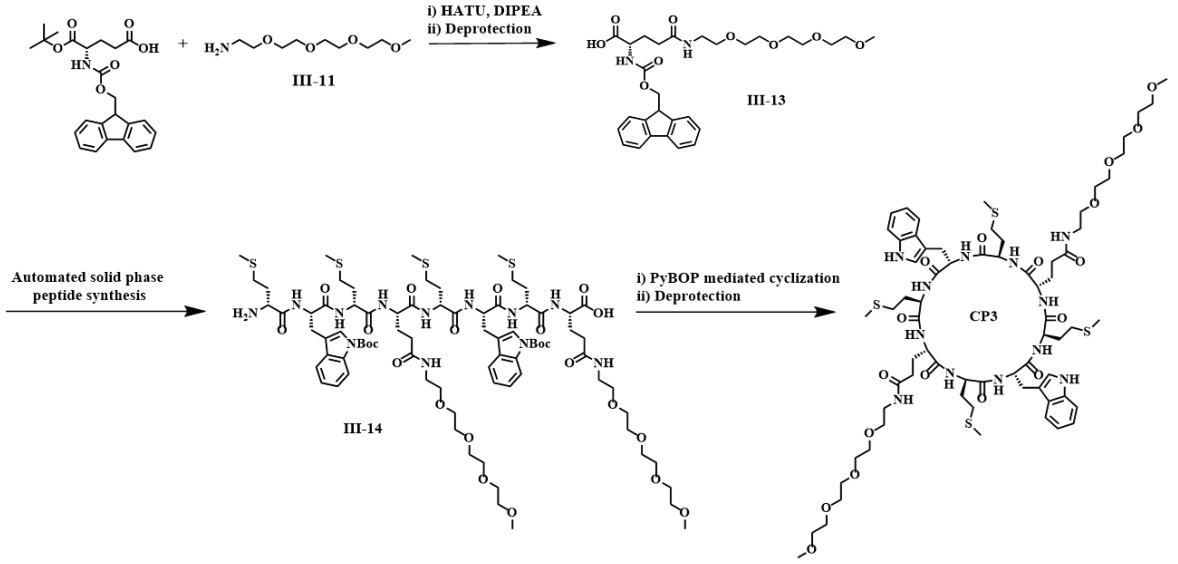

Figure 3.10: *Synthesis scheme of* ***CP3****.*

Synthesis of amine **III-11**, initiated from tetraethyleneglycol monomethyl ether, has been previously published by the BESENIUS group.[115] In the initial step the alcohol group undergoes tosylation to **III-9**, enabling the incorporation of a suitable leaving group, which is converted to an azide (**III-10**) by a S_N2 reaction with sodium azide. The final modification to amine **III-11** is achieved by a STAUDINGER reduction.[116] The multi-step synthesis of amine **III-11**, shown in figure 3.11, was achieved in yields over 50% in all steps. To ensure that the amidation with **III-11** can exclusively occur at the unprotected carboxylic acid in γ-position, Fmoc-Glu-O*t*Bu was selected as the starting compound. For the amidation reaction, HATU was chosen as the coupling reagent. To enable the utilization of the resulting amino acid **III-12** in solid-phase peptide synthesis, the carboxylic acid in α-position is deprotected using an acidic deprotection mixture comprising TFA, TIPS, and H_2O to yield compound **III-13**.

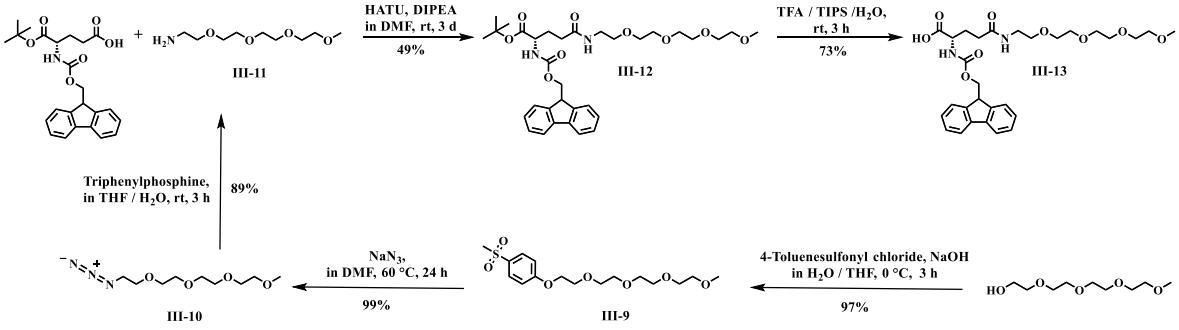

Figure 3.11: *Synthesis of* ***III-13****.*

Figure 3.12 illustrates the ^{1}H-NMR and 2D-COSY-NMR spectra of the synthesized amino acid **III-13**. The amide proton, resulting from the newly formed amide bond, is marked with a blue dot. The ^{1}H NMR signals of the aromatic protons of the Fmoc protecting group, although partially covered and therefore difficult to detect directly, can be seen in the 2D-COSY NMR spectrum through their coupling with the yellow-labeled adjacent CH_2 protons near the amide bond, allowing for clear assignment. Similarly, the orange-labeled proton of the Fmoc-protected amine is identified through its coupling with the neighboring protons of the α-carbon, marked in violet, while the green-labeled proton of the deprotected carboxylic acid is observed in the downfield region at nearly 12,7 ppm.

These spectra not only confirm the successful formation of the amide bond but also verify the retention of the Fmoc protecting group, demonstrating that the mildly basic conditions during the amide coupling reaction did not compromise its stability.

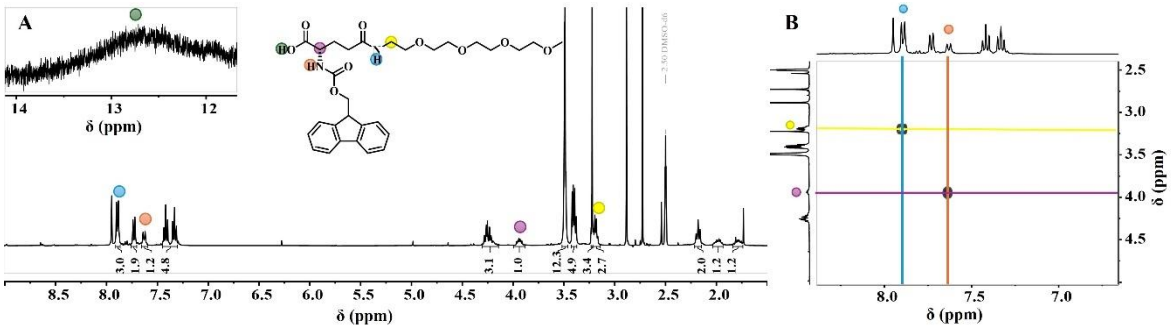

Figure 3.12: *Analytic of* ***III-13****. **A** [1]H-NMR spectrum; **B** COSY spectrum.*

Following the successful synthesis of **III-13**, peptide **III-14** was prepared *via* SPPS under identical conditions to those used for the synthesis of **III-7**, with a yield of 61%. Once more, the amidation reaction for cyclization was conducted using PyBOP as the coupling agent (figure 3.13).

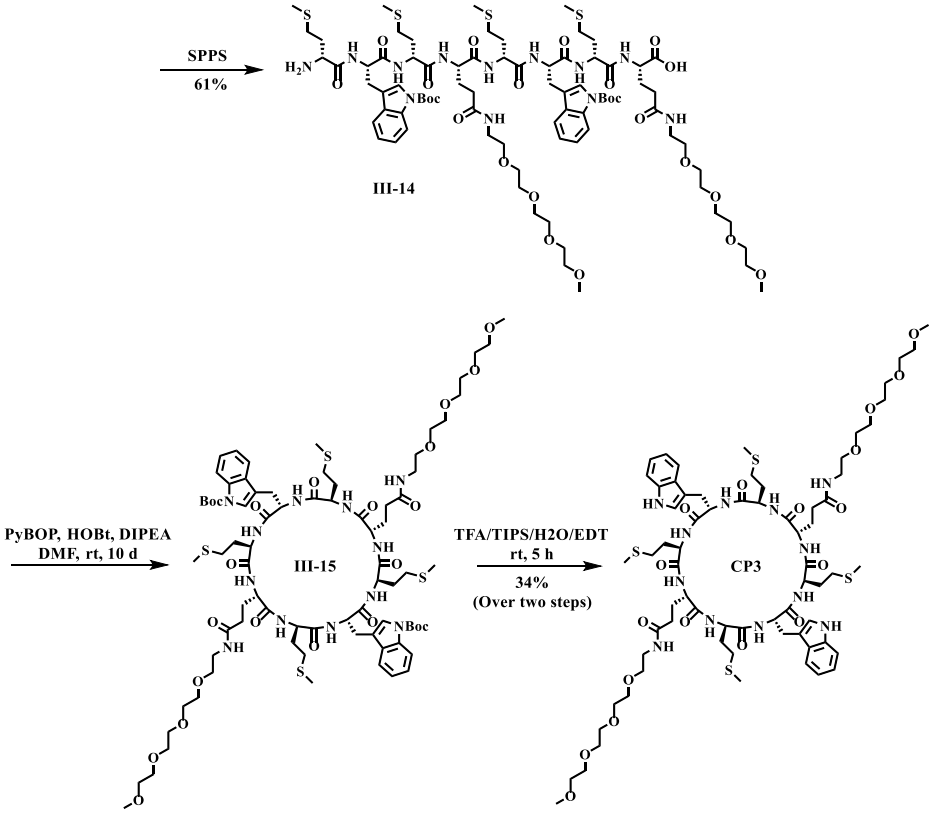

Figure 3.13: *Synthesis of* ***CP3****.*

The progress of cyclization was monitored by RP-HPLC. As a consequence of cyclization process, amidation and subsequent cleavage of a water molecule, the peptide is less hydrophilic, resulting in an increase in the retention time. Figure 3.14 represents the RP-HPLC chromatograms of linear peptide **III-14** (green) and the crude product of **III-15** (blue) following a 10-day reaction and work-up by precipitation in ice-cold ether. It is apparent that the blue chromatogram does not show any residue of the initial material **III-14**, suggesting complete cyclization. Furthermore, the cyclization process can be observed through optical means. To initiate the reaction, linear peptide **III-14** was dissolved in DMF with a addition of DIPEA. This solution was added slowly to a solution of the coupling reagents, also in DMF. The reaction mixture became increasingly turbid within 10 days, eventually forming a milky solution. The protected cyclopeptide **III-15** exhibits significantly reduced solubility, as proven by the turbidity of the reaction mixture. Due to its poor solubility, no further analysis of **III-15** was carried out, and it was directly deprotected to obtain the desired cyclopeptide **CP3**.

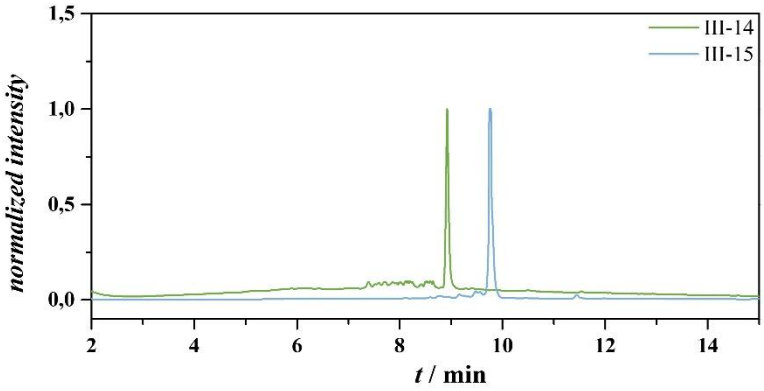

Figure 3.14: *Normalized analytical RP-HPLC chromatogram at λ=254 nm of **III-14** and **III-15** on a pyramid C18 (50 mm) gradient: 5% → 95% B in 5 minutes (solvent A: water + 0.1% TFA, solvent B: acetonitrile + 0.1%).*

Figure 3.15A and C show the ^{1}H-NMR spectrum of the protected linear peptide **III-14** and the cyclized deprotected peptide **CP3**, which are presented for comparison. The two spectra exhibit a high degree of similarity in their signal patterns. Boc protecting groups are indicated in green. The absence of this signal in **CP3** spectrum serves to confirm the successful cleavage of the protecting groups. Furthermore, the triplet ^{1}H-NMR signal of the CH group corresponding to the Cα protons next to the terminal amino group of the linear peptide is indicated in blue. Following the completion of the cyclization process, the ^{1}H signal is no longer visible, thereby confirming the successful cyclization of the process. The mass spectra (figure 3.15B and D) provide additional confirmation for formation of the two molecules. The ESI-MS spectrum of linear peptide **III-14** reveals the presence of both singly and doubly charged species. The mass spectrum of **CP3** was obtained using MALDI-TOF-MS. In this instance, a single positively charged species is also present. The synthesis of the cyclopeptide **CP3** was thus successfully completed.

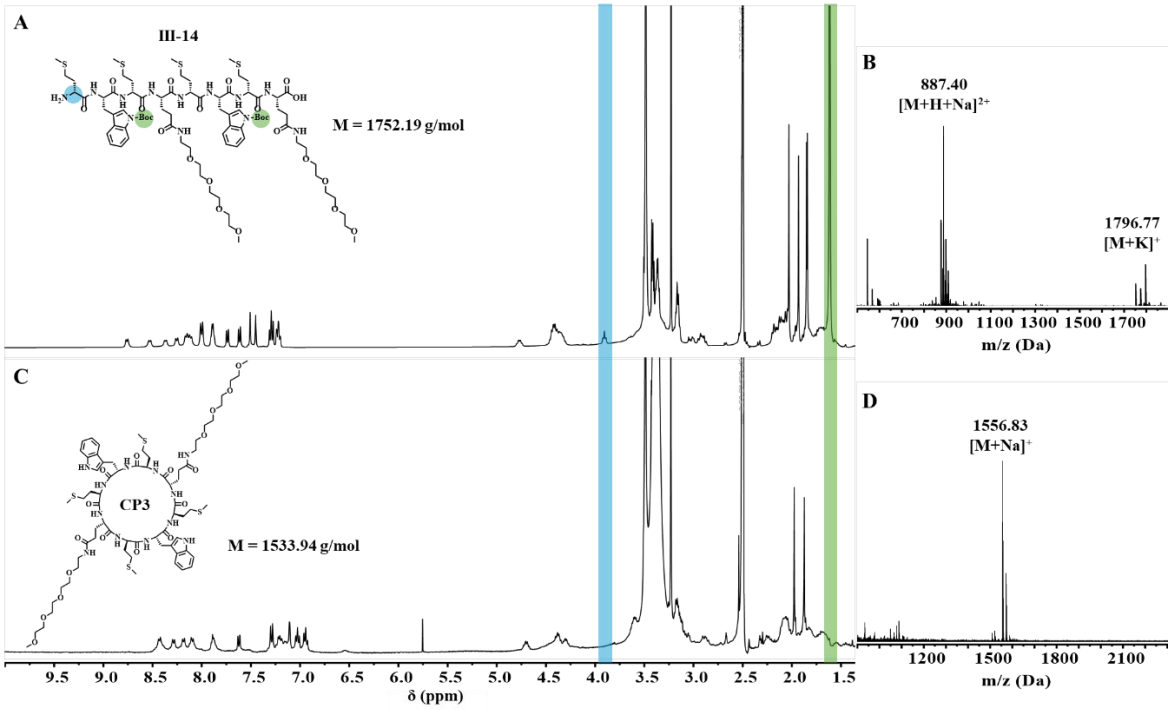

Figure 3.15: ***A*** *^{1}H-NMR spectrum of* ***III-14****;* ***B*** *ESI-MS spectrum (pos.) of* ***III-14****;* ***C*** *^{1}H-NMR spectrum of* ***CP3****;* ***D*** *MALDI-TOF-MS spectrum (pos.) of* ***CP3****.*

To analyze the formation of supramolecular structures by **CP3**, TEM images of a 100 µM solution in TRIS buffer were recorded. The limited solubility of the compound in water posed a significant challenge. To obtain a clear solution, the sample was treated in an ultrasonic bath at 80 °C for four hours, followed by centrifugation to remove undissolved particles (figure 3.16D). TEM images were taken both before and after the ultrasonic treatment to examine changes in the supramolecular structures (figure 3.16). Before the ultrasonic treatment (figure 3.16B-C), TEM images revealed well-defined tube-like nanostructures. These aggregates were predominantly isolated, with no signs of bundling. The average length of the structures was ±99.5 nm (n=44), although significant variability was observed. In addition to longer aggregates reaching up to 300 nm, shorter structures of approximately 30 nm were identified (see appendix figure 10.14). This heterogeneous distribution suggests that the aggregation of **CP3** is not fully controlled, potentially due to the limited solubility of **CP3**. After the ultrasonic treatment (figure 3.16E-F), a significant change in the structures was observed. No well-defined tube-like structures were visible, instead, unstructured and diffuse aggregates appeared. This change could be attributed to the mechanical stress of the ultrasonic treatment, which likely weakened the supramolecular bonds and caused fragmentation of the structures. The observed bundling and diffuse nature of the aggregates indicate enhanced lateral aggregation of the molecules. The results demonstrate that ultrasonic treatment has a substantial impact on the supramolecular structures. While well-defined nanostructures were present before the treatment, the mechanical stress led to fragmentation and reorganization of the aggregates. Additionally, the combination of ultrasound and elevated temperature may promote the oxidation of methionine residues, potentially contributing to structural degradation and formation of smaller assemblies.

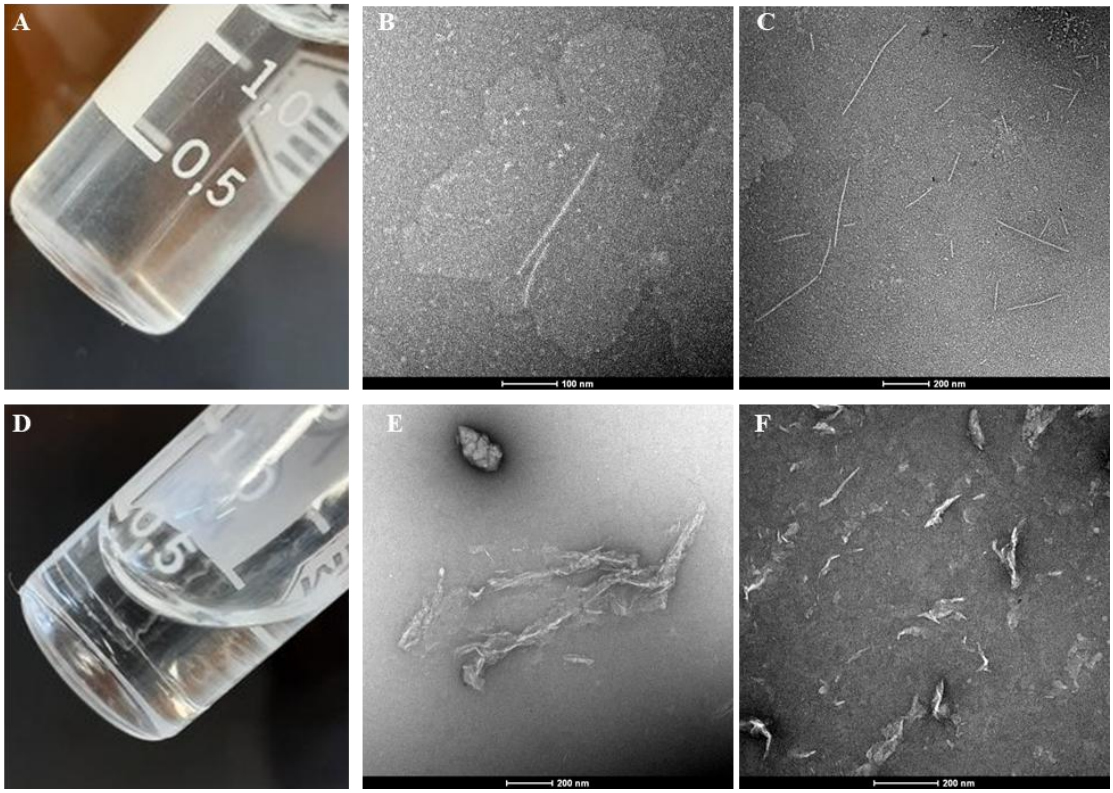

Figure 3.16: *100 µM solution of **CP3** in TRIS and TEM images **A-D** before sonication and **E-H** after heating for 4 h at 80 °C with sonication (negative stain).*

The analysis of supramolecular assemblies under the harsh conditions of 4 hours at 80 °C in an ultrasonic bath demonstrated that, while this method improves the solubility of **CP3**, it simultaneously compromises the integrity of the supramolecular structures, potentially due in part to the oxidation of methionine residues induced by ultrasound and elevated temperature. Therefore, solutions in alternative solvents and milder conditions were investigated to ensure the stability and reproducibility of the supramolecular aggregates. By switching to mixtures of water and TFE or hexafluoro-2-propanol (HFIP), the aim is to enhance the limited solubility of **CP3** and investigate its aggregation properties in the solvated state. TFE and HFIP were selected due to their slightly acidic nature and their ability to form strong hydrogen bonds between the peptides and the solvent molecules but at the same time providing solvation of hydrophilic side chains. These unique properties of the solvents offer two critical advantages: first, they facilitate the solvation of peptides, thereby increasing solubility, and second, they compete with the self-assembly of the peptides.[117,118] However, by mixing these organic solvents with water, a balance is sought where both supramolecular assembly and sufficient solubility of the peptide are achievable. These investigations were carried out in collaboration with [redacted].

To investigate supramolecular structures circular dichroism spectroscopy (CD spectroscopy) was used. This technique is based on the differential absorption of left-handed and right-handed-circularly polarized light by chiral molecules, providing insights into their conformational properties and aggregation behavior. The recording of spectra in ultraviolet range allows the secondary structures of biomolecules, including proteins and nucleic acids, to be determined. Nevertheless, the signals of different secondary structures often overlap in the resulting spectrum, which presents a challenge for clear identification. Characteristic CD spectra are known for the most common secondary structures in proteins, including the α-helix, β-sheet, and random coil, which allow for the differentiation of

these structures. Furthermore, CD spectroscopy can be employed to examine conformational alterations, folding mechanisms and protein-ligand interactions, thereby establishing it as a highly versatile biophysical technique in the field of structural biology.[119,120,121]

Figure 3.17A illustrates TFE solutions of **CP3** with varying volume fraction of water. Even in the absence of water, turbidity is evident, suggesting incomplete solvation. This phenomenon appears to intensify with the addition of water. To investigate the effect of water content on the supramolecular assembly behavior of **CP3**, a 70 µM solution in TFE was prepared and the water content was gradually increased. Then, CD spectra were recorded to analyze the structural changes depending on the water content (figure 3.17B). The spectra show two positive bands at approximately 234 nm and 283 nm. The signal at lower wavelengths is more intense and sharply defined, while the signal at higher wavelengths is broader. The signal at 234 nm is attributed to a n-π* transition of the amide groups, likely influenced by supramolecular hydrogen bonding interactions in the aggregational state.[122] The broad signal at 283 nm is assigned to a π-π* transition of the tryptophan residues, which may be influenced by π-π stacking interactions with other aromatic residues or hydrogen bonding with neighboring amides.[123] These signals reflect the electronic transitions of the peptide backbone and tryptophan residues. An increase in signal intensity suggests a more ordered supramolecular arrangement, as stronger electronic coupling between neighboring amides and tryptophan residues indicates enhanced structural organization stabilized by hydrogen bonding and π-π interactions. When the two signals at 234 nm and 283 nm are plotted as a function of increasing H_2O content (figure 3.17D), the signal intensities increase with increasing H_2O content. This indicates that increasing the volume fraction of H_2O promotes the formation of ordered superstructures. Furthermore, a slight bathochromic shift of the signals at 230 nm can be observed. It should be noted that CD measurements are dependent on the solvent used.[124,125] The addition of water to the sample also alters the solvent polarity and microenvironment, which allows not only the formation of ordered superstructures in solution, but also the slight shift of the signals. An additional potential explanation is the scattering behavior of precipitated particles. Figure 3.17C is a photograph of the CD cuvette containing a 100 µM solution comprising a 7:3 mixture of TFE and H_2O, which exhibits precipitation of solids. This is also a potential cause of a slight shift in the signal.

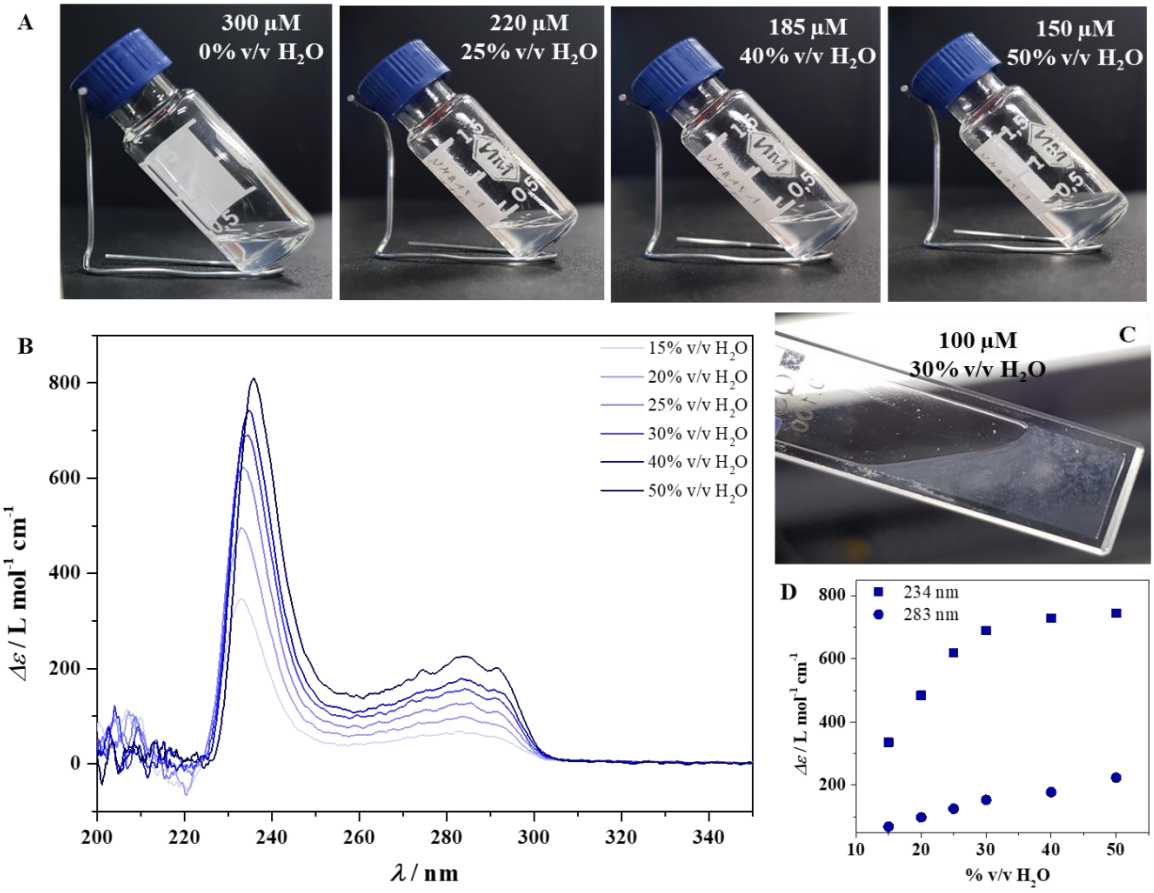

Figure 3.17: ***A*** *Solutions of* ***CP3*** *in TFE with different volume fractions of H_2O;* ***B*** *CD spectra of solutions of* ***CP3*** *in TFA with different volume fraction of H_2O;* ***C*** *CD cuvette of a 100 µM solution of* ***CP3*** *in TFE with 30% v/v H_2O;* ***D*** *CD signal at 234 nm and 283 nm depending on the volume fraction of H_2O.*

HFIP-water mixtures were selected as the second solvent mixture for further investigation. **CP3** exhibits excellent solubility in pure HFIP, forming a transparent solution. At a water content of 40% v/v, a slight turbidity is observed, which increases significantly to 50% v/v water (figure 3.18A). Similar to the TFE mixtures, the CD spectra of a 100 µM HFIP solution were recorded as the water content was gradually raised, to analyze the trends of the signals at 234 nm and 280 nm. For the signal at 234 nm, a comparable trend of growing intensity with higher water content was observed. Additionally, a shift in the CD signal was detected, which was more pronounced compared to the TFE mixtures. In contrast, the trend of the broad signal at 280 nm did not continue with greater water content, as shown in figure 3.18D. At a water content of 50% v/v, the signal intensity showed a further decline. This observation suggests that increasing the water content may promote the formation of ordered superstructures. However, the addition of water also led to precipitation, as evidenced by the solid phase observed in the CD cuvette of the 100 µM solution at 50% v/v water content (figure 3.18C).

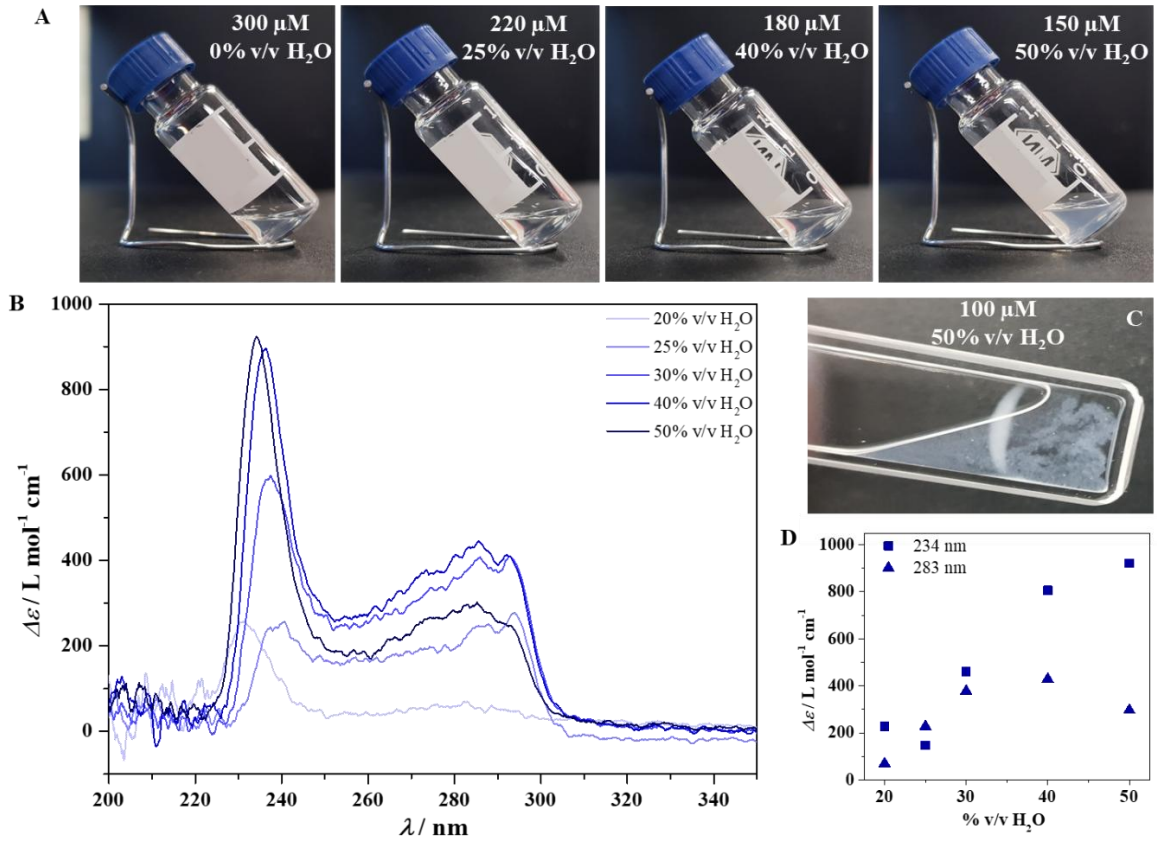

Figure 3.18: *A Solutions of **CP3** in HFIP with different volume fractions of H_2O; **B** CD spectra of solutions of **CP3** in HFIP with different volume fraction of H_2O; **C** CD cuvette of a 100 µM solution of **CP3** in HFIP with 50% v/v H_2O; **D** CD signal at 234 nm and 283 nm depending on the volume fraction of H_2O.*

The incorporation of methionine residues in the peptide structure of **CP3** provides an opportunity to study the impact of thioether group oxidation on supramolecular assemblies of cyclopeptides. Oxidation converts methionine into methionine sulfoxide, resulting in altered hydrophobicity and hydrogen-bonding properties, which can profoundly influence self-assembly behavior. Hydrogen peroxide was selected as the oxidizing agent for this investigation. To examine the behavior of the peptide under oxidative conditions, it was first to confirm the successful oxidation of **CP3** to its sulfoxide derivative, **CP3^{ox}**.

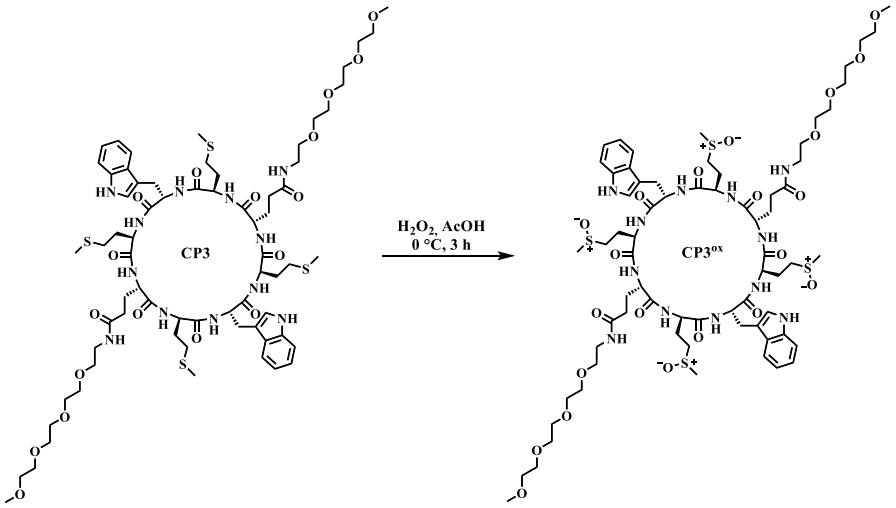

Figure 3.19: *Oxidation of **CP3** to **CP3^{ox}**.*

For this purpose, **CP3** was dissolved in a mixture of hydrogen peroxide and acetic acid (figure 3.19) and subsequently analyzed *via* LC-MS after three hours to confirm the formation of sulfoxides (figure 3.20).

A

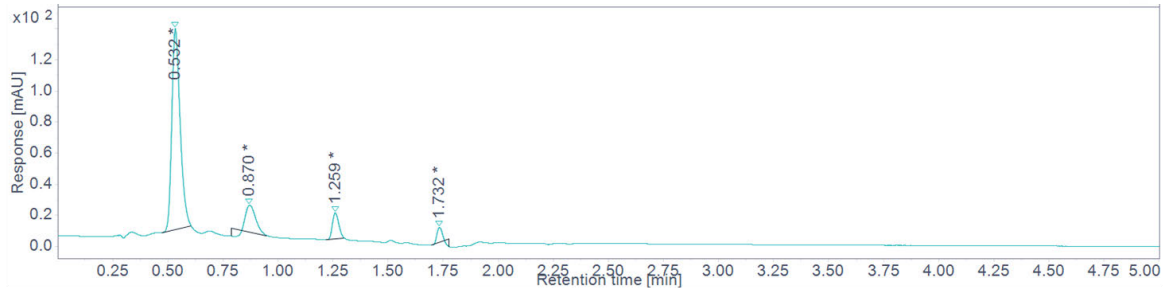

B

	calc. $[M+2H]^{2+}$	found $[M+2H]^{2+}$	Ret. time / min
CP3	767.98	-	-
CP3 1 x oxidized	775.98	775.5	1.25
CP3 2 x oxidized	783.98	783.5	0.53
CP3 3 x oxidized	791.97	-	-
CP3 4x oxidized ($CP3^{ox}$)	799.97	799.6	1.73

Figure 3.20: ***A*** *LC-MS chromatogram of the reaction mixture after 3 hours of oxidation of* ***CP3*** *to* ***CP3^{ox}*** *using H_2O_2 and AcOH (method F);* ***B*** *Table listing the calculated molecular weights of* ***CP3*** *species with varying numbers of oxidized methionine residues and the experimentally observed m/z values of the signals from spectrum shown in A.*

After 3 hours of reaction, the fully oxidized product (**CP3^{ox}**), as well as the singly and doubly oxidized species, were detected (figure 3.20B). The results indicate that the initial oxidation of a single thioether to its sulfoxide proceeds efficiently. However, oxidation of all methionine residues is not complete after a reaction time of 3 hours. It was demonstrated that complete oxidation of the methionines is possible but requires longer reaction times. These observations align with the findings of Luo *et al.*,[126] who showed that methionine oxidation is strongly influenced by the local molecular environment. Factors such as steric accessibility and interactions with neighboring groups, such as tryptophan and tetraethylene glycol side chains, can affect the oxidation rate and slow down the reaction.

TEM images of a 70 µM solution of **CP3** in a 7:3 (v/v) HFIP/water mixture were taken both before and after oxidation for 24h with H_2O_2 to its sulfoxide derivative, **CP3^{ox}**, to investigate the supramolecular superstructures in detail and to validate the hypothesis that oxidation of the thioether groups destabilizes the supramolecular structures (figure 3.21). In TEM images before oxidation (figure 3.21A-B), the structures reveal long, interconnected, almost reticular arrangements of nanotubes. These formations arise from the self-assembly of **CP3**, supported by hydrogen bonding. Most likely, the lateral aggregation of aromatic tryptophan side chains contributes to this organization, resulting in highly bundled, fiber-like structures. After oxidation of the methionine side chains (figure 3.21C-D), a significant disruption is observed. TEM images show the disappearance of the extended network structures and the appearance of shorter, predominantly bundled rod-like arrangements. This structural change is attributed to the increased hydrophilicity of the cyclic peptide, along with changing electrostatic and steric interactions of the oxidized methionine residues to reduce the cyclopeptide's driving force for aggregation.

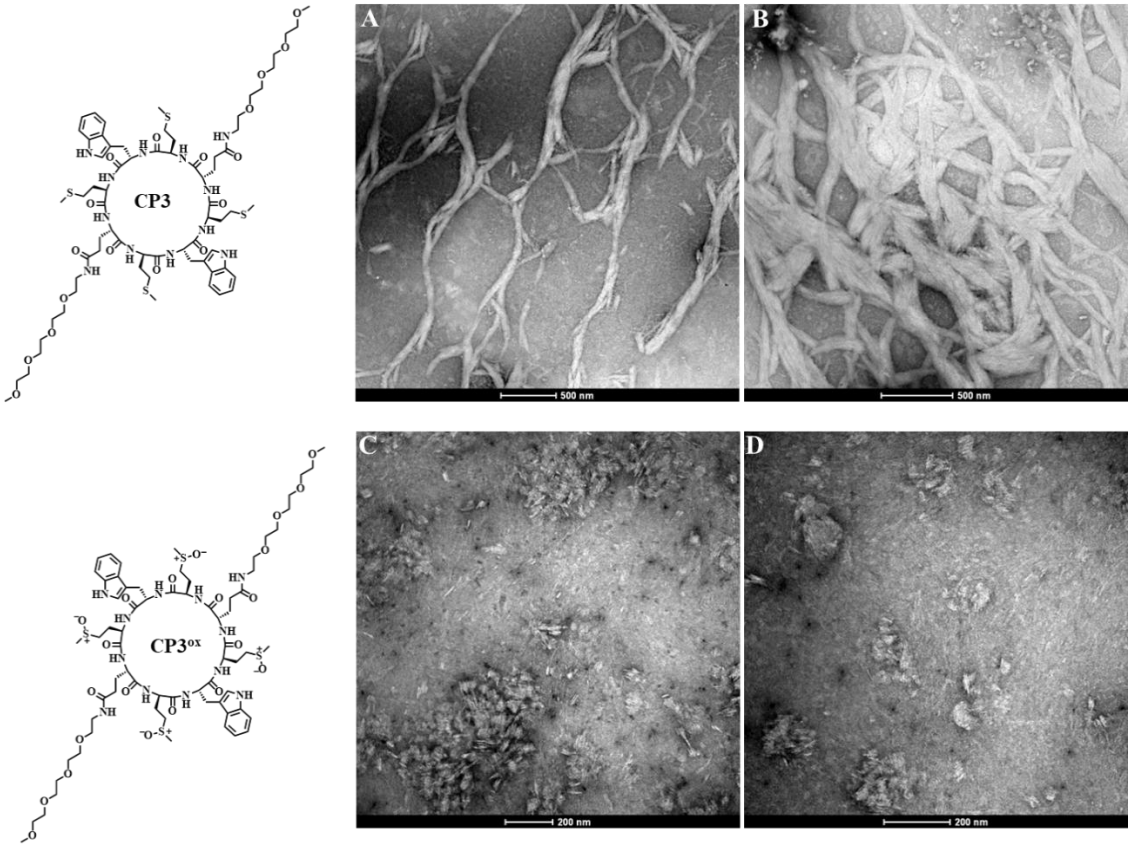

Figure 3.21: *TEM images of* ***A-B CP3*** *60 µM 7:3 v/v (HFIP/H_2O);* ***C-D CP3^{ox}*** *70 µM (HFIP/H_2O) after addition of H_2O_2 (negative stain).*

A key focus of this study was the time-dependent disassembly behavior during oxidation. To investigate this, circular dichroism spectroscopy measurements were performed over a 24-hour period after addition of hydrogen peroxide, with spectra recorded at 30-minute intervals (figure 3.21). This approach enables continuous monitoring of the disassembly process, offering a dynamic perspective in contrast to TEM images, which capture structural information at only two discrete time points. The CD spectrum after 0 minutes (figure 3.22A) again shows the two previously observed signals. An n-π* transition at 234 nm, associated with the amide groups in the peptide backbone and influenced by supramolecular hydrogen bonding interactions, and a π-π* transition at 283 nm, attributed to the aromatic tryptophan residues and their interactions. Upon addition of hydrogen peroxide, the oxidation of the methionine side chains destabilizes the supramolecular structures. This destabilization is reflected in a gradual decrease of the signal intensities at 234 nm and 283 nm over time. The signal at 234 nm shows the most pronounced decline until approximately 150 minutes, after which the intensity decreases more slowly. This suggests that structural disassembly occurs most rapidly during the initial phase of oxidation, with a slower progression thereafter. Although complete disintegration of the structures was not observed after 390 minutes, the process continued, and measurements taken at the end of the 24-hour period (black curve) showed a CD spectrum with a weak positive signal at 210 nm. While this is typically attributed to a transition into a random coil structure[127], it is possible that residual ordered structures or partially aggregated states contribute to this signal. The corresponding TEM images confirm the presence of residual structures after 24 hours.

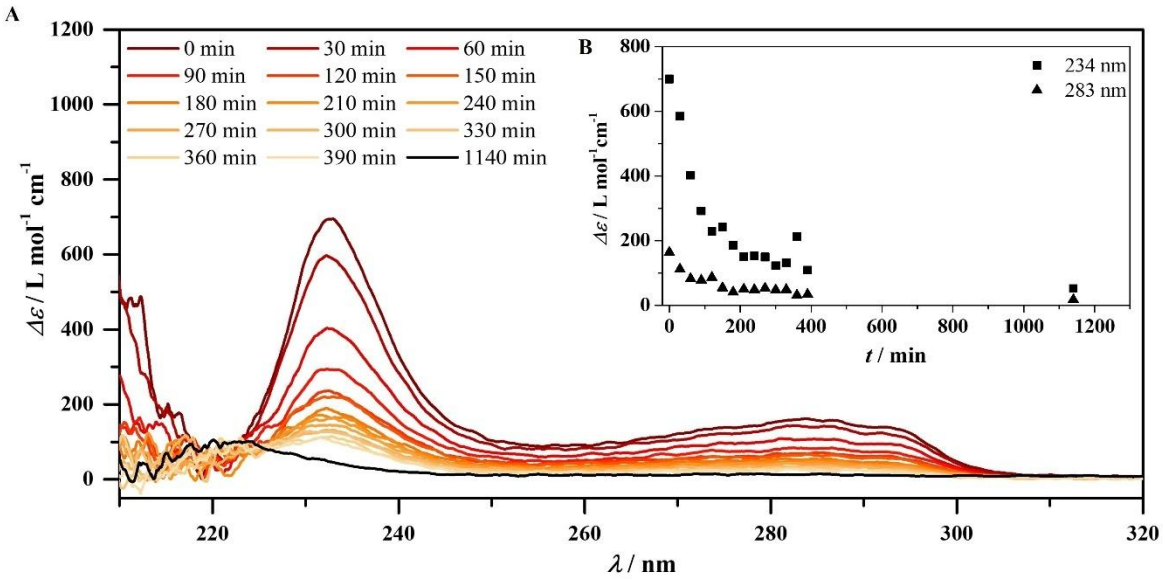

Figure 3.22: ***A*** *CD spectra of solutions of* ***CP3*** *in HFIP/H_2O (7:3 v/v) after addition of 24 mM H_2O_2. The spectra were analyzed every half hour over a period of 6.5 hours and after 24 hours;* ***B*** *CD signal at 234 nm and 283 nm depending on time.*

In addition, figure 3.22B plots the signal intensities at 234 nm and 283 nm as a function of time, further illustrating the progressive decay of the supramolecular network. The steady reduction in these CD-signals and the acquired TEM images demonstrate the successful gradual disassembly of the supramolecular nanotube network **CP3** by an oxidative stimulus.

3.3 Conclusion

Oxidation-sensitive structures offer a promising approach in drug delivery research. In combination with biocompatible materials, they enable the development of systems that can be triggered by oxidative stress in tumor microenvironments.[128] Peptide-based materials are particularly suitable for these applications due to their composition from naturally occurring building blocks and their high biocompatibility.[129] Cyclic peptides exhibit notable stability as they lack free N- and C-termini, making them resistant to exonuclease-mediated degradation under physiological conditions.[130] D,L-alternating cyclic peptides containing α-amino acids show strong tendencies for supramolecular self-assembly, leading to the formation of supramolecular nanotubes. This property makes them a promising class of carrier structures, though their limited solubility in aqueous media remains a challenge.

This chapter introduced cyclopeptide-based supramolecular systems containing methionine as an oxidation-sensitive amino acid and examined their solubility in aqueous media in detail. The cyclopeptides **CP1** and **CP3** were successfully synthesized. **CP1**, composed of L-methionine and the synthetic amino acid D-Glu(COO-TEGOMe) **III-3**, did not form pronounced superstructures in aqueous media, as confirmed by TEM images. In contrast, **CP3**, which includes the aromatic amino acid tryptophan, demonstrated the ability to assemble into supramolecular nanotubes, albeit with significantly lower water solubility. Solubility was further enhanced using solvent mixtures such as HFIP/water and TFE/water. CD spectroscopy revealed that higher water content promoted the formation of supramolecular structures, but concurrently reduced **CP3**'s solubility. Oxidation of the methionine side chain's thioether groups destabilized these superstructures. In HFIP/water mixtures, **CP3** formed nanotubes arranged in a network with strong lateral aggregation. Upon addition of H_2O_2, these structures were largely dissolved, leaving shorter nanotube bundles. Time-dependent CD spectroscopy demonstrated that these structures completely disassembled within 24 hours.

The comparison of **CP1** and **CP3** underscores that including tryptophan in the peptide sequence facilitates the formation of supramolecular assemblies but at the expense of reduced water solubility. The oxidation behavior was specifically investigated for the tryptophan-containing system, highlighting its response to oxidative conditions.

However, the desired solubility was not achieved, necessitating the use of solvent mixtures such as TFE/H_2O and HFIP/H_2O to improve dissolution and enable structural analysis. While **CP3** exhibited the ability to form supramolecular nanotubes, optimizing the solvent environment remains a challenge to ensure reproducibility and control over aggregation behavior. Future studies should explore fine-tuning the solvent ratios to balance solubility and structural integrity, employing co-solvents or buffer systems to enhance peptide dispersion, or modifying the peptide sequence to introduce neutral hydrophilic groups, such as hydroxyl groups in the amino acid chains (e.g. serine, threonine) or further tetraethyleneglycol units, which may improve solubility without disrupting supramolecular assembly.[131] These modifications could improve solubility while maintaining the system's potential for biomedical applications. Addressing these limitations could further enhance the applicability of such cyclopeptide-based systems for stimuli-responsive drug delivery and targeted therapeutic applications.

4 CYCLOPEPTIDES AND CYCLOPEPTIDE-POLYMER CONJUGATES AS BUILDING BLOCKS FOR SUPRAMOLECULAR HYDROGEL MATRICES

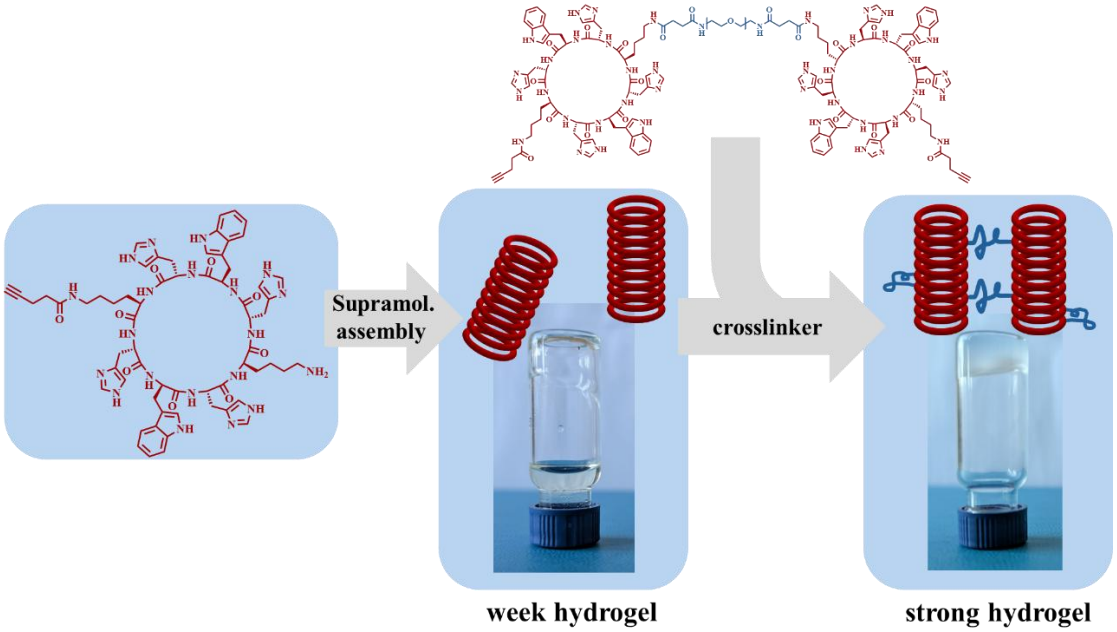

4.1 Motivation and Concept

One application of supramolecular chemistry is hydrogel formation, where molecules self-assemble into three-dimensional networks capable of retaining large amounts of water. These hydrogels are characterized by their mechanical strength and tunability in structure and properties, making them particularly suitable for biomedical applications.

This project focuses on a D,L-alternating octapeptide specifically designed to form ordered supramolecular structures for hydrogel formation. The structural design employs a regular alternation of hydrophilic histidine and hydrophobic tryptophan residues, which facilitates self-organization into H-bonded nanotubes. These structures are stabilized by hydrogen bonding along the tubular axis and serve as the foundational motif for the assembly of stable nanotubes, which, in turn, form the framework of a three-dimensional network (figure 4.1). Poor water solubility, a common challenge in peptide-based hydrogels, is typically addressed by conjugating hydrophilic polymers,[93,132,133] which can compromise biocompatibility. In this project, histidine is utilized as an ionizable amino acid to enhance solubility without the use of polymers, ensuring the biocompatibility of the system. Its polar side chain facilitates hydrogen bonding and electrostatic interactions, improving hydrophilicity. Additionally, its pH-sensitive nature modulates supramolecular interactions, providing adaptive properties that enable extended control of the gel structure. Furthermore, tryptophan stabilizes the nanotubes by facilitating π-π interactions between its aromatic side chains. Functional groups such as alkynes and amines are integrated into the peptide to enable potential chemical modification for specific applications. [96,132,134]

To optimize the mechanical properties of the hydrogel, telechelic cross-linker systems were employed, utilizing PEG chains to connect two cyclopeptides. These cross-linkers reinforce lateral aggregation of nanotubes and improve gel strength significantly while preserving the intrinsic self-assembly processes of cyclopeptides. The choice of PEG length is crucial for achieving a balance between steric hindrance and aggregation-promoting interactions. As MEIJER *et al*. demonstrated, selecting the appropriate PEG length is essential to maintain this balance and optimize the hydrogel's mechanical properties.[94] For this reason, a series of PEGs with varying lengths are examined to understand their impact on the hydrogel properties, and assembly pathway.

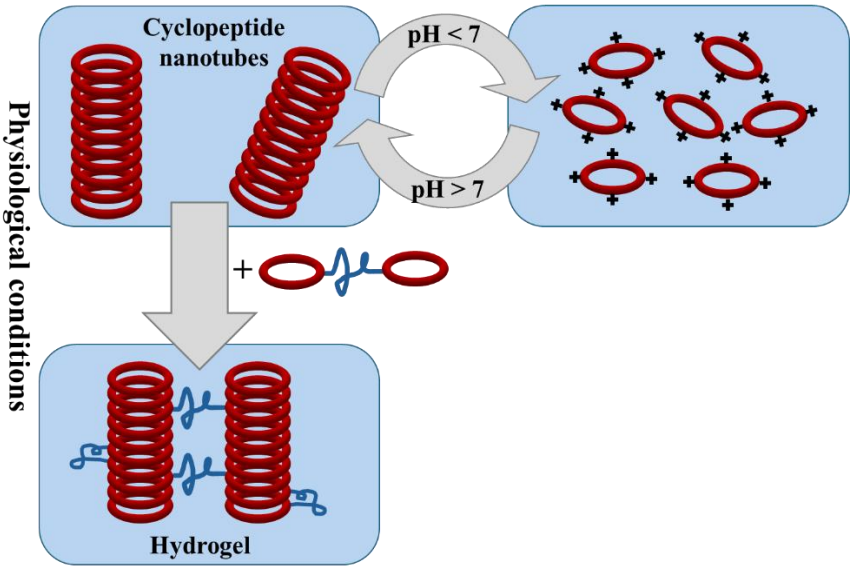

Figure 4.1: *Concept of pH responsive cyclopeptide based hydrogels.*

This project aims to explore the hydrogel properties of supramolecular cyclopeptide-based systems and assess their potential as biocompatible and biodegradable materials for biomedical applications.

4.2 Results and Discussion

4.2.1 Synthesis of water-soluble cyclopeptide

The cyclic peptide Cyclo-[L-Ser(propargyl)-D-His-L-Trp-D-His-L-Trp-D-His-L-Trp-D-His] (**CP4**) was designed as a building block for the investigation of hydrogel formation. The amide backbone of this D,L-alternating cyclooctapeptide promotes the formation of β-sheet-like structures into nanotubes via hydrogen bonding. Furthermore, the specific amino acid sequence promotes not only longitudinal but also lateral aggregation, which is supported by π-π interactions and hydrophobic interactions between the aromatic side chains of tryptophan, leading to the formation of a three-dimensional network.[135,136] This network is essential for the formation of hydrogels, as it serves to trap water and thereby create a gel-like consistency. In addition, the imidazole groups of histidine can act as a pH-dependent trigger for supramolecular assembly and increase the hydrophilicity of the system. The alternating sequence of histidine and tryptophan in the peptide sequence promotes a balance between hydrophilic and hydrophobic groups, which further supports supramolecular assembly. But network remains uncontrolled, and needs a new strategy to modulate crosslinking compromising solubility. We opted for bifunctional CP units using telechelic PEG. To enable the conjugation of PEG chains as a crosslinker between two cyclopeptides using click chemistry, the synthetic amino acid L-propargylserine (**IV-4**) was synthesized from L-serine. Crosslinkers are used to modify the mechanical properties and strength of the hydrogel.

The synthesis of **CP4** (figure 4.2) involves a multi-step process starting with the automated solid-phase synthesis of the linear peptide **IV-5**. Following synthesis, the peptide is cleaved from the resin while retaining its protecting groups. Cyclization of the linear peptide is then performed in solution using PyBOP, after the protecting groups are removed to obtain the final cyclopeptide **CP4**.

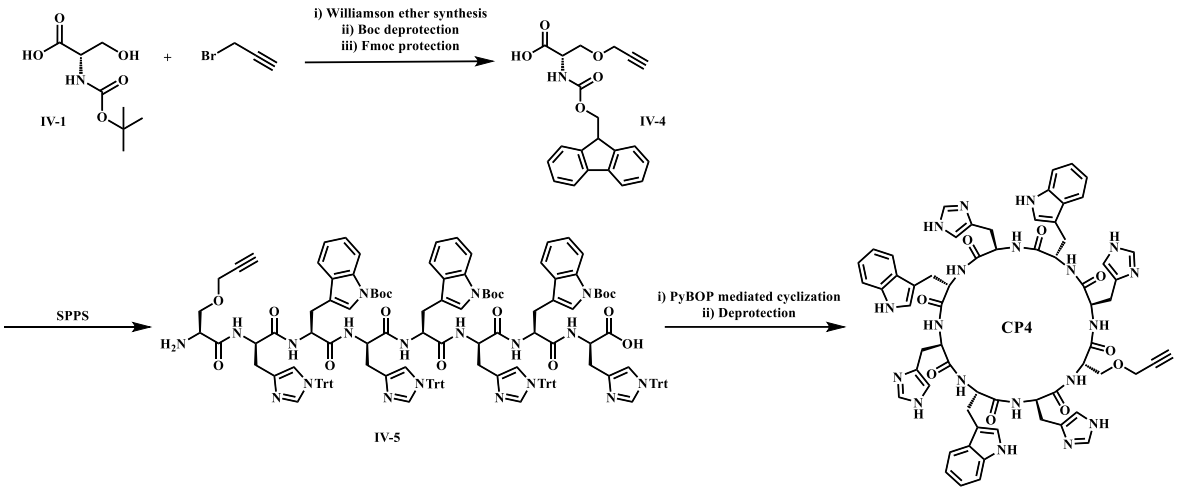

Figure 4.2: *Synthesis scheme of* ***CP4****.*

The synthetic amino acid **IV-4** was required for peptide synthesis and was synthesized from L-serine in a multi-step process (figure 4.3). In this process, L-serine is protected at the N-terminus with a Boc group using di-*tert*-butyl dicarbonate to obtain compound **IV-1**. This step prevents unwanted substitutions at the amine group during the subsequent etherification reaction. The synthesis of the ether **IV-2** is carried out using the WILLIAMSON method[137], utilizing propargyl bromide as the alkylating agent and sodium hydride (NaH) as base. The reaction is performed under anhydrous conditions and in the absence of oxygen to prevent side reactions. The carboxylic acid group of **IV-1**, having a higher p*K*a, is deprotonated first. An additional equivalent of NaH deprotonates the

hydroxyl group, which acts as a nucleophile and undergoes substitution *via* an S_N2 mechanism with propargyl bromide. The Boc-protecting group is removed under acidic conditions, and the desired amino acid **IV-4** is obtained as its hydrochloride salt by precipitation.

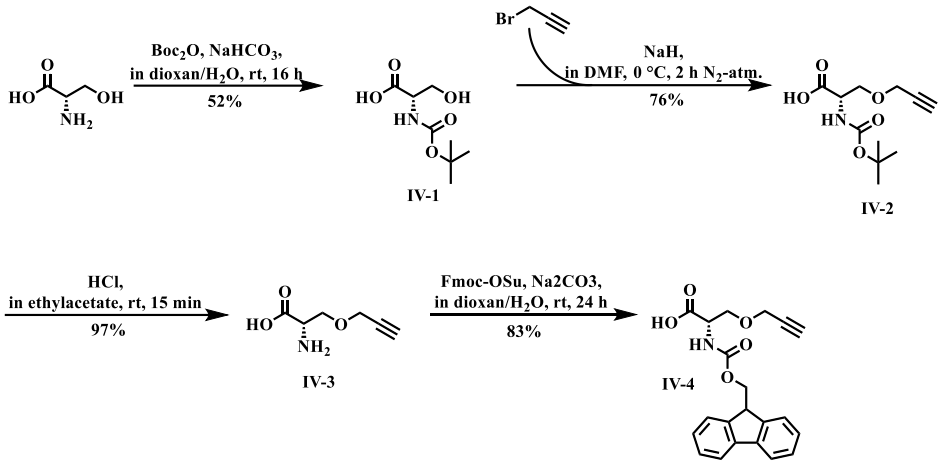

Figure 4.3: *Synthesis of* ***IV-4****.*

Each step of the synthesis proceeded with yields exceeding 50%, demonstrating the efficiency to introduce the propargyl moiety onto the serine side chain while maintaining the integrity of the functional groups, enabling its subsequent incorporation into peptide synthesis.

For peptide synthesis, the Fmoc protocol was employed. For the synthesis of **IV-5**, the coupling reagent combination DIC/Oxyma was used. To ensure complete coupling, double coupling steps were performed for one hour each at 40 °C under microwave conditions. It is not advisable to operate at elevated temperatures during peptide synthesis, as the chloro trityl ester linker, exhibits limited thermal stability.[138] The temperature susceptibility of the linker causes premature peptide cleavage from the resin at elevated temperatures, leading to decreased yields. Using this approach, the linear peptide was obtained with a yield of 38% after chromatographic purification. Cyclization was performed under high-dilution conditions (1 mmol/mL) in DMF using PyBOP/HOBt as coupling reagents, following the method established for previous cyclizations. The progress of cyclization was monitored *via* RP-HPLC. After nine days, complete conversion of the starting material was observed, and the crude product was purified by precipitation in cold ether. Due to the poor solubility of the protected cyclic peptide **IV-6**, it was used directly in the next step without further purification. The final deprotection to yield the target product **CP4** was performed using TFA/TIPS/H_2O. The overall yield for the two steps, cyclization and deprotection, was 21% (figure 4.4).

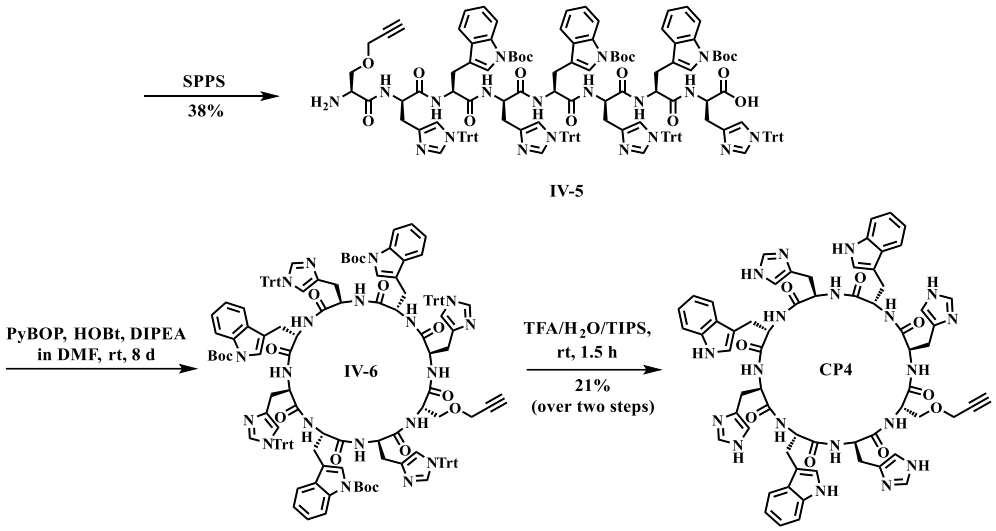

Figure 4.4: *Synthesis of* ***CP4****.*

For the analytical evaluation of cyclopeptide **CP4**, HPLC analysis was performed on a C18 column (25 cm, Pyramid) using a gradient of 0% to 40% acetonitrile + 0.1% TFA over 40 minutes. This analysis revealed two distinct signals with a difference in retention time approximately 1 minute (figure 4.5). To investigate this further, the two peaks were isolated under identical conditions using preparative HPLC. MALDI-TOF mass spectrometry confirmed that both fractions exhibited the same molecular mass of 1233 Da, which corresponds to the protonated species of **CP4** (figure 4.5B). This observation led to the hypothesis that these are epimers of the cyclopeptide **CP4**. Histidine is susceptible to epimerization during peptide synthesis because the basic imidazole ring can deprotonate the α-carbon when the C-terminus is activated, promoting racemization of the C-terminal amino acid or epimerization of the oligopeptide. This effect is particularly pronounced in the coupling of peptide fragments, as the absence of stabilizing protecting groups, such as Fmoc, at the N-terminal amide increases the likelihood of epimerization. Without the protective steric and electronic effects provided by these groups, the intermediate becomes more susceptible to racemization during activation and coupling.[139] The absence of an Fmoc group during the cyclization reaction suggests that epimerization most likely occurred at this stage, as the lack of steric hindrance facilitates proton abstraction and subsequent racemization.[140] This highlights the need for careful control and optimization of reaction conditions during synthesis to minimize such side reactions. The proposed mechanism for histidine racemization, involving the imidazole ring, is illustrated in chapter 1.1.

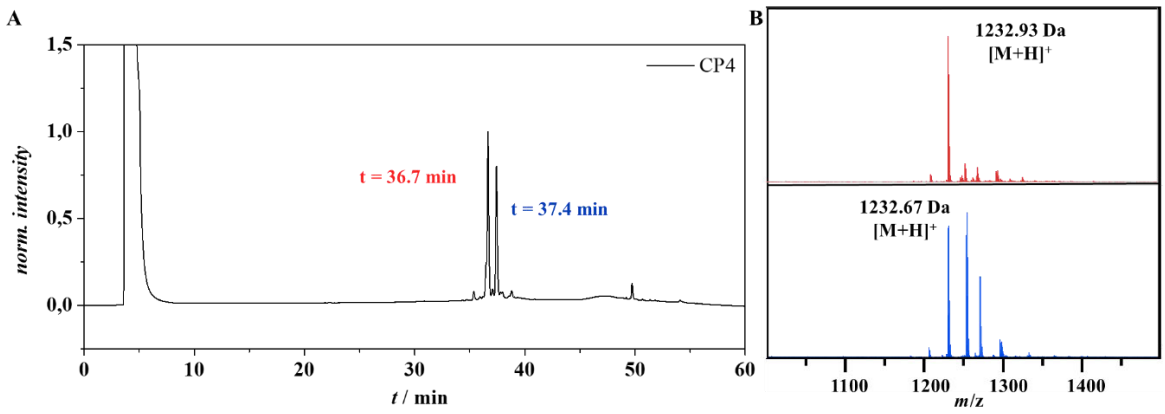

***Figure 4.5: A** Analytical RP-HPLC chromatogram at λ = 254 nm of **CP4** on a pyramid C18 (25 cm) gradient: 0% → 40% B in 40 minutes (solvent A: water + 0.1% TFA, solvent B: acetonitrile + 0.1% TFA); **B** MALDI-TOF MS spectra of the isolated signals of A at retention time 36.7 min (red) and 37.4 min (blue) in a CHCA-matrix.*

It was not possible to determine whether one of the isolated products was the targeted D,L-alternating cyclopeptide.

A model click reaction was performed on the isolated product with a retention time of 36.7 minutes to bridge two cyclopeptides via the alkynes using PEG-diazide as a cross-linker. For this copper-catalyzed azide-alkyne cycloaddition (CuAAC) click chemistry was used. Signal intensities from MALDI-TOF-MS measurements were used to qualify different reaction conversions. No conversion was observed under most of the conditions tested. Only with water and DMSO as solvent and reaction temperature at 50 °C, a low conversion to the single- and double-reacted product was observed in the MALDI-TOF-MS spectrum after six days (see appendix figure 10.21).

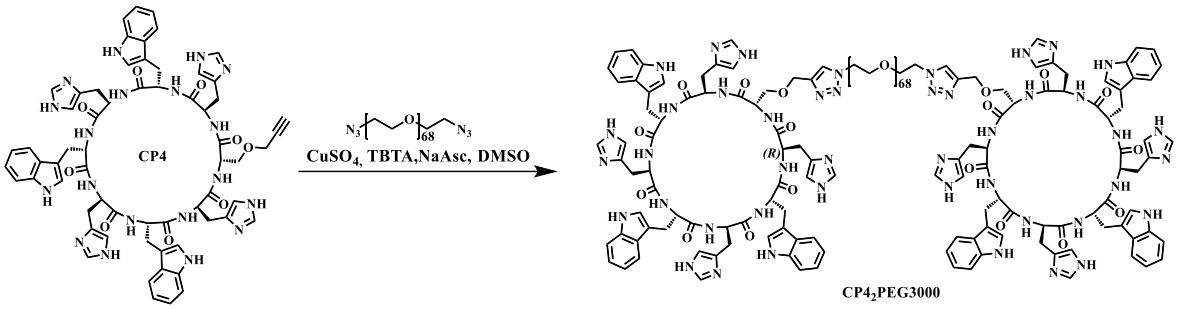

***Figure 4.6:** Synthesis scheme of **CP4$_2$PEG3000**.*

The click reaction, initially reported by SHARPLESS and MELDAL[141] in 2001 uses catalytic amounts of copper(I), which can be introduced directly as CuI or generated *in situ* by reducing $CuSO_4 \cdot 5\ H_2O$ with sodium ascorbate, enables the efficient coupling of alkynes and azides in a CuAAC, resulting in the formation of 1,2,3-triazoles. To stabilize the reactive copper(I) species, the addition of tris(benzyltriazoylmethyl)amine (TBTA) is necessary.[142] The addition of TBTA prevents the oxidation of copper(I) to copper(II), thereby maintaining catalytic activity and enhancing the efficiency of the reaction. The exact mechanism of CuAAC is still debeted. But it is postulated that a σ-, π-di(copper)-acetylide complex is formed, which then undergoes a cycloaddition with an azide group, resulting in the selective formation of a 1,4-substituted triazole (figure 4.7).[143]

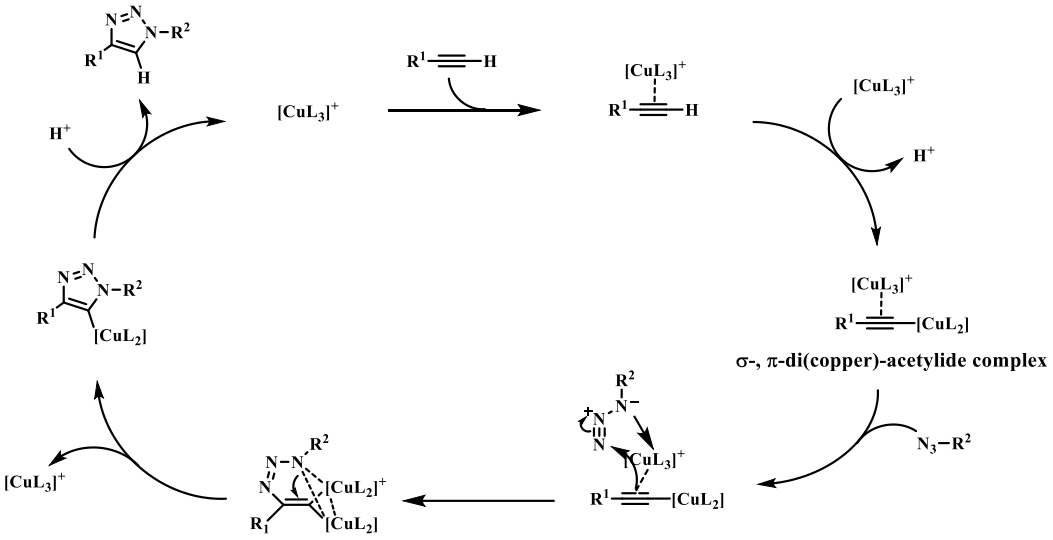

Figure 4.7: *Proposed mechanism of the CuAAC.*[143]

Despite these advantages, the low efficiency of the click reaction in the context of cyclopeptide **CP4** to **CP4$_2$PEG3000** can be attributed to its chemical composition and structural characteristics. The imidazole side chain of histidine has a marked propensity to coordinate with copper ions, thereby reducing the availability of copper for the CuAAC reaction.[144-148]This versatility in coordination can influence the reaction in different ways. While Cu(I) is the catalytically active species in CuAAC reaction, its coordination with histidine can deactivate the catalyst or slow down the reaction kinetics. Additionally, the steric environment created by the side chains of histidine and tryptophan might also impede the alkyne's interaction with the azide. Furthermore, tryptophan[149] exhibits redox activity due to its ability to be oxidized into a radical cation at a standard redox potential of approximately +1.0 V[150], which is higher than the standard redox potential for the oxidation of copper(I) to copper(II) (+0.15 V)[151]. While this suggests a potential interaction with copper species, no experimental evidence supports its role as a reducing agent for copper(I) to copper(II). Instead, such redox activity may contribute to the destabilization of the copper catalyst under specific conditions.

In light of these considerations, a novel cyclopeptide design with the peptide sequence cyclo-[D-His-L-Lys-D-His-L-Trp-D-His-L-Lys(pentynoyl)-D-His-L-Trp] (**CP5**) was devised. (figure 4.8). Initially, histidine at the C-terminus was replaced by tryptophan, as the carboxylic acid at the C-terminus is activated for cyclization, which could potentially promote epimerization of histidine. To circumvent this, the sequence was modified to relocate the histidine to the N-terminus. Furthermore, one tryptophan amino acid was replaced by a lysine residue in the peptide sequence. Lysine was introduced primarily as an alternative to click conjugation, as its amino group provides an additional opportunity for functionalization. Furthermore, the introduction of lysine enhances the hydrophilicity of the cyclopeptide, which may positively influence water solubility of the system. Instead of the synthetic amino acid propargylserine (**IV-4**), L-Lys(pentynoyl) was employed. This modification extends the distance between the alkyne and the hydrophobic region of the cyclopeptide, enhancing both the efficiency and reactivity of the click chemistry process. These changes are anticipated to improve the reaction efficiency while minimizing the occurrence of epimerization.

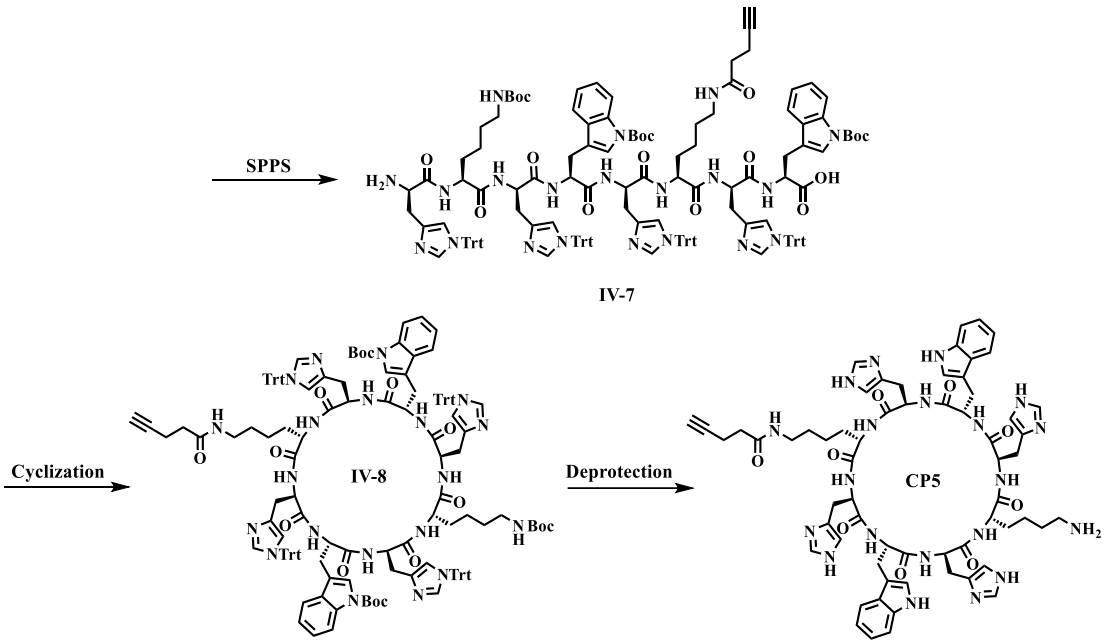

Figure 4.8: *Synthesis scheme of* ***CP5****.*

To prevent epimerization during peptide synthesis on the solid phase, DEPBT was employed as a coupling agent in combination with HOPO. DEPBT is an ideal coupling reagent because its mild reaction conditions and low tendency for side reactions reduce the epimerization of sensitive amino acids like histidine effectively.[45] HOPO is used as an additive to enhance the reactivity of DEPT, enabling efficient activation of carboxylic acids while minimizing unwanted side reactions.[29] To further reduce the risk of temperature-dependent epimerization, the couplings were performed at room temperature. The detailed mechanism of DEPBT-initiated amide coupling is explained in chapter 1.1.

To evaluate the efficacy of this approach, the model tripeptide H-L-Lys(pentynoyl)-D-His(Trt)-L-Trp(Boc)-OH (figure 4.9B) was synthesized, representing the first three amino acids of **IV-7**. This enabled the evaluation of the ability of DEPBT/HOPO to couple histidine without epimerization. LC-MS analysis of the product (figure 4.9A, blue) showed a single peak in the chromatogram and the expected mass of the tripeptide (see appendix figure 10.24), indicating successful coupling without epimerization. In contrast, the same tripeptide synthesized with HBTU/HOBt (figure 4.9A, green) exhibited three signals corresponding to the same tripeptide mass, suggesting epimerization. These results indicate that DEPBT/HOPO effectively minimizes epimerization under the tested conditions compared to HBTU/HOBt.

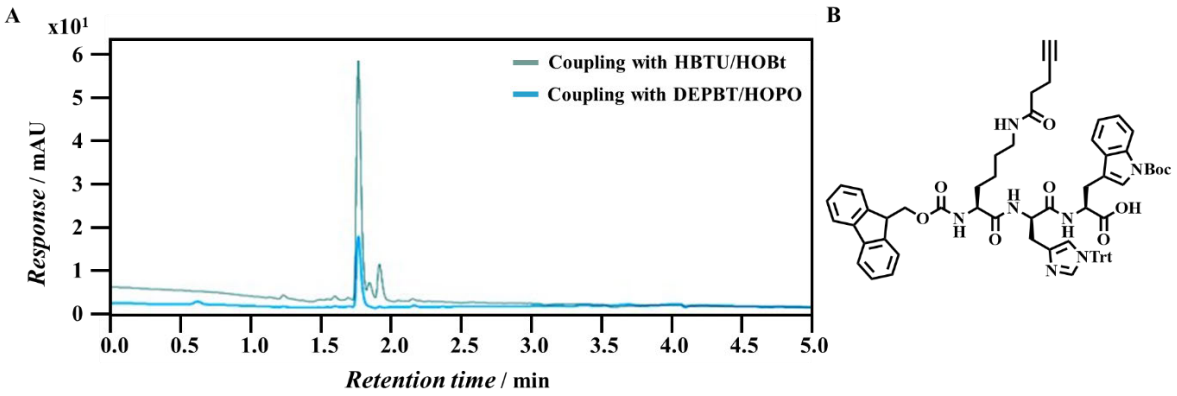

Figure 4.9: ***A*** *LC-MS chromatogram at λ = 214 nm of tripeptide H-L-Lys(pentynoyl)-D-His(trt)-L-Trp(boc)-OH synthesized by HBTU/HOBt (green line) and DEPBT/HOPO (blue line) on a nucleodur pyramid (50 mm) gradient: 30% → 99% B in 2 minutes (solvent A: water + 20 mM ammonium acetate, solvent B: acetonitrile);* ***B*** *Chemical structure of tripeptide H-L-Lys(pentynoyl)-D-His(trt)-L-Trp(boc)-OH.*

Linear peptide **IV-7** was successfully synthesized on the solid phase under these optimized conditions using DEPBT and HOPO, achieving a yield of 59%.

A model cyclization reaction to suppress epimerization involving the conversion of the linear peptide **IV-9** to the cyclic peptide **IV-10** (figure 4.10) was employed to optimize the cyclization process and various coupling reagents were tested under highly diluted solution conditions. The reagents were assessed based on their reactivity and tendency to avoid by-products, with a specific focus on their potential to induce epimerization.

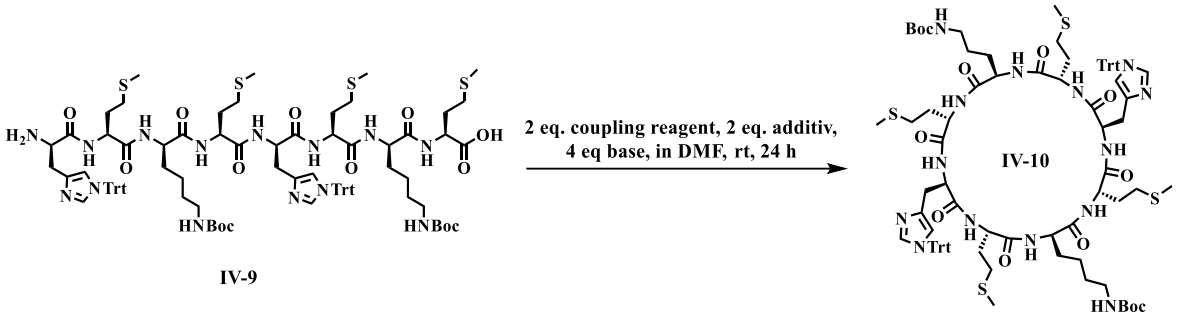

Figure 4.10: *Test cyclization of* ***IV-9*** *to* ***IV-10****.*

Different literature known coupling reagents DEPT, PyBOP, 1-ethyl-3-(3-dimethylaminopropyl)carbodiimid-hydrochlorid (EDC·HCl), DMTMM·BF_4, HBTU and diphenylphosphoryl azide (DPPA) were tested and evaluated. The phosphonium-based reagents PyBOP and HBTU were found to exhibit high reactivity, which is of particular importance for the activation of carboxylic acids in organic solvents such as DMF.[35] The formation of stable benzotriazole intermediates provides effective control over reaction kinetics and minimizes epimerization. Furthermore, HOBt was introduced as an additive, and DIPEA as a base, with the objective of enhancing the efficiency of the reaction. DMTMM·BF_4 proved to be a milder and efficacious alternative, facilitating a more gentle activation of carboxylic acids. No additional additives or bases are required for this method.[42] Due to its high solubility in polar solvents such as DMF, DMTMM was a versatile reagent that offered a significant advantage in minimizing racemization. EDC·HCl leads to the formation of water-soluble urea as a byproduct during the reaction, which can be readily removed. This reagent is particularly useful for cyclizations in mixed organic-aqueous conditions.[152] In conjunction with HOBt and DIPEA, the efficacy of the reaction

is further enhanced. DPPA also demonstrates efficacy in supporting challenging cyclizations. The reagent facilitates the removal of byproducts, thus streamlining the work-up of the products.[84] Once more, HOBt and DIPEA were introduced to further stimulate the reaction. Subsequently, DEPBT was evaluated with HOPO and DIPEA, as it had previously demonstrated efficacy in linear peptide synthesis. This reagent permitted the mild and selective activation of the carboxylic acid, as well as exact control over the reaction kinetics, which further reduced the risk of epimerization.

To assess the efficacy of these reagents, the linear peptide **IV-9**, provided by KATRINA SCHORSTEIN, was employed in test reactions. All cyclizations were conducted under identical conditions. Two equivalents of the respective coupling reagent and two equivalents of the additive, if necessary, were dissolved in DMF, and one equivalent of **IV-9** was slowly added with four equivalents of DIPEA. The reaction solutions were stirred for 24 hours at room temperature, concentrated and the cyclic peptide **IV-10** was precipitated in cold diethyl ether. An analytical RP-HPLC measurement of the crude product was performed to investigate the conversion and the formation of by-products, or potential epimerization. The following Figure illustrates sections from the chromatograms obtained following the cyclization of the individual coupling reagents, with a comparison to the linear peptide.

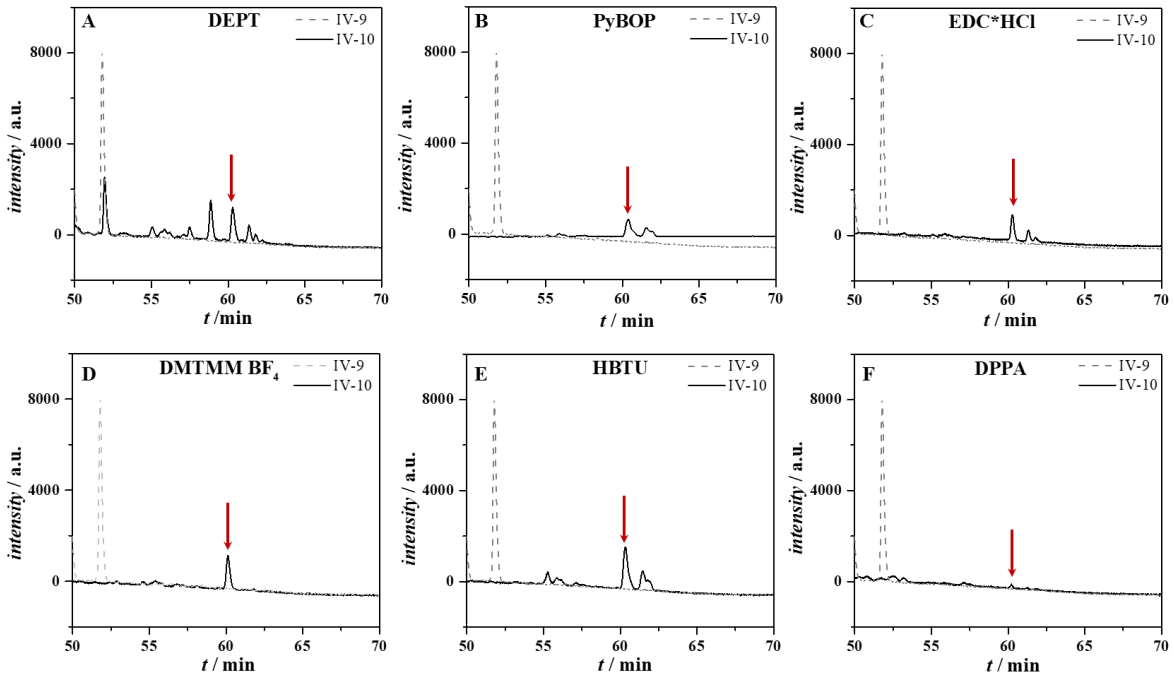

Figure 4.11: *Analytical RP-HPLC chromatogram at λ = 254 nm of the cyclization of **IV-9** to **IV-10** with the coupling reagent **A** DEPBT, **B** PyBOP, **C** EDC·HCl, **D** DMTMM·BF4, **E** HBTU, **F** DPPA on a pyramid C18 (25 cm) gradient: 5% → 99% B in 60 minutes (solvent A: water + 0.1% TFA, solvent B: acetonitrile + 0.1% TFA).*

As anticipated, the product's retention time increases following cyclization, which is attributed to the modified structure of the cyclopeptide **IV-10**. In spectra A-E, the presumed signal of the desired product **IV-10** can be observed at a retention time of approximately 60 minutes (marked in red), with the reagents exhibiting various effects on product purity.

In the cyclizations conducted with PyBOP, EDC·HCl, and HBTU, additional signals with higher retention times were observed, in addition to the product signal. This suggests the generation of by-products that may have resulted from epimerization or other undesired reactions during cyclization, such as oligomerization of peptide chains or the presence of residual coupling reagents. While these reagents are capable of efficient cyclization, they appear to be less selective, as evidenced by RP-

HPLC analysis. In contrast, the use of DEPBT (figure 4.11A) also demonstrated the occurrence of unintended side reactions, as evidenced by the presence of additional signals and the detection of starting material (**IV-9**) in the chromatogram. In the case of cyclization with DPPA, the HPLC spectrum did not exhibit any signal indicative of the product or the reactant. Therefore, DPPA is unsuitable for the cyclization reaction under the specified conditions. Of the reagents tested, DMTMM·BF_4 (figure 4.11D) yielded particularly favorable results. The HPLC chromatogram displays a single signal at the anticipated retention time for the product. This result demonstrates the successful cyclization of the reaction, with high selectivity and likely formation of a stereochemically pure product.

The results demonstrate that DMTMM·BF_4 is an optimal reagent for the synthesis of cyclopeptides with a N-terminal histidine group. Furthermore, the high efficiency and selectivity of this reagent were successfully confirmed in studies conducted by the PERRIER group for the synthesis of cyclopeptides.[40] The synthesis of DMTMM·BF_4[42] (**IV-12,** figure 4.12) can be realized in two steps, beginning with the formation of 2-chloro-4,6-dimethoxy-1,3,5-triazine and *N*-methylmorpholine (NMM). In the initial reaction, the chloride salt of DMTMM (**IV-11**) is generated *in situ*. The salt can then be converted into the more stable pentafluoroborate salt *via* anion exchange with $NaBF_4$. The synthesis can be conducted in a one-pot process, which further simplifies the procedure.

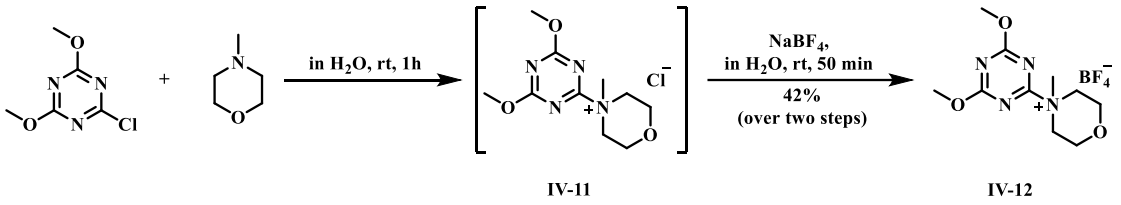

Figure 2.12: *Synthesis of* ***IV-12****.*

The cyclization of the linear peptide **IV-7** to the protected cyclopeptide **IV-8** was successfully performed by using DMTMM·BF_4. In comparison to the cyclization process conducted with PyBOP, the reaction time was markedly reduced under these optimized conditions. In contrast to a reaction time of 6-10 days, which is typically observed with PyBOP, the cyclization with DMTMM·BF_4 could be completed within only two days. The decrease of reaction time is attributed to the enhanced reactivity of the DMTMM·BF_4 coupling reagent system, which facilitates the expedited formation of the amide bond due to the more efficient activation of the carboxylic acid group. This not only reduces the reaction time but also minimizes the potential for side reactions, such as hydrolysis or racemization. Furthermore, the efficacy of this methodology is evident in the RP-HPLC analyses. Figure 4.13 depicts the HPLC chromatogram of the linear peptide **IV-7** and a reaction control after 20 hours of cyclization to **IV-8**. Already after this period, complete conversion of **IV-7** was observed.

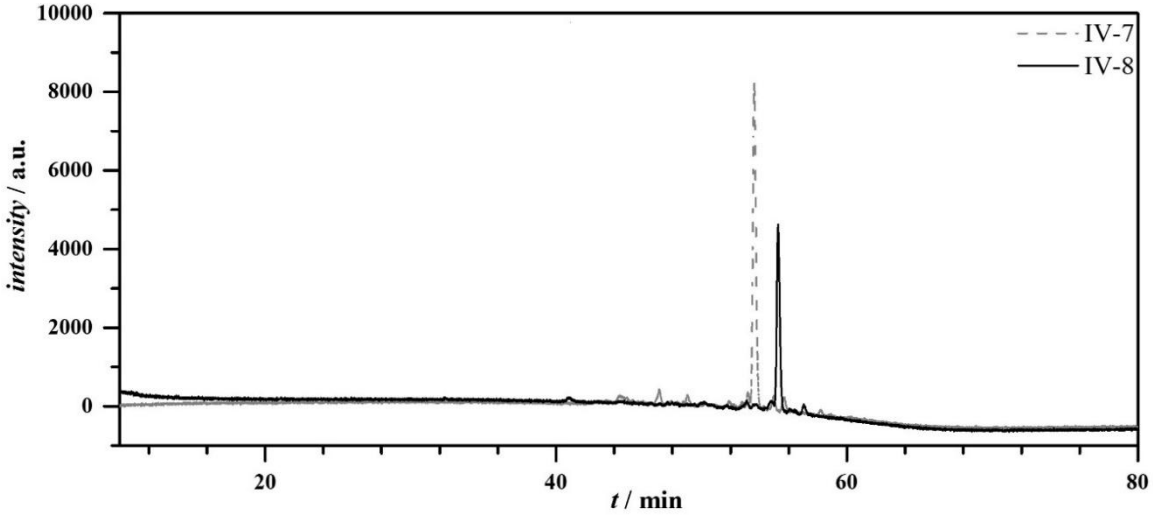

Figure 4.13: *Analytical RP-HPLC chromatogram at λ = 254 nm of **IV-7** and **IV-8** on a pyramid C18 (25 cm) gradient: 5% → 99% B in 60 minutes (solvent A: water + 0.1% TFA, solvent B: acetonitrile + 0.1% TFA).*

After completing the cyclization, it was found that the protected cyclopeptide **IV-8** exhibited poor water solubility, rendering it unsuitable for further analytical studies. To improve solubility, the side-chain protecting groups were removed in a subsequent deprotection step. This was performed using a TFA/TIPS/H_2O mixture (95:2.5:2.5). Following purification, the final cyclopeptide **CP5** (cyclo-[D-His-L-Lys-D-His-L-Trp-D-His-L-Lys(pentynoyl)-D-His-L-Trp]) was obtained with a 74% yield across two steps (cyclization and deprotection).

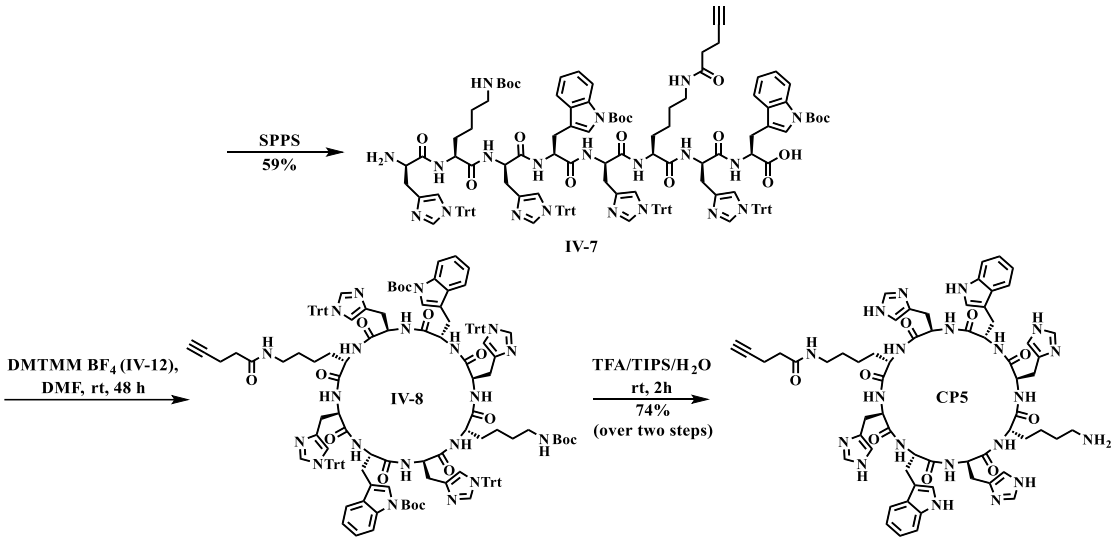

Figure 4.14: *Synthesis of **CP5**.*

The characterization of **CP5** was performed with ^{1}H-NMR, ESI-MS, and RP-HPLC to confirm its purity. In addition, this synthesized cyclopeptide exhibits excellent solubility in water under physiological conditions, surpassing the solubility of previously prepared cyclopeptides. This improved water solubility can be attributed to the incorporation of lysine into the peptide sequence. Under physiological conditions, lysine carries a positive charge due to the protonation of its ε-amino group at neutral pH.[153] This positive charge promotes interactions with water molecules via electrostatic forces and hydrogen bonding, significantly improving the overall hydrophilicity and solubility of the peptide.

To examine the influence of PEG conjugates with different chain lengths as supramolecular crosslinkers (**CL**) on supramolecular structure formation and hydrogel properties, **CL** composed of cyclopeptide **CP5** and PEG were synthesized. Each **CL** consists of two equivalents **CP5** connected by PEG bridges of varying lengths (PEG2000, PEG3000, PEG6000) to form a telechelic polymer-cyclopeptide conjugate. Instead of CuAAC click chemistry, which had previously proven challenging, chemoselective NHS ester chemistry was employed, as this enables straightforward and efficient conjugation under mild conditions. To this end, commercially available bifunctional PEG derivatives (PEG(NHCO-C_2H_4-CONHS)$_2$) were employed, which were reacted with two equivalents of **CP5** in a slightly basic pH range (pH 8). The reaction was conducted under an inert gas atmosphere to prevent the hydrolysis of the active ester and to maximize the yield of the reaction.

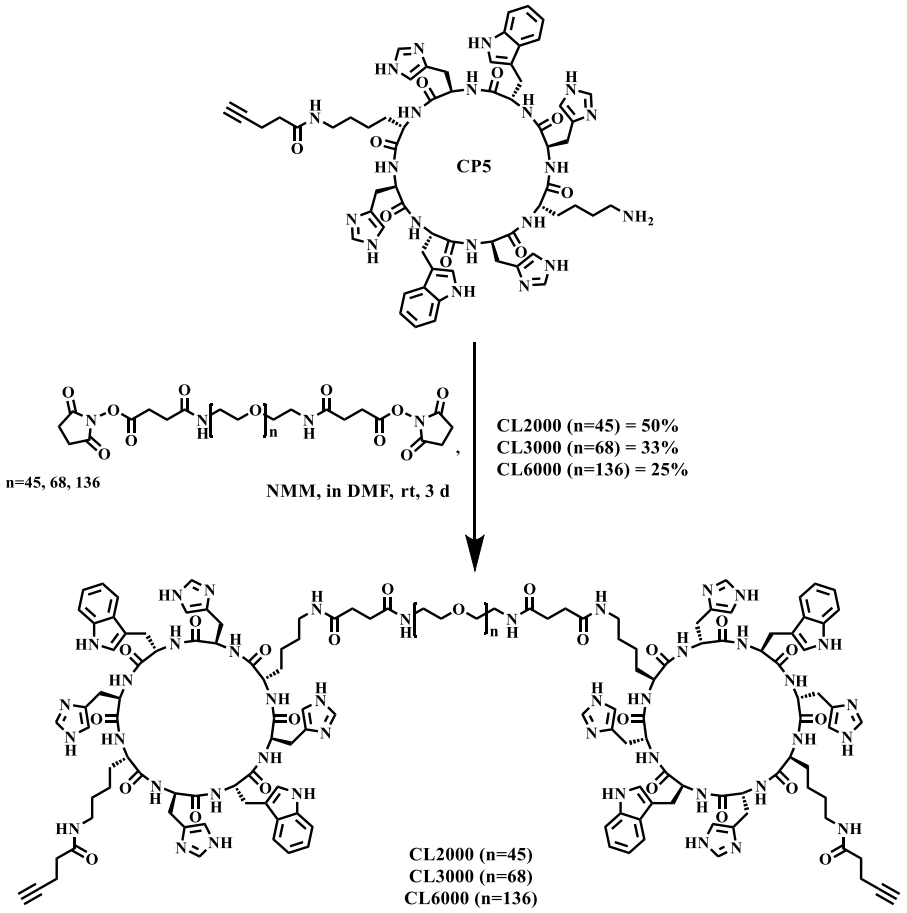

Figure 4.15: *Synthesis of* ***CL2000, CL3000*** *and* ***CL6000****.*

The reaction was monitored and controlled using RP-HPLC. Figure 4.16A shows an exemplary HPLC chromatogram of the synthesis of **CL2000**. The chromatogram depicts the profiles of the initial product **CP5** (signal I, dashed), the bifunctional PEG2000-NHS derivative (signal III, dotted), and the final product **CL2000** (signal II, blue). Nearly complete conversion was observed during the reaction, as evidenced by the significant reduction of **CP5** and PEG2000-NHS signals. Additionally, an extra signal (signal IV) was observed in the spectrum, present in both the PEG2000-NHS and the product **CL2000**. The identity of this impurity could not be determined. However, it was successfully removed via preparative HPLC.

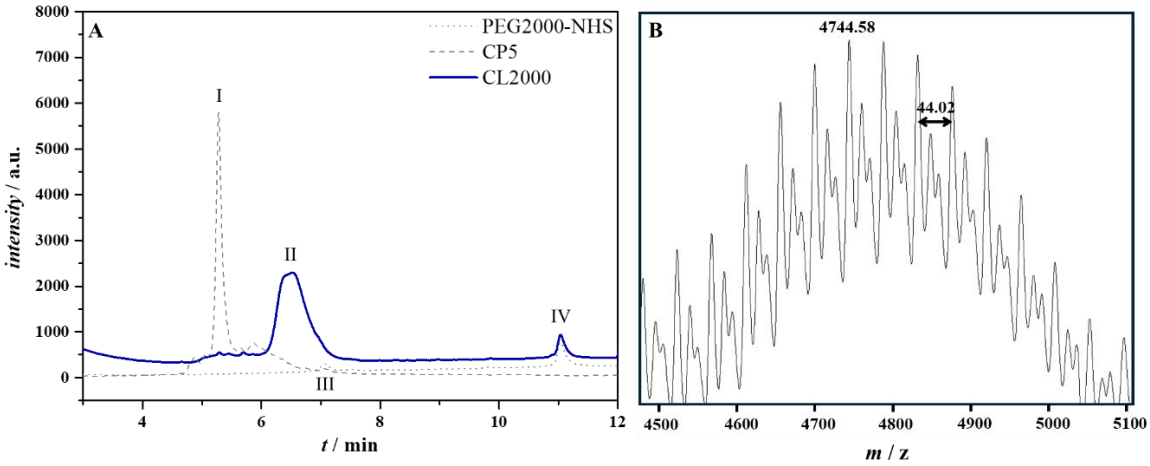

***Figure 4.16: A**: Analytical RP-HPLC chromatogram at λ = 254 nm of **PEG2000-NHS**, **CP5** and **CL2000** on a pyramid C18 (50 mm gradient (5% → 95% B in 10 minutes (solvent A: water + 0.1% TFA, solvent B: acetonitrile + 0.1% TFA); **B**: MALDI-TOF-MS spectra of **CL2000** in a DHB matrix.*

The molecular masses of the synthesized crosslinkers were verified using MALDI-TOF-MS. Figure 4.16B illustrates the MALDI-TOF mass spectrum obtained for crosslinker **CL2000**. The spectrum revealed the expected molecular mass of 4744.58 Da, corresponding to the conjugated telechelic PEG conjugate **CL2000**. Additionally, the spectrum displayed a characteristic repeat unit of 44.02 g/mol, characteristic for the PEG backbone. The structural integrity of the products was further confirmed by ^{1}H-NMR spectroscopy, confirming the successful synthesis of the crosslinkers. The specific yields for the synthesized **CL**s were 50% for **CL2000**, 33% for **CL3000**, and 25% for **CL6000**. The decreasing yield associated with increasing PEG length is attributed to steric hindrances, increased viscosity and reduced accessibility of the reactive groups in longer PEG chains. These factors hinder diffusion and reduce the reactivity of the NHS groups, which reduces conjugation efficiency.[154,155]

4.2.2 Supramolecular studies

Cyclopeptides exhibit structural properties that promote the formation of supramolecular superstructures, such as nanotubes. These nanotubes are stabilized by hydrogen bonds within the peptide backbone, which give rise to β-sheet-like structural motifs. These motifs are distinctly observed in CD spectroscopy (Figure 4.17). Characteristic β-sheet signatures include a negative CD signal at 215-218 nm and a positive bond at 195-200 nm.[127]

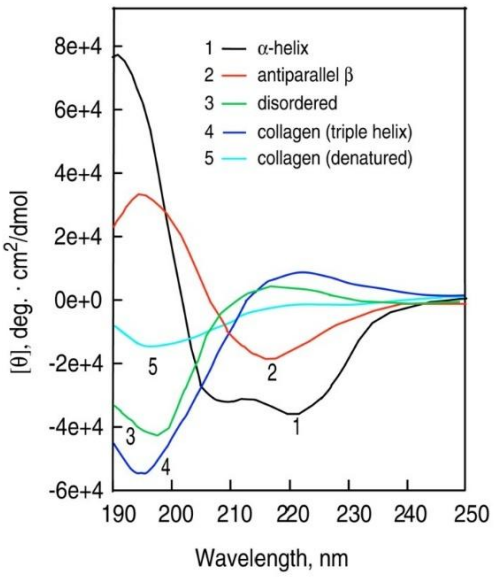

***Figure 4.17:** CD spectrum of the secondary structure elements α-helix, β-sheet random coil, triple helix and denatured collagen structure using the example of the peptide poly-L-lysine.[127]*

To further investigate the supramolecular assembly dynamics of **CP5**, its concentration dependence in Milli-Q water was analyzed using CD spectroscopy. The concentrations studied ranged from 50 µM to 400 µM. A negative band manifested at 190-197 nm, accompanied by a weak positive band at 208-213 nm (figure 4.18A, more in detail figure 4.18B). These observations align with established literature values for

random coil structures, which typically exhibit a strong negative band at 195-200 nm caused by π → π* transitions in disordered polypeptide chains.[123,150] Literature reports also mention a weak positive band at higher wavelengths, which is also observed here at 208-213 nm.[127,156] The intensity of the negative band at 192 nm was the subject of further investigation (figure 4.18C), but revealed no clear concentration dependence. The signal intensity varied with concentration, with the highest intensity observed at 400 µM, and lower intensities at 200 µM and 100 µM.

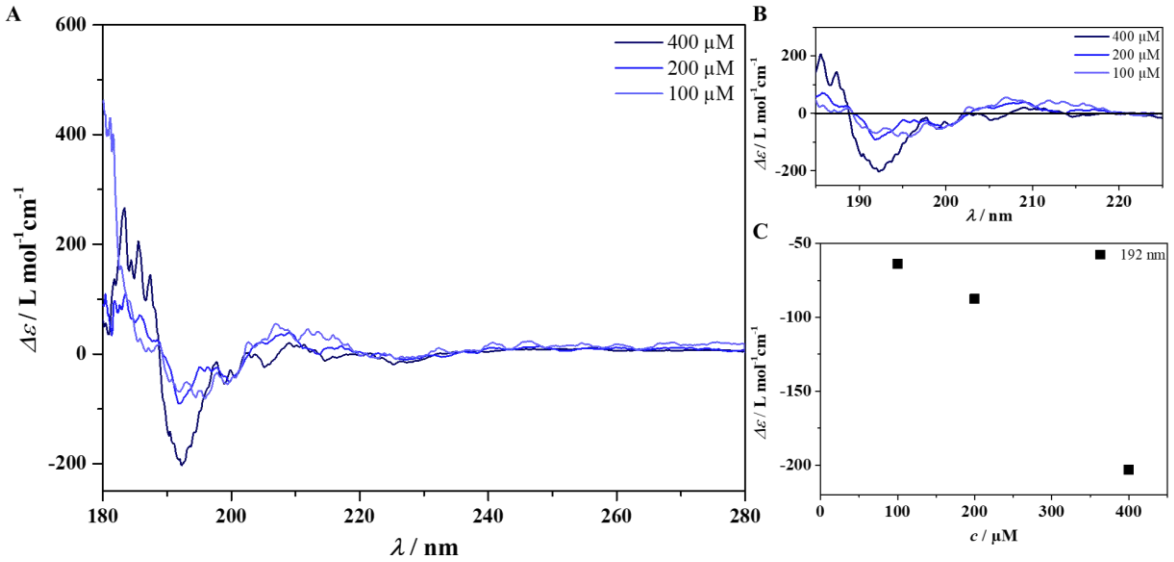

Figure 4.18: ***A*** *CD spectrum of solutions of* ***CP5*** *in MilliQ-H_2O (pH = 7.4) at different concentrations;* ***B*** *CD spectra zoomed into the wavelength range of 185 nm-225 nm,* ***C*** *CD signal at 192 nm depending on* ***CP5*** *concentration.*

The pH dependence of **CP5** was investigated at a concentration of 100 µM over a range from pH 1.75 to 9.62. At low pH values, the disassembly of supramolecular superstructures is expected due to the protonation of histidine side chains. At pH values above the p*K*a of histidine (p*K*a = 6.0[2]), the neutralization of the imidazole side chains might enable the reorganization of cyclopeptides into higher ordered structures. The resulting CD spectra exhibited signals predominantly below the cut-off wavelength of 190 nm[157], rendering reliable interpretation infeasible due to the solvent's UV absorption. Consequently, no conclusive signals above this threshold were observed that could be associated with the secondary structures of **CP5**. The data from these measurements are provided in the appendix figure 10.25. While the experiments aimed to explore potential structural transitions of **CP5** under varying pH conditions, the absence of interpretable signals above 190 nm limits the conclusions that can be drawn about supramolecular arrangements or secondary structures. However, the lack of a distinct random coil band could suggest the presence of supramolecular assemblies.

Additionally, the alternating D- and L-amino acid sequence in **CP5** may contribute to the absence of detectable CD signals for higher-order structures due to the fact that 50% are non-neutral amino acids. This can partially reduce the overall CD signal intensity and mask characteristic features of structural motifs like β-sheets.[158] Consequently, the weak or atypical CD signatures observed for CP5 may reflect these limitations, which complicate the identification of specific structural motifs, such as β-sheet formation and the morphology of alternating D,L-amino acid sequences.

To further investigate the formation of supramolecular structures by cyclopeptide **CP5**, super-resolution microscopy was performed using structured illumination microscopy (SIM). For these experiments, a 100 µM solution of **CP5** in PBS (phosphate buffered saline) was used and incubated with 10 µM thioflavine-T (Th-T). The incubation time was 12 hours to allow self-assembly of **CP5**

into supramolecular structures. Th-T, a fluorescent dye, binds specifically to aggregated β-sheet structures, and the fluorescence intensity of the dye increases significantly when it is embedded in hydrophobic pockets of β-sheet structures.[159] In the context of **CP5**, Th-T serves as a molecular reporter to visualize the formation of β-sheet-dominated superstructures.

The super-resolution microscopy images of the **CP5** sample reveal a supramolecular organization of **CP5** characterized by the formation of large 2D-sheet structures (figure 4.19A-D). This morphology has been previously documented in literature for analogous cyclopeptides.[79,80,160] The β-sheet structure is axially stabilized by hydrogen bonds along the peptide backbone, leading to the formation of nanotubes. These nanostructures serve as the basis for lateral aggregation, which might further stabilized by specific intermolecular interactions, such as π-π stacking between the indole rings of the tryptophan residues and the imidazole rings of the histidine of adjacent nanotubes. These lateral interactions seem to favour the formation of 2D flat, ordered sheet structures. On the other hand the Th-T reporter dye may influence the aggregation process by stabilizing aggregation further.

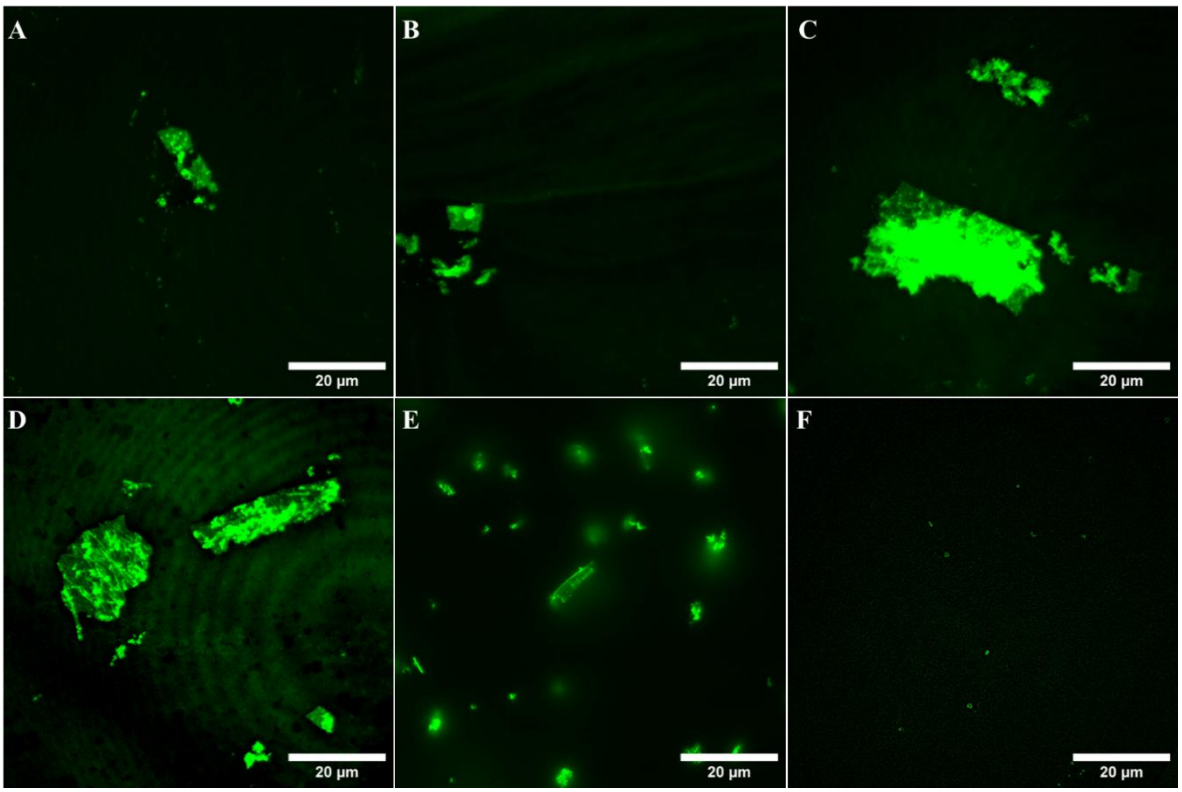

Figure 4.19: *Super-resolution microscopy images (SIM)* ***A-D CP5*** *(100 µM) in PBS with 10 µM TV-T and incubation time of 12 h;* ***E CP5*** *(100 µM) in PBS with 10 µM TV-T and incubation time of 12 h followed by ultrasonic treatment for 10 min;* ***F*** *control sample with 10 µM Th-T.*

Furthermore, the mechanical stress exerted on the supramolecular structures of **CP5** was investigated by subjecting the sample to a 10-minute ultrasonic treatment, followed by microscopic analysis, shown in figure 4.19E. While the untreated samples exhibited large sheet structures, indicative of lateral aggregation of nanotubes, the ultrasonic treatment resulted in the fragmentation of these supramolecular structures. Microscopic imaging of the treated samples revealed a significant increase in the number of small fragments, indicating a disruption of the large-area sheet structures. This finding indicates that the mechanical stress induced by ultrasound partially disrupts the supramolecular assemblies. The fragmentation process can be attributed to the physical effects of ultrasonic waves, which generate substantial shear forces and local pressure fluctuations through

cavitation processes. Notably, the tryptophan residues' π-π stacking interactions, which play a substantial role in lateral stability, are particularly vulnerable to such mechanical influences due to their comparatively weaker nature in comparison to hydrogen-bonds[161], thereby leading to a destabilization of the supramolecular architecture.

A control experiment with a 10 µM solution of Th-T showed no significant fluorescence or recognizable structures (figure 4.19F), supporting the specificity of the β-sheet specific fluorescence. This result suggest that the structures captured in the images mainly due to the specific properties of the cyclopeptide.

4.2.3 Rheological studies

The rheological properties of a material are crucial to understand its mechanical stability and behavior under stress. Rheological measurements, such as frequency sweep and amplitude sweep, provide valuable insights into viscoelastic properties. In these measurements storage modulus (G') and loss modulus (G'') as two key parameters are analyzed. Frequency sweep analysis assesses how G' and G'' vary with shear frequency while maintaining a constant amplitude, offering insights into the material's elastic and viscous behavior. Conversely, the amplitude sweep examines the stability of these moduli under varying shear amplitudes at a constant frequency, identifying the limits of the material's linear viscoelastic range (LVE). The storage modulus G' quantifies the elastic component of a material and serves as a measure of its energy storage capacity, while the loss modulus G'' describes the viscous component and measures the energy dissipated. If G' is much higher than G'' within the LVE the elastic contribution dominates, a property characteristic of hydrogels. However, when a critical threshold value is exceeded, the material transitions out of the LVE range, typically leading to a decrease in G'. Beyond this point, G'' may increase or decrease, depending on the material, as energy dissipation becomes more significant than elastic storage. This transition, commonly referred to as the gel decay point, or more technically as the flow point, is a metric for assessing the mechanical stability of a hydrogel. It represents the stress or strain threshold at which the supramolecular network structure becomes compromised, resulting in deformation or flow.[162]

Rheological measurements of **CP5** at concentrations of 1 wt%, 2 wt%, and 4 wt% in PBS (pH 7.4) were measured to investigate hydrogel formation and viscoelastic properties as a function of concentration. In frequency sweep experiments (figure 4.20A), the storage modulus G' consistently exceeds the loss modulus G'' across all concentrations, suggesting hydrogel networks with a dominating elastic component. The G' values ranged from 5 Pa to 11 Pa, with the maximum gel stiffness observed at 2 wt%, followed by 1 wt% and 4 wt% (figure 4.20B). Based on the observed G' values, the gel can be categorized as a relatively weak cyclopeptide-based hydrogel in comparison to similar systems, which typically exhibit storage moduli in the range of 100 to 150 Pa.[81,163] At higher frequencies, a transition from elastic-dominated to viscous-dominated behavior was identified, marked by the gel decay point or flow point. This transition occurred 8 Hz (4 wt%), followed by 10.1 Hz (1 wt%), and 11 Hz for 2 wt% (figure 4.20A, grey marked). These week hydrogel networks are generally susceptible to shear-induced collapse as they lack the mobility needed to reorganize under stress.

Amplitude sweep (figure 4.20C) measurements further support these observations, showing that 2 wt% demonstrated the highest yield strain with 8% shear strain, representing the maximum deformation the gel can endure while remaining in the elastic regime. This indicates enhanced mechanical resilience. The shear strength order 2 wt% > 1 wt% > 4 wt% indicates that lower concentrations support supramolecular network connectivity and mechanical stability more

favorably compared to higher concentrations (figure 4.20D).

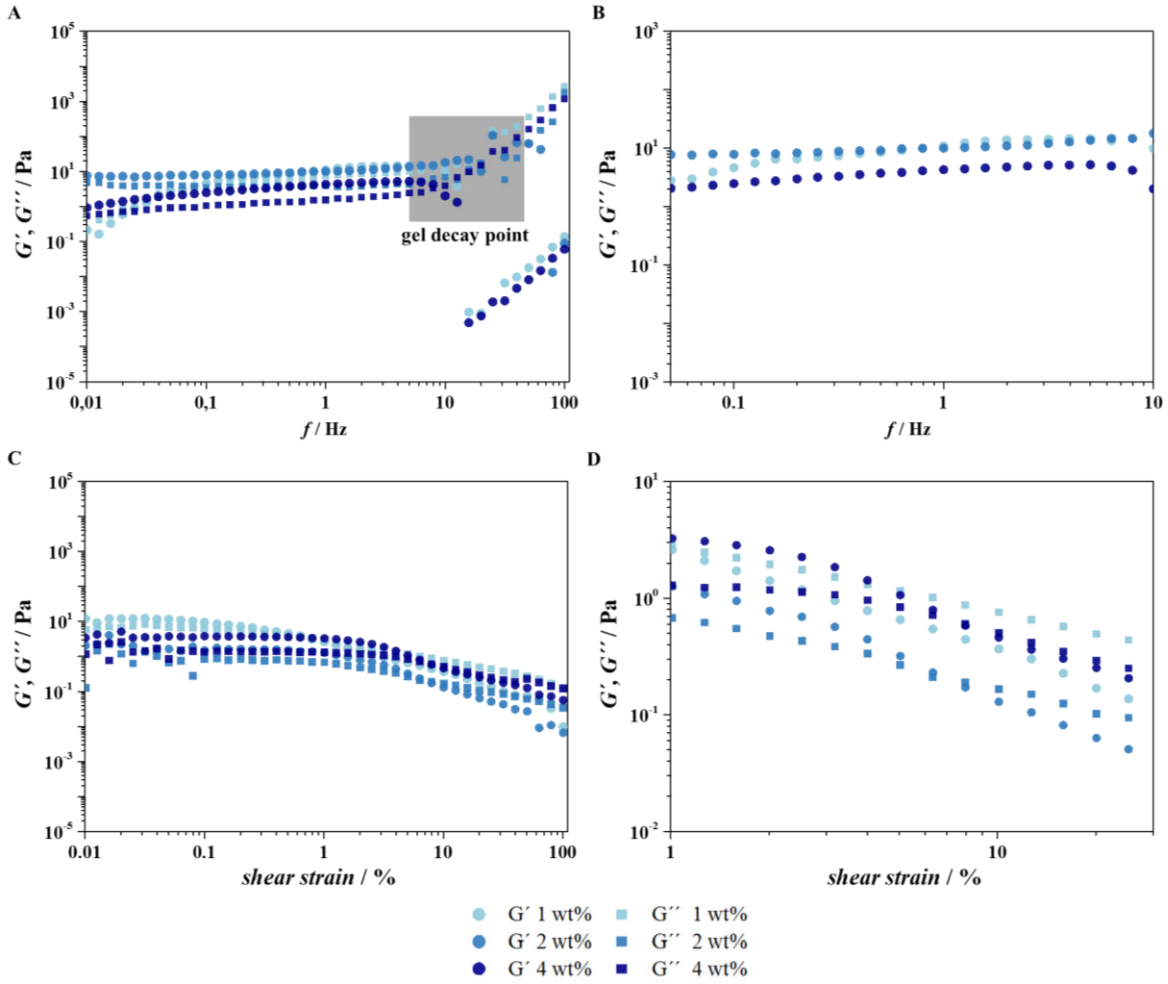

Figure 4.20: ***A*** *Frequency sweep measurements (0.1% strain, 0.01–100 Hz) grey marked the gel decay point and* ***B*** *magnified view of the LVE region from A (0.05–10 Hz);* ***C*** *Shear strain sweep measurements (1 Hz, 0.01–100% strain) and* ***D*** *zoomed-in view of C focusing on the gel decay point (1–12% strain); All measurements were performed on* ***CP5*** *in PBS (pH 7.4) at different concentrations, with storage (G') and loss moduli (G") at constant 20 °C.*

To investigate the disassembly of the hydrogel network under acidic conditions, rheological measurements were performed on a sample at pH 3.1 (2 wt%). The rheological behavior of the acidic sample was significantly altered compared to its behavior at physiological pH. Across the entire frequency range (figure 4.21A), *G″* remained higher than *G′*, indicating a predominantly viscous-dominated system and the absence of gel-like properties. In amplitude sweep experiments (figure 4.21B), both *G″* and *G′* fluctuated irregularly without a clear dominance, further confirming the lack of a stable supramolecular network. This behavior is characteristic of a disordered, fluid-like material.[162] At acidic pH, the protonation of histidine residues disrupts the formation of β-sheet-like motifs by electrostatic interactions, which results in destabilizing the supramolecular network. Consequently, the pH-responsive properties of the supramolecular system were successfully demonstrated.

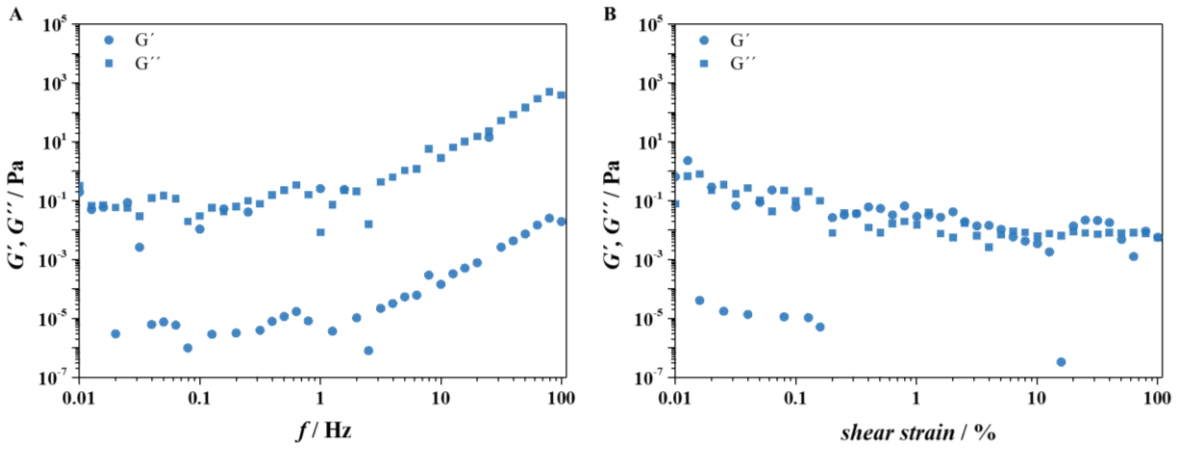

***Figure 4.21: A** Frequency sweep (0.1% strain, 0.01- 100 Hz) and **B** shear strain sweep (1 Hz, 0.01 – 100% strain) of **CP5** (2 wt% in phosphate-buffered saline, pH = 3.1) with storage (G') and loss moduli (G") at constant 20 °C.*

In order to enhance the gel's strength and stability, crosslinkers with PEG chains of varying lengths (**CL2000**, **CL3000**, and **CL6000**) were utilized in various mixing weight ratios with **CP5** (95:5, 90:10, and 80:20 (**CP5**:**CL**)). The underlying hypothesis was that the supramolecular crosslinkers would generate additional linkage points between the nanotubes, thereby enhancing the mechanical properties of the gels. The rheological measurements encompassed both frequency sweep and amplitude sweep experiments at a total concentration of 1 wt% in PBS at physiological pH (7.4). To ensure the occurrence of supramolecular co-assembly between **CP5** and the different **CL**, both components were initially combined as solids and subsequently dissolved. This approach, which is documented in the literature[94], ensures a homogeneous supramolecular co-assembly of both components and prevents the formation of segregate supramolecular systems.

For the shortest crosslinker, **CL2000** (figure 4.22), a ratio of 90:10 (**CP5**:**CL**) with a *G′* modulus of over 10 kPa demonstrated the strongest gel formation and the most stable LVE behavior in the frequency sweep (figure 4.22B) over the entire measurement range. This ratio produced the strongest hydrogel measured in this study, with a strength comparable to hydrogels designed for biomedical applications, such as tissue engineering scaffolds, mimicking the properties of soft extracellular matrix (ECM) components like those in cartilage or muscular tissue.[164,165] In amplitude sweep experiments (figure 4.22C), mechanical destabilization was observed at approximately 0.3% (figure 4.22D) shear strain, corresponding to the yield strain, where the gel transitions from elastic-dominated to viscous-dominated behavior. The 95:5 and 80:20 (**CP5**:**CL**) ratios yielded weaker gels compared to **CP5** alone, with a ratio of 80:20 (**CP5**:**CL**) exhibit particularly poor stability and *G″* dominating. This suggests that low PEG content in **CL2000** facilitates gel formation, while higher PEG content hinders intermolecular interactions of CPs nanotubes.

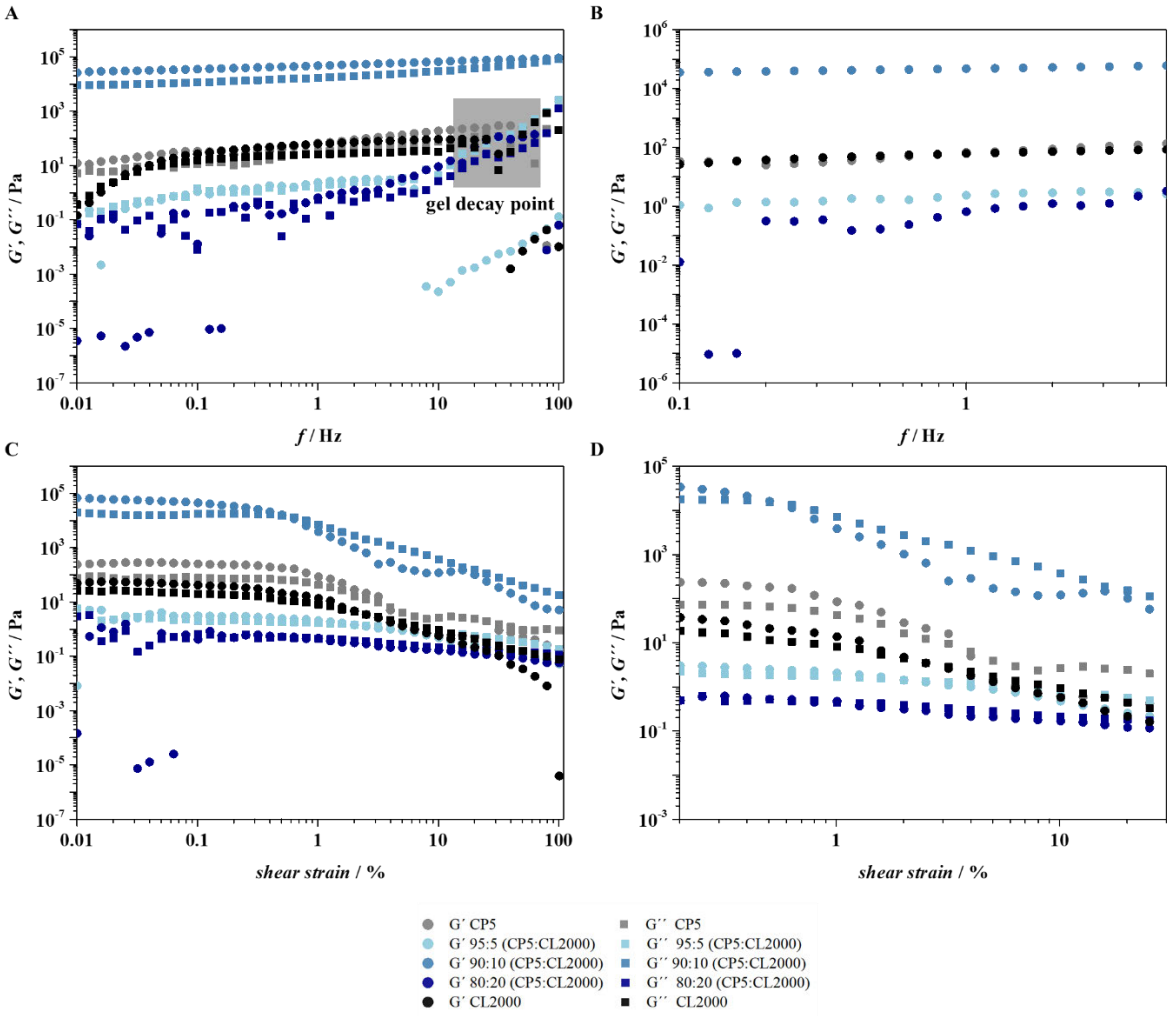

Figure 4.22: ***A*** *Frequency sweep measurements (0.1% strain, 0.01–100 Hz) grey marked the gel decay point and* ***B*** *magnified view of the LVE region from A (0.1–4 Hz);* ***C*** *Shear strain sweep measurements (1 Hz, 0.01–100% strain) and* ***D*** *zoomed-in view of C focusing on the gel decay point (0.2–12% strain); All measurements were performed on* ***CP5*** *with* ***CL2000*** *at different weight ratios in PBS(pH 7.4, 1 wt%) with storage (G') and loss moduli (G") at constant 20 °C.*

For **CL3000** (figure 4.23), the strongest gel formation was observed at a 80:20 (**CP5**:**CL**) ratio with a *G′* modulus of approximately 110 Pa, which exhibited an LVE over the entire measured range in the frequency sweep (figure 4.23B). In amplitude sweep, the gel decay point was observed at approximately 80% shear strain (figure 4.23D), indicating high mechanical stability. In contrast, the 90:10 and 95:5 (**CP5**:**CL**) ratios exhibited weaker gel properties, with 90:10 (**CP5**:**CL**) showing no improvement over **CP5** alone and a ratio of 95:5 (**CP5**:**CL**) displaying the lowest gel strength. In comparison to **CL2000**, **CL3000** demonstrates that extended PEG chains facilitate enhanced crosslinking at higher ratios.

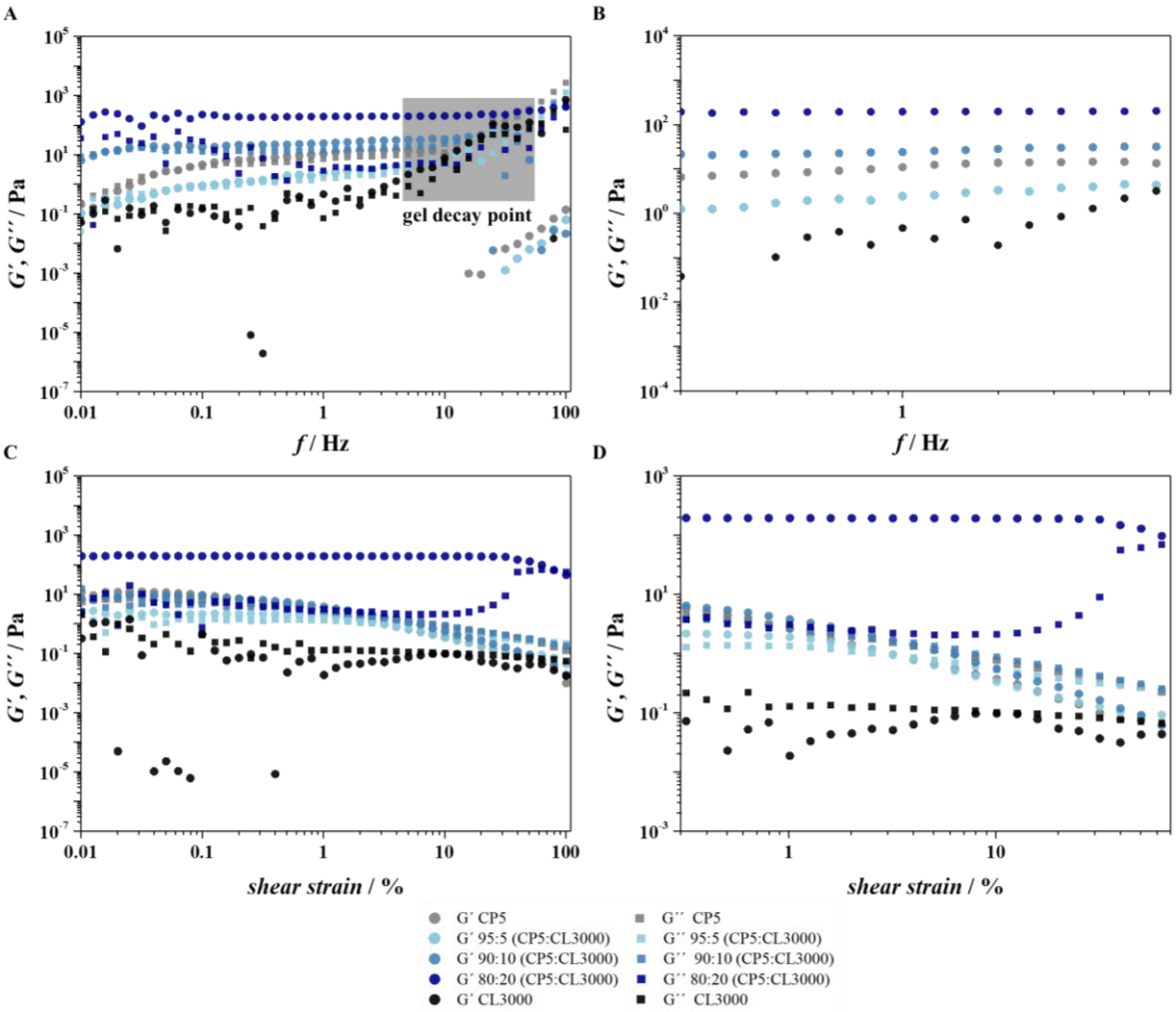

Figure 4.23: ***A*** *Frequency sweep measurements (0.1% strain, 0.01–100 Hz) grey marked the gel decay point and* ***B*** *magnified view of the LVE region from A (0.2–7 Hz);* ***C*** *Shear strain sweep measurements (1 Hz, 0.01–100% strain) and* ***D*** *zoomed-in view of C focusing on the gel decay point (0.3–16% strain); All measurements were performed on* ***CP5*** *with* ***CL3000*** *at different weight ratios in PBS(pH 7.4, 1 wt%) with storage (G') and loss moduli (G") at constant 20 °C.*

CL6000 (figure 4.24) exhibited a gel strength at a 90:10 (**CP5**:**CL**) ratio, with a *G′* modulus of approximately 10 Pa (figure 4.24B). In contrast, the 95:5 and 80:20 (**CP5**:**CL**) ratios resulted in weaker gels, with a 95:5 (**CP5**:**CL**) ratio exhibiting properties analogous to those of **CP5** alone. Notably, a 80:20 (**CP5**:**CL**) ratio exhibited the longest stability, with a *G′* modulus of 4 Pa. The LVE in amplitude sweep (figure 4.33C) remained consistent for all ratios, for the same shear strain, indicating that **CL6000** did not enhance gel stability. The presence of longer PEG chains, as observed in **CL6000**, results in enhanced shielding of intermolecular interactions at high ratios, thereby impeding network formation.

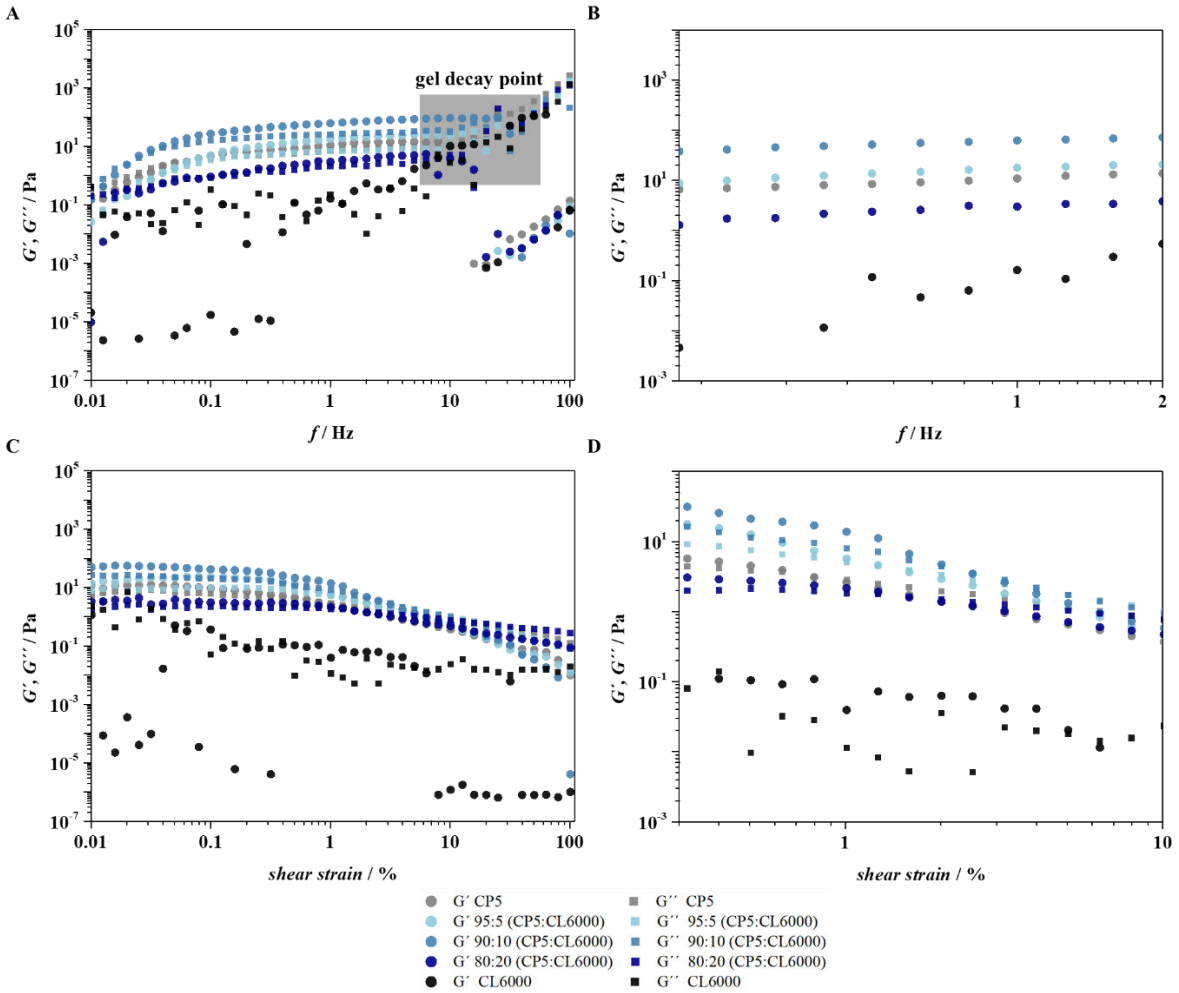

Figure 4.24: *A Frequency sweep measurements (0.1% strain, 0.01–100 Hz) grey marked the gel decay point and* ***B*** *magnified view of the LVE region from A (0.2–2 Hz);* ***C*** *Shear strain sweep measurements (1 Hz, 0.01–100% strain) and* ***D*** *zoomed-in view of C focusing on the gel decay point (0.3–10% strain); All measurements were performed on* ***CP5*** *with* ***CL6000*** *at different weight ratios in PBS(pH 7.4, 1 wt%) with storage (G') and loss moduli (G") at constant 20 °C.*

The findings indicate that the length of the PEG moiety of the crosslinkers, in conjunction with the mixing ratio, plays a pivotal role in determining the gel's strength and stability. Shorter PEG chains, such as **CL2000**, favor gel formation at lower crosslinker ratios, while medium chain lengths, such as **CL3000**, demonstrate optimal performance at higher ratios. In contrast, longer chains, such as **CL6000**, exhibit stronger steric effects at high percentages, impeding gel formation.

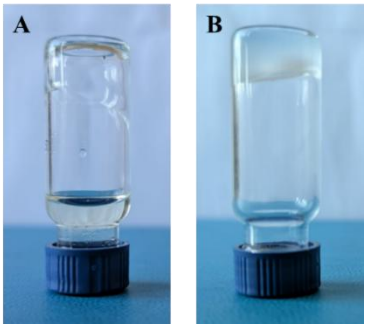

Figure 4.25: *Inverted vial test to visualize the macroscopic flow behavior of* ***A CP5*** *(1 wt%) and* ***B*** *the* ***CP5****:****CL2000*** *(90:10) hydrogel (1 wt%) in PBS (pH 7.4).*

Figure 4.25 presents photographic images of 1 wt% samples of **CP5** (Figure 4.25A) and the strongest hydrogel identified in the rheological experiments, the mixture of **CP5** with the crosslinker **CL2000** at a 90:10 ratio (Figure 4.25B), in phosphate-buffered saline (PBS, pH 7.4). The samples were photographed upside down in mass vials to visualize their macroscopic flow behavior. While the **CP5** sample exhibits a viscous character, it flows almost completely to the bottom of the vial within a few seconds, indicating insufficient structural integrity. In contrast, the **CP5**:**CL2000** (90:10) sample remains largely stationary at the inverted vial's opening and flows only slowly, demonstrating

pronounced resistance to deformation. These observations reflect a substantially higher mechanical strength and elasticity of the formed hydrogel, consistent with the rheological data and confirming the macroscopic formation of a stable, elastically dominated gel.

Notably, no hydrogel formation could be detected when the two components, **CP5** and **CL**, were initially dissolved separately and subsequently mixed in solution, as confirmed by rheological measurements (see appendix figure 10.33). This finding indicates that the supramolecular system exhibits limited dynamic exchange once self-assembled structures have formed prior to mixing in solution. In contrast, when **CP5** and **CL** are combined in the solid state prior to dissolution, coassembly can occur during the initial supramolecular structuring process upon solvation. This likely facilitates the formation of heterogeneous supramolecular networks and leads to the emergence of stable hydrogels under these conditions.

4.3 Conclusion

This chapter focused on the synthesis and characterization of a water-soluble cyclopeptide designed according to the principles of supramolecular chemistry. The objective of developing a cyclopeptide with improved water solubility without the conjugation of polymers was successfully achieved. Through the optimization of coupling reagents and reaction conditions, epimerization on C-terminal histidine groups was significantly suppressed, while cyclization reaction time was reduced and product yields improved.

Structural analysis using SIM microscopy revealed the formation of two-dimensional sheets based on the lateral aggregations of β-sheet-like structure promoted nanotubes. These structures arise from interactions between the peptide backbones via hydrogen bonds, which stabilize the axial alignment, and potential lateral π-π stacking interactions between the aromatic side chains of tryptophan. The assemblies serve as the basis for the formation of a three-dimensional network that ensures the mechanical stability of hydrogels. The formation of hydrogels was unequivocally confirmed through rheological investigations. Under acidic conditions, it was demonstrated that cyclopeptide-based hydrogels disassemble, highlighting the role of protonation processes in destabilizing the supramolecular nanotubes and networks. In contrast, CD spectroscopy proved unsuitable for analyzing such structures, most likely due to the alternating arrangement of D- and L-amino acids, which presents the formation of characteristic β-sheet signatures of natural peptides.

The synthesis of telechelic cross-linkers, consisting of PEG chains of varying lengths functionalized with cyclopeptides, was successfully achieved using NHS ester-based amidation as an efficient coupling strategy. Copper-catalyzed azide-alkyne cycloaddition click chemistry failed in histidine-rich structures, due to their tendency to complex copper ions. These supramolecular cross-linkers were combined with the cyclopeptide assemblies to modulate the mechanical properties of the hydrogels, addressing the weak properties observed in samples composed solely of the cyclopeptide. Rheological results showed that these mixed systems exhibited enhanced stability and elasticity and revealed a clear dependence of mechanical properties on concentration and composition between cross-linker and cyclopeptide. Under optimized conditions, the hydrogels formed a viscoelastic matrix, stabilized by supramolecular interactions and cross-linking. Hydrogels with mechanical strengths ranging between 10 Pa and 10 kPa are particularly suited for biomedical applications. They can function as depot systems for controlled drug release[166,167], which can be regulated by pH-sensitive histidine residues in response to environmental changes, such as in tumors or inflamed tissues. Moreover, their water-rich, ECM-like matrix promotes cell adhesion and growth, making them ideal for applications in regenerative medicine.[168]

5 Design and Development of a Supramolecular Copolymer System for Nucleotide Delivery

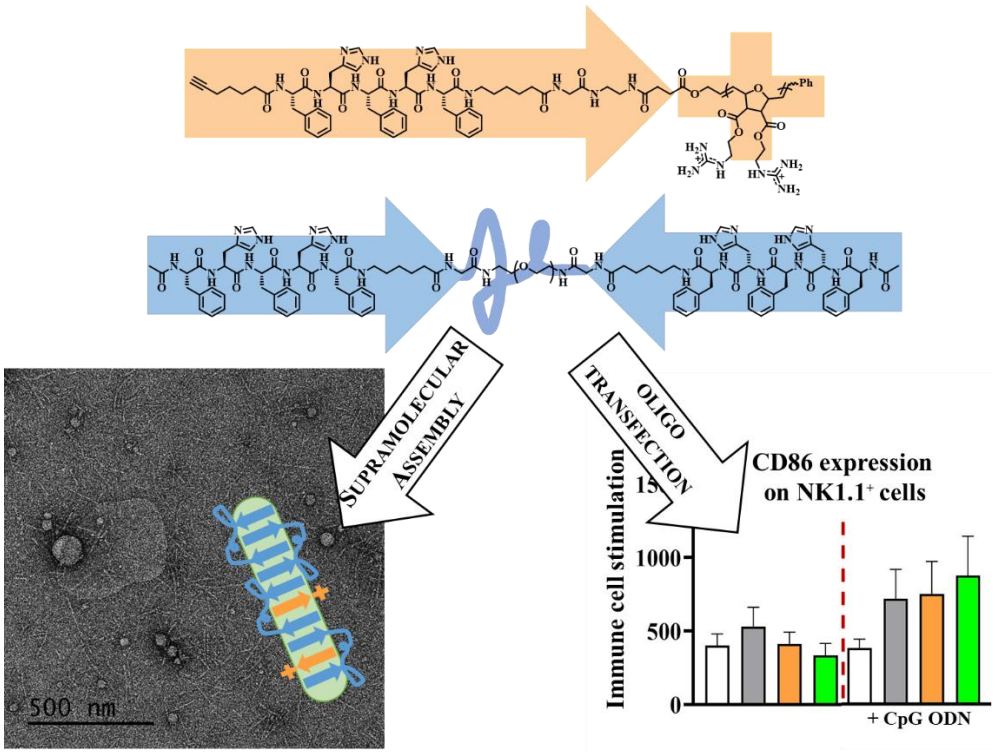

5.1 Theoretical Background

Oligonucleotide therapy, encompassing both RNA and DNA-based approaches, holds great potential for the treatment of various serious diseases, including cancer, allergies, asthma, and infectious diseases. These short nucleic acid sequences can precisely modulate molecular processes within cells, allowing for targeted regulation of gene expression and cellular signaling pathways. Their high structural flexibility enables synthetic DNA and RNA sequences to intervene at the molecular level with accuracy, establishing them as a advanced strategy in modern medicine.[169,170]

The most significant forms of oligonucleotide therapy encompass oligodeoxynucleotides (ODNs) and short interfering RNA (siRNA). Oligodeoxynucleotides (ODNs), such as CpG oligonucleotides (CpG-ODNs), which are cytosine-phosphate-guanine dinucleotide motifs recognized by the immune system as danger signals, bind to Toll-like receptor 9 (TLR9), thereby activating the innate and adaptive immune systems.[171] Consequently, they facilitate the release of pro-inflammatory cytokines and contribute to an effective immune response, as demonstrated by their success in the treatment of cancer and allergies.[172] In contrast, siRNA mediates the mechanism of RNA interference (RNAi), enabling the targeted silencing of specific genes. This property renders siRNA a particularly valuable therapeutic option for the treatment of genetic diseases and other conditions that are difficult to treat.[173] Despite their therapeutic versatility, ODNs and siRNA present several challenges in terms of their clinical application. In the absence of adequate protective mechanisms, these agents are rapidly degraded by nucleases within the bloodstream. Furthermore, their negative charge results in a low cell membrane permeability, impeding the efficient uptake of these agents into target cells. Therefore the use of so-called "carrier" systems in order to protect the nucleotides (cargos) is essential to facilitate their uptake and ensure their targeted release at the site of action.[174]

The foundation of carrier research was established with lipoplexes, cationic liposomes based on lipids that spontaneously form complexes with nucleic acids (figure 5.1A). The primary advantage of cationic lipids lies in their ability to efficiently interact with both anionic siRNA and cell membranes through electrostatic interactions, significantly enhancing cellular internalization. [175] A widely used cationic lipid is 1,2-dioleoyl-3-trimethylammonium propane (DOTAP, figure 5.1B), which forms stable cationic liposomes in solution.[175] These liposomes can encapsulate nucleic acids and efficiently transport them into cells *via* membrane fusion. Another commercially established example is lipofectamine, a commonly used transfection reagent in cell culture studies.[176] The exact chemical composition of lipofectamine® is proprietary; however, it is known to contain a mixture of cationic lipids, co-lipids, and helper lipids such as 1,2-dioleoyl-sn-glycero-3-phosphoethanolamine (DOPE, figure 5.1C), which facilitate membrane fusion and improve transfection efficiency. While DOTAP can independently form lipoplexes, its efficiency can be significantly enhanced by incorporating neutral helper lipids. DOPE is also commonly added to promote endosomal escape.[177,178] Additionally, cholesterol is often included to improve membrane stability and enhance lipoplex longevity.[179] A disadvantage of cationic lipids is their high cytotoxicity compared to neutral liposomes, as well as their shorter half-life in serum. Additionally, they can induce immunogenic responses, limiting their application in *in vivo* studies. A strategy to overcome these limitations is the PEGylation of lipoplexes. Modification with PEG can enhance serum stability, reduce immunogenicity, and extend circulation time, making lipoplexes more suitable for therapeutic applications.[180]

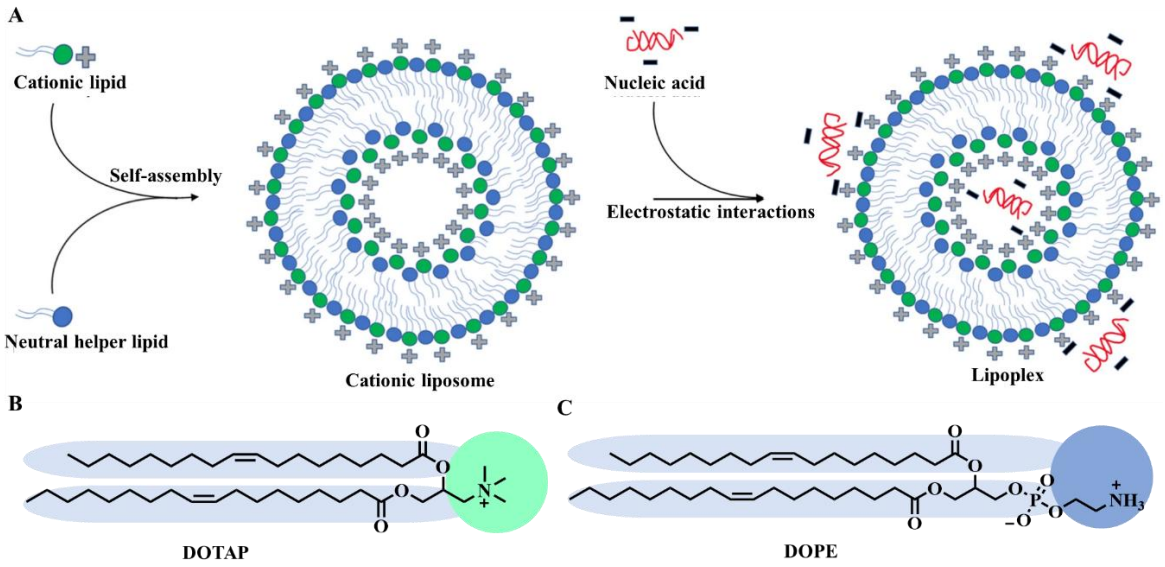

Figure 5.1: ***A*** *Diagrammatic representation of synthesis, preparation and formation of lipoplex[181] Reproduced with permission from Springer Nature;* ***B*** *Chemical structure of DOTAP;* ***C*** *Chemical structure of DOPE.*

Supramolecular oligocomplexes, so-called polyplexes, have become a novel strategy for oligotransfection to overcome the disadvantages of lipoplexes. Polyplexes are formed through electrostatic interactions between cationic polymers and the negatively charged phosphate backbone of nucleotides. These interactions condense nucleotides into stable nanostructures, protecting them from enzymatic degradation and enhancing cellular uptake.[182] Synthetic polymers are used whose properties can be precisely tailored through molecular design. Among cationic polymers, polyethylenimine (PEI) is considered the benchmark for nucleotide transfer due to its high charge density, which enables strong nucleotide binding, and its ability to destabilize endosomal membranes, facilitating cargo release.[183] With a molecular weight of 25 kDa it has shown high efficacy in siRNA transfection, but its application is limited by significant toxicity and poor biodegradability. To overcome these drawbacks, modifications such as PEGylation and alterations to its branching structure have been developed.[184] The structural adaptability of polymers allows their physicochemical properties, such as charge density, molecular weight, and solubility, to be tailored to specific therapeutic needs, making them a versatile platform for oligonucleotide delivery.

The uptake of cationic polyplexes into cells occurs through various endocytosis mechanisms, which depend on the physicochemical properties of the polyplexes and the cell type (figure 5.2). Clathrin-dependent endocytosis is the most commonly described pathway for polyplexes with a particle size of ~200 nm. Internalization can be either receptor-mediated through specific ligands or nonspecific *via* electrostatic interactions.[185] While transferrin receptors, LDL receptors, and epidermal growth factor receptors (EGFR) enable targeted uptake with appropriate ligands on the polyplex surface, highly cationic polymers such as PEI[186] or poly-L-lysine (PLL)[187] with a size of ~90 nm can directly interact with negatively charged cell membrane proteoglycans like heparan sulfate and be internalized. After internalization into clathrin-coated vesicles, the polyplexes are transported to early endosomes, where the pH decreases from approximately 6.0-6.5 in early endosomes to 5.0-5.5 in late endosomes and 5.0-4.5 in lysosomes.[188] This acidification increases the risk of enzymatic degradation, necessitating endosomal destabilization to release the nucleic acid. Highly cationic polymers such as PEI can utilize the so-called proton sponge effect, where proton uptake leads to osmotic water influx and ultimately endosomal rupture.[188] Additionally, cationic polymers can

destabilize the endosomal membrane by interacting electrostatically with membrane lipids and forming pores. In some cases, polyplexes contain pH-sensitive peptides that undergo conformational changes under acidic conditions, facilitating direct membrane fusion.[188] An alternative mechanism is caveolae-dependent endocytosis, which is preferred for smaller polyplexes (< 60 nm). This process is highly receptor-dependent. Caveolin-mediated uptake pathways allow polyplexes to bypass lysosomal degradation, enabling more efficient cellular uptake into the cytoplasm. Since cationic polyplexes rarely interact with these specific receptors, they utilize this mechanism less frequently. Highly cationic and lager polyplexes (≥ 1 µm) can also induce macropinocytosis, a nonspecific process in which extracellular fluid and dissolved molecules are internalized in large vesicles. This mechanism is particularly relevant for larger polyplexes with high surface charge. In rare cases, direct membrane fusion has also been described, where highly cationic polyplexes destabilize the cell membrane and enter the cytosol directly.[185,188]

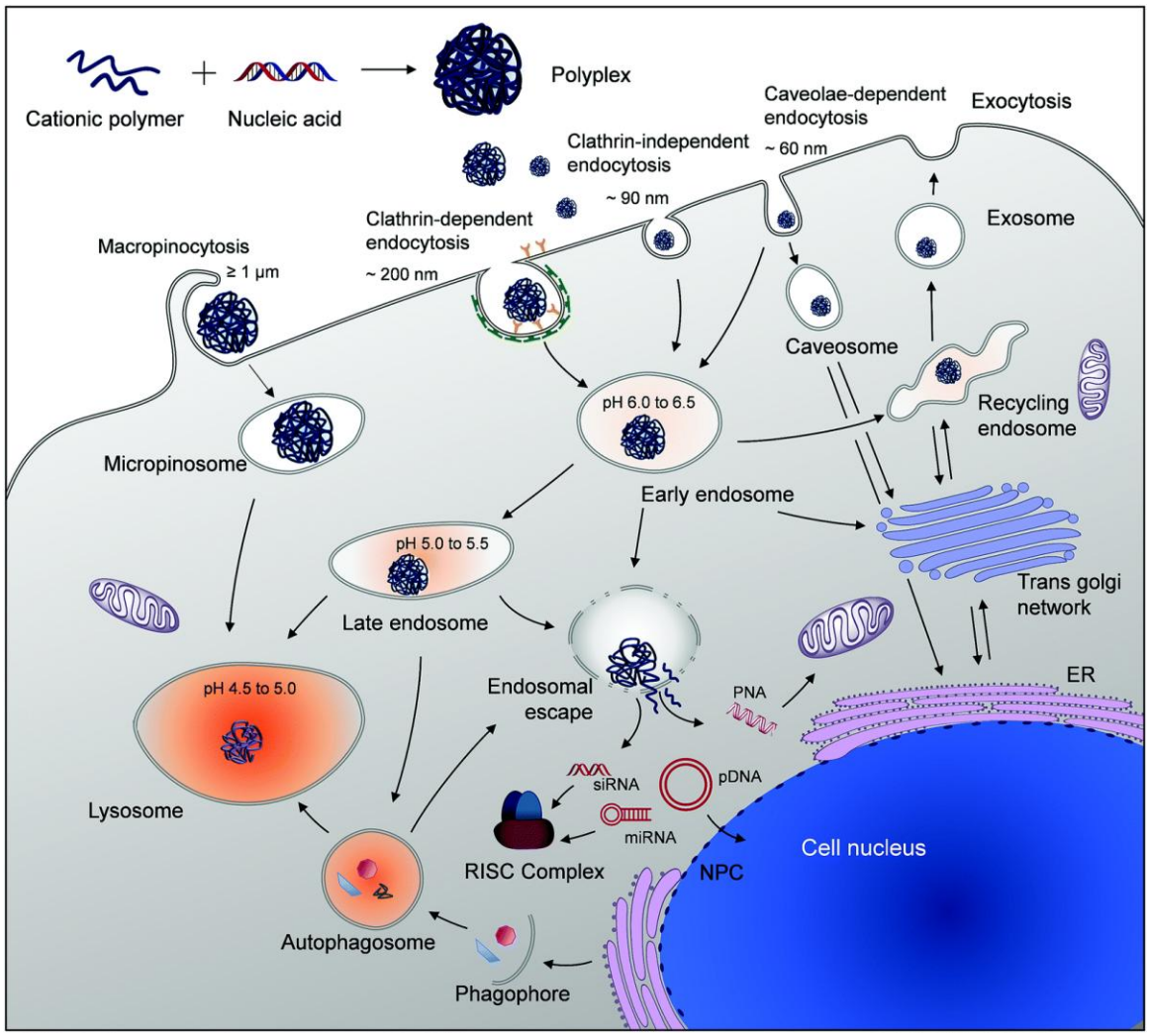

Figure 5.2: *The gene delivery process of cationic polymers including polyplex formation, intracellular uptake via various endocytosis pathways, intracellular polyplex trafficking, endosomal escape into the cytoplasm, release of the cargo from the polymer and transport to the site of action. Depending on the type of nucleic acid, the site of action is either located within the cytoplasm or in the nucleus. ER: endoplasmic reticulum; NPC: nuclear pore complex.[188] Reproduced with permission from Royal Society of Chemistry.*

In addition to synthetic polymers, peptides represent a promising class of polyplex carriers. In particular, cell-penetrating peptides (CPPs), which typically consist of a hydrophobic domain and a cationic amino acid segment, play a crucial role in enhancing nucleic acid delivery.[189] Their

positively charged residues, such as arginine and lysine, enable strong electrostatic interactions with anionic nucleic acids, promoting complex formation and facilitating efficient cellular uptake.[190] This occurs either through direct membrane translocation or *via* endocytic mechanisms such as clathrin- or caveolin-mediated endocytosis. Well-known CPPs include the TAT peptide (trans-activator of transcription) from the HIV-1 virus[191], penetratin[192], and oligoarginine peptides.[190] Despite their high efficiency, CPPs have limitations in their application, as they often utilize non-specific cellular uptake pathways or may be unstable due to enzymatic degradation. To overcome these limitations, Cell-Penetrating Peptide Mimetics (CPPMs) were developed. These systems combine the functionality of CPPs with synthetic or polymer-based structures to improve stability, specificity, and biocompatibility. CPPMs mimic the cell-penetrating capability of classical CPPs but exhibit optimized physicochemical properties that allow for more targeted uptake and controlled intracellular processing.[193]

An example of such a system is the mPEG2000-PLA3000-*b*-R_{15} triblock copolymer, developed by ZHAO *et al*.[194] It consists of monomethoxy-polyethylene glycol (mPEG), poly(D,L-lactide) (PLA), and a polyarginine block (R_{15}), which is responsible for the cationic charge and interaction with nucleic acids (figure 5.3A). While PEG enhances the biocompatibility and PLA serves as a biodegradable segment, polyarginine functions as the cationic unit for siRNA condensation. The resulting micelleplexes, i.e., self-assembled cationic nanomicelles loaded with siRNA (figure 5.3B), demonstrated high stability and improved cellular uptake in MCF-7 breast cancer cells compared to PEI. *In vitro*, transfection with EGFR-specific siRNA led to a significant reduction in EGFR expression, while *in vivo*, tumor growth inhibition was observed without detectable side effects (figure 5.3C).

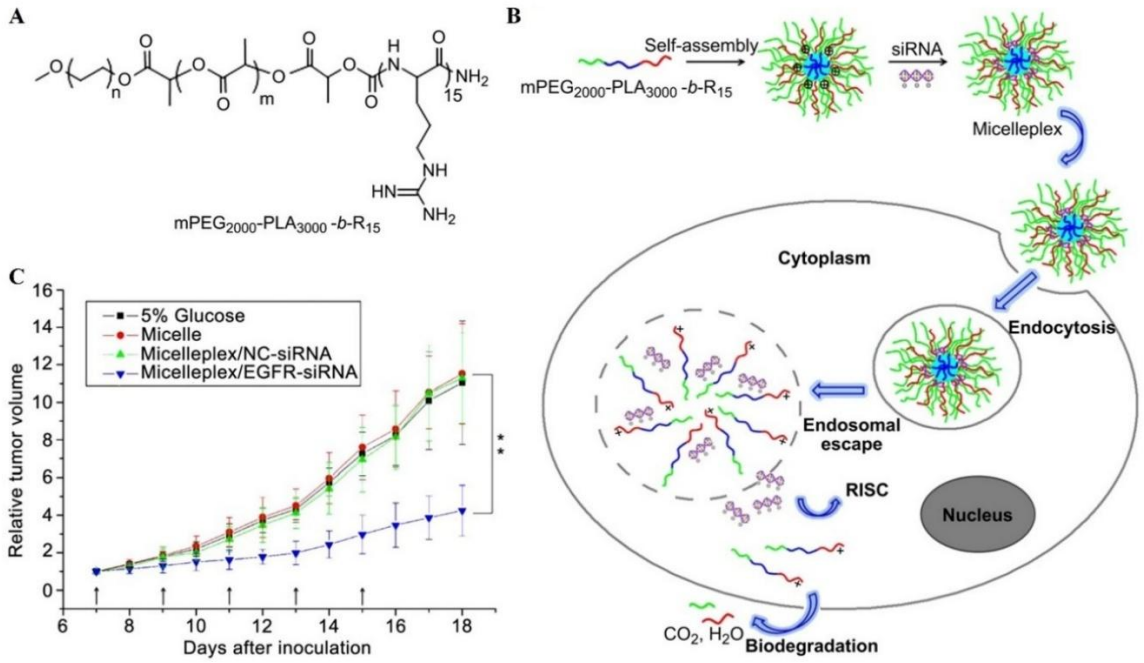

Figure 5.3: ***A*** *Chemical structure of* ***mPEG2000-PLA3000-b-R15;*** ***B*** *schematic illustration of biodegradable cationic micelles* ***mPEG2000-PLA3000-b-R15*** *for delivering siRNA into cancer cells;* ***C*** *Anti-tumor effects of micelleplexes. Female Balb/c nude mice xenografted MCF- 7 tumors were injected intravenously with micelle/siRNA complexes (each dose of 1 mg siRNA/kg interval 2 days) for a total of 5 doses MCF-7 tumor growth inhibition by micelleplex.[194] Reproduced with permission from Elsevier.*

5.2 Motivation and Concept

The targeted and efficient transfection of nucleic acids into cells is a central goal of modern gene-regulating technologies, particularly in the context of tumor therapy. A key challenge lies in the development of effective and biocompatible transport systems that protect nucleic acids from enzymatic degradation while exhibiting low toxicity. This project focuses on the development of a supramolecular polyplex system that ensures high efficiency in nucleotide transfer while maintaining biocompatibility and protection against enzymatic degradation.

For this purpose, a system comprising two peptide-polymer conjugates was developed, whose properties complement each other and together form the foundation for a supramolecular copolymer system. Both conjugates contain the same peptide sequence H-L-Phe-L-His-L-Phe-L-His-L-Phe-OH, which promotes the formation of β-sheet structures through secondary interactions such as hydrogen bonding of the amide groups and π-π stacking between aromatic residues, resulting in the supramolecular coassembly of both polymer conjugates into nanorods.

The first peptide-polymer conjugate is a cell-penetrating peptide mimetic (CPPM) inspired by the natural peptide Pep-1.[195] Like all CPPMs, it consists of a hydrophilic and a hydrophobic domain, enabling both nucleic acid binding and cellular interaction. The positively charged polymer segment, provided by the TEW group, contains guanidine moieties that facilitate strong electrostatic interactions with negatively charged nucleic acids.[196] This interaction not only promotes nucleic acid complexation but also enhances cell membrane association and endosomal escape, thereby improving intracellular delivery. The hydrophobic domain, derived from the peptide sequence, drives self-assembly into stable nanostructures. These conjugates exhibit high biocompatibility and offer additional functional versatility through synthetic modifications, making them adaptable for various biomedical applications.

The second peptide-polymer conjugate has a telechelic structure, which is known to assemble into nanorods *via* its two identical peptide segments and contains a PEG chain.[92] We hypothesis that this PEG chain could form a protective shell around the nucleic acids to shield them from enzymatic degradation. Cationic polymers often exhibit poor serum stability due to nonspecific interactions with serum proteins, leading to rapid elimination. This has also been observed for the cationic CPPM polymer.[197] To address this issue, PEG is used to shield the positive charges and reduce electrostatic interactions with serum proteins, thereby preventing rapid clearance by the reticuloendothelial system (RES).[198]

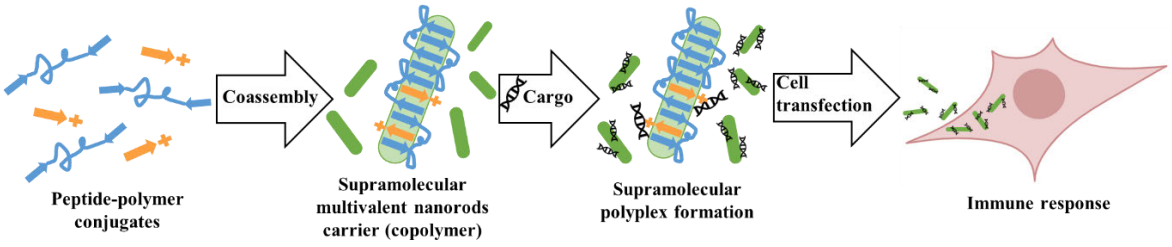

Figure 5.4: *Concept of a Supramolecular Polyplex Systems for Nucleic Acid Delivery.*

The goal of this project is the synthesis and coassembly of these two multidomain polymer-conjugates to develop a platform for the efficient and biocompatible transfer of nucleotides (figure 5.4). The transfection efficiency will be evaluated in various cell-based models. HEK-293T cells will serve as a model for siRNA transfection aimed at targeted gene regulation. In parallel, the

immunostimulatory properties of the system will be studied using CpG-ODNs in bone marrow-derived dendritic cells (BMDCs). Finally, the system will be tested in a more complex biological context with spleen cells. The spleen plays a crucial role in the immune system, particularly in the activation and regulation of immune responses.[199] Beyond tumor immunotherapy, the targeted stimulation of the spleen's immune system offers additional medical benefits, such as combating infections through enhanced immune responses and potential applications in immunodeficient conditions.

By examining cell activation and immune responses in a physiologically relevant context, the broad application potential of the supramolecular copolymer system as a carrier for immunostimulants can be evaluated, including its possible use in tumor immunotherapy.

5.3 Results and Discussion

5.3.1 Synthesis of peptide-polymer conjugates

Both conjugates for the supramolecular polyplex-carrier consist of a peptide and a polymer part. To enable supramolecular coassembly of the two polymer conjugates, the identical peptide sequence H-L-Phe-L-His-L-Phe-L-His-L-Phe-Ahx-Gly-OH **V-6** was incorporated into both conjugates. This sequence supports the formation of nanorods through secondary interactions. In addition, a spacer of aminohexanoic acid (Ahx) and glycine facilitates aggregation by creating a spatial separation between the hydrophobic peptide sequence and the hydrophilic polymer part. This separation can also reduce steric hindrance and increase the flexibility of the peptide-polymer conjugates, thereby forming self-assembly.

The peptide fragment (**V-1**) of the cationic poly-guanidine conjugate was N-terminally modified with 6-heptynoic acid to enable subsequent fluorescent dye labeling for microscopic studies. To investigate the influence of cationic charge density on cargo complexation efficiency, two poly-guanidine polymers with either five (**PG5**) or nine (**PG9**) repeating units were employed. Conjugation of the peptide with the polymer was achieved *via* active ester amidation, followed by acid-catalyzed deprotection to yield the target molecules **V-5(PG5)** and **V-5(PG9)** (figure 5.5).

The peptide sequence **V-1** was synthesized *via* solid-phase peptide synthesis using the Fmoc protocol. Amino acid coupling was performed with the HBTU/HOBt/DIPEA reagent combination. To ensure the retention of side chain protecting groups and prevent unintended side reactions in subsequent synthesis steps, **V-1** was cleaved from the resin using a 1:1 mixture of TFE and H_2O.

For conjugation with the guanidine polymers (**PG5** and **PG9**), a C-terminal modification was required to introduce a free primary amine, facilitating its reaction with the pentafluorophenyl (OPfp)-activated ester of the polymers. To achieve this, Fmoc-ethylenediamine hydrochloride was coupled to the C-terminus using PyBOP as the coupling reagent, yielding **V-2**. Following deprotection of the Fmoc group with 20% piperidine in DCM resulted in **V-3**, featuring a free primary amine at the C-terminus. The final conjugation of **V-3** to **PG5** and **PG9** was carried out via amidation under slightly basic conditions and nitrogen atmosphere. The reaction utilized OPfp-functionalized guanidine polymers provided by the TEW group at the University of Amherst, Massachusetts, USA. To counteract hydrolysis of activated esters, additional PyBOP was introduced to promote complete conjugation. Despite these optimizations, the conjugation step remained a limiting factor in the synthesis, with yields not exceeding 50%. Following conjugation, acid-labile protecting groups on both the peptide side chains and the guanidine moieties of the polymer were removed *via* TFA treatment in a stepwise manner to yield the target compounds **V-5(PG5)** and **V-5(PG9)**. While peptide side chain deprotection proceeded efficiently, the removal of Boc groups from guanidine units required prolonged reaction times of up to 16 hours.

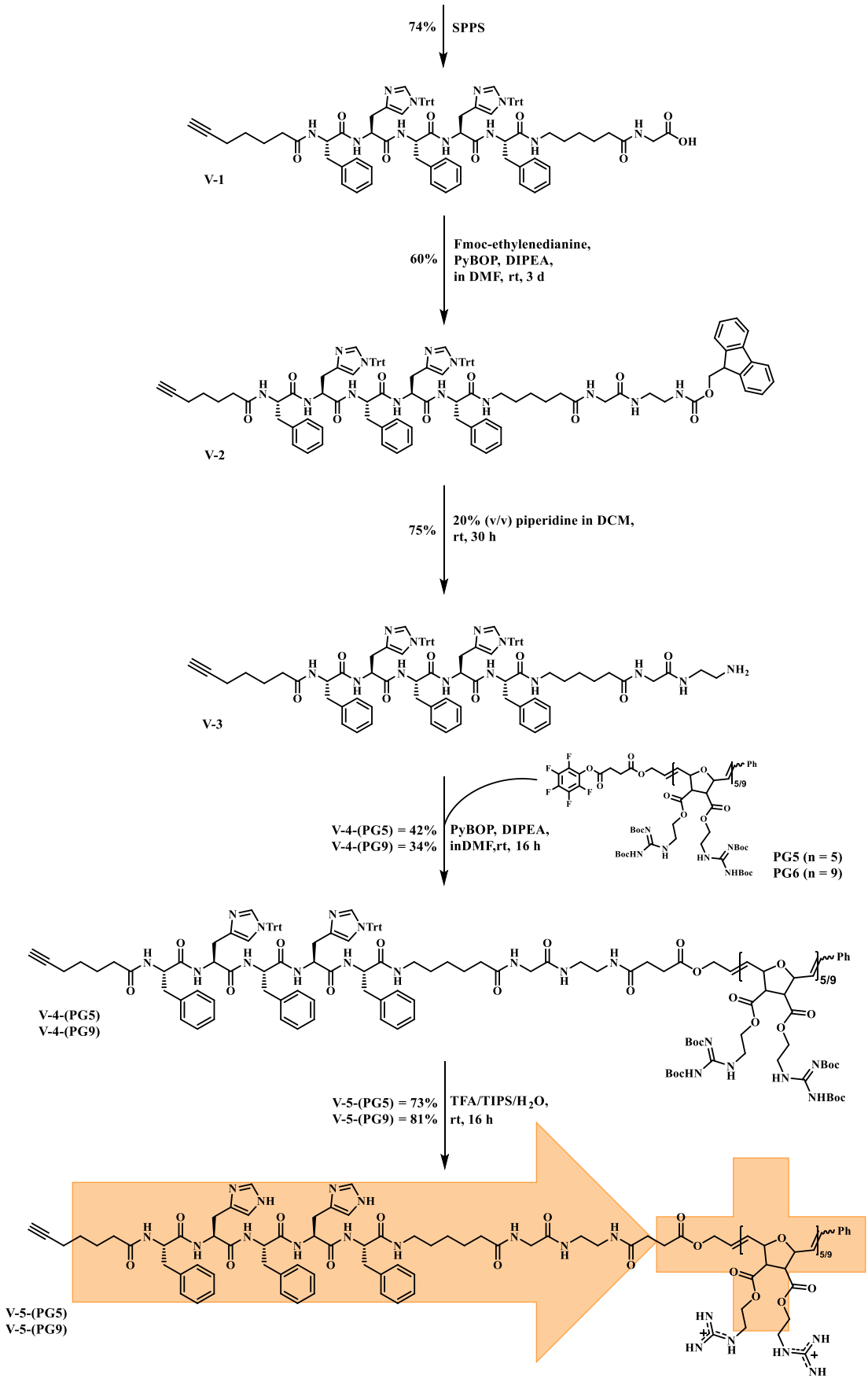

Figure 5.5: *Synthesis of* ***V-5(PG5)*** *and* ***V-5(PG9)****.*

As illustrated in figure 5.6, the gel permeation chromatography (GPC) elugrams demonstrate the molar mass distributions of the protected unconjugated polymers (**PG6** and **PG9**, represented by a dotted line), the protected conjugated polymers (**V-4**, represented by a dashed line), and the deprotected conjugated polymers (**V-5**, represented by a solid line). Interestingly, the conjugated guanidine polymers (**V-4** and **V-5**) show a higher retention time, despite its higher molecular weight compared to the unconjugated polymers (**PG**). This discrepancy is attributed to a possible reduction in the hydrodynamic volume[200] of the polymer upon peptide conjugation. However, it is more likely that peptide conjugates alters the physicochemical properties of the polymer, enhancing hydrophobic interactions with the column matrix. These altered interactions may further contribute to the prolonged retention time observed in GPC. As expected, the deprotected polymer **V-5** exhibits a longer retention time than the protected conjugates **V-4**, due to its lower molecular weight. The unconjugated polymers **PG6** and **PG9** exhibit the shortest retention times, and an additional signal is visible at higher retention times, which may be indicative of the presence of lower molecular weight species. It is noteworthy that **V-5(PG5)** displays a shoulder in the higher molecular weight region. As this impurity was only observed following deprotection and not in the preceding synthesis steps, it may be indicative of incomplete removal of the protecting groups. In addition, the deprotected conjugate **V-5(PG5)** shows an additional signal at the higher eluation volume of 21.0 mL. A similar phenomenon was observed for **V-4(PG9)**, where an impurity was present at a eluation volume of 21.5 mL, but was not detected after deprotection. It is also possible that these additional signals are the result of hydrolysis of the Pfp-ester. It is possible that during the conjugation reaction or storage, small amounts of the Pfp-ester underwent hydrolysis by water, resulting in the formation of by-products.

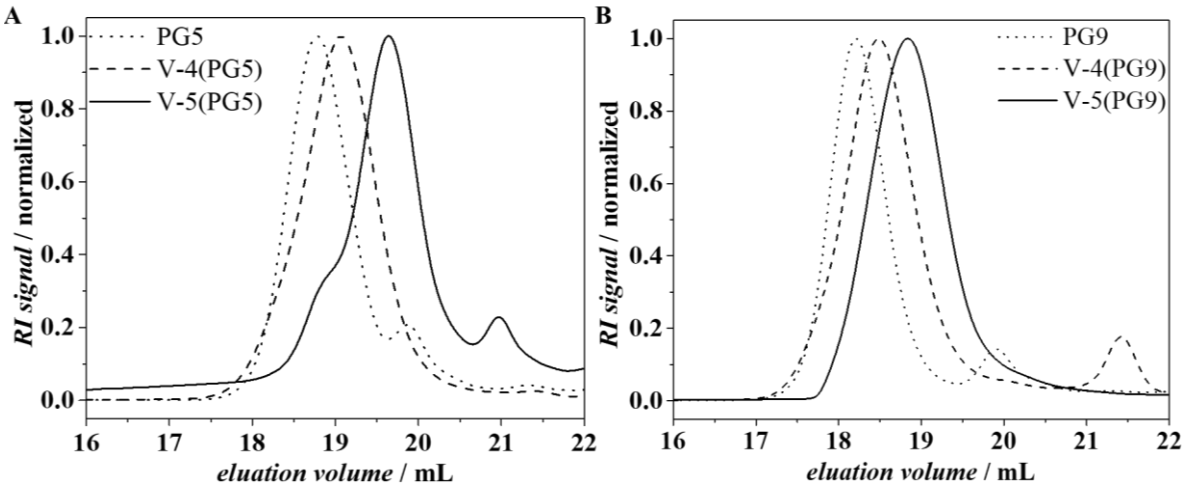

Figure 5.6: *HFIP-GPC elugrams of* ***A PG5****,* ***V-4(PG5)*** *and* ***V-5(PG5)****;* ***B PG9****,* ***V-4(PG9)*** *and* ***V-5(PG9)*** *(RI detector).*

In the case of PEG conjugate **V-8**, the N-terminal alkyne group in the peptide sequence was not required. Instead of this, the terminal amine group was acetylated to **V-6** following Fmoc deprotection. The peptide sequence was synthesized in a manner analogous to **V-1**, utilizing the Fmoc protocol and SPPS. The final capping step was conducted using acetic anhydride and DIPEA, resulting in the formation of the peptide sequence **V-6**.

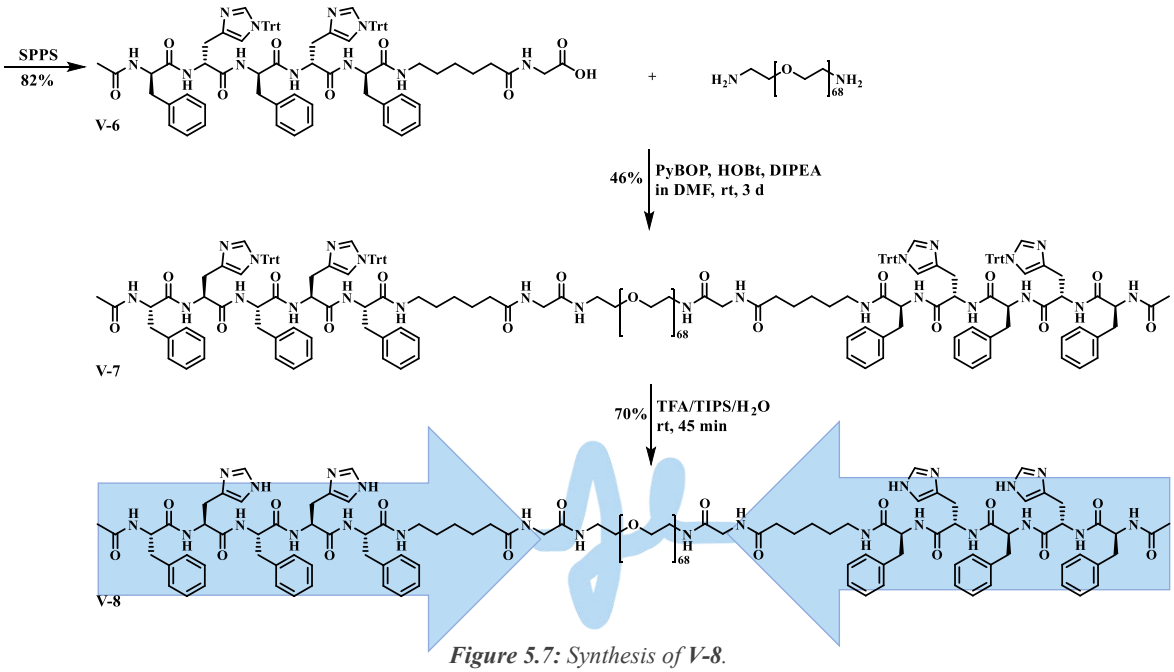

*Figure 5.7: Synthesis of **V-8**.*

Amidation of **V-5** with PEG3000 diamine was realized using PyBOP as coupling reagent, in order to produce the telechelic peptide-PEG conjugate **V-7**. Progress of the reaction was monitored daily by MALDI-TOF-MS spectrometry until near-complete conversion of PEG3000 diamine was observed after 3 days and a yield of 46% was obtained after purification by size exclusion chromatography (Biobeads®). The trityl protecting groups of the peptide sequences could be completely removed after only a few minutes in a TFA/TIPS/H2O (95:2.5:2.5) solution. The successful removal of the trityl protecting groups was also evidenced by a visible change in coloration of the reaction solution, which became yellow due to the release of trityl cations. Figure 5.8 illustrates the MALDI-TOF-MS spectra of the protected (**V-7**) and deprotected (**V-8**) PEG conjugate. The shift in molecular mass (-1148 Da) resulting from the removal of four trityl protecting groups attached to the histidine side groups, recognizable in a molecular weight reduction in molecular weight.

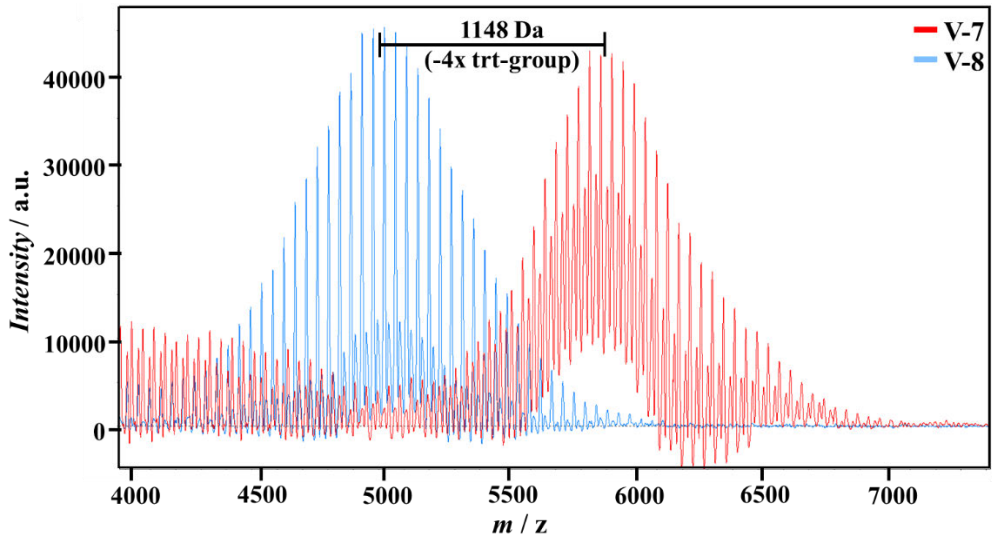

*Figure 5.8: MALDI-TOF MS of **V-7** (red) and **V-8** (blue) in a Ditranol-matrix.*

5.3.2 Supramolecular properties

The structural design of both polymer conjugates enables their assembly into ordered structures *via* the identical peptide sequence, H-L-Phe-L-His-L-Phe-L-His-L-Phe-Ahx-Gly-OH (**V-8**). This sequence facilitates supramolecular self-assembly through hydrogen bonding between the amide groups in the peptide backbone and additional interactions involving the aromatic side chains. The side chain of phenylalanine plays a critical role in promoting β-sheet formation due to its hydrophobic character and propensity for π-π-stacking interactions[201], which contribute to the stability of the structure. In addition, the inclusion of histidine through its imidazole side chain represents a pH-sensitive element that allows dynamic regulation of interactions under varying pH conditions. Due to the p*K*a of 6[2], the imidazole group is protonated at acidic pH and the supramolecular structure is dissociated by electrostatic repulsion. This is important for the endosomal release of cargo. The endosome has an acidic pH nearly 4.5, which causes the supramolecular copolymer to disassemble and release the cargo.[188] Thus, at physiological pH, the polyplex is intact and should release the cargo only in the endosomal compartment upon acidification.

To investigate the formation of nanorods and the morphology of potential aggregates, TEM was employed as an imaging technique capable of visualizing structures in the nanometer range. Samples of the PEG conjugate (**V-8**), the guanidine conjugate (**V-5**), and a **copolymer** of both conjugates with a composition of 5:1 (w/w) (**V-8/V-5**) were subjected to analysis in TRIS buffer. Each sample was prepared with a polymer concentration of 200 µM and a pH value of 7.6. The results of the imaging analysis are presented in figure 5.9.

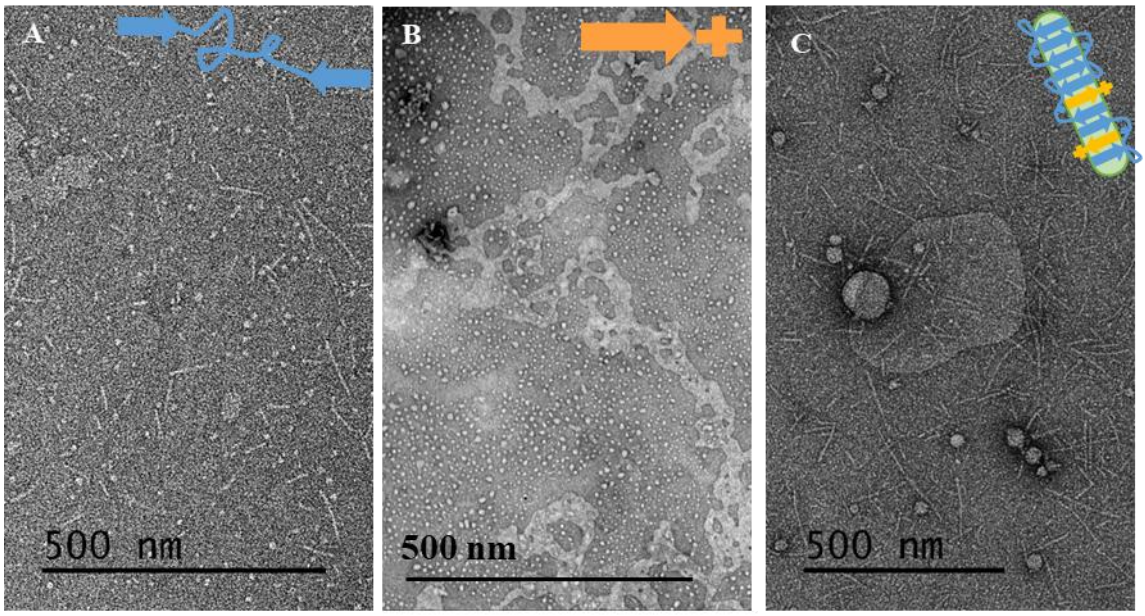

Figure 5.9: *TEM images of 200 µM TRIS buffer at pH 7.6 (negative stain) of* ***A V-8****;* ***B V-5(PG9)****;* ***C Copolymer*** *(5:1* ***V-8/V-5(PG9)****).*

The formation of nanorod-like structures with a average length of ±128 nm (n=31) was observed in the PEG polymer **V-8** (figure 5.9A), aligning with findings reported by RONJA OTTER.[92] In contrast, the cationic polymer **V-5(PG9)** formed micelle-like aggregates rather than rod-like structures with an average diameter of ±9 nm (n=41) (figure 5.9B). The same formation could be observed for the shorter **V-5(PG5)** (see appendix figure 10.43). This morphology can be attributed to the amphiphilic nature of **V-5**, which combines positively charged guanidinium groups with a hydrophobic peptide

segment. The high charge density of **V-5** induces strong repulsive interactions between the positive charges, which hinder β-sheet formation by outweighing the attractive hydrogen bonds. Interestingly, a 1:5 (w/w) mixture of **V-8** and **V-5(PG9)** revealed a higher density of nanorods (figure 5.9C) compared to the sample with only **V-8**, but with a lower average length of ±85 nm (n=47). This suggest coassembly of both peptide-polymer conjugates into β-sheet structures *via* their shared peptide sequence. The inclusion of **V-8** in the mixture likely mitigates the repulsive forces of **V-5(PG9)**, thereby promoting β-sheet formation and the resulting assembly of nanorods. The same behavior was observed for 5:1 (w/w) mixtures of **V-8** and **V-5(PG5)** (see appendix figure 10.43).

To further investigate the superstructures and their pH sensitivity, CD spectroscopic studies of **V-8**, **V-5(PG9)**, and a **copolymer** of the two conjugates in a ratio of 5:1 (w/w) (**V-8**/**V-5(PG9)**) were performed at neutral and acidic pH. All samples contained a polymer concentration of 50 µM in PBS. As previously published by RONJA OTTER, **V-8** shows a positive CD band at 218 nm in the acidic pH range, which was previously assigned to the random coil band.[92] However, recent evidence suggests that this band corresponds to a polyproline-II (PII) conformation rather than an unstructured random coil state.[202] PII represents a specific, albeit extended, secondary structure rather than a completely disordered state. Importantly, PII does not lead to supramolecular aggregation or higher order structures, meaning that the chains adopt a defined conformation but do not assemble into larger architectures.[202] The decrease of the 218 nm signal with increasing pH indicates a shift from PII-dominated conformations to β-sheet formation. No such significant band is found in the CD spectrum of the cationic polymer **V-5(PG9)**. The weak and broad signal at 220 nm for the sample at pH 2.6 falls in a similar spectral region, but its interpretation is not as clear as for **V-8**. This indicates that no defined superstructures are formed in the acidic range. In the neutral range the CD spectrum shows lower intensities due to the formation of micelle-like structures observed in the TEM images. The supramolecular **copolymer** of both also shows a significant PII-associated band in the acidic pH range. This band loses intensity in the neutral range, which is consistent with a structural reorganization towards β-sheet structures. Thus, CD spectroscopy provides evidence that a higher order supramolecular structure is present in the copolymer, which is disrupted in the acidic pH range.

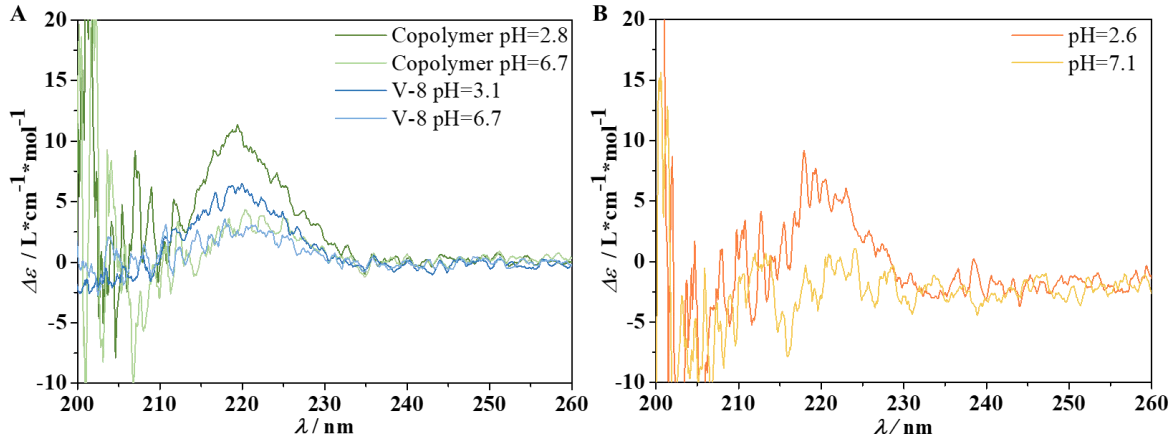

Figure 5.10: *CD spectrum of 50 µM solutions in PBS **A** of the **copolymer** and **V-8** and **B** **V-5(PG9)** at neutral and acidic pH range.*

5.3.3 Polyplex formation

To test the suitability of the supramolecular **copolymer** as a carrier for oligonucleotide transfection, the efficiency of the polyplex formation between polymer and oligonucleotide was analyzed. For this purpose, agarose gel electrophoresis was used. In this approach, samples with different charge ratios

between carrier (polymer) and cargo (oligonucleotide) are applied to an agarose gel and subjected to electrophoresis. In an electric field, negatively charged molecules such as uncomplexed oligonucleotides migrate to the positively charged anode. Successful complexation results in a neutral polyplex due to charge neutralization at the surface, preventing the migration of the oligonucleotide through the electric field during gel electrophoresis.

The complexation efficiency between the cationic polymer **V-5** and an oligonucleotide was initially optimized. For this purpose, the interaction between the plasmid DNA (pDNA) pGL3 (4818 bp)[203] and the cationic polymers **V-5(PG5)** and **V-5(PG9)** was examined at a charge ratio of 1:1 (N/P). The N:P ratio refers to the molar ratio between positively charged amine groups (N) and negatively charged phosphate groups (P) in RNA or DNA molecules. Due to the high negative charge density of the DNA strand, no complex formation was observed (see appendix figure 10.44). Increasing the charge ratio was not feasible because the low charge density of the polymers **V-5(PG5)** and **V-5(PG9)** would have required large polymer quantities, making the experiment not feasible for gel electrophoresis analysis. To overcome this limitation, a shorter 21-mer siRNA oligomer labeled with a Cy3 (cyanine 3) dye was employed. The use of fluorescence-labeled siRNA enables direct visualization under UV light, eliminating the need for gel staining (e.g. GelRed® that was used by the pDNA complexation) and thus minimizing the risk of false-positive signals caused by non-specific staining. This approach allows for the precise detection of the oligonucleotide's location and the clear differentiation between complexed and uncomplexed states. The impact of different charge ratios between the anionic siRNA and the cationic polymers **V-5(PG5)** and **V-5(PG9)** (N/P ratios between 1:1 and 50:1) was investigated. The gel electrophoresis results for the samples in Milli-Q® water are shown in figure 5.11. To serve as a control, the cationic polymer in the absence of siRNA (**V-5(PG5**) and **V-5(PG9)**) and a sample with siRNA without polymer (free siRNA) were applied, thereby ensuring that the observed band resulted exclusively from the uncomplexed free siRNA. Two gel images were recorded after 30 minutes (figure 5.11A) and 60 minutes (figures 5.11B). No complete complexation was observed for the shorter cationic polymer **V-5(PG5)** up to a charge ratio of 50:1. As the charge ratio is increased, the intensity of the uncomlexed siRNA band diminishes, indicating that partial complexation occurs when the **V-5(PG5)** percentage in the sample is increased. Conversely, With **V-5(PG9)**, which contains a higher number of cationic repeating units, complete complexation of the anionic siRNA was achieved at a charge ratio of 30:1. Here, the effect of partial complexation can be observed at lower charge ratios, too. These results demonstrate that an increase in the charge density of **V-5(PG9)** results in enhanced oligo-complexation efficacy. After 60 minutes, a band with a lower retention time appears in some samples, as indicated by the red arrow in figure 5.11B. This may reflect the stability of the complex formed between the siRNA and the polymer. In certain samples, the complexed siRNA is gradually released over time. However, since this phenomenon was only observed in two samples in this experiment that are not directly related to each other, no final conclusions can be drawn at this point.

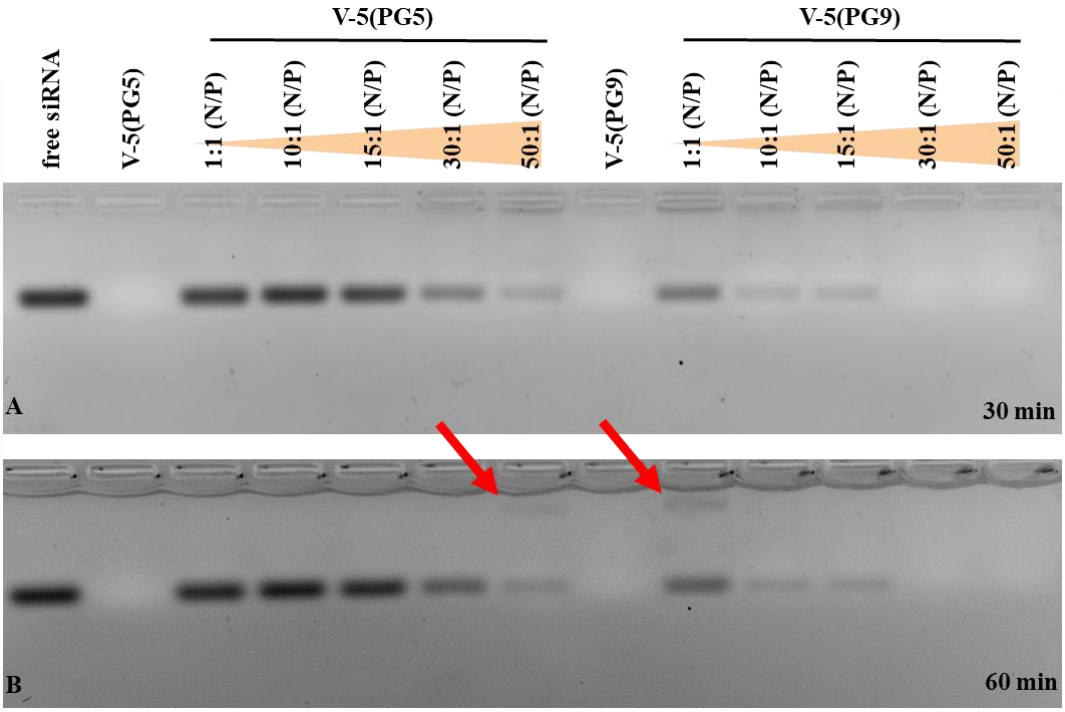

Figure 5.11: *Gel electrophoresis results for the polyplex formation between Cy3-siRNA (0.4 µM) and* ***V-5(PG5)*** *and* ***V-5(PG9)*** *at different charge ratios (N/P) with an incubation time of 20 min and the free uncomplexed Cy3-siRNA, visualized under UV light, 2.0 % agarose gel, 100 V, 117 mA, 12 W for* ***A*** *30 min and* ***B*** *60 min.*

To enhance the complexation efficiency, the same experiment was performed in PBS (pH 7.4) instead of Milli-Q® water. The buffered system can stabilize the cationic charge of **V-5**, thereby enhancing complexation efficiency. The use of PBS as a medium proved an effective method for improving polyplex formation (figure 5.12B and D). For **V-5(PG5)**, complete complexation of the siRNA was observed at a charge ratio of 50:1 (N/P) (figure 5.12B). For the longer polymer, **V-5(PG9)**, even a ratio of 4:1 to 10:1 (N/P) resulted in complete complexation (figure 5.12D). Consequently, the complexation efficiency was improved by reducing the charge ratio from 30:10 to 10:1 (N/P), which minimizes the amount of polymer required for oligonucleotide transfection and reduces the introduction of non-native materials into the cellular environment. In addition to the solvent environment, the peptide sequence may also exert an influence on complexation, given the presence of pH-dependent groups, including histidine. The unconjugated guanidine polymers **G5** and **G9** were deprotected (**dG5** and **dG9**), which exposed their amine groups also tested for their complexing efficiency in gel electrophoresis. The complexation process was found to be equally effective for peptide-conjugated cationic polymers (**V-5(PG5)** and **V-5(PG9)**) and cationic polymers lacking a peptide sequence (**dG5** and **dG9**) across all investigated charge ratios (figure 5.12A and C). In this way, it could be shown that the peptide sequence does not have any impact on the complexation of the oligonucleotide, but rather is necessary for the formation of the supramolecular, multivalent nanorod carrier, as shown in Chapter 5.3.2.

Given the superior complexation efficiency of **V-5(PG9)** compared to **V-5(PG5)**, subsequent investigations focused exclusively on **V-5(PG9)**.

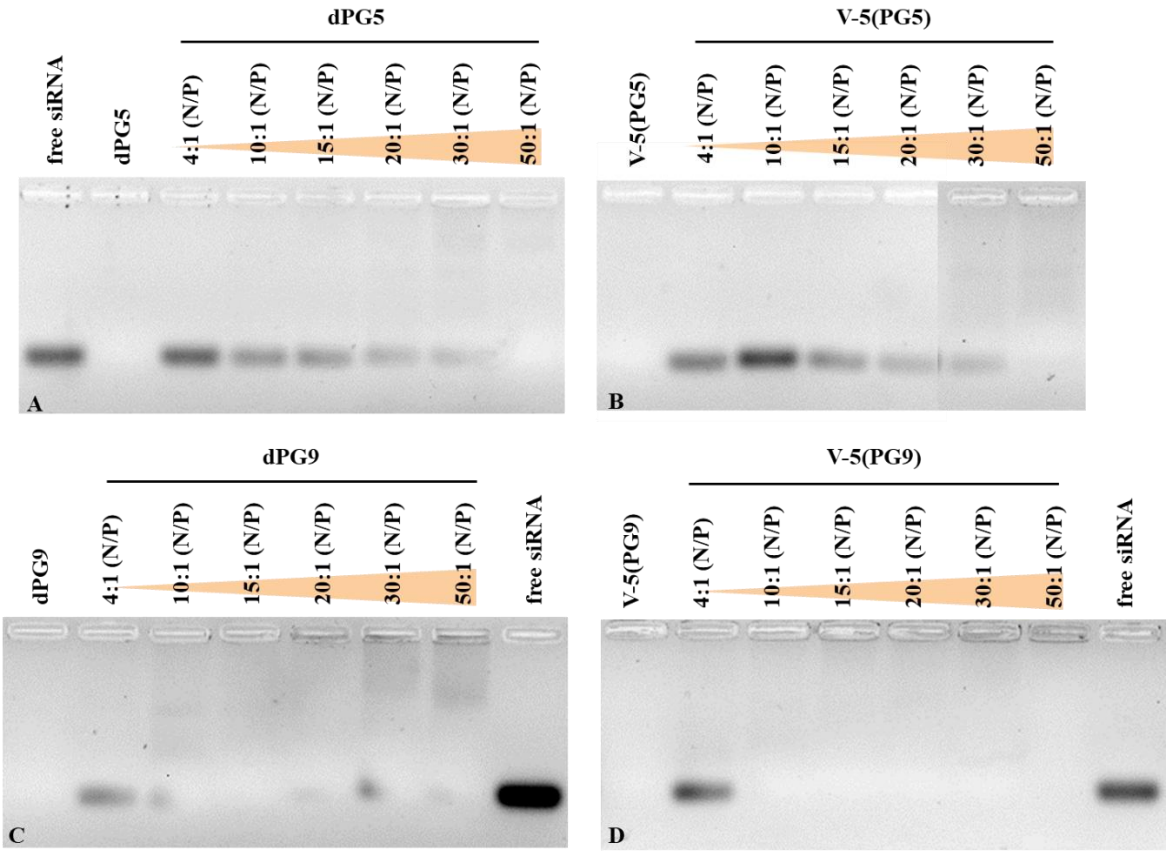

Figure 5.12: *Gel electrophoresis results for the polyplex formation between Cy3-siRNA (0.4 µM) and* ***A dPG5****;* ***B V-5(PG5)****;* ***C dPG9****;* ***D V-5(PG9)*** *at different charge ratios (N/P)with an incubation time of 20 min and the free uncomplexed Cy3-siRNA, visualized under UV light, 2.0% agarose gel, 100 V, 117 mA, 12 W for 30 min.*

To enhance the stability of siRNA against enzymatic degradation and to reduce non-specific interactions of **V-5** with serum proteins, the PEG conjugate **V-8** was introduced as a second component to the cationic polymer **V-5(PG9)**, resulting in a supramolecular **copolymer** system, as described in the previous chapter. Figure 5.13 depicts the investigation of the complexation efficiency between Cy3-siRNA and the copolymer system at a charge ratio of 20:1 (N/P) in PBS, where the cationic polymer shows complete complexation of the siRNA in the electrophoresis performed previously. Various mass ratios (ζ) of the two polymers (**V-8**/**V-5(PG9)**) ranging from 0:1 to 2:1 were tested to evaluate the effect of **V-8** on the complexation process. The sample preparation methods exhibited notable differences. In figure 5.13A, the two polymer conjugates were first combined, followed by the addition of siRNA. This approach failed to achieve complete complexation of siRNA, even at low concentrations of the PEG conjugate, despite such complete complexation being observed at the same charge ratio in figure 5.12D. In contrast, the second approach involved pre-incubating siRNA with the cationic **V-5(PG9)** for 20 minutes before adding **V-8**. This method resulted in complete siRNA complexation across all tested mass ratios of **V-5(PG9)** to **V-8**. It should be noted that, in this sample preparation, the PEG conjugate **V-8** was added after the initial complexation of **V-5(PG9)** with the siRNA. Nonetheless, it was assumed that coassembly of both polymer conjugates still occurs under these conditions. Further experiments are required to validate this assumption. These findings suggest a shielding effect of the PEG conjugate **V-8**. Upon coassembly of **V-5(PG9)** and **V-8** *via* peptide interactions, the PEG chains of **V-8** form a hydrophilic layer around the nanorods. This layer renders the positively charged guanidine groups of **V-5(PG9)** inaccessible to siRNA, thereby inhibiting electrostatic interactions between the polymer and the

negatively charged siRNA, preventing efficient complexation. By contrast, the alternative preparation method depicted in figure 5.13B avoids this issue. Pre-incubation of siRNA with cationic **V-5(PG9)** ensures the complexation of the negatively charged oligonucleotide with the guanidine groups. Subsequent coassembly of the two polymers into a copolymer upon the addition of **V-8** does not interfere with siRNA complexation.

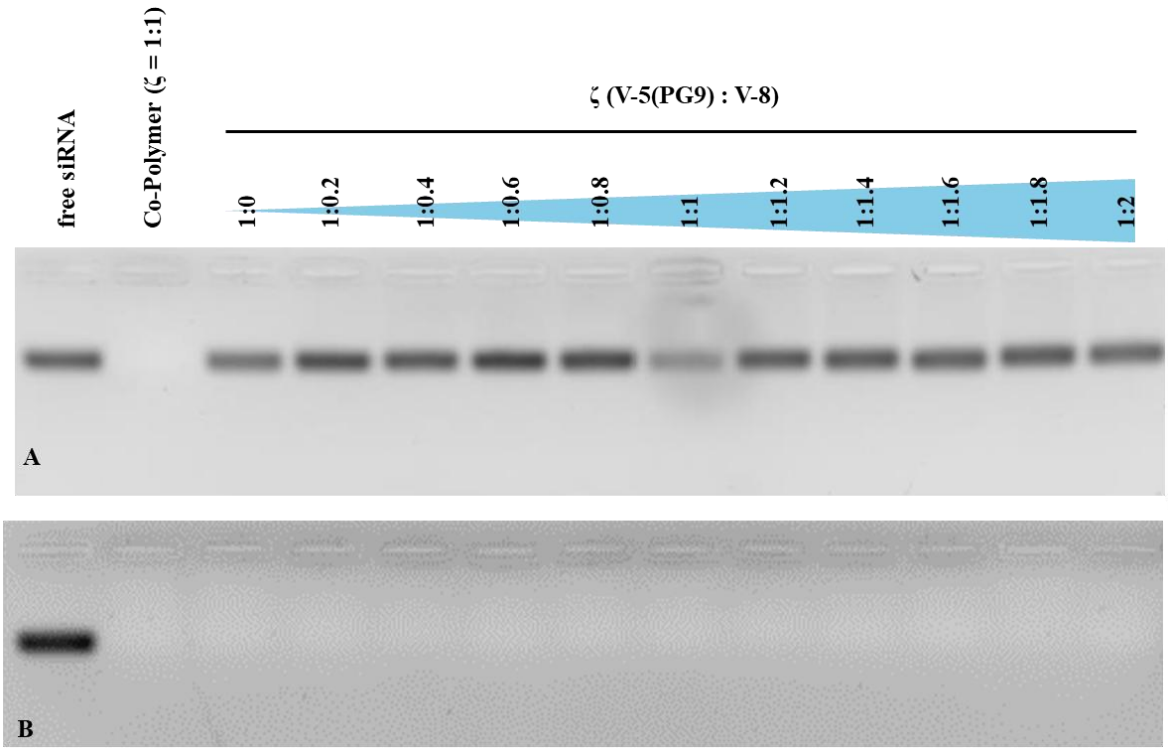

Figure 5.13: *Gel electrophoresis results showing the polyplex formation of Cy3-siRNA (0.4 µM) with* ***copolymers*** *(**V-5(PG9)**:**V-8**) at a 20:1 (N/P) charge ratio across different weight ratios (ζ) of **V-5(PG9)** to **V-8**.; **A** Premixing of the **copolymer**; **B** Pre-complexation of siRNA with **V-5(PG9)** for 20 minutes; visualized under UV light, 2.0 % agarose gel, 100 V, 117 mA, 12 W for 30 min.*

To evaluate the effect of **V-8** in relation to the charge ratio, experiments were conducted across a range of charge ratios (N/P) from 4:1 to 10:1 (figure 5.14). Additionally, the influence of varying mass ratios between **V-5(PG9)** and **V-8** was investigated. Sample preparation followed the protocol described in figure 5.13B, where siRNA was pre-incubated with **V-5(PG9)** before the addition of **V-8**, to ensure the best possible complexation. The results indicate that a charge ratio of 8:1 (N/P) (figure 5.14D) is sufficient to achieve complete siRNA complexation across all tested mass ratios. At lower charge ratios, the influence of **V-8** on complexation becomes evident. This is reflected in the agarose gel electrophoresis results, where higher mass ratios correlate with more intense bands, indicating an increased amount of free, uncomplexed siRNA, as best visualized in figure 5.14B at a charge ratio of 4:1 (N/P).This phenomenon may be attributed to a high amount of PEG, which can compete with electrostatic interactions between the cationic polymer and siRNA. The hydrophilic PEG chains effectively shield the polymer's positive charges, reducing its binding efficiency and competing with the formation of stable complexes. While PEG portions improves stability and prolongs circulation time in the bloodstream, excessive PEG content can adversely affect complexation and transfection efficiency.[204]

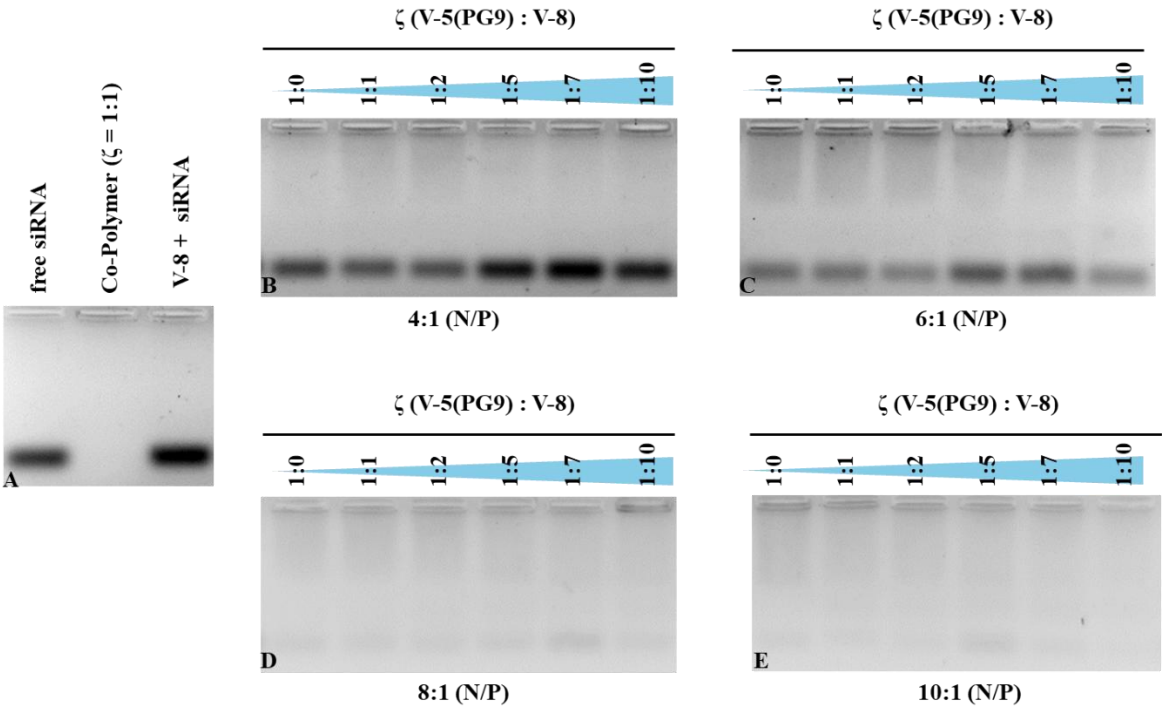

Figure 5.14: *Gel electrophoresis results showing the polyplex formation of Cy3-siRNA (0.4 µM) with* ***copolymers*** *(**V-5(PG9)**:**V-8**) at different charge ratios **B** 4:1; **C** 6:1; **D** 8:1; **E** 10:1 (N/P) across different weight ratios (ζ) of **V-8** to **V-5(PG9)** and **A** controls; visualized under UV light, 2.0 % agarose gel, 100 V, 117 mA, 12 W for 30 min.*

The results emphasize that the balance between the charge ratio (N/P) of the cationic polymer conjugate **V-5(PG9)** and the negatively charged siRNA, as well as the mass ratio between the two polymer conjugates, plays a crucial role in the complexation process. For the analyzed supramolecular **copolymer** system, a charge ratio of 8:1 (N/P) was sufficient to achieve complete siRNA complexation. At lower charge ratios, the presence of PEG in **V-8** can compete with the cationic polymer and accessibility to siRNA. This finding is consistent with existing literature, which indicates that polyplexes typically achieve optimal functionality at N/P ratios ranging from 5:1 to 20:1, depending on the polymer's charge density.[205] Polymers with steric shielding, such as PEG-conjugated systems, generally require higher N/P ratios (>10:1) to ensure efficient siRNA complexation.[206]

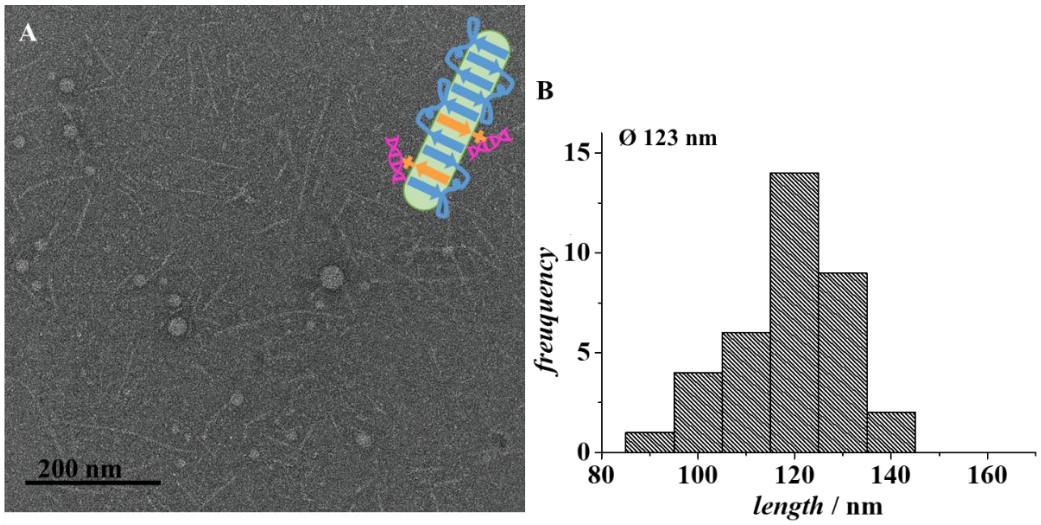

Figure 5.15: ***A*** *TEM images of polyplex formation between Cy3-siRNA and* ***copolymer*** *(5:1 N/P), 200 µM in PBS at pH 7.6 (negative stain);* ***B*** *Frequency of nanorod length from TEM image (n=38).*

To investigate the supramolecular structure of the polyplex, transmission electron microscopy was performed in PBS (figure 5.15A). The TEM images of the copolymer (5:1) complexed with Cy3-siRNA (N/P 10:1) reveal rod-like structures that closely resemble those observed for the copolymer without siRNA complexation. The measured average rod length is ±123 nm (n=38) (figure 5.15B), which falls within the range of the rod length of the copolymer without siRNA. This indicates that siRNA loading does not significantly alter the supramolecular organization of the polymer. Based on these structural size, it can be concluded that the cellular uptake of the polyplexes predominantly should occur *via* a clathrin-independent endocytosis mechanism.[188]

To ensure complete siRNA complexation and maintain stable polyplexes for subsequent cellular assays, a charge ratio (N/P) of 8:1 and 10:1 and a mass ratio (ζ) of 5:1 was selected. These conditions provide an optimal balance between siRNA charge neutralization and polyplex stability.

5.3.4 Cell viability and cellular uptake of siRNA in HEK cells

To assess the impact of the copolymer on cell viability and to evaluate the intracellular uptake of cargo, non-functional siRNA labeled with Cy3 dye was complexed with various polymer compositions (table 5.1) and transfected into HEK-293T cells (human embryonic kidney cells). This cell line was chosen as the standard cell line for these transfection assays due to their ease of culture, high transfection efficiency, and high robustness, which simplifies handling.[207] For sample preparation, siRNA was incubated with **V-5(PG9)** for 20 minutes, followed by the addition of **V-8** in **carrier 2** and **carrier 4**. The samples were then applied to the cells, resulting in final siRNA concentrations of 5 nM, 25 nM, and 50 nM. Following transfection, the cells were incubated for 24 hours and then stained with the viability dye FVD-eFluor450.

Table 5.1: *Carrier composition and charge ratio (N/P) between siRNA and carrier for cell assays.*

	charge ratio (N/P)	**compositions**
Carrier 1	8:1	V-5(PG9)
Carrier 2	8:1	5:1 V-5(PG9): V-8
Carrier 3	10:1	V-5(PG9)
Carrier 4	10:1	5:1 V-5(PG9): V-8

A quantitative analysis of cell viability and siRNA uptake was conducted using fluorescence-activated cell sorting (FACS).[208] The data are typically displayed in the form of scatter plots, which allow for the comparison of two or more parameters simultaneously, such as viability and siRNA uptake. In this experiment, the fluorescence intensity of the viability dye FVD-eFluor450 was compared with Cy3-labeled siRNA to assess cell viability in the context of intracellular uptake of siRNA. Since FACS detects fluorescence signals from both intracellular and membrane-associated components, a positive Cy3 signal is correlated with either binding or uptake of the carrier. Untreated cells served as a negative control to eliminate any potential autofluorescent background signals.

These studies were conducted in collaboration with [redacted], department of dermatology at the University Medical Center Mainz. The results obtained from the assay were transferred from dot plots to bar charts (figure 5.16) to facilitate a clearer and more comprehensive interpretation of the data. DOTAP, a conventional and widely used transfection reagent[175], was included as a positive control to provide a standard for comparison with the experimental carriers. The analysis indicates that both the control samples, including those transfected with DOTAP, and the four carrier systems tested maintained a high cell viability, exceeding 95 % in HEK-293T cells (figure 5.16A). This observation shows the high biocompatibility of the tested carriers under the experimental conditions. In addition, a concentration-dependent uptake of Cy3-labeled siRNA into the cells was observed (figure 5.16B). The fluorescence intensity corresponding to intracellular siRNA was evaluated at three concentrations (5 nM, 25 nM, 50 nM), and the data were normalized to the transfection achieved with DOTAP at 50 nM, which served as the reference. Notably, **carrier 1** and **carrier 3**, the two carriers without **V-8** (represented in orange), demonstrated a higher cell uptake efficiency of 50 nM Cy3-labeled siRNA compared to the reference transfection reagent DOTAP (represented in gray) at the tested charge ratios. Conversely, the **copolymer** system, **carrier 2** and **carrier 4** (represented in green), exhibited a slightly reduced cell uptake efficiency relative to DOTAP at the same siRNA concentration. The slightly reduced siRNA uptake observed in **carrier 2** and **carrier 4** may be attributed to the presence of PEG, which forms a hydrophilic layer around the carrier. This layer can sterically shield the positive charges of the carrier, reducing its interaction with the negatively charged cell membrane and hindering cellular uptake and ability to interact effectively with endocytic pathways (chapter 5.1), contributing to the observed decrease in cellular uptake efficiency.[209,210]

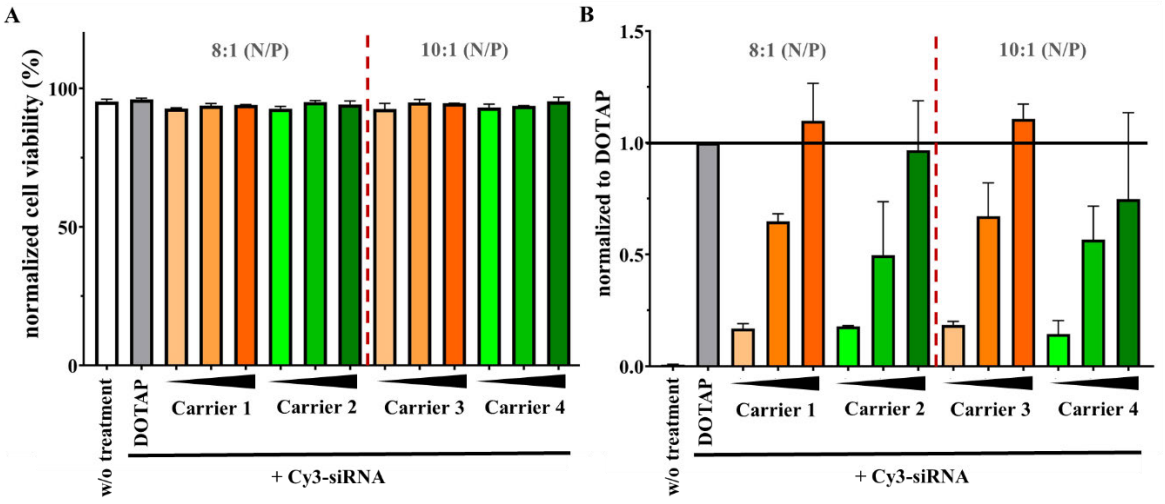

Figure 5.16: *FACS analysis of Cy3-siRNA transfection at varying concentrations (5 nM, 25 nM, 50 nM) using* ***carrier 1*** *(**V-5(PG9)**, orange),* ***carrier 2*** *(**copolymer**, green),* ***carrier 3*** *(**V-5(PG9)**, orange)**, carrier 4*** *(**copolymer**, green), and DOTAP (gray), evaluating **A** cell viability and **B** Cy3-siRNA cellular uptake in HEK-293T cells (n=3).*

The results confirm the high viability of the cells and the successful internalization of the cargo *via* the carriers. Nonetheless, these findings do not allow for direct conclusions regarding the transfection efficiency, specifically the intracellular release of siRNA. To address these aspects, two functional assays are introduced in the following sections to evaluate the intracellular efficacy of the transfected cargo.

5.3.5 Transfection of IL-8 specific siRNA for gene therapy

Interleukin-8 (IL-8), also known as CXCL8, represents a promising target for transfection due to its critical role in cancer progression. IL-8 is a pro-inflammatory chemokine essential for the recruitment of immune cells to sites of inflammation. In the tumor microenvironment, it promotes tumor growth by attracting immunosuppressive cells such as neutrophils, myeloid-derived suppressor cells, and monocytes, which collectively impair the immune response and facilitate tumor progression. Additionally, IL-8 contributes to angiogenesis, tumor cell migration, and metastasis, showing its potential as a therapeutic target in cancer treatment. The expression of IL-8 is regulated by various factors, including tumor necrosis factor-α (TNF-α), chemotherapeutic agents, steroid hormones, and the transcription factors NF-κB and activator protein-1.[211,212,213]

The present study investigated the transfection of IL-8-specific siRNA using **carrier 3** and **carrier 4** to inhibit IL-8 expression in cells. Figure 5.17 illustrates the mechanism of cell transfection with IL-8-specific siRNA. The internalization of siRNA-loaded carriers can occur *via* endocytic uptake. Once released into the cytosol, the IL-8 specific siRNA binds to argonaute family proteins and integrates

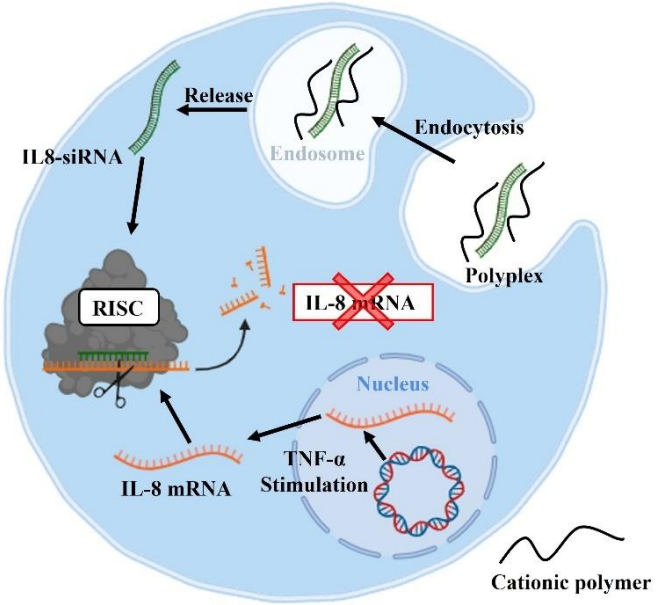

Figure 5.17: *Mechanism of IL-8 siRNA cell transfection[215] (created with BioRender.com).*

into the RNA-induced silencing complex (RISC). Within the RISC complex, the double-stranded siRNA is unwound, retaining the guide strand while the passenger strand is degraded. The guide strand then binds specifically to complementary IL-8 mRNA, leading to the activation of further argonaute proteins, which cleave and degrade the target mRNA. This effectively suppresses the translation of the IL-8 protein.[214,215]

HEK-293T cell lines were used to evaluate the transport and release of IL-8-specific siRNA by carriers, as measured by its efficacy in reducing IL-8 expression. To induce a measurable production of IL-8, the cells were stimulated with TNF-α (figure 5.18). In addition to **carrier 3** and **carrier 4**, as detailed in table 5.1, lipofectamine® was used as a positive control due to its well-established and validated status as a transfection reagent.[216] Additional control experiments were performed, including the treatment of cells with IL-8 specific siRNA without a carrier to confirm the necessity of a polyplex system, as well as transfection with unspecific siRNA to verify the specificity of the observed effects. Furthermore, untreated cells and cells stimulated with TNF-α without transfection were included as additional controls.

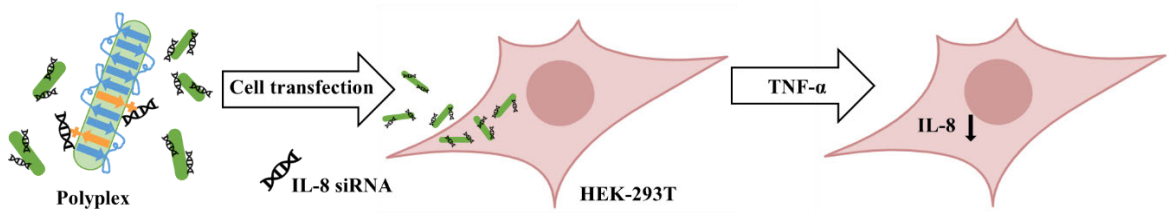

Figure 5.18: *Mechanistic representation of IL-8-specific siRNA transfection in HEK-293T cells using polyplexes and subsequent TNF-α stimulation.*

To quantify IL-8 levels in the cells, the cytometric bead array (CBA) technique was employed. This method is a well-established standard for chemokine quantification in biological samples, including cell culture media. The CBA technique is based on a sandwich immunoassay, in which bead surfaces are conjugated with specific capture antibodies. After sample addition, the mixture is incubated with the capture beads to allow analyte binding. Later on, a fluorescently labeled detection antibody is introduced, followed by further incubation to form a sandwich complex consisting of the capture bead, the analyte (e.g., the chemokine IL-8), and the detection antibody. This approach ensures specific target molecule binding to the beads. Quantification is performed *via* flow cytometry, where the fluorescence intensity of the bound detection antibody is measured and is directly proportional to the analyte concentration in the sample. Due to the high specificity of the antibodies and the method's sensitivity in detecting low analyte concentrations, the CBA technique is particularly well-suited for analyzing IL-8.[217]

Figure 5.19 (left side) presents the results of the polyplex transfection experiments conducted with **carrier 3** and **carrier 4**, alongside the positive control using lipofectamine®. These studies were conducted in collaboration with [redacted], department of dermatology at the University Medical Center Mainz. To explore potential concentration-dependent effects, siRNA concentrations of 5, 10, 25, and 50 nM were tested. The data are normalized to the IL-8 levels of non-transfected cells stimulated with TNF-α. Additionally, non-transfected cells without TNF-α stimulation served as a negative control (black bar), exhibiting the expected low IL-8 concentration which shows the necessity of TNF-α in upregulating of IL-8. The positive control with lipofectamine® (grey bars) revealed a clear concentration-dependent effect, with the highest siRNA concentration tested (50 nM) resulting in a substantial reduction by 48% in IL-8 production. The successful transfection with IL-

8 siRNA can also downregulate IL-8 production induced by TNF-α stimulation. The transfection results reveal a concentration-dependent effect for both **carrier 3** (orange), consisting exclusively of the cationic polymer **V-5(PG9)**, and **carrier 4** (green), which incorporates the **copolymer**. Notably, **carrier 3** consistently achieves lower IL-8 levels compared to **carrier 4** across all tested siRNA concentrations, indicating that transfection with **carrier 3** is more effective. At a siRNA concentration of 50 nM, **carrier 3** achieves a reduction in IL-8 levels by 34%, while **carrier 4** only reduces IL-8 levels by 25%. The same results were observed with Cy3-siRNA cellular uptake using **carrier 3** and **carrier 4** in the previous assay (figure 5.16). This observation suggests that the PEG component in **carrier 4** may act as a steric protective coating, enhancing polyplex stability but simultaneously reducing its interaction with the cell membrane and delaying endosomal release due to the shielding effect of the PEG shell. Despite this, the transfection efficiencies of both carriers remain inferior to that of the positive control, lipofectamine®. The control without a carrier (blue bars) shows a modest IL-8 reduction by 25%, even with IL-8-specific siRNA. This may be attributed to non-specific mechanisms, such as passive siRNA transport into the cells or slight non-specific adsorption of siRNA to the cell membrane, resulting in internalization.[218] Consequently, it cannot be conclusively stated that the observed effects with the two carriers are solely attributable to their transfection capabilities.

The use of unspecific siRNA as a control further highlights the specificity of the observed inhibition of IL-8 expression (figure 5.19 right side). For lipofectamine® (grey bars), the non-functional siRNA only results in an 18% reduction in IL-8 production, confirming that the IL-8 expression inhibition effect is specifically mediated by IL-8 siRNA. In contrast, the use of unspecific siRNA with the **carrier 3** (orange bars) and **carrier 4** (green bars) shows a reduction in IL-8 production ranging from 20% to 50%, with no concentration dependence observed. This behavior may be explained by the inherent properties of the carriers. Firstly, the cationic polymer **V-5(PG9)** in the carriers could potentially induce cellular stress through interactions with the cell membrane or endosomal compartments, activating anti-inflammatory signaling pathways that lead to a general downregulation of IL-8 production, independent of siRNA specificity. Secondly and more likely. the carriers modulate the cellular response to TNF-α, potentially altering signal transmission of this pro-inflammatory cytokine and indirectly reducing IL-8 production. Additionally, a reduction in IL-8 levels of 20–30% is observed in controls without carriers but employing non-specific siRNA (purple bars). This reduction may result from two potential mechanisms. Firstly, non-specific siRNA could exert off-target effects due to partial homology with other cellular mRNAs, indirectly affecting genes involved in IL-8 production or TNF-α signaling. Secondly, the recognition of non-specific siRNA as foreign genetic material may trigger a cellular defense response. Such responses, mediated by interferon or antiviral signaling pathways, could also contribute to a general reduction in IL-8 production.

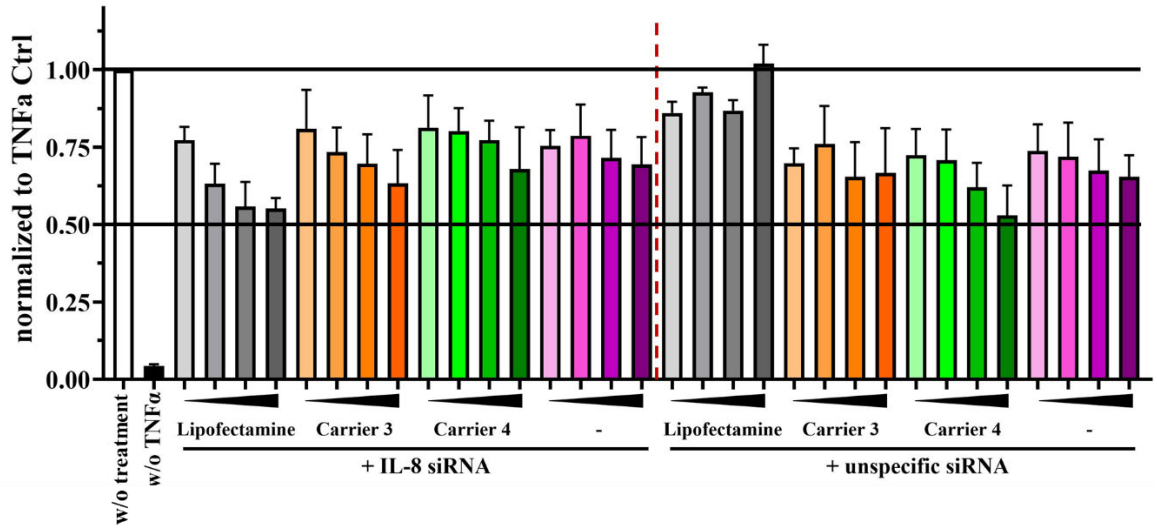

Figure 5.19: *IL-8 production in HEK-293T cells following siRNA transfection at different concentrations (5, 10, 25, and 50 nM) with* ***carrier 3*** *(orange),* ***carrier 4*** *(green), and lipofectamine® (grey), compared to control conditions (purple) measured by CBA (n=4), normalized on w/o treatment (white).*

The results reveal that while the tested carriers, particularly **carrier 3**, demonstrated some capacity to reduce IL-8 levels, the overall transfection efficiency remained inferior to the positive control, lipofectamine®. Additionally, non-specific effects observed in control conditions, such as IL-8 reduction without a carrier or with unspecific siRNA, indicate that the assay lacks specificity in attributing the observed effects solely to the carriers. In conclusion, the assay is not suitable for accurately assessing the transfection efficiency and specificity of these polyplex carriers for IL-8-targeted siRNA.

5.3.6 Transfection of CpG ODN oligo for immunotherapy in spleen cells

Considering the preceding results, this chapter focuses on the transfection of CpG oligonucleotides (CpG ODNs) *via* the polyplexes to evaluate the carriers' ability to facilitate immune stimulation. These assays provide the advantage of inducing a direct immune response independent of external stimuli such as TNF-α. By minimizing potential influencing factors, this approach enables a more precise assessment of the efficiency of polyplex-mediated CpG delivery. CpG ODNs are composed of specific CpG dinucleotides, which are hallmarks of microbial DNA and play a central role in immunological processes. In this assay, ODN SL03, a synthetic CpG oligonucleotide with the sequence 5'-TCG CGA ACG TTC GCC GCG TTC GAA CGC GG-3', was used. ODN SL03 belongs to the class of C-type CpG ODNs, characterized by its strong immunostimulatory properties.[219] Its palindromic sequence enhances the activation of innate immune cells, such as B cells, NK cells, and mononuclear cells, across multiple species. Additionally, the phosphorothioate backbone of ODN SL03 increases its stability by protecting it from enzymatic degradation, ensuring its effectiveness in stimulating immune responses. These CpG motifs are recognized by Toll-like receptor 9 (TLR9), a pattern recognition receptor located in the endosomal compartments of dendritic cells and other

immune cells. Through the transfection process, polyplexes facilitate the endosomal uptake of ODN SL03, delivering it directly to TLR9. The interaction with TLR9 triggers a signaling cascade that activates NF-κB- and IRF-mediated pathways (figure 5.20). This activation induces the expression of proinflammatory genes and costimulatory markers, such as the surface proteins CD40, CD80, and CD86, which subsequently activate immune cells.[172,220]

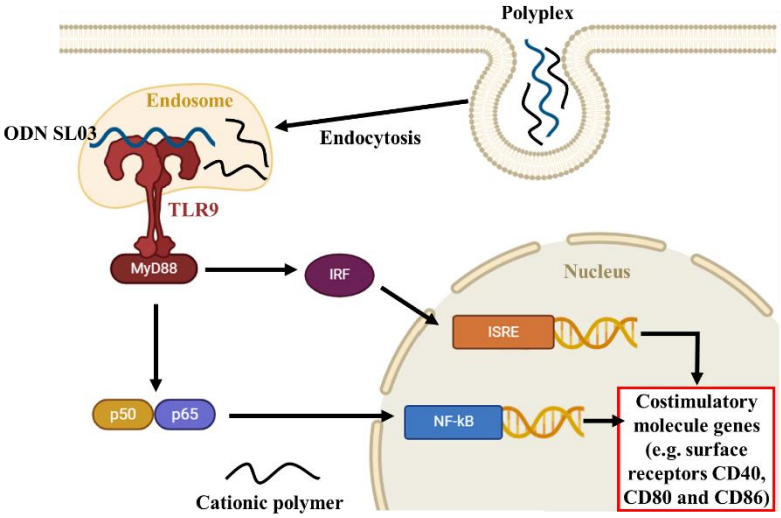

Figure 5.20: *Mechanism of ODN SL03 cell transfection[230] (created with BioRender.com).*

To evaluate the transfection efficiency of the carriers, BMDCs were employed as a model system, as they serve as precursors to dendritic cells (DCs), a subset of antigen-presenting cells (APCs). In the assay, FLT3 ligand-supplemented culture medium was used to induce the differentiation of dendritic cell subsets from progenitor cells.[221] Under these conditions, progenitor cells differentiate into conventional dendritic cells (cDC1 and cDC2), which are of myeloid origin, and plasmacytoid dendritic cells (pDCs), which originate from both myeloid and lymphoid progenitors. Each subset plays a distinct role in linking innate and adaptive immunity. cDC1 and cDC2 specialize in antigen uptake, processing, and presentation to T cells, whereas pDCs are primarily involved in the production of type I interferons during viral infections. The stimulation of BMDCs with CpG ODNs serves as a robust method to evaluate their immunostimulatory capacity. This leads to the upregulation of costimulatory markers such as CD40, CD80, and CD86 on the surface of dendritic cells. These cluster of differentiation (CD) markers are essential surface proteins that mediate interactions with T cells and other immune cells, playing a key role in orchestrating immune responses. The upregulation of these costimulatory markers following CpG ODN stimulation is not only a hallmark of dendritic cell activation but also a reliable indicator of the efficiency of CpG ODN delivery systems.[222,223]

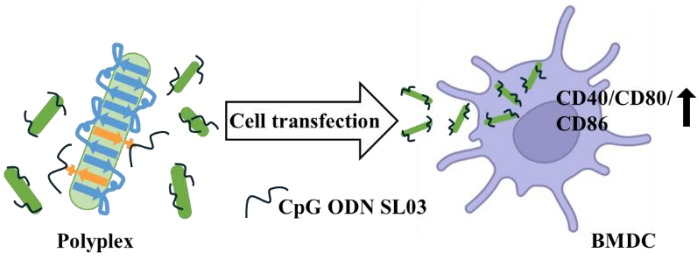

Figure 5.21: *Mechanistic representation of CpG ODN transfection in BMDC cells using polyplexes.*

In this essay, polyplexes were formed using the supramolecular copolymer system (**carrier 4**) and CpG ODN SL03 to transfect BMDCs (figure 5.21). To compare the influence of the PEG content on transfection efficiency, the cationic polymer (**carrier 3**) was also used for polyplex formation and transfection.

Figure 5.22 presents the results of BMDC stimulation with CpG ODNs using **carrier 3** (yellow), **carrier 4** (green) and DOTAP (gray). Furthermore, the influence on the upregulation of the costimulatory markers by the carriers without

cargo was examined in order to exclude non-specific influences of the carriers on the upregulation of the markers. The study investigated how these conditions affected the expression of the costimulatory markers CD40, CD80, and CD86, following the transfection of 250 ng/mL CpG ODN, as measured by FACS. The study was conducted in collaboration with [redacted], department of dermatology at the University Medical Center Mainz. When CpG ODNs were transfected using DOTAP, all dendritic cell subtypes showed a significant increase in the expression of CD40, CD80 and CD86. This confirms the successful delivery of CpG ODNs into BMDCs, resulting in a strong immune response. Similarly, both **carrier 3** and **carrier 4** induced significant increases in marker expression compared to the negative control, underscoring their potential as effective delivery systems. No considerable differences in marker expression were observed between the two carriers for most dendritic cell subtypes. However, in pDCs (figure 5.22C), CD40 expression was significantly higher on **carrier 4** than on **carrier 3**. This suggests that the PEG modification in **carrier 4** improves the stability or uptake of the polyplex, thereby enhancing immune activation. In the negative controls, where CpG ODN was not added (figure .5.22 left side of the diagrams), the expression levels of CD40, CD80 and CD86 in conventional DCs remained at the level of untreated cells. This confirms that the observed increase in marker expression is specifically caused by CpG-ODN stimulation and not by non-specific effects of the carriers. Interestingly, pDCs showed slightly increased expression of all three markers in the absence of CpG ODNs. This phenomenon may be attributable to the intrinsic basal activity of pDCs, which, under specific conditions, can express co-stimulatory markers in minimal amounts without external stimulation.[224] In this study, this is particularly pronounced for the CD80 marker, so that in this case no significant conclusion can be drawn about upregulation by transfected CpG ODNs. In contrast, a significant increase in the levels of the markers CD40 and CD86 can be observed with CpG ODN SL03, so that these values can be considered meaningful.

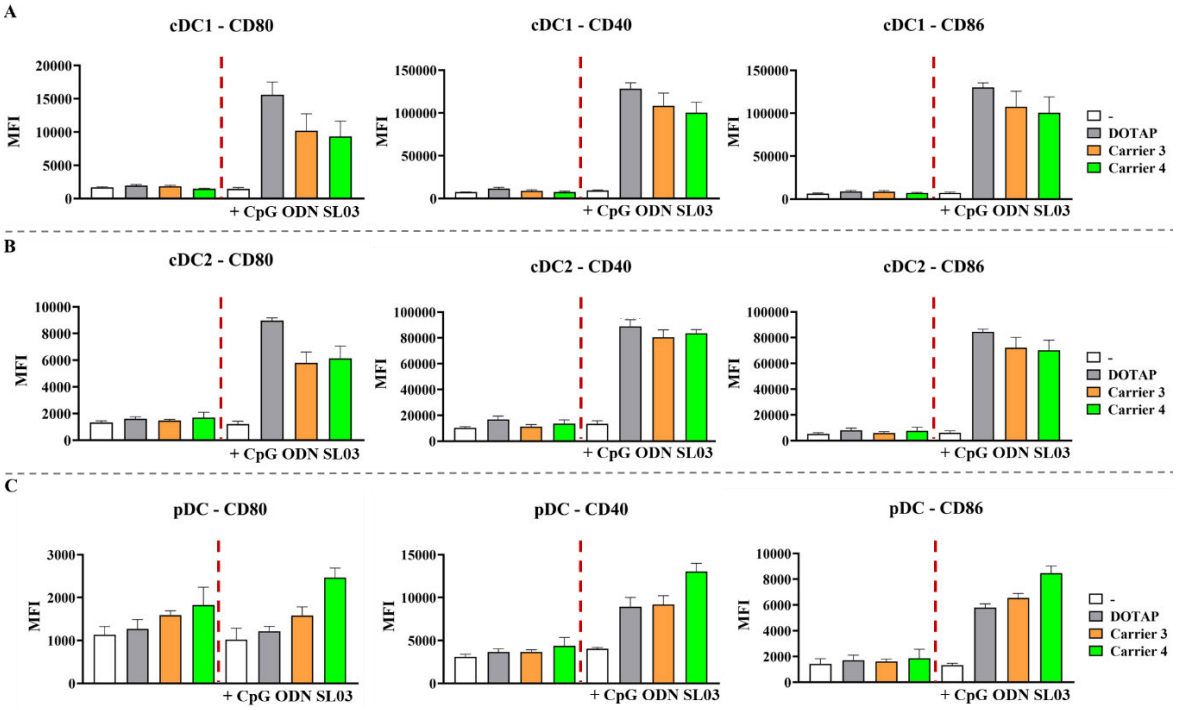

Figure 5.22: *Expression of costimulatory markers (CD40, CD80, CD86) in dendritic cells (DC) of BMDCs following transfection with polyplexes formed using **carrier 3** (orange), **carrier 4** (green), DOTAP (grey) and CpG ODN SL03 (250 ng/mL) and untreated cells (white) as negative controls measured by FACS (n=4; MFI= mean fluorescence intensity).*

Building on the promising findings from BMDC experiments, the following study investigated the transfection of CpG-ODN SL03 into spleen cells to evaluate their immune activation potential in a more physiologically complex environment. The spleen, a central organ in the immune system, filters blood, presents antigens, and facilitates interactions among key immune cells, including B cells (CD19+), natural killer cells (NK1.1+), DCs, and macrophages (MACs). These cells play critical roles in both innate and adaptive immunity.[225] The spleen's role in immune surveillance also links it to tumor immunotherapy. Activation of dendritic cells and B cells enhances antigen presentation and supports the recruitment of cytotoxic T cells, crucial for targeting tumor cells. Additionally, macrophage stimulation triggers pro-inflammatory responses that can suppress tumor progression.[199,226]

By focusing on spleen cells, the study aimed to assess the performance of CpG-ODN delivery systems under conditions that better approximate *in vivo* scenarios (figure 5.23). A CpG-ODN SL03 concentration of 250 ng/mL, was used to evaluate cell activation and to ensure meaningful comparisons, DOTAP was utilized as a positive control due to its proven efficacy as a transfection reagent. Negative controls included carrier without cargo and cargo without carrier to confirm specificity of the immune response. After transfection, cells were incubated for 24 hours and analyzed by FACS to assess upregulation of co-stimulatory markers CD80 and CD86. The study was conducted in collaboration with [redacted], department of dermatology at the University Medical Center Mainz.

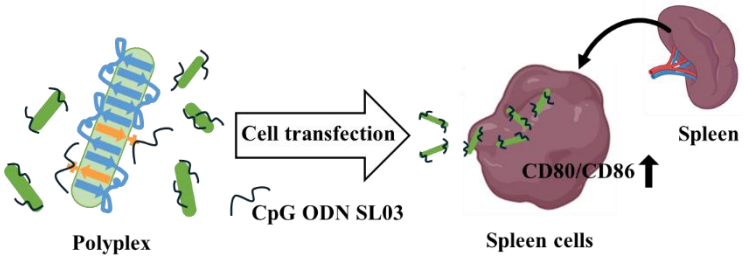

Figure 5.23: *Mechanistic representation of CpG ODN transfection in spleen cells using polyplexes.*

The results (figure 5.24) demonstrated a significant elevation in CD86 expression across all evaluated cell types. Among the analyzed cell populations, MACs, neutrophils (PMNs) and DCs exhibited the most substantial upregulation, indicating robust immune activation. Notably, for NK1.1 cells and PMNs, **carrier 4** demonstrated superior performance compared to **carrier 3**, while no pronounced differences between the carriers were observed in the other cell types. In contrast, the expression levels of CD80 exhibited greater variability. CD19+ cells displayed no significant upregulation of CD80 compared to untreated samples or controls lacking CpG-ODN. NK1.1+ cells and MACs cells exhibited minimal changes, with occasional upregulation observed even in the absence of CpG-ODN, likely due to carrier-related effects. DCs showed a clear increase in CD80 expression. Similarly, neutrophils PMNs exhibited a modest increase in CD80 expression, although the effect was less pronounced than in dendritic cells.

The observed differences in CD86 and CD80 expression likely result from the distinct ways these markers are regulated during immune activation. CD86 is typically upregulated quickly in response to immune stimuli, playing a key role in activating T cells early in the immune response. CD80, on the other hand, is involved in secondary signaling pathways that become important under specific conditions or during extended immune activation.[227] The activation of CD80 by carriers without CpG-ODNs or by CpG-ODNs without carriers may be attributed to nonspecific cellular stress or membrane interactions induced by the cationic properties of the carrier. Additionally, CpG-ODNs alone could trigger partial immune responses through direct interaction with TLR9, albeit less efficiently than when delivered *via* carriers.[228]

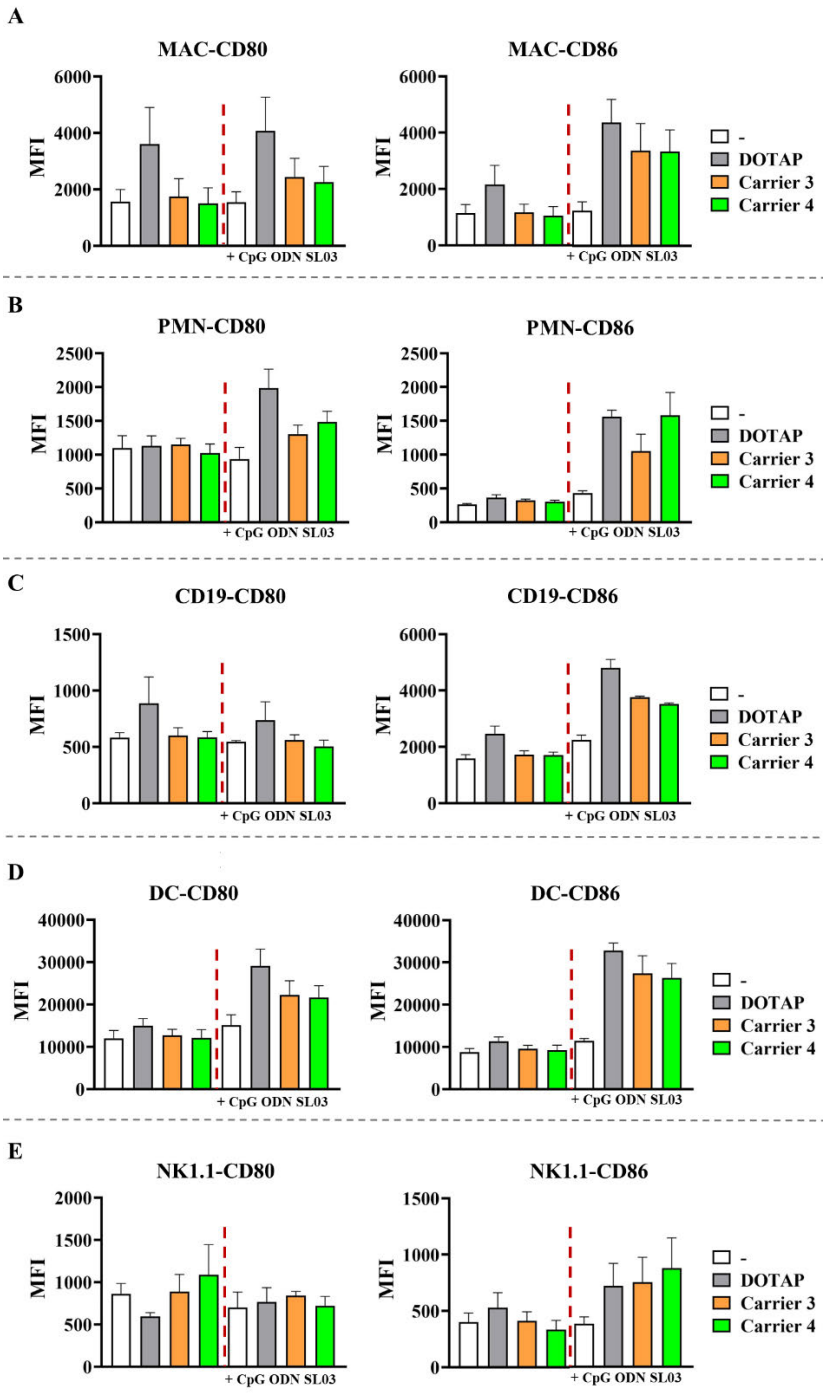

Figure 5.24: *Expression of costimulatory markers (CD80, CD86) in dendritic cells (DC) of spleen cells following transfection with polyplexes formed using* ***carrier 3*** *(orange),* ***carrier 4*** *(green), DOTAP (grey) and CpG ODN SL03 (250 ng/mL) and untreated cells (white) as negative controls measured by FACS (n=4; MFI= mean fluorescence intensity).*

The results provide valuable insights into the suitability of these carriers for CpG ODN transfection in spleen cells. The pronounced upregulation of CD86, particularly in dendritic cells and macrophages, highlights the carriers' ability to efficiently deliver CpG ODNs and activate key immune pathways. However, the variability in CD80 expression, including responses observed in DOTAP controls, suggests that non-specific effects may arise from factors beyond the carrier system itself. Notably, effective transfection was achieved at a remarkably low polymer concentration. In

this assay, 250 ng/mL CpG ODN SL03 was successfully transfected using a copolymer concentration of only 0.5 µM, leading to the activation of immune-modulatory cells.

5.4 Conclusion

In this chapter, a polyplex system was developed and evaluated for the targeted transfection of oligonucleotides. Such carriers must overcome several challenges, including the protection of oligonucleotides from enzymatic degradation, efficient cellular uptake, and controlled release at the site of action without compromising cell viability. Moreover, they should exhibit biocompatibility and minimal immunogenicity to prevent adverse effects. This work aimed to design a supramolecular copolymer carrier system that realized these criteria while maintaining structural flexibility through its modular supramolecular composition and architecture.

The developed supramolecular copolymer system consists of two main components: a cationic CPPM polymer-peptide conjugate, responsible for cargo complexation and cell membrane internalization, and a PEG-based polymer-peptide conjugate, which provides protection for the cargo. The identical peptide sequence was incorporated into the chemical structure of both conjugates, enabling supramolecular coassembly of the amide bonds *via* β-sheet structures to form nanorods. The synthesis of these two polymer conjugates was successfully completed. CD spectroscopy and TEM studies confirmed that both polymers can form stable nanostructured aggregates *via* their peptide sequences. The coassembly of the polymer conjugates also exhibits pH-responsiveness through the integration of histidine residues into the peptide sequence, so that the supramolecular system can dissociate under acidic conditions due to electrostatic repulsion of the protonated imidazole groups of histidine. This is critical for the efficient release of oligonucleotides from mildly acidic endosomes. In addition, the pH-sensitive properties of the system may facilitate targeted cargo release in tumor tissues, which are characterized by a reduced pH value.[229]

Complexation studies using gel electrophoresis demonstrated that Cy3-labeled siRNA efficiently binds to the copolymer at a ratio of 10:1 (N/P). These polyplexes were successfully used for initial cell-based studies to evaluate cell viability and the cellular uptake of siRNA in HEK-293T cells. The results showed that the carrier systems ensure high cell viability and effectively transport siRNA into the cells. However, the subsequent attempt to inhibit IL-8 production in HEK-293T cells using IL-8-specific siRNA revealed that the knockdown efficiency of the polyplexes was limited. It was observed that carriers without specific cargo could trigger nonspecific responses, possibly due to cellular stress or interactions with the cell membrane. This complicates the clear attribution of the knockdown effect to the specific properties of the carriers in this system.

The transfection of CpG-ODN SL03 into bone marrow-derived dendritic cells demonstrated significant immune stimulation, particularly reflected in the upregulation of the costimulatory markers CD86 and, to a lesser extent, CD80. These results indicated that the polyplexes are suitable for the activation of immune cells. The cell assays suggested that the PEG component not only enhances the stability of the polyplexes but also influences their cellular uptake and endosomal release. The system was subsequently tested in spleen cells to evaluate the immune response in a more complex cellular environment. Here, a marked upregulation of CD86 was observed, particularly in dendritic cells and macrophages, while CD80 showed a lower, but cell-type-dependent regulation. These findings demonstrate the system's potential for immunomodulatory applications, particularly in vaccine adjuvant development or targeted immune therapies, where controlled activation of antigen-presenting cells is crucial.

6 SUMMARY

Supramolecular peptide chemistry offers versatile approaches for the development of adaptive and stimuli-responsive materials. This work focuses on the targeted self-assembly of supramolecular peptide and peptide-polymer systems to create new material classes with potential biomedical applications. The study investigates oxidation-sensitive supramolecular nanotubes, hydrogel-forming cyclic peptides, and a supramolecular peptide-polymer copolymer system for targeted nucleic acid transfection. The main emphasis lies in controlling these supramolecular multi-component assemblies to develop adaptive and multi-functional materials with specific response mechanisms.

The investigation of oxidation-sensitive nanotubes demonstrated that oxidation led to a nearly complete dissassembly of the network-like nanotube structures. This controlled destabilization highlights the potential of oxidation-induced structural changes for controlled drug release applications. However, due to the poor water solubility of the peptide structures used, biological testing of these systems was not possible, as they were only stable in HFIP/H_2O or TFE/H_2O solvent mixtures. Future work should focus structural modifications of the peptide sequences to improve solubility and facilitate their adaptation to biological environments.

The study of hydrogel-forming cyclic peptides revealed that these peptides assemble into two-dimensional networks, which further organize into supramolecular hydrogels with high structural stability. The mechanical properties of these hydrogels were further optimized by incorporating tailormade telechelic PEG cross-linkers. The length of the PEG segment and the cross-linking ratio proved to be critical to optimize gel strength. Shorter PEG chains facilitated gel formation at lower cross-linker concentrations, while medium-length chains provided optimal stability at higher ratios. In contrast, longer PEG chains led to steric effects that hindered gel formation at high cross-linker concentrations. While the mechanical properties of these hydrogels were thoroughly characterized, further studies on their biological stability are required to assess their long-term usability in biomedical applications.

The developed peptide-polymer copolymer system for nucleic acid transfection combined the controlled self-assembly driven by the peptide component with a cationic polymer moiety responsible for nucleic acid complexation and cellular transport. The system demonstrated efficient siRNA binding at an N:P ratio of 8:1, comparable to other established methods. Additionally, a pH-sensitive disassembly of the copolymer system in acidic environments was installed successfully, indicating a controlled structural response under physiologically relevant conditions. Initial cell studies confirmed successful uptake of the polyplexes and excellent cell viability across different cell types, including HEK-293T cells, BDMCs, and spleen cells. The immunostimulation observed in dendritic cells was induced by the transfected CpG ODN, leading to a significant upregulation of costimulatory markers. Furthermore, investigations into the self-assembly behavior under biologically relevant conditions could provide new insights into the stability and interaction mechanisms of these supramolecular polyplexes. These findings are crucial for further evaluating the potential of this system in targeted nucleic acid transfection and immunological research.

The results of this work highlight the potential of supramolecular multi-component peptide and peptide-polymer systems for biomedical applications. The oxidation-sensitive nanotubes demonstrate the ability to destabilize supramolecular structures in response to oxidative stimuli, while the hydrogel-forming cyclic peptides represent a versatile material for applications in regenerative medicine and depot-based drug release. The supramolecular polyplex system expands the scope of supramolecular peptide chemistry toward the functional delivery of nucleic acids for targeted gene modulation and immunotherapy. The combination of structural design controlled self-

assembly, and stimuli-responsive properties presents a promising strategy for advancing supramolecular peptide materials. The insights gained from this study contribute to the development of stimuli-responsive biomaterials with broad applications in personalized medicine and biomedical research.

7 EXPERIMENTAL SECTION

7.1 Instrumentation and Materials

7.1.1 Solvents and Chemicals

All solvents and reagents were obtained from commercial sources and used without further purification unless stated otherwise. Suppliers included abcr (abcr GmbH, Karlsruhe, Germany), Acros Organics (Thermo Scientific GmbH, Nidderau, Germany), Alfa Aesar (Alfa Aesar GmbH & Co. KG, Karlsruhe, Germany), Carbolution Chemicals (Carbolution Chemicals GmbH, Saarbrücken, Germany), Iris Biotech (Iris Biotech GmbH, Marktredwitz, Germany), Merck (Merck KGaA, Darmstadt, Germany), Rapp Polymere (Rapp Polymere GmbH, Tuebingen, Germany), Sigma-Aldrich (Sigma-Aldrich Chemie GmbH, Taufkirchen, Germany), Tokyo Chemical Industry and (TCI Deutschland GmbH, Eschborn, Germany).

Anhydrous solvents were either purchased directly in dry form or purified prior to use. Peptide-grade DMF was used for peptide synthesis and amide couplings.

Ultra-pure water was obtained using an Elga PURELAB® flex water purification system (ELGA LabWater, Veolia Water Technologies Deutschland GmbH, Celle, Germany).

All reactions involving air- or moisture-sensitive reagents, intermediates, or products were performed under a nitrogen atmosphere using standard Schlenk techniques. Glassware was either oven-dried at 120 °C or subjected to high vacuum drying with a heat gun before use. Solvents for air- and moisture-sensitive reactions were degassed by multiple freeze-pump-thaw cycles until no gas bubble formation was observed. Liquid reagents and solvents were transferred via syringes through septa, while solids were added under an argon counterflow.

Solvent removal was performed using rotary evaporators equipped with membrane pumps, with the water bath temperature maintained at 40 °C to prevent degradation of sensitive substances. Solvents used for flash chromatography were purchased in technical quality and used without further purification.

7.1.2 Nuclear magnetic resonance spectroscopy

Nuclear magnetic resonance (NMR) spectra were recorded using Bruker spectrometers (Bruker, Rheinstetten, Germany), including the Avance II HD 300 (^{1}H NMR: 300 MHz, ^{13}C NMR: 75 MHz), Avance II 400 (^{1}H NMR: 400 MHz, ^{13}C NMR: 101 MHz), Avance III HD 400 (^{1}H NMR: 400 MHz, ^{13}C NMR: 101 MHz), and Avance III 600 (^{1}H NMR: 600 MHz, ^{13}C NMR: 151 MHz). The measurements were performed at the Department of Chemistry, Johannes Gutenberg-University Mainz. The Avance II HD 300, Avance II 400, and Avance III HD 400 spectrometers were equipped with a 5 mm broadband observe probe head (z gradient), while the Avance III 600 was equipped with a 5 mm cryogenic triple-band inverse probe head. Standard Bruker pulse sequences were applied for all measurements. All samples were dissolved in deuterated solvents obtained from Deutero GmbH (Kastellaun, Germany), including DMSO-d_6, C*D*Cl$_3$ and D_2O. Chemical shifts (δ) are reported in parts per million (ppm) relative to the residual solvent peaks: DMSO-d_6 (δ = 2.50 ppm), C*D*Cl$_3$ (δ = 7.26 ppm), and D_2O (δ = 4.79 ppm), referenced to tetramethylsilane (TMS, δ = 0.00 ppm). Spin multiplicities were assigned as follows: *s* (singlet), *d* (doublet), *t* (triplet), *q* (quartet), *m* (multiplet), *dd* (doublet of doublets), *quint* (quintet), and *br* (broad signal). All measured coupling constants (J) are reported in hertz (Hz). Data analysis was performed using MestReNova software (Version 14.3.3-33362, Mestrelab Research, Santiago de Compostela, Spain).

7.1.3 Column Chromatography

For column chromatography, silica gel with a particle size of 0.035–0.070 mm and a pore size of 60 Å (Acros Organics, New Jersey, USA) was used. Unless stated otherwise, eluents were freshly prepared using technical grade solvents. For flash chromatography, a nitrogen pressure of 0.2–0.6 bar was applied.

7.1.4 Size exclusion Chromatography

Size exclusion chromatography (SEC) was performed using Sephadex® LH-20 (GE Healthcare, Pittsburgh, USA) or Bio-Beads® S-X1 (Bio-Rad Laboratories GmbH, Feldkirchen, Germany). The eluent used for each separation is specified individually.

7.1.5 Medium pressure liquid chromatography

Medium pressure liquid chromatography (MPLC) was performed using a Sepacore® X50 Flash purification system (Büchi, Essen, Germany). Fractions were collected using a C-660 fraction collector and analyzed via UV-Photometer C-640 (Büchi, Essen, Germany) and thin-layer chromatography (TLC). Purifications were conducted using normal-phase chromatography with self-packed columns containing silica gel (SiO_2, particle size: 35–70 µm, pore size: 60 Å from Acros Organics, Schwerte, Germany).

7.1.6 Thin Layer Chromatography

Thin-layer chromatography (TLC) was performed on silica-coated aluminum sheets (ALUGRAM Xtra SIL G/UV254, Macherey-Nagel, Düren, Germany). Commercially available solvents were used without further purification. Analytes were detected using UV absorption at λ = 210 nm or 254 nm or by applying staining reagents.

The following staining solutions were used for visualization, with staining achieved upon heating:

- Ninhydrin stain: 1.5 g ninhydrin and 15 mL acetic acid in 500 mL methanol for detecting amine-containing compounds.
- $KMnO_4$ stain: 6 g $KMnO_4$, 40 g K_2CO_3, and 13 mg NaOH in 600 mL water for visualizing reductive compounds.
- Vanillin stain: 5 g vanillin, 60 mL acetic acid, and 20 mL saturated sulfuric acid in 600 mL methanol for detecting alcohols and carboxylic acids.

7.1.7 Mass spectrometry

Mass spectrometry (MS) measurements were performed using an Agilent 6545 QTOF-MS (Agilent, Santa Clara, USA), operating in electrospray ionization (ESI) mode. For sample preparation, analytes were dissolved at a concentration of 0.1–1 mg/mL in methanol, acetonitrile, or a methanol/chloroform (1:1) mixture. High molecular weight compounds were analyzed using matrix-assisted laser desorption/ionization time-of-flight (MALDI-TOF/TOF) mass spectrometry, performed on a Bruker Autoflex maX MALDI-TOF/TOF (Bruker, Bremen, Germany). The specific MALDI matrices used for ionization, including α-cyano-4-hydroxycinnamic acid (CHCA), 2,4-dihydroxylbenzoeacid (DHB) or dithranol, are detailed in the synthetic procedures. Where explicitly stated, KTFA-salt was added. Data acquisition for MALDI-TOF was carried out using Bruker flexControl 3.4, and spectral analysis was performed using Bruker flexAnalysis 3.4 (Bruker, Bremen, Germany) and mMass (Version 5.5.0, Martin Strohalm, Prague, Czech Republic). ESI measurements

were conducted at the Department of Chemistry, Johannes Gutenberg-University Mainz, while MALDI-TOF measurements were performed by [redacted] and [redacted].

7.1.8. High-Performance Liquid Chromatography (HPLC)

High performance liquid chromatography (HPLC) analyses were performed using a JASCO LC-4000 HPLC system equipped with a CO-4060 column oven, an AS-4050 autosampler, and a PU-4086 semi-preparative binary pump module (JASCO, Pfungstadt, Germany). Signal detection was carried out using a MD-4015 photodiode array (PDA) detector at λ = 210 nm and λ = 254 nm. A CHF122SC fraction collector (Advantec MFS Inc., Dublin, USA) was used for fraction collection.

Analytical runs were performed using the following reversed-phase columns:

- NUCLEODUR C18 Pyramid (Macherey-Nagel, pore size: 110 Å, 50 mm × 4.6 mm)
- NUCLEODUR C18 Pyramid (Macherey-Nagel, pore size: 100 Å, 250 mm × 4.6 mm)
- Chromolith® Performance RP-18e (Merck KGaA, pore size:130 Å, 100 mm × 4.6 mm)

The flow rate for analytical separations was set to 1.0 mL/min, except for the Chromolith® Performance RP-18e column, which was operated at 2.0 mL/min. For preparative HPLC, purifications were also performed using a JASCO LC-400 system. The reversed-phase NUCLEODUR C18 Pyramid column (Macherey-Nagel, pore size: 110 Å, 250 mm × 21 mm) was used for both systems. The flow rate for preparative HPLC was set to 19 mL/min. The binary solvent system used for analytical and preparative runs consisted of deionized water and acetonitrile (ACN, HPLC grade), both modified with 0.1% (v/v) trifluoroacetic acid (TFA). Chromatograms were plotted using OriginPro 9.0.0 (64-bit) (OriginLab, Northampton, USA).

***Table 7.1: Method A**: Solvent gradient for analytical RP-HPLC runs using Chromolith® Performance RP-18e column (100 mm).*

Time /min	H_2O + 0.1 vol% TFA /vol%	Acetonitrile + 0.1 vol% TFA /vol%
0	95	5
1	95	5
11	5	95
15	5	95

***Table 7.2: Method B**: Solvent gradient for analytical RP-HPLC runs using NUCLEODUR C18 Pyramid column (250 mm).*

Time /min	H_2O + 0.1 vol% TFA /vol%	Acetonitrile + 0.1 vol% TFA /vol%
0	100	0
2	100	0
42	60	40
60	60	40

***Table 7.3: Method C**: Solvent gradient for analytical RP-HPLC runs using NUCLEODUR C18 Pyramid column (250 mm).*

Time /min	H_2O + 0.1 vol% TFA /vol%	Acetonitrile + 0.1 vol% TFA /vol%
0	95	5
2	95	5
62	1	99
80	1	99

***Table 7.4: Method D**: Solvent gradient for analytical RP-HPLC runs using NUCLEODUR C18 Pyramid column (50 mm).*

Time /min	H_2O + 0.1 vol% TFA /vol%	Acetonitrile + 0.1 vol% TFA /vol%
0	95	5
1	95	5
6	5	95
15	5	95

***Table 7.5: Method E**: Solvent gradient for semi-preparative RP-HPLC runs using NUCLEODUR C18 Pyramid column (250 mm).*

Time /min	H_2O + 0.1 vol% TFA /vol%	Acetonitrile + 0.1 vol% TFA /vol%
0	95	5
1	95	5
46	0	100
60	0	100

7.1.9 Liquid chromatography-mass spectrometry

Liquid chromatography-mass spectrometry (LC-MS) measurements were performed using an Agilent InfinityLab LC/MSD XT system (Agilent Technologies Inc., Santa Clara, USA). Separations were carried out on a NUCLEODUR C18 Pyramid column (Macherey-Nagel, pore size: 110 Å, 50 mm × 2 mm) with a flow rate of 0.4 mL/min. Ionization was achieved using an Agilent Jet Stream (AJS) electrospray ionization (ESI) source, operating with a capillary voltage of 3500 V. Signal detection was performed using a UV detector at λ = 210 nm and λ = 254 nm. The mobile phase consisted of LC-MS-grade acetonitrile and an aqueous 20 mM ammonium acetate. Data acquisition and analysis were conducted using Agilent OpenLab software (Version 3.6, Agilent Technologies Inc).

***Table 7.6: Method F**: Solvent gradient for semi-preparative RP-HPLC runs using NUCLEODUR C18 Pyramid column (50 mm).*

Time /min	20 mM NH_4OAc in H_2O /vol%	Acetonitrile /vol%
0	70	30
0.5	70	30
2.5	1	99
5.5	1	99
6.0	70	30

7.1.10 Gel Permeation Chromatography

Analytical gel permeation chromatography (GPC) was performed using an Agilent 1100 Series system (Agilent Technologies Inc., Santa Clara, USA) equipped with UV and refractive index (RI) detection. Separations were carried out on PSS PFG 7 µm columns (PSS Polymer Standard Services GmbH, pore size: 100 Å and 1000 Å) using HFIP as eluent, each supplemented with potassium trifluoroacetate (KTFA) at a concentration of 3 g/L. All samples were prepared at a concentration of 1 mg/mL and calibrated against a PEG standard. Data acquisition and analysis were performed using WinGPC UniChrom® software (Version 8.33, PSS Polymer Standard Services GmbH). Chromatograms were further processed and visualized using OriginPro 9.0.0 (64-bit) (OriginLab, Northampton, USA).

7.1.12 Circular Dichroism Spectroscopy

Circular dichroism (CD) spectroscopy was performed using a J-815 CD spectrometer (Jasco, Pfungstadt, Germany) equipped with a Jasco PTC-423S/15 Peltier temperature control unit. Measurements were conducted in SUPRASIL quartz cuvettes (Hellma, Mühlheim, Germany) with path lengths of 1 mm, depending on the experimental setup. Spectra were recorded at 293 K, with pH variations applied where indicated and were recorded between 280 nm and 400 nm. Each measurement was performed in triplicate and averaged. Data acquisition and analysis were carried out using Spectra Manager 2.12.00 (Jasco) and further processed with OriginPro 9.0.0 (64-bit) (OriginLab, Northampton, USA). All spectra were background-corrected using the corresponding pure solvent spectrum.

7.1.13 Transmission Electron Microscopy

Transmission electron microscopy (TEM) imaging was performed using a FEI Tecnai T12 or a FEI Tecnai G2 Spirit transmission electron microscope (FEI, Hillsboro, USA), both equipped with a LaB_6 cathode operating at 120 kV. The Tecnai T12 was fitted with a BioTWIN objective lens, while the Tecnai G2 Spirit utilized a TWIN lens. Samples were prepared on freshly glow-discharged copper grids (CF300-Cu, 300 mesh, Electron Microscopy Sciences, Hatfield, USA) coated with a 3–4 nm carbon film. A 5 µL aliquot of the sample was deposited onto the grid and incubated for 60 seconds before removing excess liquid with Whatman® grade 1 or No. 4 filter paper (GE Healthcare Biosciences, Uppsala, Sweden). Negative staining was performed by applying 5 µL of a 2 wt.% uranyl acetate solution for 15–20 seconds, followed by careful blotting of the excess stain. Digital electron micrographs were acquired using either a TVIPS 4k × 4k CMOS camera or a MEGASYS 1k × 1k CCD camera. Image analysis was conducted using ImageJ v1.53o (Wayne Rasband and contributors, National Institutes of Health, USA). TEM imaging was performed by [redacted] and [redacted].

7.1.14 Widefield Microscopy

Widefield microscopy was performed using a Zeiss Elyra 7 system (Zeiss, Oberkochen, Germany) equipped with two sCMOS cameras on the Elyra 7 Duolink module. Laser-widefield imaging and structured illumination microscopy (SIM) were conducted on this system. Fluorescence imaging of Thioflavin-T-stained samples was conducted with an excitation wavelength of 450 nm and an emission detection range of 480–490 nm. SIM images were acquired in Lattice SIM mode using a lattice spot pattern, with 13 phase acquisitions per image. Image reconstruction was performed using dual-iterative SIM² processing in Zeiss Zen Black software (Zeiss, Oberkochen, Germany). Image

analysis was conducted using ImageJ v1.53o (Wayne Rasband and contributors, National Institutes of Health, USA). Microscopy was performed by [redacted].

7.1.15 Solid-Phase Peptide Synthesis

Solid-phase peptide synthesis (SPPS) was performed using a CS136XT Peptide Synthesizer (CS Bio Co., Menlo Park, USA) and, where applicable, a microwave-assisted Biotage Initiator+ Alstra system (Biotage, Uppsala, Sweden). The synthesis followed the standard Fmoc-protocol. As solid supports, 2-chlorotrityl chloride resin (loading capacity: 1.0–1.6 mmol/g, Iris Biotech, Marktredwitz, Germany) and Fmoc-AA-TentaGel® S TRT Resin preloaded with Trp(Boc)-Fmoc (loading density: 0.17 mmol/g, Rapp Polymere, Tübingen, Germany) were used. All reactions were conducted using peptide-grade solvents (DCM and DMF) without further purification. The coupling, capping, and deprotection reagents were purchased from commercial sources, and their respective solutions were prepared before synthesis.

7.1.16 Rheology

The rheological properties of the hydrogel before and after irradiation were analyzed using a stress-controlled MCR 302e rheometer (Anton Paar, Ostfildern-Scharnhausen, Germany). Measurements were performed with a 25 mm diameter cone-plate geometry on a silica glass plate, maintaining a gap width of 0.05 mm. Oscillatory rheological measurements were performed in amplitude and frequency sweep mode. Data acquisition and analysis were performed using RheoCompass 1.19 software (Anton Paar, Ostfildern-Scharnhausen, Germany). Chromatograms were further processed and visualized using OriginPro 9.0.0 (64-bit) (OriginLab, Northampton, USA).

7.1.17 Agarose Gel Electrophoresis

Agarose gel electrophoresis (AGE) was performed to analyze the migration behavior of nucleic acid-containing samples. Gels were prepared using 0.8% agarose (Agarose NEEO Ultra-Quality, Carl Roth GmbH+Co.KG, Karlsruhe, Germany) (w/v) dissolved in 1× TAE and heated until completely dissolved. After cooling to approximately 50°C, the solution was poured into a gel tray, a comb was inserted to create sample wells, and the gel was allowed to solidify. Electrophoresis was conducted in 1× TAE at 100 V for 20-60 min in a gel electrophoresis system (Carl Roth GmbH+Co.KG, Karlsruhe, Germany). The migration of nucleic acid-containing complexes was assessed under standard electrophoretic conditions. For visualization, the bands were detected under UV illumination. Data analysis was performed using ImageJ v1.53o (Wayne Rasband and contributors, National Institutes of Health, USA).

7.1.18 Fluorescence Activated Cell Sorting

Fluorescence-activated cell sorting (FACS) was performed to analyze cell samples using a FACS Canto II (BD Biosciences, Heidelberg, Germany) equipped with BD FACS Diva™ software (BD Biosciences, San Diego, USA). Data were analyzed using FlowJo™ software (FlowJo, Ashland, USA). Data were further processed and visualized using GraphPad Prism 9 (V. 9.5.1, GraphPad Software, Boston, USA). FACS measurements were performed by [redacted].

7.1.19 Cytometric Bead Array Assay

A cytometric bead array (CBA) assay was performed to quantify IL-8 chemokine in cell culture using BD™ CBA Human IL-8 Flex Set (BD Biosciences, Heidelberg, Germany). Measurements were conducted on a LSR-II flow cytometer (BD Biosciences, Heidelberg, Germany). A calibration curve

ranging from 10 to 2500 pg/mL was used to determine IL-8 concentrations. Results were analyzed using FCAP Array Analysis Software (BD Biosciences, Heidelberg, Germany). Data were further processed and visualized using GraphPad Prism 9 (V. 9.5.1, GraphPad Software, Boston, USA). CBA measurements were performed by [redacted].

7.2 Standard Operating Procedures (SOP)

7.2.1 Resin Loading (SOP 1)

The Fmoc-protected amino acid (2.0 equivalents, relative to the resin loading capacity) was dissolved in DCM (10 mL/g resin). If necessary, a small amount of DMF was added to aid solubility. The solution was transferred to a Merrifield reaction vessel containing 2-chlorotrityl chloride resin, followed by the addition of DIPEA (2.0 equivalents). The mixture was shaken for 5 minutes, after which an additional 3.0 equivalents of DIPEA were added, and shaking continued for 1 hour at room temperature. To cap unreacted sites, methanol (1 mL/g resin) was added, and the mixture was shaken for an additional 15 minutes. The resin was then washed sequentially with DCM (3 × 10 mL), DMF (3 × 10 mL) and DCM (3 × 10 mL) before being dried under high vacuum overnight. For the preparation of low-loading resin, the same procedure was applied with a reduced number of equivalents. The loading capacity was determined by gravimetric analysis.

7.2.2 Coupling Method HBTU/HOBt (SOP 2)

The loaded resin was placed in a reaction vessel and swollen in DCM for 10 minutes under continuous shaking (180° inversion mixing). After draining the solvent, Fmoc deprotection was performed by adding 20% piperidine in DMF and shaking for 20 minutes. The resin was then washed with DMF and DCM, and the deprotection step was repeated for 10 minutes to ensure complete removal of the Fmoc group. For the coupling reaction, a solution of the Fmoc-protected amino acid (4.0 eq.0.4 mol/L, relative to resin loading capacity), HBTU (4.0 eq., 0.4 mol/L), HOBt (4.0 eq., 0.4 mol/L) and DIPEA (6.0 eq., 0.6 mol/L) in DMF was added to the reaction vessel. The mixture was shaken for 1 hour by room temperature. After coupling, the solution was drained, and the resin was washed with DMF (2×) and DCM (1×). To prevent side reactions, free amine groups were capped using a solution of acetic anhydride (1.0 eq., 0.5 mol/L), DIPEA (0.27 eq., 0.13 mol/L), and HOBt (0.03 eq., 0.02 mol/L) in NMP for 20 minutes. The Fmoc deprotection and coupling steps were repeated according to the desired amino acid sequence. After the final coupling step, the resin was thoroughly washed with DCM.

7.2.3 Coupling Method DIC/Oxyma (SOP 3)

The loaded resin was placed in a reaction vessel and swollen in DCM for 1 hour under continuous shaking. After draining the solvent, Fmoc deprotection was performed by adding 20% piperidine in DMF and shaking for 5 minutes. The resin was then washed with DMF and DCM, and the deprotection step was repeated for 10 minutes to ensure complete removal of the Fmoc group. For the coupling reaction, a solution of the Fmoc-protected amino acid (4.0 eq., 0.5 mol/L, relative to resin loading capacity), DIC (3.0 eq., 0.5mol/L) and Oxyma (4.0 eq., 0.5 mol/Lin DMF was added to the reaction vessel. The mixture was shaken for 20 minutes by 40 °C in microwave. After coupling, the solution was drained, and the resin was washed with DMF (3×) and DCM (1×). The coupling was repeated one time. To prevent side reactions, free amine groups were capped using a solution of acetic anhydride (20.8 eq., 5.0 mol/L) and DIPEA (20.8 eq., 2.0 mol/L) in NMP for 20 minutes. The Fmoc deprotection and coupling steps were repeated according to the desired amino acid sequence. After the final coupling step, the resin was thoroughly washed with DCM.

7.2.4 Coupling Method DEPBT/HOPO (SOP 4)

The loaded resin was placed in a reaction vessel and swollen in DCM for 1 hour under continuous shaking. After draining the solvent, Fmoc deprotection was performed by adding 20 % piperidine in DMF and shaking for 10 minutes. The resin was then washed with DMF and DCM, and the deprotection step was repeated for 20 minutes to ensure complete removal of the Fmoc group. For the coupling reaction, a solution of the Fmoc-protected amino acid (3.0 eq., 0.4 mol/L relative to resin loading capacity), DEPBT (4.5 eq., 0.8 mol/L), HOPO (3.0 eq., 0.8 mol/L), and DIPEA (9.0 eq., 2.0 mol/L) in DMF was added to the reaction vessel. The mixture was shaken for 1 hour by room temperature. After coupling, the solution was drained, and the resin was washed with DMF (3×) and DCM (1×). The coupling was repeated one time. To prevent side reactions, free amine groups were capped using a solution of acetic anhydride (31.3 eq., 5.0 mol/L) and DIPEA (31.3 eq., 2.0 mol/L) in NMP. The Fmoc deprotection and coupling steps were repeated according to the desired amino acid sequence. After the final coupling step, the resin was thoroughly washed with DCM.

7.2.5 Cleavage from the Resin (SOP 5)

For peptides containing Boc-protected groups, tert-butyl ethers, and trityl groups, the resin was treated with a mixture of TFE and DCM in a ratio of 2:8 (v/v, TFE/DCM) for 1 hour. After draining, the resin was washed with DCM, and the procedure was repeated twice. The combined solutions were concentrated under reduced pressure, and the crude product was precipitated by adding the solution to a cold mixture of diethyl ether, followed by centrifugation. Alternatively, the solvent was removed by co-distillation with toluene and subsequent freeze-drying.

7.2.6 Polyplex Formation for Agarose Gel Electrophoresis

To investigate the formation of siRNA-polyplexes, samples were prepared at defined N/P ratios by mixing Cy3-labeled siRNA (Cy3-labeled luciferase GL2 duplex, 20 nmol, Dharmacon Inc., Colorado, USA) with the cationic polymers **V-5(PG9)**, **V-5(PG5)**, and a **copolymer** in phosphate-buffered saline (PBS). For each sample, 1.0 µL of siRNA solution (5.0 µM, PBS) was transferred to a microcentrifuge tube. The required volume of cationic polymer (40.0 µM, PBS) was then added to achieve the desired N/P ratio, followed by gentle pipette mixing. The volume was adjusted to 25 µL with PBS, resulting in a final siRNA concentration of 0.4 µM. The samples were incubated at 25 °C for 20 min to allow complex formation. For the preparation of **copolymer**-based polyplexes, **V-5(PG9)** was first incubated with siRNA, followed by the addition of **V-8**. Prior to electrophoresis, 5.0 µL of loading buffer (Gel Loading Dye Purple (6×) without SDS, New England BioLabs, Frankfurt am Main, Germany) was added to each sample. Free siRNA was prepared as a control by mixing siRNA with PBS instead of the cationic polymer.

7.2.7 Cell viability and Cy3-siRNA uptake

HEK-293T cells were seeded in 12-well plates at a density of 1×10^5 cells/mL per well in culture medium and incubated at 37°C for at least 2 h to allow attachment. For transfection, cells were treated with polyplexes consisting of Cy3-labeled siRNA (Cy3-labeled luciferase GL2 duplex, 20 nmol, Dharmacon Inc., Colorado, USA) and **copolymer** or **V-5(PG9)** at a final siRNA concentration of 5–50 nM and an N/P ratio of 8:1 and 10:1 in PBS. **V-5(PG9)** was added together with the siRNA and incubated for 20 min at RT. Then **V-8** was added and the sample was diluted with PBS to a volume of 100 µL and carefully added to the cells. Cells were incubated with the polyplexes for 24 h before further processing. Untreated cells and cells treated with free siRNA served as controls. After

incubation, cells were harvested and subsequently centrifuged at 300 × g for 8 min at 4 °C. The supernatant was discarded, and the cell pellet was resuspended in D-PBS, followed by a second centrifugation step under the same conditions. After removing the supernatant, cells were resuspended in FACS buffer. For cell viability assessment, Fixable Viability Dye eFluor™ 450 (FVD-eFluor 450, Invitrogen, USA) was added to each sample, gently vortexed, and incubated for 30 min at 4 °C in the dark. After incubation, D-PBS were added, and the samples were centrifuged at 300 × g for 5 min at 4 °C. The supernatant was removed, and the pellet was resuspended in FACS buffer, followed by another centrifugation under the same conditions. The final cell pellet was resuspended in FACS buffer for analysis. For Cy3-siRNA uptake analysis, cells were directly analyzed by flow cytometry to assess Cy3 fluorescence intensity without additional staining. DOTAP (DOTAP CellPure ready-to-use, Carl Roth GmbH+Co.KG, Karlsruhe, Germany) was used as a transfection reagent as a positive control (50 nM siRNA).

7.2.8 IL-8 siRNA Transfection in HEK-Cells

HEK-293T cells were seeded at a density of 1×10^5 cells/mL per well in 12-well plates and incubated overnight. For transfection, polyplexes were prepared by incubating IL-8-specific siRNA (IL-8 siRNA (h): sc-39631; Satna Cruz Biotechnology, INC., Dallas, USA) or nonspecific siRNA (Control siRNA-A: sc-37007; Santa Cruz Biotechnology, INC., Dallas, USA) with **V-5(PG9)**, **copolymer** or lipofectamine (Lipofectamine RNAiMAX; Invitrogen, Waltham, USA) at an N/P ratio of 10:1 in PBS. The final siRNA concentration ranged from 5–50 nM. Initially, siRNA and V-5(PG9) were incubated for 20 min at room temperature, followed by the addition of V-8 to the complex. The final volume was adjusted to 100 µL with PBS and added to the cells. After 12 h, cells were stimulated with TNF-α (100 ng/mL) and incubated overnight under standard culture conditions. For IL-8 quantification via Cytometric Bead Array (CBA), 100 µL of the cell culture supernatant and BD™ CBA Human IL-8 Flex Set (BD Biosciences, Heidelberg, Germany) were used. The assay was performed in PBS supplemented with 1% FCS (Assay buffer). Each sample was mixed with 0.2 µL Capture Beads and PE Detection Reagent. Beads were vortexed vigorously for 15 s before pipetting the calculated volumes into the reaction tubes. Samples were incubated for 1 h at room temperature with the Capture Beads, followed by an additional 2 h incubation with the PE detection reagent in the dark.

7.2.9 CpG ODN SL03 Transfection in BMDC

BMDCs (Wild-type mice (C57BL/6) by one-week cultivation with GM-CSF) were seeded in 12-well plates at a density of 1×10^5 cells/mL per well in culture medium and incubated at 37°C for at least 4 h to allow attachment. For transfection, cells were treated with polyplexes consisting of CpG ODN SL03 (ODN-D SL03, InvivoGen, San Diego, USA) and **copolymer** or **V-5(PG9)** and an N/P ratio of 10:1 in PBS at a final cPG concentration of 250 ng/mL. For this **V-5(PG9)** was added together with the siRNA and incubated for 20 min at RT. Then **V-8** was added, and the sample was diluted with PBS to a volume of 40 µL and carefully added to the cells. . DOTAP (DOTAP CellPure ready-to-use, Carl Roth GmbH+Co.KG, Karlsruhe, Germany) was used as a transfection reagent as a positive control. After incubation of 24 h, cells were harvested and centrifuged at 300 × g for 8 min at 4 °C. The supernatant was discarded, and the cell pellet was resuspended in 1 mL D-PBS, followed by a second centrifugation step under the same conditions. After removing the supernatant, 25 µL 2.4G2 Fc-block (1:100 in FACS buffer) was added to the cells, and the samples were vortexed. After a 10 min incubation at room temperature (RT), 25 µL of antibody master mix (diluted in FACS buffer) was added to each sample. Samples were incubated for 20 min at 4°C in the dark, followed by the addition of 2 mL D-PBS and centrifugation at 300 × g for 5 min at 4°C. After discarding the

supernatant, 0.5 µL Fixable Viability Dye eFluor™ 450 (FVD-eFluor 450, Invitrogen, USA) per 500 µL D-PBS was added to each sample, vortexed, and incubated for 30 min at 4°C in the dark. After incubation, 2 mL FACS buffer were added, and the samples were centrifuged at 300 × g for 5 min at 4°C. The supernatant was discarded, and the cell pellet was resuspended in 400 µL FACS buffer for analysis.

7.2.10 CpG ODN SL03 Transfection in Spleen Cells

Spleen cells isolated from mice were used. For transfection, cells were treated with polyplexes consisting of CpG ODN SL03 (ODN-D SL03, InvivoGen, San Diego, USA) and **copolymer** or **V-5(PG9)** and an N/P ratio of 10:1 in PBS at a final cPG concentration of 250 ng/mL. For this **V-5(PG9)** was added together with the siRNA and incubated for 20 min at RT. Then **V-8** was added, and the sample was diluted with PBS to a volume of 40 µL and carefully added to the cells. DOTAP (DOTAP CellPure ready-to-use, Carl Roth GmbH+Co.KG, Karlsruhe, Germany) was used as a transfection reagent as a positive control. After incubation of 24 h, cells were harvested and centrifuged at 300 × g for 8 min at 4 °C. The supernatant was discarded, and the cell pellet was resuspended in 1 mL D-PBS, followed by a second centrifugation step under the same conditions. After removing the supernatant, 25 µL 2.4G2 Fc-block (1:100 in FACS buffer) was added to the cells, and the samples were vortexed. After a 10 min incubation at room temperature (RT), 25 µL of antibody master mix (diluted in FACS buffer) was added to each sample. Samples were incubated for 20 min at 4°C in the dark, followed by the addition of 2 mL D-PBS and centrifugation at 300 × g for 5 min at 4°C. After discarding the supernatant, 0.5 µL Fixable Viability Dye eFluor™ 450 (FVD-eFluor 450, Invitrogen, USA) per 500 µL D-PBS was added to each sample, vortexed, and incubated for 30 min at 4°C in the dark. After incubation, 2 mL FACS buffer were added, and the samples were centrifuged at 300 × g for 5 min at 4°C. The supernatant was discarded, and the cell pellet was resuspended in 400 µL FACS buffer for analysis.

7.3 Synthesis

H-L-Met-D-Glu(tBu)-L-Met-D-Glu(tBu)-L-Met-D-Glu(tBu)-L-Met-D-Glu(tBu)-OH (**III-1**)

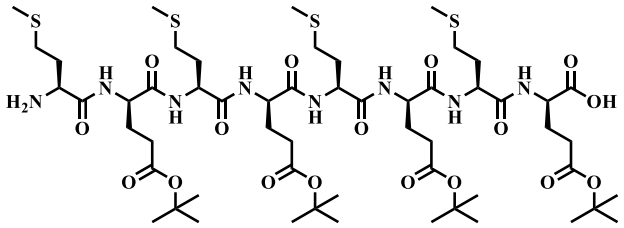

Compound **III-1** was synthesized following SOP 2, starting with 0.5 g of 2-chlorotrityl chloride resin (loading capacity: 1.6). The resin was preloaded according to SOP 1. After synthesis, the peptide was cleaved as outlined in SOP 5 and subsequently purified using RP-HPLC (Method E).

Yield: 0.53 g (0.41 mmol, 53%); colorless lyophilizate.

MF: $C_{56}H_{98}N_8O_{17}S_4$ MW 1283.68 g/mol [1282.59]

HR-TOF-MS (ESI, pos. MeOH) m/z: 1283.5984 $[M+H]^+$ calc.: 1283.6003

^{1}H NMR (400 MHz, DMSO-*d*6, 296 K, COSY): δ / ppm = 9.21 (s, 1H, α-N*H*), 8.86 (s, 1H, α-N*H*), 8.70 (s, 1H, α-N*H*), 8.36 (t, *J* = 7.5 Hz, 2H, N*H*$_2$), 8.06 (s, 1H, α-N*H*), 7.49 (s, 1H, α-N*H*), 4.36 (m, 4H, *α*-C*H*), 4.32 – 4.14 (m, 3H, *α*-C*H*), 4.06 (tt, *J* = 5.8, 5.1 Hz, *α*-C*H*^{Glu}), 2.48 – 2.08 (m, 8H, γ-C*H*$_2^{Met}$), 2.04 (s, 3H, S-C*H*$_3$), 2.03 (s, 3H, S-C*H*$_3$), 2.02 (s, 3H, S-C*H*$_3$), 1.98 (s, 3H, S-C*H*$_3$), 1.98 – 1.70 (m, 16H, β-C*H*$_2^{Met}$, γ-C*H*$_2^{Glu}$), 1.68 – 1.51 (m, 8H, β-C*H*$_2^{Glu}$), 1.39 (m, 36H, C*H*$_3^{Boc}$).

Cyclo[-(L-Met-D-Glu(tBu))$_4$-] (**III-2**)

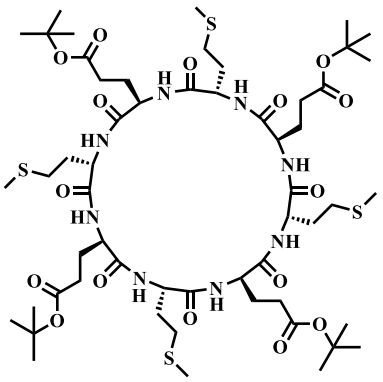

III-1 (50.0 mg, 0.039 mmol, 1.0 eq), PyBOP (24.3 mg, 0.047 mmol, 1.2 eq) and HOBt (6.3 mg, 0.047 mmol, 1.2 eq) were dissolved in 50 mL DCM and cooled with an ice bath to 0 °C. DIPEA (0.009 mL, 0.051 mmol, 1.3 eq.) in 1 mL DCM was added dropwise with a fine-dose dropping funnel over 20 min with stirring. The reaction solution was stirred for 6 d under N_2-atmosphere. Everyday PyBOP (1 eq.) and DIPEA (1 eq.) were added. The solvent was removed under reduced pressure. Due to the poor solubility of the product **III-2** obtained, no further purification steps were undertaken. The crude product was converted directly to **III-3**.

Yield: 24.5 mg crude product; colorless solid.

MF: $C_{56}H_{96}N_8O_{16}S_4$ MW 1265.6640 g/mol [1264.5827]

Cyclo[-(L-Met-D-Glu)$_4$-] (**III-3**)

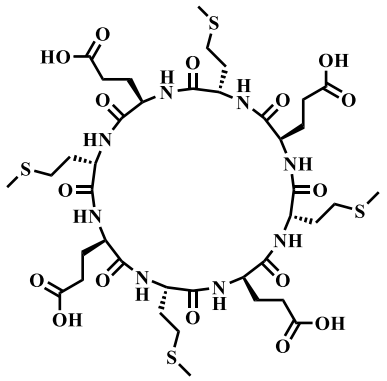

III-2 (24.5 mg, 0.019 mmol, 1.0 eq) was dissolved in 3 mL TFA/TIPS/H_2O/EDT (94:1:2.5:2.5) (reagent L) and stirred for 4 h at room temperature. Solvent was removed under reduced pressure and codestilled with 5x10 mL toluene.

Yield: no product obtained.

MF: $C_{40}H_{64}N_8O_{16}S_4$ MW 1041.2320 g/mol [1040.3323]

H_2N-D-Glu(COO-TEGOMe)-COOH (**III-4**)

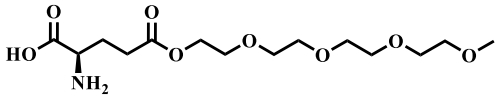

D-Glutamic acid (8.00 g, 0.054 mol, 1.0 eq) and tetraethyleneglycol monomethyl ether (42.3 mL, 0.227 mol, 4.0 eq) were placed in a round bottle flask and cooled with an ice bath to 0 °C. Sulfuric acid conc. (5 mL, 0.092 mol, 1.7 eq) was added dropwise over 5 min with stirring. The reaction solution was stirred for 16 h at room temperature and splashed into a solution of 250 mL NEt_3/isopropanol (3:10) for participation. The suspension was centrifuged, and the residue was washed with 2x30 mL isopropanol.

Yield: 14.03 g (0.41 mol, 76 %); colorless solid.

MF: $C_{14}H_{27}NO_8$ MW 337.3690 g/mol [337.1737]

HR-TOF-MS (ESI, pos. MeOH) m/z: 338.1816 $[M+H]^+$ calc.: 338.745

376.1342 $[M+K]^+$ calc.: 376.1374

^{1}H NMR (400 MHz, DMSO-*d*6, 296 K): δ / ppm = 4.13 (t, *J* = 4.7 Hz, 2H, CH_2^{EG}), 3.56 – 3.31 (m, 15H, CH_2^{EG}, α-C*H*), 3.24 (s, 3H, CH_3), 2.38 (q, *J* = 7.5, 2H, γ-CH_2), 1.89 (q, *J* = 7.5 Hz, 2H, β-CH_2), 1.04 (d, *J* = 6.1 Hz, 2H, NH_2).

Fmoc-D-Glu(COO-TEGOMe)-COOH (**III-5**)

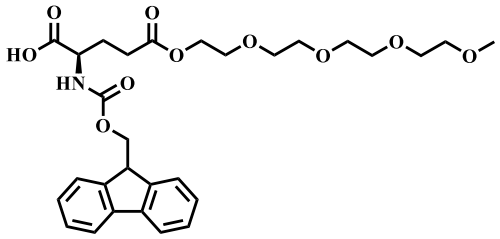

III-4 (3.28 g, 9.73 mmol, 1.0 eq) and $NaHCO_3$ (1.63 g, 19.45 mmol, 2.0 eq) were dissolved in 10 mL water and stirred at room temperature. Fmoc-OSu (4.26 g, 12.64 mmol, 1.3 eq) was dissolved in 10 mL acetone and added dropwise to the other solution over 20 min. The reaction solution was stirred for 24 h at room temperature. After 12 h 1 eq Fmoc-OSu was added. Acetone was removed under reduced pressure and the aqueous solution was extracted with 2x50 mL DCM. The organic phase was washed with 2x50 mL 1M HCl, 2x50 mL brine and dried over $MgSO_4$. The Solvent was removed under reduced pressure. Purification was performed *via* silica column chromatography (100% DCM → 10:1 DCM/MeOH) follow by size exclusion (Sephadex; MeOH).

Yield: 2.03 g (3.62 mmol, 37%); yellowish oil.

MF: $C_{29}H_{37}NO_{10}$ MW 559.6120 g/mol [559.2417]

HR-TOF-MS (ESI, neg. MeOH) m/z: 558.2337 $[M+H]^-$ calc.: 558.2344

^{1}H NMR (400 MHz, C*D*Cl$_3$, 296 K): δ / ppm = 12.85 – 12.05 (m, 1H, CO-O*H*), 7.89 (d, *J* = 7.6 Hz, 2H, C*H*^{Fmoc}), 7.72 (d, *J* = 7.4 Hz, 2H, C*H*^{Fmoc}), 7.66 (d, *J* = 7.8 Hz, 1H, N*H*), 7.42 (td, *J* = 7.5, 1.3 Hz, 2H, C*H*^{Fmoc}), 7.33 (td, *J* = 7.5, 1.4 Hz, 2H, C*H*^{Fmoc}), 4.58 (t, *J* = 5.3 Hz, 1H, C*H*^{Fmoc}), 4.36 – 4.15 (m, 2fH, C*H*$_2^{Fmoc}$), 3.99 (td, *J* = 9.0, 4.9 Hz, 1H, *α*-C*H*), 3.53 – 3.39 (m, 16H, C*H*$_2^{EG}$), 3.24 (s, 3H, O-C*H*$_3$), 2.31 (t, *J* = 7.6 Hz, 2H, γ-C*H*$_2$), 1.97 (td, *J* = 13.5, 8.1 Hz, 1H, β-C*H*$_2$), 1.79 (dt, *J* = 14.6, 7.7 Hz, 1H, β-C*H*$_2$).

H-L-Met-D-Glu(-COO-TEGOMe)-L-Met-D-Glu(-COO-TEGOMe)-L-Met-D-Glu(-COO-TEGOMe)-L-Met-D-Glu(-COO-TEGOMe)-OH (**III-6**)

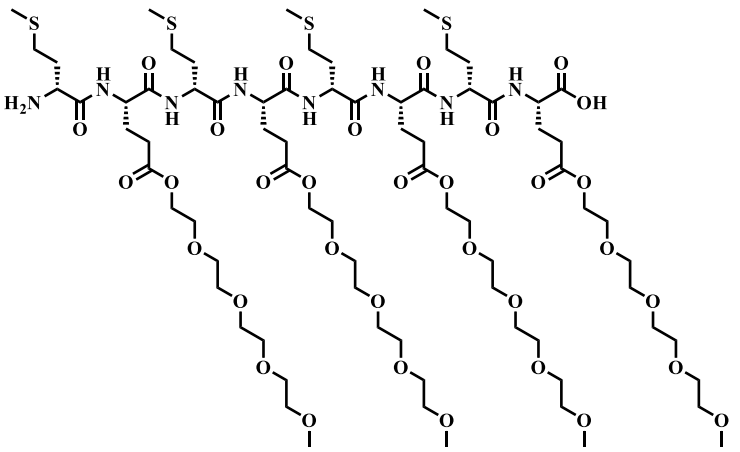

Compound **III-6** was synthesized following SOP 2, starting with 0.5 g of 2-chlorotrityl chloride resin (loading capacity: 1.0). The resin was preloaded according to SOP 1. After synthesis, the peptide was cleaved as outlined in SOP 5 and subsequently purified using RP-HPLC (Method E).

Yield: 0.24 g (0.13 mmol, 26%); colorless lyophilizate.

MF: $C_{76}H_{138}N_8O_{33}S_4$ MW 1820.2030 g/mol [1818.8249]

HR-TOF-MS (MALDI, CHCA, pos. DMF) m/z: 1842.390 $[M+Na]^+$ calc.:1842.8147

^{1}H NMR (400 MHz, DMSO-*d*6, 296 K, COSY, 296 K): δ / ppm = 8.94 (d, 1H, α-N*H*), 8.70 – 8.57 (m, 1H, α-N*H*), 8.41 – 8.14 (m, 4H, α-N*H*), 8.10 (d, *J* = 8.3 Hz, 1H, α-N*H*), 7.80 (d, *J* = 7.5 Hz, 1H, α-N*H*), 7.74 (d, *J* = 7.5 Hz, 1H), 4.50 – 4.23 (m, 3H, *α*-C*H*), 4.16 – 4.03 (m, 4H, *α*-C*H*), 3.91 – 3.84 (m, 1H, *α*-CH^{Glu}), 3.63 – 3.56 (m, 8H, CH_2^{EG}), 3.55 – 3.47 (m, 48H, CH_2^{EG}), 3.46 – 3.36 (m, 8H, CH_2^{EG}), 3.23 (s, 12H,O-CH_3), 2.47 – 2.23 (m, 16H, γ-CH_2), 2.03 (s, 12H, S-CH_3), 1.99 – 1.68 (m, 16H, β-CH_2).

Cyclo[-(L-Met-D-Glu(-COO-TEGOMe))$_4$-] (**CP1**)

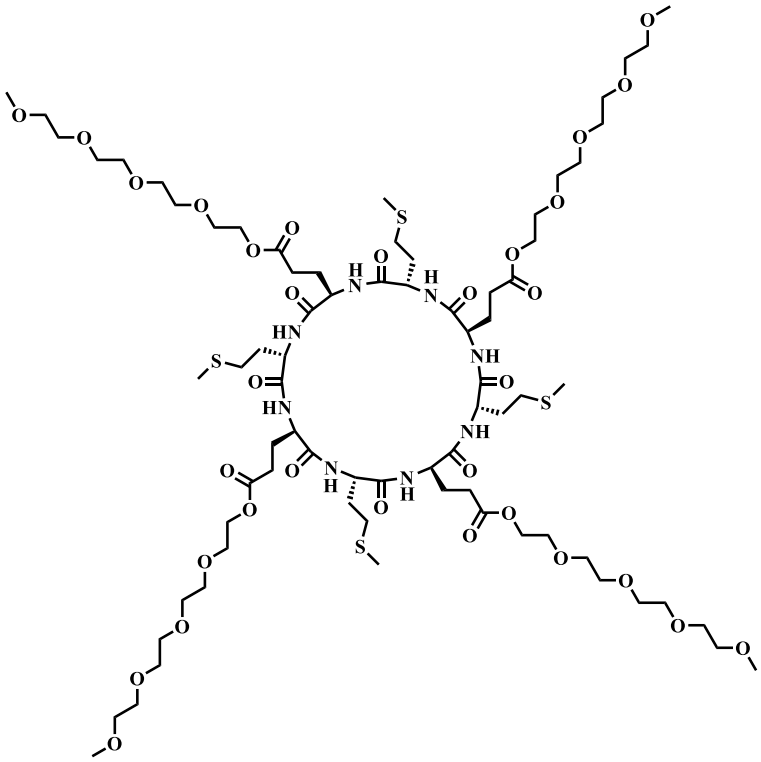

III-6 (70.0 mg, 0.038 mmol, 1.0 eq), PyBOP (24.0 mg, 0.046 mmol, 1.2 eq) and HOBt (6.2 mg, 0.046 mmol, 1.2 eq) were dissolved in 70 mL DCM and cooled with an ice bath to 0 °C. DIPEA (8.5 µL, 0.05 mmol, 1.3 eq.) in 1 mL DCM was added dropwise with a fine-dose dropping funnel over 20 min with stirring. The reaction solution was stirred for 7 d under N_2-atmosphere. Everyday PyBOP (1 eq.) and DIPEA (1 eq.) were added. The solvent was removed under reduced pressure. Purification was performed by size exclusion (Sephadex; MeOH).

Yield: 13.4 mg (4.6 µmol, 19%); colorless lyophilizate.

MF: $C_{76}H_{136}N_8O_{32}S_4$ MW 1802.1880 g/mol [1800.8143]

HR-TOF-MS (MALDI, CHCA, pos. DMF) m/z: 1823.9351 $[M+Na]^+$ calc.: 1823.8041

1840.6496 $[M+K]^+$ calc.: 1839.7780

^{1}H NMR (400 MHz, DMSO-*d*6, 296 K, COSY, 296 K): δ / ppm = 8.39 – 7.89 (m, 9H, α-N*H*), 4.46 – 4.19 (m, 4H, *α*-C*H*), 4.17 – 4.03 (m, 4H, *α*-C*H*), 3.62 – 3.55 (m, 8H, CH_2^{EG}), 3.55 – 3.46 (m, 48H, CH_2^{EG}), 3.45 – 3.38 (m, 8H, CH_2^{EG}), 3.23 (s, 12H, O-CH_3), 2.36 (m, 16H, γ-CH_2), 2.06 – 1.99 (m, 12H, S-CH_3), 1.97 – 1.68 (m, 16H, β-CH_2).

H-L-Met-D-Trp(Boc)-L-Met-D-Glu(-COO-TEGOMe)-L-Met-D-Trp(Boc)-L-Met-D-Glu(-COO-TEGOMe)-OH (**III-7**)

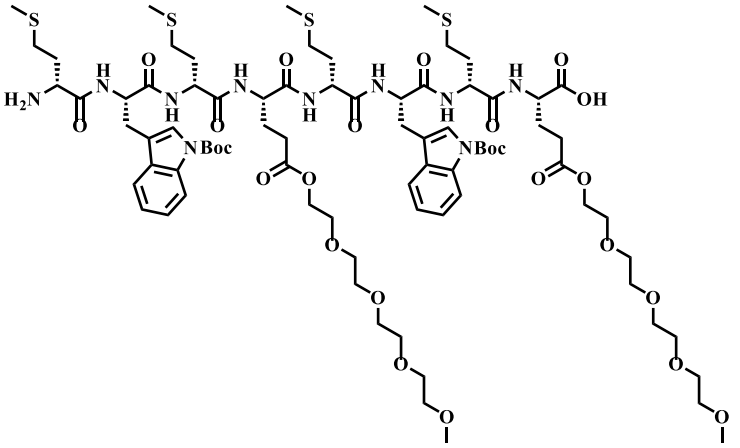

Compound **III-7** was synthesized following SOP 2, starting with 0.5 g of 2-chlorotrityl chloride resin (loading capacity: 1.0). The resin was preloaded according to SOP 1. After synthesis, the peptide was cleaved as outlined in SOP 5 and subsequently purified using RP-HPLC (Method E).

Yield: 0.97 g (0.55 mmol, 57%); colorless lyophilizate.

MF: $C_{80}H_{124}N_{10}O_{25}S_4$ MW 1754.1570 g/mol [1752.7622]

HR-TOF-MS (ESI, pos. MeOH) m/z: 1753.7695 $[M+H]^+$ calc.: 1753.7630

^{1}H NMR (400 MHz, DMSO-*d*6, 296 K, COSY): δ / ppm = 8.91 (s, 1H, α-N*H*), 8.54 (m, 1H, α-N*H*), 8.41 (s, 1H, α-N*H*), 8.18 (s, 1H, α-N*H*), 8.00 (d, *J* = 8.2 Hz, 2H, NH_2), 7.95 (s, 1H, α-N*H*), 7.54 (s, 1H, α-N*H*), 7.50 (s, 1H, α-N*H*), 7.32 – 7.08 (m, 10H, CH^{Trp}), 4.76 – 3.87 (m, 8H, *α*-C*H*), 3.61 – 3.43 (m, 32H, CH_2^{EG}), 3.22 (s, 5H, O-CH_3), 2.89 (s, 6H, S-CH_3), 2.73 (s, 6H, S-CH_3), 2.50 – 2.21 (m, 8H, γ-CH_2), 2.18 – 2.03 (m, 4H, γ-CH_2), 2.00 – 1.79 (m, 16H *β*-CH_2), 1.61 (d, *J* = 2.7 Hz, 18H, CH_3^{Boc}).

Cyclo[-(L-Met-D-Trp(Boc)-L-Met-D-Glu(COO-TEGOMe))$_2$-] (**III-8**)

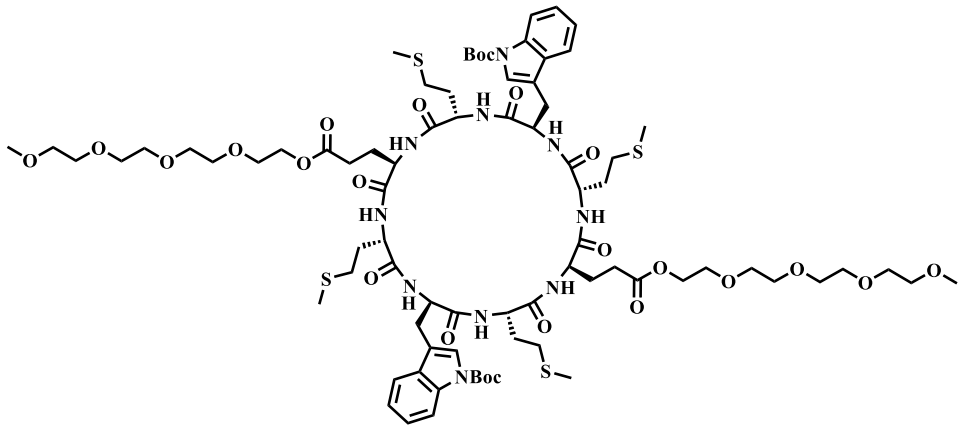

III-7 (100.0 mg, 0.055 mmol. 1.0 eq), PyBOP (34.3 mg, 0.066 mmol, 1.2 eq) and HOBt (8.9 mg, 0.066 mmol, 1.2 eq) were dissolved in 100 mL DCM and cooled with an ice bath to 0 °C. DIPEA (12.1 µL, 0.071 mmol, 1.3 eq) in 1 mL DCM was added dropwise with a fine-dose dropping funnel over 20 min with stirring. The reaction solution was stirred for 8 d under N_2-atmosphere. Everyday PyBOP (1 eq.) and DIPEA (1 eq.) were added. The solvent was removed under reduced pressure. Due to the poor solubility of the product obtained, no further purification steps were undertaken. The crude product was converted directly to **CP2**.

Yield: 30.4 mg crude product; colorless solid.

MF: $C_{80}H_{122}N_{10}O_{24}S_4$ MW 1736.1420 g/mol [1734.7516]

HR-TOF-MS (ESI, pos. MeOH) m/z: 1757.7407 $[M+Na]^+$ calc.: 1757.7414

Cyclo[-(L-Met-D-Trp-L-Met-D-Glu(COO-TEGOMe))$_2$-] (**CP2**)

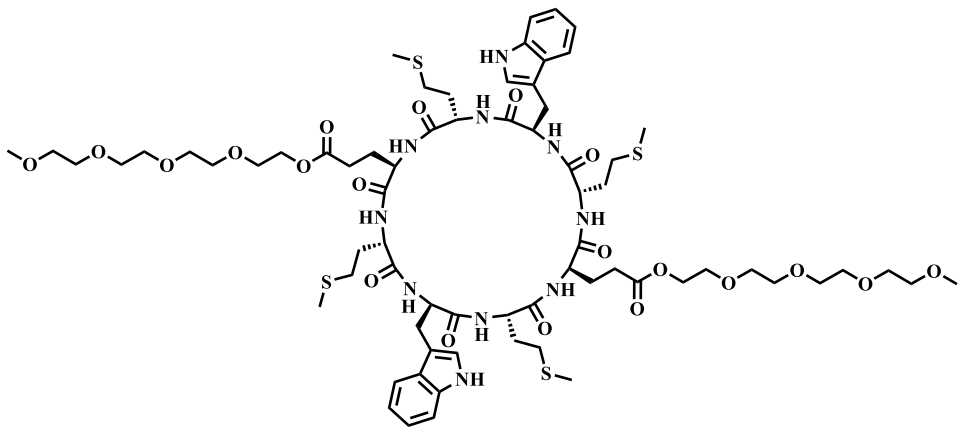

III-8 (30.4 mg, 0.018 mmol, 1.0 eq) was dissolved in 5 mL TFA/TIPS/H_2O/EDT (94:1:2.5:2.5) (reagent L) and stirred for 2 h at room temperature. Solvent was removed under reduced pressure and codestilled with 5x10 mL toluene. The residue was suspended in 10 mL DCM and centrifuged. The residue was washed with 3x10 mL DCM and lyophilized.

Yield: 25.9 mg crude product; colorless solid.

MF: $C_{70}H_{106}N_{10}O_{20}S_4$ MW 1535.9080 g/mol [1534.6468]

HR-TOF-MS (MALDI, CHCA, pos. DMF) m/z: 1557.4199 $[M+Na]^+$ calc.: 1557.6366

1573.5044 $[M+K]^+$ calc.: 1573.6105

Tos-TEGOMe (**III-9**)

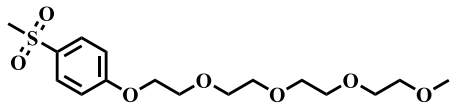

Tetraethyleneglycol monomethyl ether (5.00 g, 0.024 mol, 1.0 eq) was dissolved in 35 mL H_2O/THF (3:1). NaOH (4.99 g, 0.124 mol, 5.2 eq) was added and the solution cooled with an ice bath to 0 °C. A Solution of 4-toluenesulfonyl chloride (5.49 g, 0.029 mol, 1.2 eq) in 33 mL THF was added dropwise with stirring. The reaction solution was stirred for 3 h at room temperature. The solution was extracted with 5x100 mL diethyl ether, washed with 50 mL H_2O and dried over $MgSO_4$. The Solvent was removed under reduced pressure.

Yield: 8.50 g (0.23 mol, 97%); yellow oil.

MF: $C_{16}H_{26}O_7S$ MW 362.4370 g/mol [362.1399]

^{1}H NMR (300 MHz, DMSO-*d*6, 296 K): δ / ppm = 7.84 – 7.74 (m, 2H, C*H*^{Tos}), 7.52 – 7.42 (m, 2H, C*H*^{Tos}), 4.18 – 4.06 (m, 2H, TsO-C*H*$_2$), 3.62 – 3.54 (m, 2H, C*H*$_2$-OCH3), 3.53 – 3.40 (m, 12H, C*H*$_2^{EG}$), 3.23 (s, 3H, O-C*H*$_3$), 2.42 (s, 3H, C*H*$_3^{Tos}$).

N_3-TEGOMe (**III-10**)

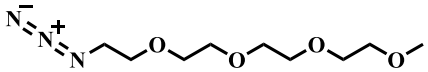

III-9 (7.70 g, 21.24 mmol, 1.0 eq.) was dissolved in 30 mL DMF and sodium azide (2.76 g, 42.49 mmol, 2.0 eq.) was added portion wise. The suspension was stirred at 60 °C for 24 hours. The mixture was diluted with water to solve the precipitate. The aqueous phase was extracted with 3x25 mL DCM. The combined organic layers were washed with brine and dried over $MgSO_4$. The Solvent was removed under reduced pressure.

Yield: 4.91 g (21.06 mmol, 99%); yellow oil.

MF: $C_9H_{19}N_3O_4$ MW 233.2680 g/mol [233.1376]

^{1}H NMR (400 MHz, DMSO-*d*6, 296 K): δ / ppm = 3.62 – 3.58 (m, 2H, N_3-C*H*$_2$), 3.57 – 3.47 (m, 10H, C*H*$_2^{EG}$), 3.45 – 3.38 (m, 4H, C*H*$_2^{EG}$), 3.23 (s, 3H, O-C*H*$_3$).

H_2N-TEGOMe (**III-11**)

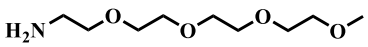

III-10 (4.91 g, 21 mmol, 1.0 eq.) was dissolved in 40 mL THF and 1 mL water. Triphenylphosphine (6.82 g, 26 mmol, 1.1 eq.) was added and the reaction solution was stirred for 3 h at room temperature. The solvent was removed under reduced pressure and the residue was dissolved in a

mixture of 100 mL toluene and 100 mL water. The organic layer was washed 3x70 mL water and dried over $MgSO_4$. The Solvent was removed under reduced pressure.

Yield: 3.86 g (18.63 mmol, 88%); yellow oil.

MF: $C_9H_{21}NO_4$ MW 207.2700 g/mol [207.1471]

HR-TOF-MS (ESI, pos. MeOH) m/z: 208.1549 $[M+H]^+$ calc.: 208.1544

^{1}H NMR (300 MHz, DMSO-d*6*, 296 K): δ / ppm = 3.58 – 3.45 (m, 12H, CH_2^{EG}), 3.44 – 3.40 (m, 2H, NH_2), 3.34 (t, *J* = 5.8 Hz, 2H, CH_2^{EG}), 3.24 (s, 3H, O-CH_3), 2.63 (t, *J* = 5.8 Hz, 2H, NH_2-CH_2).

Fmoc-L-Glu(CONH-TEGOMe)-tBu (**III-12**)

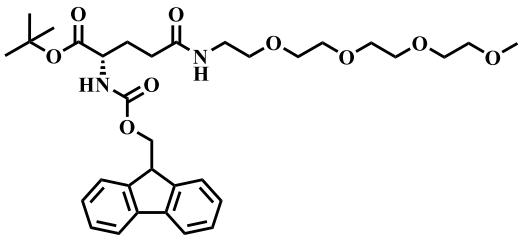

Fmoc-L-Glu-Boc (5,0 g 11.75 mmol 1.0 eq), HATU (5.81 mg, 15.28 mmol, 1.3 eq) and HOBt (793.9 mg, 5.88 mmol, 0.5 eq) was solved in 20 mL DMF. DPIEA (4 mL, 23.50 mmol 2.0 eq) was added and stirred for 30 min at room temperature. **III-11** (3.17 g, 15.28 mmol, 1.3 eq) was dissolved in 5 mL DCM and added. The reaction solution was stirred for 16 h at room temperature. At the next day 0.3 eq of each HATU, HOBt, DIPEA and **III-11** were added and stirred for 16 h at room temperature. The solvent was removed under reduced pressure. The crude product was purified *via* silica column chromatography (100% DCM → 10:1 DCM/MeOH).

Yield: 4.98 g (7.55 mmol, 49%); yellow oil.

MF: $C_{33}H_{46}N_2O_9$ MW 614.7360 g/mol [614.3203]

HR-TOF-MS (ESI, pos. MeOH) m/z: 537.2204 $[M+Na]^+$ calc.: 637.3101

^{1}H NMR (300 MHz, DMSO-*d*6, 296 K, COSY): δ / ppm = 7.88 (d, 2H, CH^{Fmoc}), 7.76 – 7.66 (m, 3H, CH^{Fmoc}, N*H*), 7.45 – 7.26 (m, 4H, CH^{Fmoc}), 4.38 – 4.16 (m, 3H, CH^{Fmoc}, CH_2^{Fmoc}), 3.99 – 3.88 (m, 1H, *α*-C*H*), 3.52 – 3.45 (m, 10H, CH_2^{EG}), 3.44 – 3.34 (m, 4H, CH_2^{EG}), 3.22 (s, 3H, O-CH_3), 3.18 – 3.07 (m, 2H, NH-CH_2), 2.21 (t, *J* = 7.6 Hz, 2H, *γ*-CH_2), 2.05 – 1.71 (m, 2H, *β*-CH_2), 1.39 (s, 9H, C$H_3^{t\text{-}Bu}$).

Fmoc-L-Glu(CONH-TEGOMe)-COOH (**III-13**)

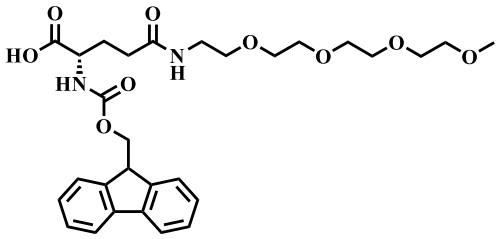

III-12 (7.33 g, 11.94 mmol, 1.00 eq) was dissolved in 20 mL of TFA/TIPS/H_2O (95:2.5:2.5) and stirred at room temperature for 3 h. Solvent was removed under reduced pressure and codestilled with 5x10 mL toluene. The residue was dissolved in 0.5 mL DCM and filtered. The solvent was removed under reduced pressure and the crude product was purified *via* silica column chromatography (DCM/MeOH 20:1).

Yield: 5.72 g (10.23 mmol, 86%); light yellow viscos liquid.

MF: $C_{29}H_{38}N_2O_9$ MW 558.6280 g/mol [558.2577]

HR-TOF-MS (ESI, neg. MeOH) m/z: 557.2498 $[M+H]^-$ calc.: 557.2504

^{1}H NMR (400 MHz, DMSO-*d*6, 296 K, COSY): δ / ppm = 12.60 (s, 1H, CO-O*H*), 7.80 (m, 2H, C*H*^{Fmoc}), 7.73 (d, *J* = 7.5 Hz, 2H, C*H*^{Fmoc}), 7.65 – 7.61 (m, 1H, N*H*), 7.42 (tt, *J* = 7.4, 1.2 Hz, 2H, C*H*^{Fmoc}), 7.33 (tt, *J* = 7.4, 1.1 Hz, 2H, C*H*^{Fmoc}), 4.31 – 4.16 (m, 3H, C*H*^{Fmoc}, CH_2^{Fmoc}), 3.98 – 3.90 (m, 1H, *α*-C*H*), 3.51 – 3.48 (m, 10H, CH_2^{EG}), 3.43 – 3.37 (m, 4H, CH_2^{EG}), 3.22 (s, 3H, O-CH_3), 3.19 (q, *J* = 5.8 Hz, 2H, NH-CH_2), 2.18 (t, *J* = 7.8 Hz, 2H, *γ*-CH_2), 2.04 – 1.76 (m, 2H, *β*-CH_2).

H-D-Met-L-Trp(Boc)-D-Met-L-Glu(-CONH-TEGOMe)-D-Met-L-Trp(Boc)-D-Met-L-Glu(-CONH-TEGOMe)-OH (**III-14**)

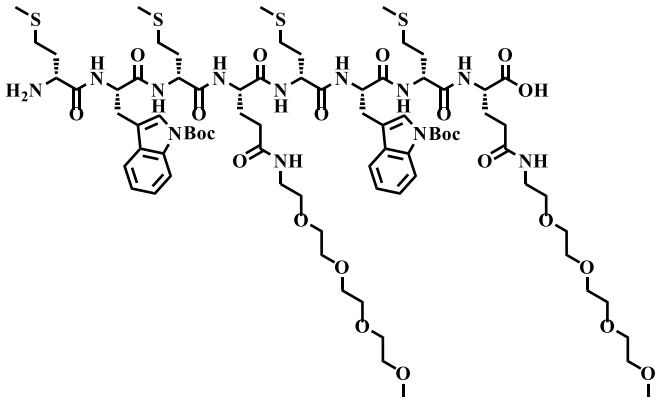

Compound **III-14** was synthesized following SOP 2, starting with 0.3 g of 2-chlorotrityl chloride resin (loading capacity: 1.0). The resin was preloaded according to SOP 1. After synthesis, the peptide was cleaved as outlined in SOP 5 and subsequently purified using RP-HPLC (Method E).

Yield: 0.214 g (0.21 mmol, 58%); colorless lyophilisate.

MF: $C_{80}H_{126}N_{12}O_{23}S_4$ MW 1752.1890 g/mol [1750.7942]

HR-TOF-MS (ESI, pos. MeOH) m/z: 1751.8014 $[M+H]^+$ calc.: 1751.8913

887.3962 $[M+H+Na]^{2+}$ calc.: 887.3958

^{1}H NMR (400 MHz, DMSO-*d*6, 296 K, COSY): δ / ppm = 8.78 (d, *J* = 7.9 Hz, 1H, α-N*H*), 8.58 (d, *J* = 8.4 Hz, 1H, α-N*H*), 8.38 – 8.32 (m, 2H, α-N*H*), 8.27 – 8.11 (m, 2H, α-N*H*), 8.01 (d, *J* = 8.2 Hz, 2H, NH_2), 7.93 – 7.85 (m, 3H, α-N*H*), 7.75 (d, *J* = 7.6 Hz, 2H, CH^{Trp}), 7.62 (d, *J* = 7.7 Hz, 2H, CH^{Trp}), 7.52 (s, 1H, CH^{Trp}), 7.44 (s, 1H, CH^{Trp}), 7.29 (t, *J* = 7.6 Hz, 2H, CH^{Trp}), 7.22 (t, *J* = 7.6 Hz, 2H, CH^{Trp}), 4.85 – 4.77 (m, 2H, *α*-CH^{Trp}), 4.47 – 4.39 (m, 2H, *α*-CH^{Glu}), 4.39 – 4.27 (m, 3H, *α*-CH^{Met}), 3.91 (t, *J* = 6.4 Hz,1H, *α*-C*H*-NH_2), 3.51 – 3.47 (m, 20H, CH_2^{EG}), 3.45 – 3.34 (m, 12H, CH_2^{EG}), 3.24 (s, 6H, O-CH_3), 3.16 (d, *J* = 5.9 Hz, 7H, γ-CH_2), 2.25 – 2.05 (m, 5H, γ-CH_2), 2.03 (s, 3H, S-CH_3), 1.95 (s, 3H, S-CH_3), 1.86 (s, 3H, S-CH_3), 1.85 (s, 3H, S-CH_3), 1.71 (d, *J* = 15.5 Hz, 12H, *β*-CH_2), 1.62 (d, *J* = 2.5 Hz, 18H, CH_3^{Boc}).

Cyclo[-(D-Met-L-Trp(Boc)-D-Met-L-Glu(CONH-TEGOMe))$_2$-] (**III-15**)

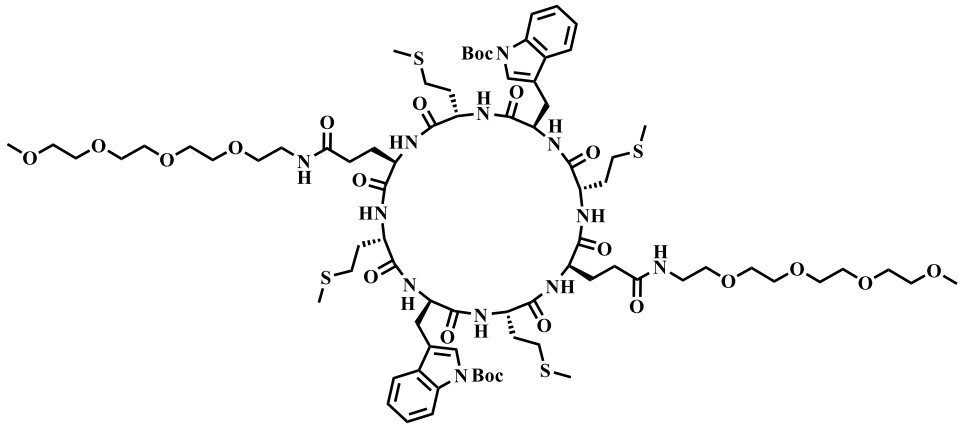

PyBOP (148.5 mg, 0.0285 mmol, 5.0 eq) and HOBt (38.6 mg, 0.285 mmol, 5.0 eq) were dissolved in 80 mL DMF and cooled with an ice bath to 0 °C. **III-14** (100.0 mg, 0.057 mmol, 1.0 eq) and DIPEA (97.1 µL, 0.571 mmol, 10.0 eq) were dissolved in 20 mL DMF and added dropwise with a fine-dose dropping funnel over 16 h with stirring. The reaction solution was stirred for 5 d under N_2-atmosphere. After two and four days PyBOP (1 eq.) and DIPEA (1 eq.) were added. The solvent was removed under reduced pressure. Due to the poor solubility of the product obtained, no further purification steps were undertaken. The crude product was converted directly to **CP3**.

Yield:83.1 mg crude product; colorless solid.

MF: $C_{80}H_{124}N_{12}O_{22}S_4$ MW 1734.1740 g/mol [1732.7836]

HR-TOF-MS (MALDI, CHCA, pos. DMF) m/z: 1755.2177 $[M+Na]^+$ calc.:1757.7414

Cyclo[-(D-Met-L-Trp-D-Met-L-Glu(CONH-TEGOMe))$_2$-] (**CP3**)

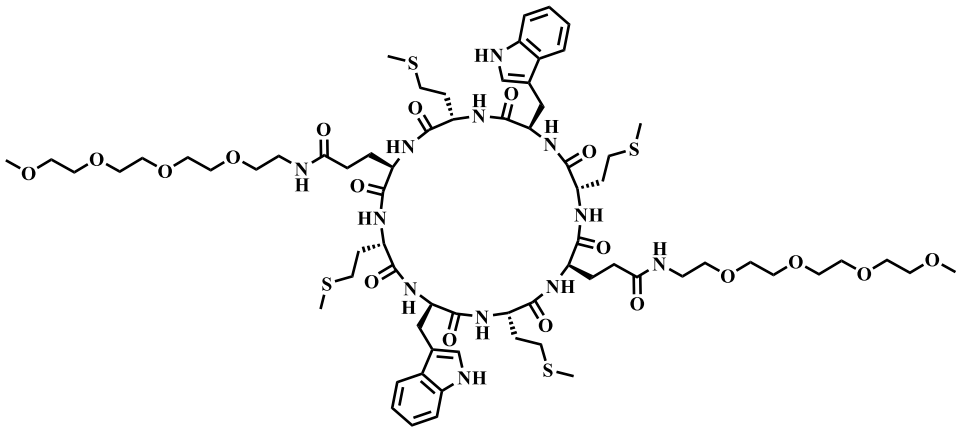

III-15 (70.0 mg, 0.04 mmol, 1.0 eq) was dissolved in 8 mL TFA/TIPS/H_2O/EDT (94:1:2.5:2.5) (reagent L) and stirred for 2 h at room temperature. Solvent was removed under reduced pressure and codestilled with 5x10 mL toluene. The residue was suspended in 13 mL H_2O and centrifuged. The residue was washed with 2x13 mL H_2O and lyophilized.

Yield: 29.14 mg (0.019 mmol, 34% over two steps); colorless lyophilisate.

MF: $C_{70}H_{108}N_{12}O_{18}S_4$ MW 1533.9400 g/mol [1532.6787]

HR-TOF-MS (MALDI, CHCA, pos. DMF) m/z: 1555.8294 $[M+Na]^+$ calc.: 1555,6685

1571.4421 $[M+K]^+$ calc.: 1571,6424

^{1}H NMR (400 MHz, DMSO-*d*6, 296 K, COSY): δ / ppm = 10.79 (s, 2H, N*H*^{Trp}), 8.44 (d, 4H, α-N*H*), 8.30 (d, *J* = 8.6 Hz, 1H, α-N*H*), 8.19 (d, *J* = 7.7 Hz, 2H, α-N*H*), 8.11 (d, *J* = 8.4 Hz, 1H, α-N*H*), 7.89 (d, *J* = 7.4 Hz, 2H, α-N*H*), 7.63 (d, *J* = 8.0 Hz, 2H, C*H*^{Trp}), 7.30 (d, *J* = 8.1 Hz, 2H, C*H*^{Trp}), 7.22 (q, *J* = 8.6 Hz, 1H), 7.08 – 7.00 (m, 2H, C*H*^{Trp}), 7.00 – 6.91 (m, 2H, C*H*^{Trp}), 6.56 (s, 2H, C*H*^{Trp}), 4.75 – 4.66 (m, 2H, *α*-C*H*), 4.43 – 4.34 (m, 1H, *α*-C*H*), 4.34 – 4.26 (m, 1H, *α*-C*H*), 3.67 – 3.57 (m, 10H, CH_2^{EG}), 3.53 – 3.47 (m, 22H, CH_2^{EG}), 3.24 (s, 6H, , O-CH_3), 3.21 – 3.09 (m, 6H, γ-CH_2), 2.94 – 2.82 (m, 2H, γ-CH_2), 2.39 – 2.19 (m, 2H, γ-CH_2), 2.16 – 2.01 (m, 6H, γ-CH_2), 1.98 (s, 6H, S-CH_3), 1.88 (s, 6H, S-CH_3), 1.87 – 1.79 (m, 10H, *β*-CH_2), 1.78 – 1.61 (m, 2H, *β*-CH_2).

Cyclo[-(D-Met(Ox)-L-Trp-D-Met(Ox)-L-Glu(CONH-TEGOMe))$_2$-] (**CP3^{ox}**)

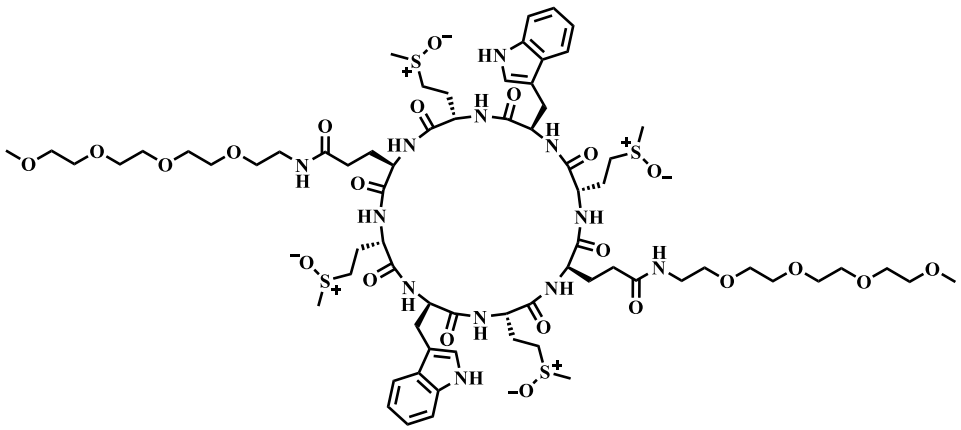

CP3 (5.0 mg, 3.0 µmol, 1.0 eq) was dissolved in 0.6 mL H2O2 and 0.01 mL AcOH for 3 h in an ice bath. Conversation was analyzed by LC-MS. Product was not isolated.

MF: $C_{70}H_{108}N_{12}O_{22}S_4$ MW 1597.9360 g/mol [1596.6584]

HR-TOF-MS (LC-ESI, pos., DMF): m/z: 799.6 $[M+H]^{2+}$ calc.: 799.9760

Boc-L-Ser-COOH (**IV-1**)

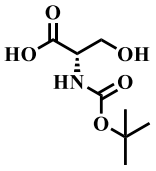

140 mL of semi-saturated $NaHCO_3$ solution were prepared and 2 spatula Na_2CO_3 were added while stirring to bring the solution to pH 9. L-serin (10.50 g, 0.10 mol, 1.0 eq) dissolved in 100 mL Dioxan/H_2O ((1:5 v/v) was added dropwise under stirring and ice-cooling. Di-*tert*-butyl dicarbonate (23.99 g, 0.110 mol, 1.1 eq) was added in one portion. Ice-cooling was removed, and the reaction was stirred at room temperature overnight. The solution is reduced to a third of its volume under reduced pressure. The remaining reaction solution was acidified to pH 2-3 with concentrated HCl (approx. 15 mL) and extracted with 6x50 mL ethyl acetate. Solvent was removed under reduced pressure.

Yield: 11.48 g (0.056 mol, 56%); colorless viscous oil.

MF: $C_8H_{15}NO_5$ MW 205.0950 g/mol [205.2100]

HR-TOF-MS (ESI, pos. MeOH) m/z: 228.0838 $[M+Na]^+$ calc.: 228.0842

244.0573 $[M+K]^+$ calc.: 244.0582

^{1}H NMR (400 MHz, C*D*Cl$_3$, 296 K): δ / ppm = 6.57 (s, CO-O*H*) 5.80 (d, *J* = 7.8 Hz, 1H, N*H*), 4.34 (d, *J* = 7.3 Hz, 1H, α-C*H*), 4.01 (dd, *J* = 11.4, 3.6 Hz, 1H, β-CH_2), 3.84 (dd, *J* = 11.5, 3.6 Hz, 1H, β-CH_2), 1.42 (s, 9H, CH_3^{Boc}).

Boc-L-Ser(Propargyl)-COOH (**IV-2**)

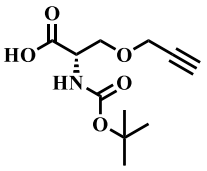

IV-1 (5.39 g, 0.056 mol, 1.0 eq) was dissolved in 160 mL dry DMF under N_2 atmosphere. Under ice-cooling sodium hydride (2.10 g, 0.111 mol, 2.0 eq) was added in portion. Once the addition was complete, the mixture was stirred for 40 min under nitrogen and ice-cooling. Propargyl bromide (2.77 mL, 0.062 mol, 1.1 eq) was added dropwise. The reaction solution was stirred under N_2 atmosphere and room temperature overnight. The reaction was quenched with 100 mL of H_2O and the solvent was removed under reduced pressure. Residue was taken off in 100 mL H_2O and extracted 5x50 mL ethyl acetate. The water phases were combined and adjusted to pH 3 with 50 mL of a 0.5 M $KHSO_4$ solution. The Solution was extracted with 3x100 mL DCM. The organic phases were combined, washed with 3x50 mL of a 0.5 M $KHSO_4$ solution and dried over $MgSO_4$. Solvent was removed under reduced pressure. Purification was performed via silica column chromatography (95:3:1 DCM/MeOH/ acetic acid).

Yield: 5.40 g (0.022 mol, 84%); brownish solid.

MF: $C_{11}H_{17}NO_5$ MW 243.1107 g/mol [243.2590]

HR-TOF-MS (ESI, neg. MeOH) m/z: 242.1040 $[M+H]^-$ calc.: 242.1034

^{1}H NMR (300 MHz, C*D*Cl$_3$, 296 K): δ / ppm = 6.75 (s, 1H, CO-O*H*), 5.38 (d, *J* = 8.5 Hz, 1H, N*H*), 4.52 – 4.43 (m, 1H, α-C*H*), 4.18 (dd, *J* = 2.4, 1.5 Hz, 2H, O-CH_2), 3.99 (dd, *J* = 9.5, 3.2 Hz, 1H, β-CH_2), 3.81 (dd, *J* = 9.4, 3.5 Hz, 1H, β-CH_2), 2.46 (t, *J* = 2.4 Hz, 1H, ≡C*H*), 1.45 (s, 9H, CH_3^{Boc}).

H_2N-L-Ser(Propargyl)-COOH (**IV-3**)

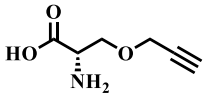

IV-2 (4.87 g, 0.02 mol, 1.0 eq) was dissolved in 10 mL ethyl acetate and 12 mL conc. HCl was slowly added under stirring. Reaction solution was stirred for 20 min at room temperature. Solvent was removed under reduced pressure. Residue was dissolved in 20 mL H_2O and washed with 3x30 mL and 3x30 mL DCM. Solvent was removed under reduced pressure.

Yield: 2.42 g (0.017 mol, 84%); brownish solid.

MF: $C_6H_9NO_3$ MW 143.1420 g/mol [143.0582]

HR-TOF-MS (ESI, pos. MeOH) m/z: 144.0654 $[M+H]^+$ calc.: 144.0655

^{1}H NMR (400 MHz, *D*$_2$O, 296 K): δ / ppm = 4.28 – 4.24 (m, 1H, α-C*H*), 4.17 (d, *J* = 2.4 Hz, 2H, O-CH_2), 4.02 (dd, *J* = 11.0, 4.5 Hz, 1H, β-CH_2), 3.89 (dd, *J* = 11.0, 3.2 Hz, 1H, β-CH_2), 2.82 (t, *J* = 2.4 Hz, 1H, ≡C*H*).

Fmoc-L-Ser(Propargyl)-COOH (**IV-4**)

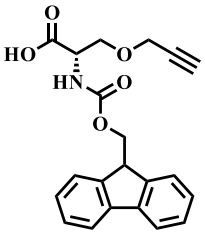

IV-3 (2.42 g, 0.017 mol, 1.0 eq) was dissolved in 85 mL dioxane/H_2O (2:1). Na_2CO_3 (1.85 g, 0.022 mol, 1.3 eq) was added under stirring at room temperature. Fmoc-OSu (7.41 g, 0.022 mol, 1.3 eq) was dissolved in 30 mL dioxane and added dropwise. Reaction solution was stirred at room temperature overnight. On the next day 0.5 eq Fmoc-OSu in 10 mL dioxane was added and stirred at room temperature overnight, again. The solution was adjusted to pH 2 with 1 N HCl and extracted with 150 mL ethyl acetate. The organic phase was washed with 150 mL 1 N HCl, 20 mL H_2O and 200 mL brine. The organic phase was dired over $MgSO_4$ and the solvent was removed under reduced pressure. The residue was suspended in 20 mL DCM and the product was collected by filtration.

Yield: 5.10 g (0.014 mol, 83%); colorless solid.

MF: $C_{21}H_{19}NO_5$ MW 365.3850 g/mol [365.1263]

HR-TOF-MS (ESI, pos. MeOH) m/z: 366.1330 $[M+H]^+$ calc.: 366.1336
388.1155 $[M+Na]^+$ calc.: 388.1155

^{1}H NMR (400 MHz, DMSO-*d*6, 296 K): δ / ppm = 12.85 (s, 1H, CO-O*H*), 7.89 (d, *J* = 7.4 Hz, 2H, C*H*^{Fmoc}), 7.75 (d, *J* = 7.5 Hz, 2H, C*H*^{Fmoc}), 7.70 (d, *J* = 8.2 Hz, 1H, N*H*), 7.42 (tt, *J* = 7.5, 1.2 Hz, 2H, C*H*^{Fmoc}), 7.33 (tt, *J* = 7.4, 1.3 Hz, 2H, C*H*^{Fmoc}), 4.30 – 4.20 (m, 4H, C*H*^{Fmoc}, C*H*$_2^{Fmoc}$, α-C*H*), 4.17 (d, *J* = 2.4 Hz, 2H, O-C*H*$_2$), 3.72 (d, *J* = 5.5 Hz, 2H, β-C*H*$_2$), 3.47 (t, *J* = 2.4 Hz, 1H, ≡C*H*).

H-L-Ser(propargyl)-D-His(Trt)-L-Trp(Boc)-D-His(Trt)-L-Trp(Boc)-D-His(Trt)-L-Trp(Boc)-D-His(Trt)-OH (**IV-5**)

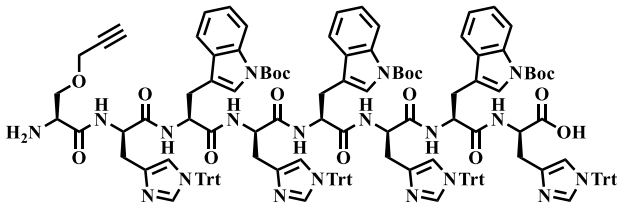

Compound **IV-5** was synthesized following SOP 3, starting with 0.13 g of 2-chlorotrityl chloride resin (loading capacity: 1.5). The resin was preloaded according to SOP 1. After synthesis, the peptide was cleaved as outlined in SOP 5 and subsequently purified using RP-HPLC (Method E).

Yield: 0.189 g (0.075 mmol, 38%); colorless lyophilizate.

MF: $C_{154}H_{147}N_{19}O_{16}$ MW 2519.9870 g/mol [1260.5725]

HR-TOF-MS (ESI, pos. MeOH) m/z: 1260.5718 $[M+2H]^{2+}$ calc.: 1283,6003

^{1}H NMR (600 MHz, C*D*Cl$_2$, 296 K, COSY): δ / ppm 8.22 – 7.78 (m, 7H, α-N*H*), 7.53 – 6.96 (m, 83H, C*H*$^{Trp, His, Trt}$), 6.80 (d, *J* = 7.7 Hz, 2H, α-N*H*$_2$), 4.94 – 4.38 (m, 8H, *α*-C*H*), 3.98 – 2.85 (m, 18H, β-C*H*$_2$, , O-C*H*$_2$-C ≡CH), 2.19 (s, 1H, ≡C*H*), 1.61 (s, 27H, C*H*$_3^{Boc}$).

Cyclo-[L-Ser(propargyl)-D-His(Trt)-L-Trp(Boc)-D-His(Trt)-L-Trp(Boc)-D-His(Trt)-L-Trp(Boc)-D-His(Trt)] (**IV-6**)

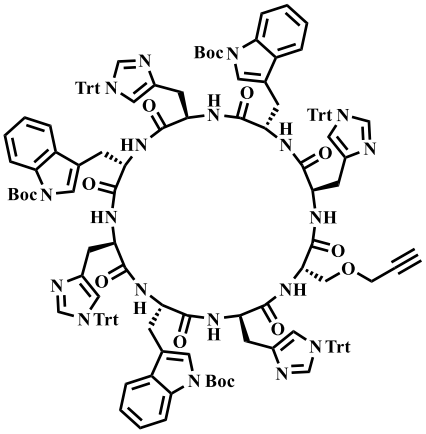

IV-5 (62.5 mg, 0.025 mmol, 1.0 eq) was dissolved in 60 mL DMF. DIPEA (8.4 µL, 0.05 mmol, 2.0 eq) was added. PyBOP (64.6 mg, 0.124 mmol, 5.0 eq) and HOBt (16.8 mg, 0.124 mmol, 5.0 eq) were dissolved in 5 mL DMF and added. The reaction solution was stirred for 8 d at room temperature. Everyday PyBOP (2.5 eq.) and DIPEA (0.5 eq.) to adjust the pH to 8-9. Solvent was removed under reduced pressure. Due to the poor solubility of the product obtained, no further purification steps were undertaken. The crude product was converted directly to **CP4**.

Yield: 53.3 mg crude product; colorless solid.

MF: $C_{154}H_{145}N_{19}O_{15}$ MW 2501.9720 g/mol [2500.1168]

Cyclo-[L-Ser(propargyl)-D-His-L-Trp-D-His-L-Trp-D-His-L-Trp-D-His] (**CP4**)

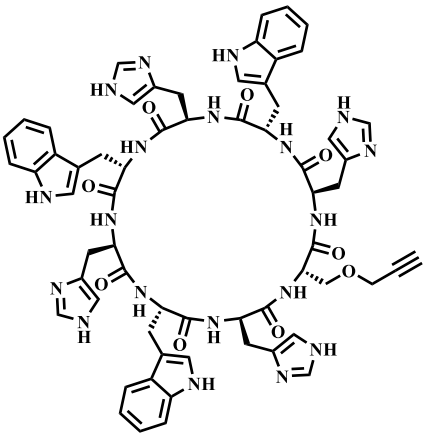

IV-6 (53.3 mg, 0.021 mmol, 1.0 eq) was dissolved in 8 mL TFA/TIPS/H_2O (95:2.5:2.5) and stirred for 1.5 h at room temperature. Solvent was removed under reduced pressure and codestilled with 3x30 mL toluene. Crude product was purified *via* RP-HPLC (Method E).

Yield: 5.5 mg (4.46 µmol, 21% over two steps); colorless lyophilizate.

MF: $C_{63}H_{65}N_{19}O_9$ MW 1232.3370 g/mol [1231.5213]

HR-TOF-MS (ESI, pos. MeOH) m/z: 1254.5115 $[M+Na]^+$ calc.: 1254.5111

^{1}H NMR (400 MHz, DMSO-d_6, 296 K, COSY): δ / ppm = 10.90 – 10.64 (m, 3H, N*H*^{Trp}), 8.98 – 8.81 (m, 4H, N*H*^{His}), 8.67 (d, *J* = 8.7 Hz, 1H, α-N*H*), 8.56 (d, *J* = 8.7 Hz, 1H, α-N*H*), 8.52 (d, *J* = 8.6 Hz, 1H, α-N*H*), 8.44 (d, *J* = 8.8 Hz, 1H, α-N*H*), 8.37 – 8.14 (m, 5H, α-N*H*), 7.69 (d, *J* = 7.8 Hz, 1H, C*H*$^{Trp, His}$), 7.64 (d, *J* = 7.9 Hz, 1H, C*H*$^{Trp, His}$), 7.61 – 7.51 (m, 1H, C*H*$^{Trp, His}$), 7.47 (d, *J* = 7.9 Hz, 0H, C*H*$^{Trp, His}$), 7.38 – 7.19 (m, 4H, C*H*$^{Trp, His}$), 7.14 – 6.88 (m, 11H, C*H*$^{Trp, His}$), 6.88 – 6.83 (m, 1H, C*H*$^{Trp, His}$), 6.78 (d, *J* = 8.2 Hz, 1H, C*H*$^{Trp, His}$), 4.90 – 4.42 (m, 8H, *α*-C*H*), 3.97 (t, *J* = 2.4 Hz, 1H, ≡C*H*), 3.39 (d, *J* = 4.6, 2.3 Hz, 2H, O-C*H*$_2$-C ≡CH), 3.28 (d, *J* = 5.8 Hz, 2H, β-C*H*$_2^{Ser}$), 3.14 – 2.56 (m, 12H, β-C*H*$_2$), 2.46 – 2.29 (m, 2H, β-C*H*$_2$).

(Cyclo-[L-Ser(propargyl)-D-His-L-Trp-D-His-L-Trp-D-His-L-Trp-D-His])$_2$-PEG3000 (**CP4$_2$-PEG3000**)

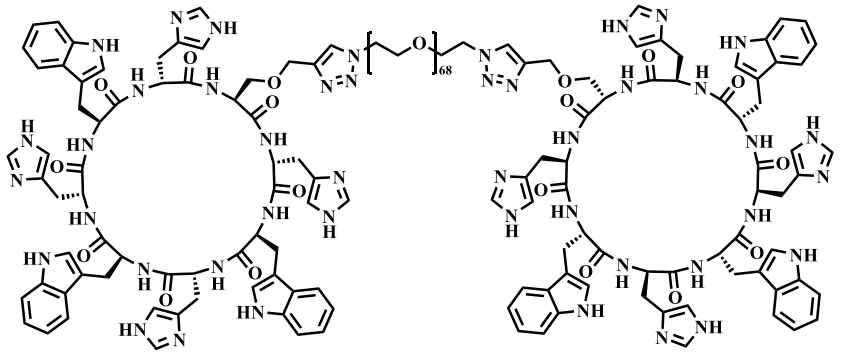

Solvents were degassed by the freeze-pump-throw method. PEG3000 diazude (2.64 mg, 0.5 µmol, 1.0 eq.), **CP4** (8.36 mg, 2 µmol, 4 eq.), $CuSO_4 \cdot 5\ H_2O$ (0.42 mg, 1.00 µmol, 2.0 eq.), and TBTA (1.80 mg, 2.00 µmol, 4 eq.) were dissolved in 782 µL of solvent and degassed by a stream of N_2. Na-ascorbate (0.67 mg, 2.00 µmol, 4.0 eq.) was added in the N_2 countercurrent and stirred for several days at rt or 50 °C under N_2 atmosphere. Every day 0.5 eq. CP4, $CuSO_4 \cdot 5\ H_2O$, TBTA and Na-ascorbate were added daily. The exact reaction conditions are given in the following table. Product was not isolated.

Table 7.7: *Reaction conditions for Synthesis of* ***CP5$_2$-PEG3000****.*

Synthesis	Reaction time	Solvent	Temperature
1	7 d	DMSO, H_2O	rt
2	6 d	DMSO,H_2O	50 °C
3	5 d	DMF/TFE (1:1); H_2O	rt
4	6 d	DMF/TFE (1:1); H_2O	50 °C

MF: $C_{63}H_{65}N_{19}O_9$-$(OCH_2CH_2)_n$- $C_{63}H_{65}N_{19}O_9$ ((n ≈ 68 for PEG3000)

MW 5500.27 g/mol (Theoretical average molecular weight: ~3000 Da.) [5496.81]

HR-TOF-MS (MALDI, CHCA+KTFA, pos. DMF) m/z: 5550.01 $[M+K]^+$ (most abundant mass, PEG-polydisperse distribution) calc.: 5535.77

H-D-His(Trt)-L-Lys(Boc)-D-His(Trt)-L-Trp(Boc)-D-His(Trt)-L-Lys(pentynoyl)-D-His(Trt)-L-Trp(Boc)-OH (**IV-7**)

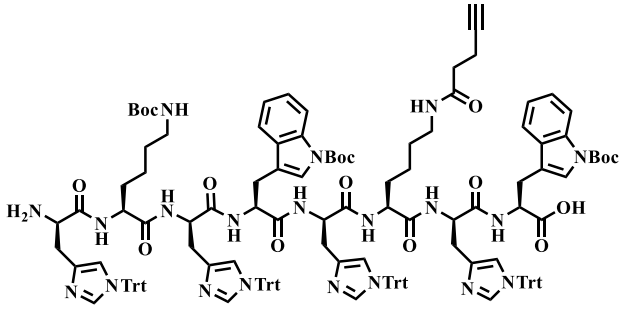

Compound **IV-7** was synthesized following SOP 4, starting with 0.2 g of Fmoc-Trp(Boc) Tentagel® R TRT resin (loading capacity: 0.17). After synthesis, the peptide was cleaved as outlined in SOP 5 and subsequently purified using RP-HPLC (Method E).

Yield: 240 mg (0.094 mmol, 59%); colorless lyophilizate.

MF: $C_{154}H_{158}N_{20}O_{16}$ MW 2545.0820 g/mol [2543.2165]

HR-TOF-MS (ESI, pos. MeOH) m/z: 1273.1180 $[M+2H]^{2+}$ calc.: 1273.1180

^{1}H NMR (300 MHz, DMSO-*d*6, 296 K, COSY): δ / ppm = 8.63 – 8.28 (m, 4H, α -N*H*), 7.96 (d, *J* = 8.0 Hz, 1H, α-N*H*), 7.78 (t, *J* = 7.2, 1H, O=C-N*H*^{Lys}), 7.56 (d, *J* = 7.6 Hz, 1H, α-N*H*), 7.49 (d, *J* = 7.7 Hz, 1H, α-N*H*), 7.39 – 7.11 (m, 56H, C*H*$^{Trp,\ His,\ Trt}$), 7.12 – 6.90 (m, 27H, C*H*$^{Trp,\ His,\ Trt}$), 6.68 (s, 1H, N*H*-Boc^{Lys}), 6.59 (d, *J* = 8.8 Hz, 2H, α-N*H*$_2$), 4.71 – 4.42 (m, 6H, *α*-C*H*), 4.35 – 4.15 (m, 2H, *α*-C*H*), 4.14 – 4.03 (m, 1H, *α*-C*H*$^{Trp\text{-}NH2}$), 2.89 (s, 1H), 2.87 – 2.74 (m, 10H, β-C*H*$_2$), 2.74 – 2.71 (m, 4H, C*H*$_2$-NH^{Lys}), 2.69 (t, *J* = 2.5 Hz, 1H, ≡C*H*), 2.66 – 2.55 (m, 4H, β-C*H*$_2$), 2.34 – 2.14 (m, 2H, β-C*H*$_2$), 1.49 (s, 18H, C*H*$_3^{Trp\text{-}Boc}$), 1.30 (s, 9H, C*H*$_3^{Lys\text{-}Boc}$), 1.65 – 0.94 (m, 8H, C*H*$_2^{Lys}$).

Cyclo-[D-His(Trt)-L-Lys(Boc)-D-His(Trt)-L-Trp(Boc)-D-His(Trt)-L-Lys(pentynoyl)-D-His(Trt)-L-Trp(Boc)] (**IV-8**)

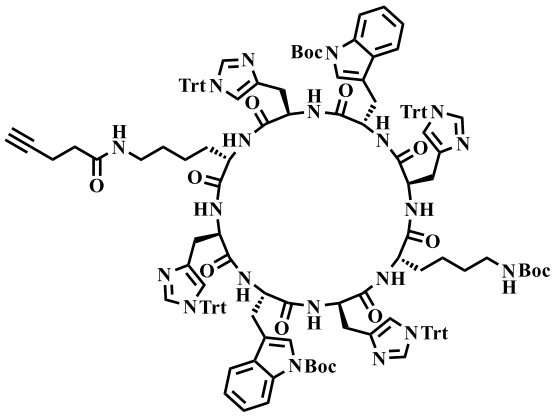

IV-7 (50.0 mg, 0.020 mmol, 1.0 eq) and DMTMM BF_4 (**IV-12**, 8.4 mg, 0.026 mmol, 1.3 eq) were dissolved in 50 mL DMF and stirred overnight at room temperature. Solvent was removed under reduced pressure. Due to the poor solubility of the product obtained, no further purification steps were undertaken. The crude product was converted directly to **CP5**.

Yield: 49.0 mg crude product; colorless solid.

MF: $C_{154}H_{156}N_{20}O_{15}$ MW 2527.0670 g/mol [2525.2059]

HR-TOF-MS (ESI, pos. MeOH) m/z: 1264.1118 $[M+2H]^{2+}$ calc.: 1264.5413

Cyclo-[D-His-L-Lys-D-His-L-Trp-D-His-L-Lys(pentynoyl)-D-His-L-Trp] (**CP5**)

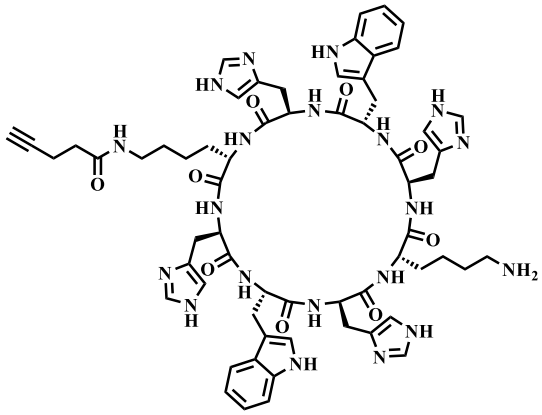

IV-8 (30.0 mg, 0.012 mmol, 1.0 eq) was dissolved in 2 mL TFA/TIPS/H_2O (95:2.5:2.5) and stirred for 2 h at room temperature. Solvent was removed under reduced pressure and the residue was deprotect with 4 mL DM for 1 h at room temperature, again. Solvent was removed under reduced pressure and codestilled with 5x10 mL toluene. Crude product was purified *via* RP-HPLC (Method E).

Yield: 23.89 mg (0.019 mmol, 74% over two steps); colorless lyophilizate.

MF: $C_{63}H_{76}N_{20}O_9$ MW 1257.4320 g/mol [1256.6104]

HR-TOF-MS (ESI, pos. MeOH) m/z: 1279.6060 $[M+Na]^+$ calc.: 1279.5998

^{1}H NMR (300 MHz, DMSO-*d*6, 296 K, COSY): δ / ppm = 10.69 (s, 2H, N*H*^{Trp}), 8.96 – 8.59 (m, 6H, α-N*H*, N*H*^{His}), 8.32 – 8.17 (m, 3H, α-N*H*), 8.16 – 8.07 (m, 2H, α-N*H*), 7.94 – 7.85 (m, 2H, α-N*H*, O=C-N*H*^{Lys}), 7.63 (d, *J* = 7.5 Hz, 2H, N*H*$_2^{Lys}$), 7.39 – 6.75 (m, 18H, C*H*$^{Trp, His}$), 4.87 – 4.61 (m, 6H, *α*-C*H*), 4.40 – 4.19 (m, 2H, *α*-C*H*), 4.07 – 3.74 (m, 6H, C*H*$_2$-NH^{Lys}, O-CH$_2$-C*H*$_2$-C ≡CH), 2.99 – 2.85 (m, 2H, O-C*H*$_2$-CH$_2$-C ≡CH), 2.75 (t, *J* = 2.5 Hz, 1H, ≡C*H*), 2.38 – 2.17 (m, 4H, β-C*H*$_2$), 1.53 – 1.08 (m, 12H, β-C*H*$_2$), 1.03 – 0.66 (m, 8H, C*H*$_2^{Lys}$).

H-D-His(Trt)-L-Met-D-Lys(Boc)-L-Met-D-His(Trt)-L-Met-D-Lys(Boc)-L-Met-OH (**IV-9**)

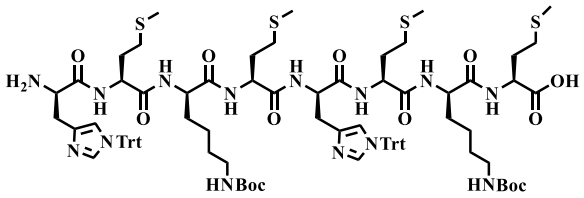

Compound **IV-9** was synthesized following SOP 2, starting with 1.29 g of 2-chlorotrityl chloride resin (loading capacity: 0.8). The resin was preloaded according to SOP 1. After synthesis, the peptide was cleaved as outlined in SOP 5 and subsequently purified using RP-HPLC (Method E).

Yield:1.22 g (0.776 mmol, 72%); colorless lyophilizate.

MF: $C_{29}H_{120}N_{14}O_{13}$ MW 1758.2978 g/mol [1756.8042]

HR-TOF-MS (ESI, pos. MeOH) m/z: 1757.7398$[M+H]^+$ calc.: 1757.8120

^{1}H NMR (300 MHz, DMSO-*d*6, 296 K, COSY): δ / ppm = 8.73 – 8.57 (m, 1H, α-N*H*), 8.27 – 8.18 (m, 3H, α-N*H*), 8.01 – 7.96 (m, 3H, α-N*H*), 7.75 –7.11 (m, 34H, C*H*$^{His,\ Trt}$), 6.71 (t, *J* = 5.7 Hz, 2H, N*H*-Boc^{Lys}), 4.85 – 4.83 (m, 1H, *α*-C*H*), 4.45 – 4.29 (m, 7H, *α*-C*H*), 3.21 – 2.80 (m, 8H, C*H*$_2$-NH^{Lys}, β-C*H*$_2^{His}$), 2.27 – 2.08 (m, 8H, β-C*H*$_2^{Met}$), 2.02 – 1.69 (m, 18H, S-C*H*$_3$, γ-C*H*$_2^{Met}$), 1.64 – 1.13 (m, 26H, C*H*$_3^{Lys\text{-}Boc}$ C*H*$_2^{Lys}$).

Cyclo-[D-His(Trt)-L-Met-D-Lys(Boc)-L-Met-D-His(Trt)-L-Met-D-Lys(Boc)-L-Met] (**IV-10**)

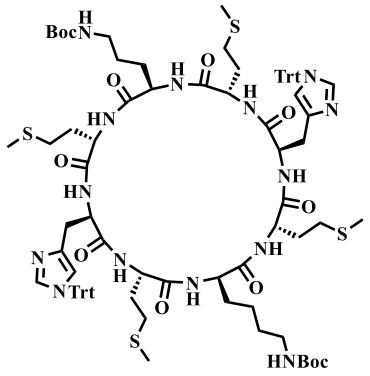

IV-9 (10.0 mg, 6.3 µmol, 1.0 eq), was dissolved in 10 mL DMF. Coupling reagents were added and stirred at room temperature for 1 d. Solvent was removed under reduced pressure. residue was taken up in a small amount of DCM, precipitated in cold ether and centrifuged. The participate was analyzed using analytical RP-HPLC (Method C).

Table 7.8: *Reaction conditions for Synthesis of* ***IV-10****.*

Synthesis		M [g/mol]	m [mg]	n [mmol]	V [mL]	eq
A	DEPBT	299.22	3.77	0.0126		2
	HOPO	111.10	1.40	0.0126		2
	DIPEA	129.25		0.0252	0.0043	4
B	PyBOP	520.39	6.56	0.0126		2
	HOBt	135.13	1.70	0.0126		2
	DIPEA	129.25		0.0252	0.0043	4
C	EDC*HCl	191.70	2.42	0.0126		2
	HOAt	136.11	1.68	0.0126		2
	DIPEA			0.0252	0.0043	4
D	DMTMM BF_4	328.13	2.70	0.0082		1,3
E	HBTU	379.24	4.78	0.0126		2
	HOBt	125.13	1.58	0.0126		2
	DIPEA	129.25		0.0252	0.0043	4
F	DPPA	275.2	3.47	0.0126		2
	HOAt	136.11	1.68	0.0126		2
	DIPEA			0.0252	0.0043	4

MF: $C_{91}H_{116}N_{14}O_{12}S_4$ MW 1726.2550 g/mol [1724.7780]

DMTMM·Cl (**IV-11**)

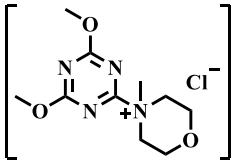

2-Chloro-4,6-dimethoxy-1,3,5-triazine (5.00 g, 0.028 mol, 1.0 eq) was suspended in 75 mL water. *N*-methylmorpholine (3.44 mL, 0.031 mol, 1.0 eq) was added in one portion and stirred for 45 min at room temperature until the solid had dissolved to a colorless solution. The raw material in solution was converted without isolation.

MF: $C_{10}H_{17}N_4O_3$ Cl MW 276.7210 g/mol [276.0989]

DMTMM·BF_4 (**IV-12**)

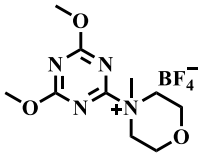

To the solution of **IV-11** in water sodium tetrafluoroborate (3.44 mL, 0.034 mol, 1.2 eq) dissolved in 37 mL water was added dropwise over 10 min with stirring at room temperature. Crystallization begun immediately. After complete addition the suspension was stirred for a further 50 min at room

temperature. Solid was collected by vacuum filtration and washed with 3x20 mL water and 30 mL methanol.

Yield: 3.96 g (0.012 mol, 42%); colorless solid.

MF: $C_{10}H_{17}N_4O_3\,BF_4$ MW 328.0746 g/mol [328.1330]

HR-TOF-MS (ESI, pos. MeOH) m/z: 242.1322 $[M+NH_4]^+$ calc.: 241.1295

^{1}H NMR (400 MHz, MeCN-*d*$_3$, 296 K): δ / ppm = 4.50 – 4.40 (m, 2H, CH_2), 4.12 (s, 6H, CH_3), 4.05 – 3.91 (m, 2H, CH_2), 3.80 – 3.68 (m, 4H, CH_2), 3.40 (s, 3H, CH_3).

(Cyclo-[D-His-L-Lys-D-His-L-Trp-D-His-L-Lys(pentynoyl)-D-His-L-Trp])$_2$-PEG2000 (**CL2000**)

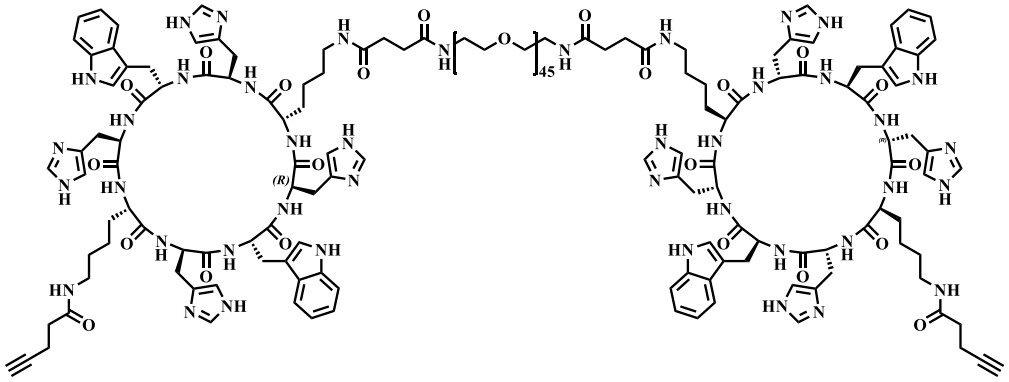

CP5 (15.1 mg, 0.012 mmol, 3.0 eq) and PEG2000(NHCO-C_2H_4-CONHS)$_2$ (10.0 mg, 0.004 mmol, 1.0 eq) were dissolved in 5 mL dry DMF. NMM (5 µL, 0.072 mmol, 6.0 eq) was added and stirred at room temperature over 3 d under N_2-athmosphere. Everyday 0.5 eq. **CP5** and NMM were added to adjust the pH to 8. Solvent was removed under reduced pressure. Crude product was purified *via* RP-HPLC (Method E).

Yield: 10.8 g (0.002 mol, 50%); colorless solid.

MF: $C_{63}H_{76}N_{20}O_9$-$(OCH_2CH_2)_n$-$C_{63}H_{76}N_{20}O_9$ (n ≈ 45 for PEG2000)

MW 4729.08 g/mol (Theoretical average molecular weight: ~2000 Da.) [4726.09]

HR-TOF-MS (MALDI, DHB+KTFA, pos. DMF) m/z: 4744.74 $[M+Na]^+$ (most abundant mass, PEG-polydisperse distribution) calc.: 4748.99

^{1}H NMR (400 MHz, DMSO-*d*6, 296 K, COSY): δ / ppm = 10.72 (s, 2H, NH^{Trp}), 9.06 – 8.87 (m, 10H, α-N*H*, NH^{His}), 8.72 – 8.62 (m, 2H, α-N*H*), 8.30 – 8.21 (m, 4H, α-N*H*), 8.20 – 8.08 (m, 2H, α-N*H*), 8.02 – 7.78 (m, 8H, α-N*H,* NH^{PEG}), 7.67 – 7.49 (m, 4H, NH^{Lys}), 7.41 – 6.88 (m, 36H, C$H^{Trp,\,His}$), 4.91 – 4.52 (m, 12H, *α*-C*H*), 4.29 (s, 4H, *α*-C*H*), 3.51 (s, 180H, CH_2^{PEG}), 3.22 – 2.70 (m, 24H, C$H_2^{Lys,\,NHS}$), 2.67 (t, *J* = 2.5 Hz, 2H, ≡C*H*) 2.38 – 2.14 (m, 18H, β-CH_2), 1.33 – 1.06 (m, 14H, β-CH_2), 0.91 – 0.68 (m, 16H, CH_2^{Lys}).

(Cyclo-[D-His-L-Lys-D-His-L-Trp-D-His-L-Lys(pentynoyl)-D-His-L-Trp])$_2$-PEG3000 (**CL3000**)

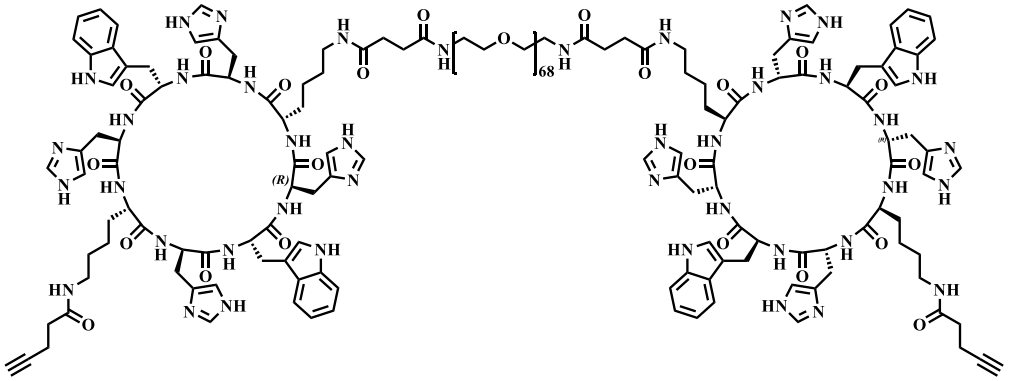

CP5 (10.9 mg, 0.009 mmol, 3.0 eq) and PEG3000(NHCO-C_2H_4-CONHS)$_2$ (10.0 mg, 0.003 mmol, 1.0 eq) were dissolved in 5 mL dry DMF. NMM (5 µL, 0.052 mmol, 6.0 eq) was added and stirred at room temperature over 5 d under N_2-athmosphere. Everyday 0.5 eq. **CP5** and NMM were added to adjust the pH to 8. Solvent was removed under reduced pressure. Crude product was purified *via* RP-HPLC (Method E).

Yield: 5.8 g (0.001 mmol, 33%); colorless solid.

MF: $C_{63}H_{76}N_{20}O_9$-$(OCH_2CH_2)_n$-$C_{63}H_{76}N_{20}O_9$ (n ≈ 68 for PEG3000)

MW 5726.05 g/mol (Theoretical average molecular weight: ~3000 Da.) [5723.67]

HR-TOF-MS (MALDI, DHB+KTFA, pos. DMF) m/z: 5767.54 $[M+K]^+$ (most abundant mass, PEG-polydisperse distribution) calc.: 5765.03

^{1}H NMR (400 MHz, DMSO-*d*6, 296 K, COSY): δ / ppm = 10.70 (s, 2H, N*H*^{Trp}), 9.09 – 8.58 (m, 6H, α-N*H*, N*H*^{His}), 8.32 – 8.02 (m, 2H, α-N*H*), 7.97 – 7.75 (m, 4H, α-N*H*, N*H*^{PEG},), 7.69 – 7.40 (m, 0H, α-N*H*, N*H*^{Lys}), 7.41 – 6.85 (m, 36H, C*H*$^{Trp,\ His}$), 4.96 – 4.42 (m, 12H, *α*-C*H*), 4.41 – 4.01 (m, 4H, *α*-C*H*), 3.84 (d, *J* = 1.8 Hz, 4H, C*H*$_2$-C≡CH), 3.51 (s, 272H, C*H*$_2^{PEG}$), 3.12 – 2.71 (m, 24H, C*H*$_2^{Lys,\ NHS}$), 2.68 (t, *J* = 2.7 Hz, 2H, ≡C*H*), 2.38 – 2.21 (m, 12H, β-C*H*$_2$), 1.39 – 0.94 (m, 20H, β-C*H*$_2$), 0.98 – 0.45 (m, 16H, C*H*$_2^{Lys}$).

(Cyclo-[D-His-L-Lys-D-His-L-Trp-D-His-L-Lys(pentynoyl)-D-His-L-Trp])$_2$-PEG6000 (**CL6000**)

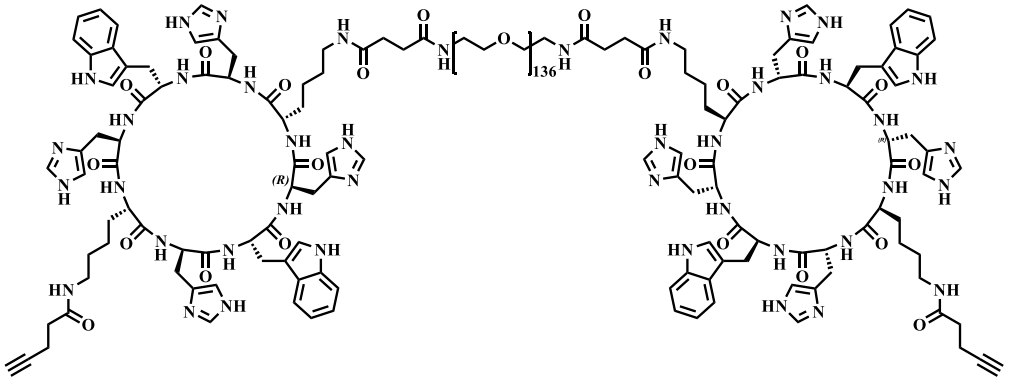

CP5 (5.9 mg, 0.005 mmol, 3.0 eq) and PEG6000(NHCO-C_2H_4-CONHS)$_2$ (10.0 mg, 0.002 mmol, 1.0 eq) were dissolved in 5 mL dry DMF. NMM (5 µL, 0.028 mmol, 6.0 eq) was added and stirred at room temperature over 3 d under N_2-athmosphere. Everyday 0.5 eq. **CP5** and NMM were added to adjust the pH to 8. Solvent was removed under reduced pressure. Crude product was purified *via* RP-HPLC (Method E).

Yield: 8.4 g (0.001 mmol, 25%); colorless solid.

MF: $C_{63}H_{76}N_{20}O_9$-$(OCH_2CH_2)_n$-$C_{63}H_{76}N_{20}O_9$ (n ≈ 136 for PEG6000)

MW 8726.07 g/mol (Theoretical average molecular weight: ~6000 Da.) [8723.67]

HR-TOF-MS (MALDI, DHB+KTFA, pos., DMF) m/z: 8772.08 $[M+K]^+$ (most abundant mass, PEG-polydisperse distribution) calc.: 8765.03

^{1}H NMR (400 MHz, DMSO-*d*6, 296 K, COSY): δ / ppm = 10.69 (s, 4H, N*H*^{Trp}), 9.00 – 8.85 (m, 7H, α-N*H*, N*H*^{His}), 8.36 – 8.05 (m, 4H, α-N*H*), 7.96 – 7.76 (m, 5H, α-N*H*, N*H*^{PEG}), 7.69 – 7.61 (m, 1H, α-N*H*), 7.37 – 7.19 (m, 4H, N*H*^{Lys}), 7.13 – 6.81 (m, 36H, C*H*$^{Trp, His}$), 4.93 – 4.53 (m, 12H, *α*-C*H*), 4.40 – 4.20 (m, 4H, *α*-C*H*), 3.51 (s, 544H, CH_2^{PEG}), 3.42 – 3.29 (m, 5H, C$H_2^{Lys, NHS}$), 3.25 – 3.12 (m, 5H), 3.05 – 2.72 (m, 32H), 2.38 – 2.12 (m, 19H, β-CH_2), 1.37 – 1.03 (m, 13H, β-CH_2), 0.99 – 0.67 (m, 26H, CH_2^{Lys}).

6-Heptionic acid-L-Phe-L-His(Trt)-L-Phe-L-His(Trt)-L-Phe-Ahx-Gly-OH (**V-1**)

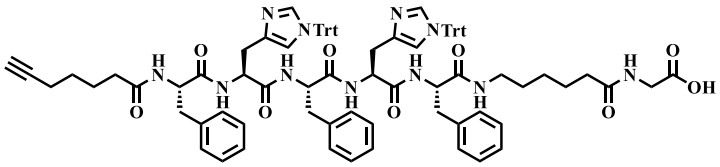

Compound **V-1** was synthesized following SOP 2, starting with 1.00 g of 2-chlorotrityl chloride resin (loading capacity: 1.6). The resin was preloaded according to SOP 1. After synthesis, the peptide was cleaved as outlined in SOP 5.

Yield: 1.78 g (1.60 mmol, 74%); colorless lyophilizate.

MF: $C_{92}H_{93}N_{11}O_9$ MW 1496.8240 g/mol [1495.716]

HR-TOF-MS (ESI, pos. MeOH) m/z: 1497.7292 $[M+H]^+$ calc.:1496.7278

749.3667$[M+2H]^{2+}$ calc.:748.8678

^{1}H NMR (400 MHz, DMSO-*d*6, 296 K, COSY): δ / ppm = 8.52 (d, *J* = 7.5 Hz, 1H, α-N*H*), 8.17 (d, *J* = 7.4 Hz, 1H, α-N*H*), 8.14 – 8.04 (m, 3H, α-N*H*), 8.00 – 7.93 (m, 2H, α-N*H*), 7.90 (d, *J* = 8.2 Hz, 1H, α-N*H*), 7.41 – 6.99 (m, 47H*,* C*H*$^{Phe, His, Trt}$*),* 6.69 (s, 1H, C*H*^{His}), 6.58 (s, 1H, C*H*^{His}), 4.54 – 4.32 (m, 5H, *α*-C*H*), 3.72 (d, *J* = 5.8 Hz, 2H, *α*-C*H*^{Gly}), 3.06 – 2.59 (m, 16H, *β*-CH_2, CH_2-CO-NH, CO-NH-CH_2), 2.70 (t, *J* = 2.6 Hz, 1H, ≡C*H*), 2.14 – 1.78 (m, 6H, CH_2^{Ahx}, CH_2^{Alkin}), 1.52 – 1.01 (m, 6H, CH_2^{Ahx}, CH_2^{Alkin}).

6-Heptionic acid-L-Phe-L-His(Trt)-L-Phe-L-His(Trt)-L-Phe-Ahx-Gly-ethyldiamine-Fmoc (**V-2**)

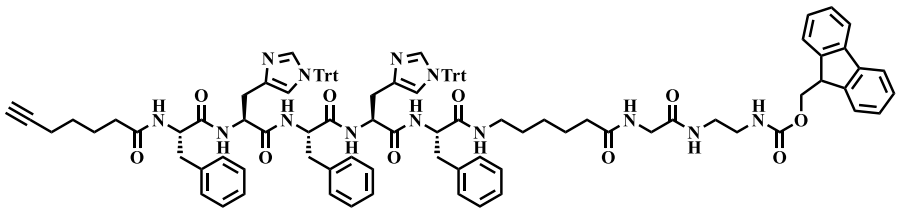

V-1 (250.00 mg; 0.17 mmol; 1.0 eq), Fmoc-ethylenediamine hydrochloride (106.50 mg; 0.33 mmol; 2.0 eq)) and PyBOP (347.70 mg; 0.67 mmol; 4.0 eq.) was dissolved in 20.0 mL DMF. DIPEA (0.74 ml; 1.34 mmol; 8.0 eq.) was added, and the reaction solution was stirred for three days at room temperature. DMF was removed under reduced pressure. Purification was performed by size exclusion (Sephadex; MeOH).

Yield: 173.44 mg (0.010 mmol, 60%); colorless lyophilizate.

MF: $C_{108}H_{107}N_{13}O_{10}$ MW 1747.1250 g/mol [1745.8264]

HR-TOF-MS (ESI, pos. MeOH) m/z: 874.193$[M+2H]^{2+}$ calc.:873.921

6-Heptionic acid-L-Phe-L-His(Trt)-L-Phe-L-His(Trt)-L-Phe-Ahx-Gly-ethyldiamine (**V-3**)

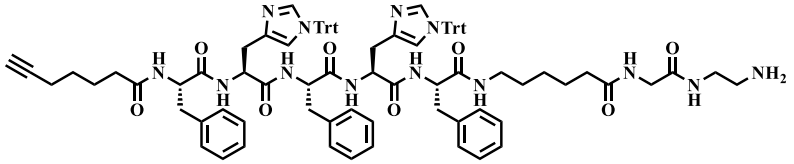

V-2 (150.00 mg; 0.086 mmol) was dissolved in 20 mL piperidine 20 % (v/v) in DCM and stirred for 30 h at room temperature. The solvent was removed under reduce pressure. Purification was performed by size exclusion (Sephadex; MeOH) and lyophilized.

Yield: 0.103 g (0.067 mmol, 75%); colorless lyophilizate.

MF: $C_{94}H_{99}N_{13}O_{8}$. MW 1538.90 g/mol [1537.7740]

HR-TOF-MS (ESI, pos. MeOH) m/z: 1539.7843 $[M+H]^{+}$ calc.: 1539.7818

770.3959 $[M+2H]^{2+}$ calc.: 770.4048

^{1}H NMR (400 MHz, DMSO-*d*6) δ / ppm = 8.50 (d, *J* = 7.1 Hz, 1H, α-N*H*), 8.17 (d, *J* = 7.5 Hz, 1H, α-N*H*), 8.06 (m, 3H, α-N*H*), 7.96 (d, *J* = 7.8 Hz, 2H, α-N*H*), 7.88 (d, *J* = 7.8 Hz, 1H α-N*H*), 7.83 (s, 2H, NH_2), 7.41 – 6.97 (m, 47H, C$H^{Phe,\ His,\ Trt}$), 6.70 (s, 1H, CH^{His}), 6.57 (s, 1H, CH^{His}), 4.41 (m, (m, 5H, *α*-C*H*), 3.67 (d, *J* = 5.7 Hz, 3H, *α*-CH^{Gly}), 3.06 – 2.59 (m, 20H, *β*-CH_2, CH_2-CO-NH, NH-CH_2), 2.70 (t, *J* = 2.6 Hz, 1H, ≡C*H*), 2.13 – 1.88 (m, 4H, CH_2^{Ahx}, CH_2^{Alkin}), 1.45 – 1.06 (m, 8H, CH_2^{Ahx}, CH_2^{Alkin}).

6-Heptionic acid-L-Phe-L-His(Trt)-L-Phe-L-His(Trt)-L-Phe-Ahx-Gly-ethyldiamine PG5(Boc) (**V-4(PG5)**)

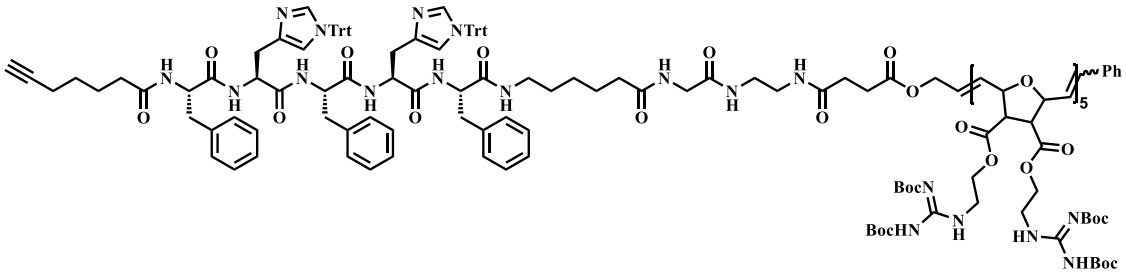

V-3 (30.00 mg, 0.019 mmol, 1.2 eq), polyguanidine(Boc) (**PG5**) (61.9 mg, 0.018 mmol, 1.0 eq) and PyBOP (12.2 mg, 0.023 mmol, 1.2 eq) was dissolved in 1.0 mL DCM. DIPEA (0.02 mL, 0.117 mmol, 6.0 eq) was added, and the reaction solution was stirred overnight under N_2-atmosphere. On the next day PyBOP (1 eq.) and DIPEA (1 eq.) were added and stirred under N_2-atmosphere overnight. The reaction solution was participated in 15 mL of cold diethyl ether. The participate was discarded. Diethyl ether was removed under reduced pressure. Purification was performed by size exclusion (Sephadex; MeOH) and lyophilized.

Yield: 44.8 mg (0.008 mmol, 42%); colorless lyophilizate.

MF $C_{277}H_{381}N_{43}O_{76}$. MW 5529.32 g/mol [5525.7270]

^{1}H NMR (400 MHz, DMSO-*d*6, 296 K) δ / ppm = 8.49 (d, *J* = 7.2 Hz, 1H, α-N*H*), 8.42 – 8.35 (m, 20H, α-N*H*), 8.16 (d, *J* = 7.3 Hz, 1H, α-N*H*), 8.06 (d, *J* = 7.1 Hz, 1H, α-N*H*), 7.96 (d, *J* = 7.2 Hz, 1H, α-N*H*), 7.94 – 7.82 (m, 2H, α-N*H*), 7.43 – 6.94 (m, 52H, C*H*$^{Phe, His, Trt}$), 6.68 (s, 1H, C*H*^{His}), 6.56 (s, 1H, C*H*^{His}), 5.81 (s, 5H, =C*H*^{dG5}), 5.58 (s, 5H, =C*H*^{dG5}), 4.98 (s, 5H, =C*H*^{dG5}), 4.66 (d, *J* = 49.3 Hz, 5H, =C*H*^{dG5}), 4.51 – 4.33 (m, 5H, *α*-C*H*), 4.11 (s, 20H, O-C*H*$_2$-^{dG5}), 3.63 (d, *J* = 5.6 Hz, 2H, *α*-C*H*$_2^{Gly}$), 3.52 (s, 20H, O-CH$_2$-C*H*$_2$-^{dG5}), 2.69 (t, *J* = 2.6 Hz, 1H, ≡C*H*), 3.08 (s, 1H,), 3.00 – 2.58 (m, 10 H, β-C*H*$_2$, C*H*$_2$-CO-NH, NH-C*H*$_2$), 2.34 (t, *J* = 6.5 Hz, 2H, C*H*$_2^{Alkin}$), 2.07 (m, 2H, C*H*$_2^{Ahx}$), 2.03 – 1.85 (m, 2H, C*H*$_2^{Alkin}$), 1.44 (s, 90H, C*H*$_3^{Boc}$), 1.36 (s, 90H, C*H*$_3^{Boc}$), 1.26 – 1.14 (m, 6H, C*H*$_2^{Ahx}$, C*H*$_2^{Alkin}$).

6-Heptionic acid-L-Phe-L-His(Trt)-L-Phe-L-His(Trt)-L-Phe-Ahx-Gly-ethyldiamine PG9(Boc) (**V-4(PG9)**)

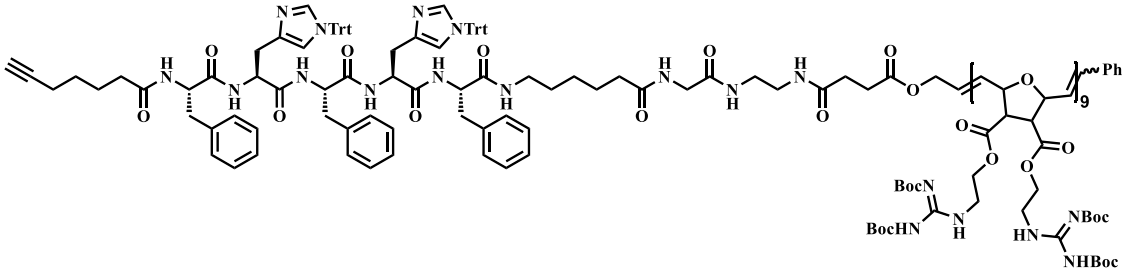

V-3 (12.00 mg, 0.009 mmol, 1.2 eq.), polyguanidine(Boc) (**PG9**) (42.00 mg, 0.008 mmol, 1.0 eq.), PyBOP (4.90 mg, 0.009 mmol, 1.2 eq.) was dissolved in 1.0 mL DCM. 0.01 mL DIPEA was added, and the reaction solution was stirred overnight under N_2-atmosphere. On the next day PyBOP (1 eq.) and DIPEA (1 eq.) were added and stirred under N_2-atmosphere overnight. The reaction solution was participated in 15 mL of cold diethyl ether. The participate was discarded. Diethyl ether was removed under reduced pressure. Purification was performed by size exclusion (Sephadex; MeOH).

Yield: 17.0 g (0.002 mmol, 26%); colorless lyophilizate.

MF: $C_{323}H_{453}N_{67}O_{92}$. MW 6746.55 g/mol [6742.2828]

^{1}H NMR (400 MHz, DMSO-*d*6, 296 K) δ / ppm = 8.78 – 8.28 (m, 30H, α-N*H*), 8.01 (d, *J* = 7.7 Hz, 2H, α-N*H*), 7.96 (d, *J* = 6.1 Hz, 2H, α-N*H*), 7.87 (d, *J* = 11.6 Hz, 3H, α-N*H*), 7.43 – 6.93 (m, 52H, C*H*$^{Phe,\ His,\ Trt}$), 6.67 (s, 2H, C*H*^{His}), 6.57 (s, 2H, C*H*^{His}) , 5.81 (s, 9H, =C*H*^{dG5}), 5.56 (s, 9H, =C*H*^{dG5}), 4.98 (s, 9H, =C*H*^{dG5}), 4.59 (s, 5H, =C*H*^{dG5}), 4.32 – 3.92 (m, 5H, *α*-C*H)*, 3.63 (d, *J* = 5.5 Hz, 2H, *α*-C*H*$_2^{Gly}$), 3.52 (s, 36H O-CH$_2$-C*H*$_2$-^{dG5}), 3.03 – 2.57 (m, 10H, β-C*H*$_2$), 2.38 – 2.29 (m, 4H, C*H*$_2^{Alkin}$), 2.18 – 1.85 (m, 4H, C*H*$_2^{Ahx}$), 1.43 (s, 162H, C*H*$_3^{Boc}$), 1.36 (s, 162H, C*H*$_3^{Boc}$), 1.28 – 1.02 (m, 6H, C*H*$_2^{Ahx}$, C*H*$_2^{Alkin}$).

6-Heptionic acid-L-Phe-L-His-L-Phe-L-His-L-Phe-Ahx-Gly-ethyldiamine PG9 (**V-5(PG5)**)

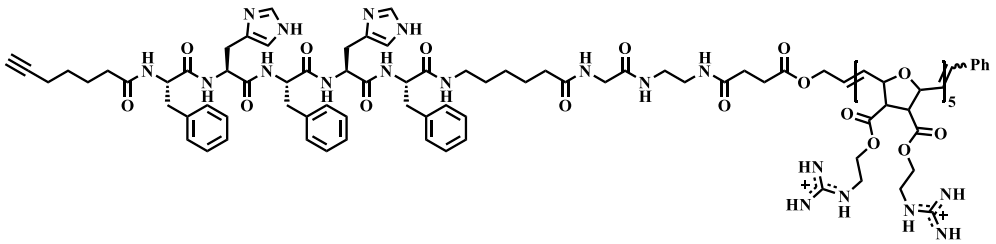

V-4(PG5) (12.0 mg, 0.002 mmol, 1.0 eq.) was dissolved in 1 mL TFA/TIPS/H_2O (95:2.5:2.5) and stirred at room temperature overnight. The product was participated in cold diethyl ether.

Yield:4.9 mg (0.0015 mmol, 73%); colorless lyophilizate.

MF: $C_{144}H_{213}N_{43}O_{36}^{10+}$. MW 3122.55 g/mol [3120.6104]

^{1}H NMR (400 MHz, DMSO-*d*6, 296 K) δ / ppm = 8.96 (d, *J* = 9.1 Hz, 2H, α-N*H*), 8.53 – 8.46 (m, 1H, α-N*H*), 8.32 (d, *J* = 8.1 Hz, 1H, α-N*H*), 8.24 – 7.70 (m, 24H, α-N*H*), 7.59 – 7.06 (m, 22H, C*H*$^{Phe,\ His}$), 6.35 (d, *J* = 6.8 Hz, 1H, C*H*^{His}), 6.31 (d, *J* = 6.8 Hz, 1H, C*H*^{His}), 5.87 (s, 5H, =C*H*^{dG5}), 5.62 (s, 5H, =C*H*^{dG5}), 4.97 (s, 5H, =C*H*^{dG5}), 4.71 – 4.50 (m, 5H, =C*H*^{dG5}), 4.48 – 4.33 (m, 5H, *α*-C*H*), 4.08 (s, 20H, O-C*H*$_2$-^{dG5}), 3.75 (s, 2H, *α*-C*H*$_2^{Gly}$), 3.43 (s, 20H, O-CH$_2$-C*H*$_2$-^{dG5}), 3.26 – 2.59 (m, 11H, β-C*H*$_2$, C*H*$_2$-CO-NH, NH-C*H*$_2$, ≡C*H*), 2.41 – 1.30 (m, 10H, C*H*$_2^{Ahx}$, C*H*$_2^{Alkin}$), 1.02 – 0.63 (m, 2H, C*H*$_2^{Ahx}$, C*H*$_2^{Alkin}$).

6-heptionic acid-L-Phe-L-His-L-Phe-L-His-L-Phe-Ahx-Gly-ethyldiamine PG9 (**V-5(PG9)**)

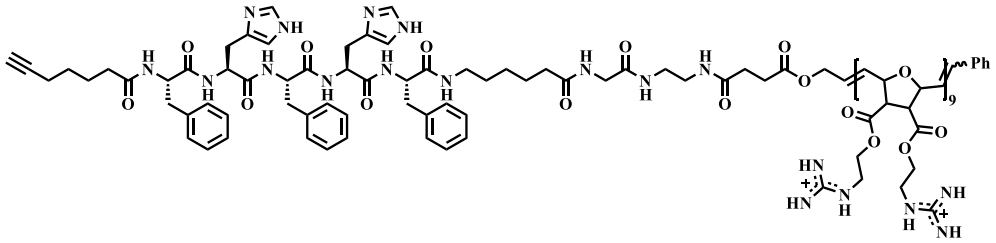

V-4(PG9) (17.0 mg, 0.002 mmol, 1.0 eq.) was dissolved in 1 mL TFA/TIPS/H_2O (95:2.5:2.5) and stirred at room temperature overnight. The product was participated in cold diethyl ether.

Yield: 7.36 g (0.016 mmol, 81%); colorless lyophilizate.

MF: $C_{204}H_{317}N_{67}O_{56}^{18+}$. MW 4604.18 g/mol [4601.3918]

^{1}H NMR (400 MHz, DMSO-*d*6, 296 K) δ / ppm = 9.08 – 8.35 (m, 10H, α-N*H*, N*H*), 8.13 – 7.77 (m, 21H, α-N*H*, N*H*), 7.57 – 7.02 (m, 72H, C*H*$^{Phe,\ His}$, N*H*), 6.65 (d, *J* = 14.3 Hz, 1H, C*H*^{His}), 6.33 (d, 1H, C*H*^{His}), 5.82 (s, 9H, =C*H*^{dG5}), 5.58 (s, 9H=C*H*^{dG}), 4.96 (s, 9H, =C*H*^{dG}), 4.57 (s, 9H, =C*H*^{dG5}), 4.48 – 4.35 (m, 5H, *α*-C*H*), 4.05 (s, 36H, O-CH_2-CH_2-^{dG5}), 3.53(m, 2H, *α*-CH_2^{Gly}), 3.04 – 2.58 (m, 11H, β-CH_2, CH_2-CO-NH, NH-CH_2, ≡C*H*), , 1.73 – 1.04 (m, 12H, CH_2^{Ahx}, CH_2^{Alkin}).

Ac-L-Phe-L-His(Trt)-L-Phe-L-His(Trt)-L-Phe-Ahx-Gly (**V-6**)

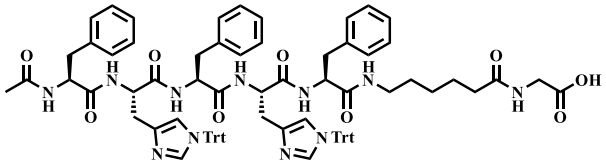

Compound **V-6** was synthesized following SOP 2, starting with 1.00 g of 2-chlorotrityl chloride resin (loading capacity: 1.6) and a capping step after the final Fmoc deprotection. The resin was preloaded according to SOP 1. After synthesis, the peptide was cleaved as outlined in SOP 5.

Yield: 1.15 g (0.8 mmol, 82%); colorless lyophilizate.

MF: $C_{87}H_{87}N_{11}O_9$. MW 1430.72 g/mol [1429.6680]

^{1}H NMR (400 MHz, DMSO-*d*$_6$, 296 K) δ / ppm = 8.48 (d, *J* = 7.5 Hz, 1H, α-N*H*), 8.19 (d, *J* = 7.5 Hz, 1H, α-N*H*), 8.12 – 7.99 (m, 3H, α-N*H*), 7.99 – 7.93 (m, 1H, α-N*H*), 7.89 (d, *J* = 8.1 Hz, 1H, α-N*H*), 7.43 – 6.94 (m, 47H, C*H*$^{Phe,\ His,\ Trt}$), 6.67 (s, 1H, C*H*^{His}), 6.57 (s, 1H, C*H*^{His}), 4.45 – 4.30 (m, 5H, α-C*H*), 3.70 (d, *J* = 5.8 Hz, 2H, CH_2^{Gly}), 3.08 – 2.56 (m, 12H, β-CH_2^{His}, CH_2^{Phe}, CH_2^{Ahx}), 2.05 (t, *J* = 7.5 Hz, 2H, CH_2^{Ahx}), 1.66 (s, 3H, CH_3), 1.42 – 1.31 (m, 2H, CH_2^{Ahx}), 1.24 – 1.16 (m, 2H, CH_2^{Ahx}), 1.18 – 1.04 (m, 2H, CH_2^{Ahx}).

(Ac-L-Phe-L-His(Trt)-L-Phe-L-His(Trt)-L-Phe-Ahx-Gly)$_2$PEG3000 (**V-7**)

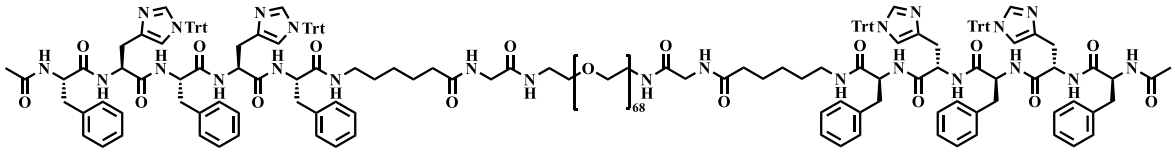

V-6 (286.14 mg; 0.20 mmol; 3.0 eq), H_2N-PEG(3000)-NH_2 (200.00 mg; 0.07 mmol; 1.0 eq), PyBOP (111.02 mg; 0.21 mmol; 3.2 eq), HOBt (28.83 mg; 0,21 mmol; 3.2 eq) and DIPEA (37.16 mL; 0,21 mmol; 3.2 eq) was solved in DMF (5.0 mL) and stirred at room temperature for 3 days. Solvent was removed under reduced pressure. Purification was performed by size exclusion (Biobeads; DMF).

Yield: 0.536 g (0.09 mmol, 46%); colorless lyophilizate.

MF: $C_{87}H_{87}N_{11}O_9$-$(OCH_2CH_2)_n$- $C_{87}H_{87}N_{11}O_9$ (n ≈ 68 for PEG3000)

MW 5837.06 g/mol (Theoretical average molecular weight: ~3000 Da.) [5833.1417]

HR-TOF-MS (MALDI, Dit+KTFA, pos., DMF) m/z: 5879.57 $[M+K]^+$ (most abundant mass, PEG-polydisperse distribution) calc.: 5872.10

^{1}H NMR (400 MHz, DMSO-*d*6, 296 K) δ / ppm 8.46 (d, *J* = 7.5 Hz, 2H, α-N*H*), 8.18 (d, *J* = 7.5 Hz, 2H, α-N*H*), 8.08 – 7.81 (m, 12H, α-N*H*), 7.42 – 6.92 (m, 94H, C*H*$^{Phe, His, Trt}$), 6.67 (s, 1H, C*H*^{His}), 6.57 (s, 1H, C*H*^{His}), 4.45 – 4.30 (m, 10H, α-C*H*), 3.67 – 3.62 (m, 4H, CH_2^{Gly}), 3.50 (s(br), 264H, PEG-CH_2), 3.20 (td, *J* = 5.8 Hz, 4H, PEGCH$_2$-CH_2-NH), 3.08 – 2.57 (m, 24H, β-CH_2), 2.06 (t, *J* = 7.6 Hz, 4H, CH_2^{Ahx}), 1.67 (s, 6H, NHCO-CH_3), 1.50 – 1.32 (m, 6H, CH_2^{Ahx}), 1.25 (t, *J* = 7.5 Hz, 4H, CH_2^{Ahx}), 1.14 – 1.05 (m, 4H, CH_2^{Ahx}).

(Ac-L-Phe-L-His-L-Phe-L-His-L-Phe-Ahx-Gly)$_2$PEG3000 (**V-8**)

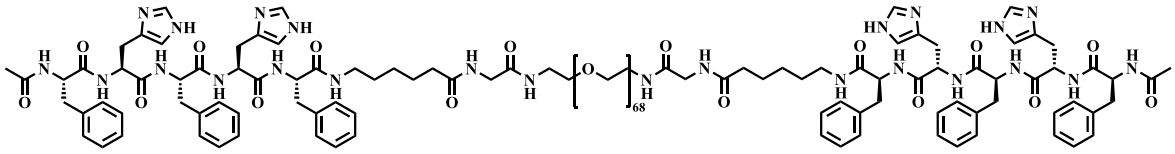

V-7 (300.00 mg; 0.051 mmol; 1.0 eq) was dissolved in 2.0 mL TFA/TIPS/H_2O (95:2.5:2.5) and stirred for 45 min at room temperature. Solvent was removed under reduced pressure and co-distilled with toluene (3x5.0 mL). Crude product was participated in 20 mL of cold diethyl ether and the residue was suspended in water and subjected to lyophilization.

Yield: 182.80 mg (0.035 mmol, 70%); colorless lyophilizate.

MF: $C_{49}H_{59}N_{11}O_9$-$(OCH_2CH_2)_n$- $C_{49}H_{59}N_{11}O_9$ (n ≈ 68 for PEG3000).

MW 5091.48 g/mol (Theoretical average molecular weight: ~3000 Da.) [5088.7035]

HR-TOF-MS (MALDI, Dit+KTFA, pos., DMF) m/z: 5088.09 $[M+H]^+$ (most abundant mass, PEG-polydisperse distribution) calc.: 5089.71

^{1}H NMR (400 MHz, DMSO-*d*6, 296 K) δ / ppm = 8.68 (d, *J* = 7.8 Hz, 4H), 8.45 (d, *J* = 7.9 Hz, 2H, α-N*H*), 8.30 (d, *J* = 8.0 Hz, 2H, α-N*H*), 8.20 – 8.12 (m, 4H, α-N*H*, N*H*^{Ahx}), 8.06 (d, *J* = 7.5 Hz, 2H, α-N*H*), 7.99 (t, *J* = 6.0 Hz, 2H, N*H*^{Gly}), 7.89 (t, *J* = 5.6 Hz, 2H, PEG-N*H*), 7.29 – 7.12 (m, 34H, C*H*$^{Phe, His}$), 4.63 – 4.37 (m, 10H, α-C*H*), 3.68 – 3.64 (m, 4H, C*H*$_2^{Gly}$), 3.51 (s(br), 264H, PEG-C*H*$_2$), 3.43 – 3.37 (m, 4H,PEG-C*H*$_2$CH$_2$NH), 3.25 – 3.18 (m, 4H, PEGCH$_2$-C*H*$_2$-NH), 3.13 – 2.61 (m, 24H, β-C*H*$_2$), 2.11 (t, *J* = 7.5 Hz, 4H, C*H*$_2^{Ahx}$), 1.76 (s, 6H, NHCO-C*H*$_3$), 1.46 (t, *J* = 7.5 Hz, 4H, C*H*$_2^{Ahx}$), 1.40 – 1.13 (m, 8H, C*H*$_2^{Ahx}$).

8. References

[1] J. Clayden, N. Greeves, S. G. Warren, *Organic chemistry*, Oxford University Press, Oxford, New York, **2012**.

[2] L. Stryer, J. Berg, J. Tymoczko, G. Gotto, *Biochemie,* Springer Spektrum, Germany, Berlin **2018**.

[3] L. Paulig, R. B. Corey, H. R. Branson, *J. Mater. Sci. Chem. Eng.* **1951**, *37*, 205.

[4] R. B. Merrifield in *The Chemistry of Polypeptides*. *Essays*, Springer US, Boston, **1973**, pp. 335–361.

[5] W. C. Chan, *Fmoc solid phase peptide synthesis*. *A practical approach*, Oxford University Press, New York, **2004**.

[6] P. Lloyd-Williams, F. Albericio, E. Giralt, *Chemical approaches to the synthesis of peptides and proteins*, CRC Press, Boca Raton, **2020**.

[7] S. B. Kent, *Annu. Rev. Biochem.* **1988**, *57*, 957.

[8] G. B. Fields, R. L. Noble, *Int. J. Pept. Protein Res.* **1990**, *35*, 161.

[9] G. A. Grant, *Synthetic Peptides A User´s Guide* UWBC biotechnical resource series, Vol. 2, W.H. Freeman and Company, New York, **1992**.

[10] O. F. Luna, J. Gomez, C. Cárdenas, F. Albericio, S. H. Marshall, F. Guzmán, *Molecules* **2016**, *21*.

[11] N. Zinieris, L. Leondiadis, N. Ferderigos, *J. Comb. Chem.* **2005**, *7*, 4.

[12] J. D. Wade, J. Bedford, R. C. Sheppard, G. W. Tregear, *Pept. Res.* **1991**, *4*, 194.

[13] S. A. Kates, N. A. Solé, M. Beyermann, G. Barany, F. Albericio, *Pept. Res.* **1996**, *9*, 106.

[14] D. A. Pearson, M. Blanchette, M. L. Baker, C. A. Guindon, *Tetrahedron Lett.* **1989**, *30*, 2739.

[15] S. L. Pedersen, K. J. Jensen, *Methods Mol Biol.* **2013**, *1047*, 43.

[16] K. Barlos, D. Gatos, J. Kallitsis, G. Papaphotiu, P. Sotiriu, Y. Wenqing, W. Schäfer, *Tetrahedron Lett.* **1989**, *30*, 3943.

[17] K. B. O. Chatzi, D. Gatos, G. Stavropoulos, *Int. J. Pept. Protein Res.* **1991**, *37*, 513.

[18] J. Bedford, C. Hyde, T. Johnson, W. Jun, D. Owen, M. Quibell, R. C. Sheppard, *Int. J. Pept. Protein Res.* **1992**, *40*, 300.

[19] R. Behrendt, P. White, J. Offer, *J. Pept. Sci.* **2016**, *22*, 4.

[20] D. Krois, *Organisch-chemische Methoden*, Springer Berlin Heidelberg, Berlin, Heidelberg, **2017**.

[21] S. Duengo, M. I. Muhajir, A. T. Hidayat, W. J. A. Musa, R. Maharani, *Molecules* **2023**, *28*, 8017.

[22] Y. Han, F. Albericio, G. Barany, *J. Org. Chem.* **1997**, *62*, 4307.

[23] H. Huang, D. L. Rabenstein, *J. Pept. Sci.* **1999**, *53*, 548.

[24] E. I. Vrettos, N. Sayyad, E. M. Mavrogiannaki, E. Stylos, A. D. Kostagianni, S. Papas, T. Mavromoustakos, V. Theodorou, A. G. Tzakos, *RSC Adv* **2017**, *7*, 50519.

[25] C. A. Montalbetti, V. Falque, *Tetrahedron* **2005**, *61*, 10827.

[26] J. C. Sheehan, G. P. Hess, *J. Am. Chem. Soc.* **1955**, *77*, 1067.

[27] D. Krois, *Organisch-chemische Methoden* in *Biochemie, Biologischer Chemie, Molekularbiologie und Medizinischer Chemie*, Springer Berlin Heidelberg, Berlin, Heidelberg, **2017**.

[28] F. Albericio, L. A. Carpino, *Methods in Enzymology : Solid-Phase Peptide Synthesis*, Academic Press, **1997**.

[29] W. König, R. Geiger, *Chem. Ber.* **1970**, *103*, 788.

[30] L. A. Carpino, *J. Am. Chem. Soc.* **1993**, *115*, 4397.

[31] F. Kurzer, K. Douraghi-Zadeh, *Chem. Rev.* **1967**, *67*, 107.

[32] C. A. Montalbetti, V. Falque, *Tetrahedron* **2005**, *61*, 10827.

[33] S. R. Manne, D. C. Akintayo, O. Luna, A. El-Faham, B. G. de La Torre, F. Albericio, *Org. Process Res. Dev.* **2022**, *26*, 2894.

[34] T. Fantoni, A. Orlandin, I. Di Stefano, M. Macis, A. Tolomelli, A. Ricci, W. Cabri, L. Ferrazzano, *Green Chem* **2024**, *26*, 10929.

[35] E. Valeur, M. Bradley, *Chem. Soc. Rev.* **2009**, *38*, 606.

[36] C. Nájera, *Synlett* **2002**, *2002*, 1388.

[37] L. A. Carpino, H. Imazumi, A. El-Faham, F. J. Ferrer, C. Zhang, Y. Lee, B. M. Foxman, P. Henklein, C. Hanay, C. Mügge et al., *Angew. Chem. Int. Ed.* **2002**, *41*, 441.

[38] F. Albeiicio, R. Chinchilla, D. J. Dodsworth, C. Nájera, *Org. Prep. Proced. Int.* **2001**, *33*, 203.

[39] J. Coste, E. Frerot, P. Jouin, *J. Org. Chem.* **1994**, *59*, 2437.

[40] R. Chapman, M. Danial, M. L. Koh, K. A. Jolliffe, S. Perrier, *Chem. Soc. Rev.* **2012**, *41*, 6023.

[41] S. K. Hill, R. M. England, S. Perrier, *J. Contr. Release.* **2024**, *367*, 687.

[42] S. A. Raw, *Tetrahedron Lett.* **2009**, *50*, 946.

[43] M. Kunishima, C. Kawachi, K. Hioki, K. Terao, S. Tani, *Tetrahedron* **2001**, *57*, 1551.

[44] M. D'Este, D. Eglin, M. Alini, *Carbohydr. Polym.* **2014**, *108*, 239.

[45] Y.-H. Ye, H. Li, X. Jiang, *Biopolymers* **2005**, *80*, 172.

[46] Y. Tang, H.-B. Xie, G. Tian, Y.-H. Ye, *Pept. Res.* **2002**, *60*, 95.

[47] J.-M. Lehn, *Angew. Chem. Int. Ed.* **1988**, *27*, 89.

[48] J.-M. Lehn, *Supramolecular chemistry*. *Concepts and perspectives*, VCH, Weinheim, New York, **1995**.

[49] T. S. Moore, T. F. Winmill, *J. Chem. Soc., Trans.* **1912**, *101*, 1635.

[50] C. A. Hunter, *Angew. Chem. Int. Ed.* **2004**, *43*, 5310.

[51] R. P. Sijbesma, E. W. Meijer, *Chem.Commun.* **2003**, *5*, 1556.

[52] C. K. McLaughlin, G. D. Hamblin, H. F. Sleiman, *Chem. Soc. Rev.* **2011**, *40*, 5647.

[53] T. F. A. de Greef, M. M. J. Smulders, M. Wolffs, Schenning, Albert P. H. J., R. P. Sijbesma, E. W. Meijer, *Chem. Rev.* **2009**, *109*, 5687.

[54] H. Staudinger, *Chem. Ber.* **2006**, *53*, 1073.

[55] G. Mellot, J.-M. Guigner, L. Bouteiller, F. Stoffelbach, J. Rieger, *Angew. Chem. Int. Ed.* **2019**, *58*, 3173.

[56] S. Yagai, Y. Monma, N. Kawauchi, T. Karatsu, A. Kitamura, *Org. Lett.* **2007**, *9*, 1137.

[57] R. Otter, K. Klinker, D. Spitzer, M. Schinnerer, M. Barz, P. Besenius, *Chem. Commun.* **2018**, *54*, 401.

[58] M. R. Ghadiri, J. R. Granja, R. A. Milligan, D. E. McRee, N. Khazanovich, *Nature* **1993**, *366*, 324.

[59] K. Bauri, M. Nandi, P. De, *Polym. Chem.* **2018**, *9*, 1257.

[60] D. Spitzer, L. L. Rodrigues, D. Straßburger, M. Mezger, P. Besenius, *Angew. Chem. Int. Ed.* **2017**, *129*, 15664.

[61] D. J. Craik, *Science* **2006**, *311*, 1563.

[62] F. Albericio, *Solid-Phase Synthesis*. *A Practical Guide*, CRC Press, Boca Raton, FL, **2000**.

[63] K. M. Corbett, L. Ford, D. B. Warren, C. W. Pouton, D. K. Chalmers, *J. Med. Chem.* **2021**, *64*, 13131.

[64] J. Dantal, E. Pohanka, *Nephrol. Dial. Transplant.***2007**, *22,* 4-10.

[65] G. Leng, R. I. Leng, *Journal of neuroendocrinology* **2021**, *33*, e13014.

[66] C. A. Burtis, E. R. Ashwood, D. E. Bruns, N. W. Tietz, *Tietz textbook of clinical chemistry and molecular diagnostics*, Saunders, St. Louis, **2013**.

[67] Q. Song, Z. Cheng, M. Kariuki, S. C. L. Hall, S. K. Hill, J. Y. Rho, S. Perrier, *Chem. Rev.* **2021**, *121*, 13936.

[68] P. de Santis, S. Morosetti, R. Rizzo, *Macromolecules* **1974**, *7*, 52.

[69] Q. Song, Z. Cheng, M. Kariuki, S. C. L. Hall, S. K. Hill, J. Y. Rho, S. Perrier, *Chem. Rev.* **2021**, *121*, 13936.

[70] M. Engels, D. Bashford, M. R. Ghadiri, *J. Am. Chem. Soc.* **1995**, *117*, 9151.

[71] A. Khondker, R. J. Alsop, M. C. Rheinstädter, *Membranes* **2017**, *7*.

[72] S. Peluso, T. Rückle, C. Lehmann, M. Mutter, C. Peggion, M. Crisma, *ChemBioChem* **2001**, *2*, 432.

[73] R. DAHIYA, *J. Chil. Chem. Soc.* **2007**, *52*.

[74] N. Khazanovich, J. R. Granja, D. E. McRee, R. A. Milligan, M. R. Ghadiri, *J. Am. Chem. Soc.* **1994**, *116*, 6011.

[75] M. R. Ghadiri, J. R. Granja, L. K. Buehler, *Nature* **1994**, *369*, 301.

[76] J. D. Hartgerink, J. R. Granja, R. A. Milligan, M. R. Ghadiri, *J. Am. Chem. Soc.* **1996**, *118*, 43.

[77] D. J. Rubin, S. Amini, F. Zhou, H. Su, A. Miserez, N. S. Joshi, *ACS Nano* **2015**, *9*, 3360.

[78] T. D. Clark, L. K. Buehler, M. R. Ghadiri, *J. Am. Chem. Soc.* **1998**, *120*, 651.

[79] I. Insua, J. Montenegro, *J. Am. Chem. Soc.* **2020**, *142*, 300.

[80] S. Díaz, I. Insua, G. Bhak, J. Montenegro, *Chem. Eur. J.* **2020**, *26*, 14765.

[81] H. Shaikh, J. Y. Rho, L. J. Macdougall, P. Gurnani, A. M. Lunn, J. Yang, S. Huband, E. D. H. Mansfield, R. Peltier, S. Perrier, *Chem. Eur. J.* **2018**, *24*, 19066.

[82] A. Méndez-Ardoy, J. R. Granja, J. Montenegro, *Nanoscale Horiz.* **2018**, *3*, 391.

[83] H. Y. Chow, Y. Zhang, E. Matheson, X. Li, *Chem. Rev.* **2019**, *119*, 9971.

[84] J. S. Davies, *J. Pept. Sci.* **2003**, *9*, 471.

[85] P. Rovero, L. Quartara, G. Fabbri, *Tetrahedron Lett.* **1991**, *32*, 2639.

[86] A. Trzeciak, W. Bannwarth, *Tetrahedron Lett.* **1992**, *33*, 4557.

[87] J. Chen, B. Zhang, C. Xie, Y. Lu, W. Wu, *Chin. Chem. Lett.* **2010**, *21*, 391.

[88] K. S. Harris, T. Durek, Q. Kaas, A. G. Poth, E. K. Gilding, B. F. Conlan, I. Saska, N. L. Daly, N. L. van der Weerden, D. J. Craik et al., *Nat. Commun.* **2015**, *6*, 10199.

[89] X. Yan, F. Wang, B. Zheng, F. Huang, *Chem. Soc. Rev.* **2012**, *41*, 6042.

[90] B. Tieke, *Makromolekulare Chemie*. *Eine Einführung*, Wiley-VCH, Weinheim, **2014**.

[91] J. Venkatraman, S. C. Shankaramma, P. Balaram, *Chem. Rev.* **2001**, *101*, 3131.

[92] R. Otter, N. A. Henke, C. Berac, T. Bauer, M. Barz, S. Seiffert, P. Besenius, *Macromol. Rapid Commun.* **2018**, *39*, e1800459.

[93] E. D. H. Mansfield, M. Hartlieb, S. Catrouillet, J. Y. Rho, S. C. Larnaudie, S. E. Rogers, J. Sanchis, J. C. Brendel, S. Perrier, *Soft matter* **2018**, *14*, 6320.

[94] R. E. Kieltyka, A. C. H. Pape, L. Albertazzi, Y. Nakano, M. M. C. Bastings, I. K. Voets, P. Y. W. Dankers, E. W. Meijer, *J. Am. Chem. Soc.* **2013**, *135*, 11159.

[95] E. Krieg, M. M. C. Bastings, P. Besenius, B. Rybtchinski, *Chem. Rev.* **2016**, *116*, 2414.

[96] J. Y. Rho, S. Perrier, *ACS Macro Lett.* **2021**, *10*, 258.

[97] M. Wei, Y. Gao, X. Li, M. J. Serpe, *Polym. Chem.* **2017**, *8*, 127.

[98] C. Wu, H. Wang, *ChemBioChem* **2023**, *24*, e202300018.

[99] J. R. Requena, M. N. Dimitrova, G. Legname, S. Teijeira, S. B. Prusiner, R. L. Levine, *Arch. Biochem. Biophys.* **2004**, *432*, 188.

[100] H. G. Batz, V. Hofmann, H. Ringsdorf, *Makromol. Chem.* **1973**, *169*, 323.

[101] P. Carampin, E. Lallana, J. Laliturai, S. C. Carroccio, C. Puglisi, N. Tirelli, *Macromol. Chem. Phys.* **2012**, *213*, 2052.

[102] D. Spitzer, L. L. Rodrigues, D. Straßburger, M. Mezger, P. Besenius, *Angew. Chem. Int. Ed.* **2017**, *56*, 15461.

[103] C. M. Berac, L. Zengerling, D. Straβburger, R. Otter, M. Urschbach, P. Besenius, *Macromol. Rapid Commun.* **2020**, *41*, e1900476.

[104] R. Otter, C. M. Berac, S. Seiffert, P. Besenius, *Eur. Polym. J.* **2019**, *110*, 90.

[105] C. Glorieux, S. Liu, D. Trachootham, P. Huang, *Nat. Rev. Drug Discov.* **2024**, *23*, 583.

[106] E. Fischer, J. von Mering, (1924). *Ueber eine neue Klasse von Schlafmitteln*. Springer, Berlin, Heidelberg, **1924**.

[107] H. D. :. J. H. Jakubke, *Aminosäuren, Peptide, Proteine*, Verlag Chemie, Weinheim, **1982**.

[108] T. Schirmeister, C. Schmuck, P. R. Wich, *Organische Chemie*, Hirzel Verlag, Stuttgart, **2016**.

[109] E. Fischer, A. Speier, *Ber. Dtsch. Chem. Ges.* **1895**, *28*, 3252.

[110] Q. N. N. Nguyen, J. Schwochert, D. J. Tantillo, R. S. Lokey, *Phys. Chem. Chem. Phys.* **2018**, *20*, 14003.

[111] J. Hjalte, S. Hossain, A. Hugerth, H. Sjögren, M. Wahlgren, P. Larsson, D. Lundberg, *Mol. Pharm.* **2022**, *19*, 904.

[112] J. G. Stempak, R. T. Ward, . *Cell Biol.* **1964**, *22*, 697.

[113] B. G. Poulson, K. Szczepski, J. I. Lachowicz, L. Jaremko, A.-H. Emwas, M. Jaremko, *RSC Adv.* **2019**, *10*, 215.

[114] K. L. Zapadka, F. J. Becher, A. L. Gomes Dos Santos, S. E. Jackson, *Interface focus* **2017**, *7*, 20170030.

[115] P. Ahlers, H. Frisch, P. Besenius, *Polym. Chem.* **2015**, *6*, 7245.

[116] H. Staudinger, J. Meyer, *Helv. Chim. Acta.* **1919**, *2*, 635.

[117] M. Ji, M. L. Mason, D. A. Modarelli, J. R. Parquette, *Chem. Sci.* **2019**, *10*, 7868.

[118] H. Shao, J. Seifert, N. C. Romano, M. Gao, J. J. Helmus, C. P. Jaroniec, D. A. Modarelli, J. R. Parquette, *Angew. Chem. Int. Ed.* **2010**, *49*, 7688.

[119] D. Corrêa, C. Ramos, *Afr. J. Biochem. Res.* **2009**, *3*, 164.

[120] J. Reed, T. A. Reed, *Anal. Biochem.* **1997**, *254*, 36.

[121] A. Rodger, B. Nordén, *Circular dichroism and linear dichroism*, Oxford University Press, Oxford, **1997**.

[122] W. Moffitt, *J. Chem. Phys.* **1956**, *25*, 467.

[123] S. Roy, A. Dasgupta, P. K. Das, *Langmuir* **2007**, *23*, 11769.

[124] V. Madison, K. D. Kopple, *J. Am. Chem. Soc.* **1980**, *102*, 4855.

[125] M. Kajtár, J. Kajtár, Z. Majer, M. Zewdu, M. Hollósi, *Spectrochim Acta A Mol Biomol Spectrosc.* **1992**, *48*, 87.

[126] X. Liang, A. Kaya, Y. Zhang, D. T. Le, D. Hua, V. N. Gladyshev, *BMC Biochem.* **2012**, *13*, 21.

[127] N. J. Greenfield, *Nat. Protoc.* **2006**, *1*, 2876.

[128] A. Chauhan, R. Kamal, R. Bhatia, T. G. Singh, A. Awasthi, *AAPS PharmSciTech.* **2024**, *26*, 10.

[129] J. L. Lau, M. K. Dunn, *Bioorg. Med. Chem.* **2018**, *26*, 2700.

[130] M. Werle, A. Bernkop-Schnürch, *J. Amino Acids* **2006**, *30*, 351.

[131] P. J. M. Stals, J. F. Haveman, R. Martín-Rapún, C. F. C. Fitié, A. R. A. Palmans, E. W. Meijer, *J. Mater. Chem.* **2009**, *19*, 124.

[132] B. M. Blunden, R. Chapman, M. Danial, H. Lu, K. A. Jolliffe, S. Perrier, M. H. Stenzel, *Chem. Eur. J.* **2014**, *20*, 12745.

[133] S. Catrouillet, J. C. Brendel, S. Larnaudie, T. Barlow, K. A. Jolliffe, S. Perrier, *ACS Macro Lett.* **2016**, *5*, 1119.

[134] J. Yang, J.-I. Song, Q. Song, J. Y. Rho, E. D. H. Mansfield, S. C. L. Hall, M. Sambrook, F. Huang, S. Perrier, *Angew. Chem. Int. Ed.* **2020**, *59*, 8860.

[135] A. J. Lander, L. D. Mercado, X. Li, I. M. Taily, B. L. Findlay, Y. Jin, L. Y. P. Luk, *Communications Chemistry* **2023**, *6*, 154.

[136] S. Khemaissa, S. Sagan, A. Walrant, *Crystals* **2021**, *11*.

[137] A. Williamson, *Lond. Edinb. Dubl. Phil. Mag.* **1850**, *37*, 350.

[138] T. Román, G. Acosta, B. G. de La Torre, C. Cárdenas, F. Guzmán, F. Albericio, *Methods Protoc.* **2023**, *6*.

[139] S. Duengo, M. I. Muhajir, A. T. Hidayat, W. J. A. Musa, R. Maharani, *Molecules* **2023**, *28*.

[140] A. Thakkar, T. B. Trinh, D. Pei, *ACS Comb. Sci.* **2013**, *15*, 120.

[141] H. C. Kolb, M. G. Finn, K. B. Sharpless, *Angew. Chem. Int. Ed.* **2001**, *40*, 2004.

[142] T. R. Chan, R. Hilgraf, K. B. Sharpless, V. V. Fokin, *Org. Lett.* **2004**, *6*, 2853.

[143] B. T. Worrell, J. A. Malik, V. V. Fokin, *Science* **2013**, *340*, 457.

[144] L. M. Franklin, S. M. Walker, G. Hill, *J. Mol. Model.* **2020**, *26*, 116.

[145] P. Manikandan, B. Epel, D. Goldfarb, *Inorg. Chem.* **2001**, *40*, 781.

[146] V. T. Panyushkin, I. N. Shcherbakov, V. A. Volynkin, S. N. Bolotin, N. N. Bukov, T. V. Shvydko, L. K. Dzhabrailova, M. K. Shamsutdinova, *J. Struct. Chem.* **2017**, *58*, 508.

[147] K. Ősz, Z. Nagy, G. Pappalardo, G. Di Natale, D. Sanna, G. Micera, E. Rizzarelli, I. Sóvágó, *Chem. Eur. J.* **2007**, *13*, 7129.

[148] A. Matera, J. Brasuń, M. Cebrat, J. Świątek-Kozłowska, *Polyhedron* **2008**, *27*, 1539.

[149] K. Matelková, K. Ossberger, J. Hudák, J. Vatrál, R. Boča, W. Linert, *Monatsh. Chem.* **2013**, *144*, 937.

[150] A. Harriman, *J. Phys. Chem.* **1987**, 91, 24, 6102–6104.

[151] E. Riedel, C. Janiak, *Anorganische Chemie*, DE GRUYTER, **2010**.

[152] Y. E. Jad, S. N. Khattab, B. G. de La Torre, T. Govender, H. G. Kruger, A. El-Faham, F. Albericio, *Eur J Org Chem* **2015**, *2015*, 3116.

[153] *CRC handbook of chemistry and physics*. *A ready-reference book of chemical and physical data*, CRC Press, Boca Raton, Fla., **1991**.

[154] A. A. D'souza, R. Shegokar, *Expert Opin. Drug Deliv.* **2016**, *13*, 1257.

[155] C. J. Fee, J. M. Van Alstine, *Chem. Eng. Sci.* **2006**, *61*, 924.

[156] P. Christen, R. Jaussi, R. Benoit, *Biochemie und Molekularbiologie*, Springer Berlin Heidelberg, Berlin, Heidelberg, **2016**.

[157] V. K. Sousa, J. A. F. Pedro, P. S. Kumagai, J. L. S. Lopes, *Eur. Biophys. J.* **2021**, *50*, 687.

[158] Y. Scolnik, I. Portnaya, U. Cogan, S. Tal, R. Haimovitz, M. Fridkin, A. C. Elitzur, D. W. Deamer, M. Shinitzky, *Phys. Chem. Chem. Phys.* **2006**, *8*, 333.

[159] R. N. M. Macsween, *J. Clin. Pathol.* **1977**, *30*, 1089.

[160] I. Insua, A. Cardellini, S. Díaz, J. Bergueiro, R. Capelli, G. M. Pavan, J. Montenegro, *Chem. Sci.* **2023**, *14*, 14074.

[161] M. C. Capello, F. J. Hernández, M. Broquier, C. Dedonder-Lardeux, C. Jouvet, G. A. Pino, *Phys. Chem. Chem. Phys.* **2016**, *18*, 31260.

[162] H. A. Barnes, J. F. Hutton, K. Walters, *An Introduction to Rheology*, Elsevier Science, **1989**.

[163] A. Bayón-Fernández, A. Méndez-Ardoy, C. Alvarez-Lorenzo, J. R. Granja, J. Montenegro, *J. Mater. Chem. B* **2023**, *11*, 606.

[164] A. M. Rosales, K. S. Anseth, *Nat Rev Mater* **2016**, *1*, 1.

[165] E. C. González-Díaz, S. Varghese, *Gels* **2016**, *2*, 20.

[166] S. Bernhard, M. W. Tibbitt, *Adv. Drug Deliv. Rev.* **2021**, *171*, 240.

[167] M. reza Saboktakin, R. M. Tabatabaei, *Int. J. Biol. Macromol.* **2015**, *75*, 426.

[168] A. C. H. Pape, P. Y. W. Dankers in *Supramolecular Polymer Networks and Gels*, Springer International Publishing, Cham, **2015**.

[169] L. Moumné, A.-C. Marie, N. Crouvezier, *Pharmaceutics* **2022**, *14*.

[170] V. Sharma, J. Watts, *Future Med. Chem.* **2015**, *7*, 2221.

[171] N. Kayraklioglu, B. Horuluoglu, D. M. Klinman, *Methods Mol. Biol.* **2021**, *2197*, 51.

[172] H. L. Wilson, A. Dar, S. K. Napper, A. M. Lopez, L. A. Babiuk, G. K. Mutwiri, *Int. Rev. Immunol.* **2006**, *25*, 183.

[173] B. Hu, L. Zhong, Y. Weng, L. Peng, Y. Huang, Y. Zhao, X.-J. Liang, *Signal Transduct. Target. Ther.* **2020**, *5*, 101.

[174] Y. Dong, D. J. Siegwart, D. G. Anderson, *Adv. Drug Deliv. Rev.* **2019**, 133.

[175] D. Simberg, S. Weisman, Y. Talmon, Y. Barenholz, *Crit. Rev. Ther. Drug Carrier Syst.* **2004**, *21*, 257.

[176] M. Hashida, S. Kawakami, F. Yamashita, *Chem. Pharm. Bull.* **2005**, *53*, 871.

[177] B.-K. Kim, G.-B. Hwang, Y.-B.Seu, J.-S. Choi, K. Sik Jin, K.-O. Doh, *Biochim. Biophys. Acta* **2015**, *1848*, 1996.

[178] L. G. de la Torre, R. Silva Rosada, A. P. Fávaro Trombone, F. Frantz, A. Coelho-Castelo, C. Lopes Silva, M. H. A. Santana, *Colloids Surf. B Biointerfaces.* **2009**, *73*, 175.

[179] D. Pozzi, F. Cardarelli, F. Salomone, C. Marchini, H. Amenitsch, G. La Barbera, G. Caracciolo, *Appl. Phys. Lett.* **2014**, *105*, 73701.

[180] Y. Hattori, K. Tamaki, S. Sakasai, K.-I. Ozaki, H. Onishi, *Mol Med Rep* **2020**, *22*, 4183.

[181] S. A. El-Zahaby, L. Kaur, A. Sharma, A. G. Prasad, A. K. Wani, R. Singh, M. Y. Zakaria, *AAPS PharmSciTech* **2024**, *25*, 131.

[182] H. Wang, S. Zhang, J. Lv, Y. Cheng, *VIEW* **2021**, *2*.

[183] Anne-Laure Bolcato-Bellemin, Marie-Elise Bonnet, Gaëlle Creusat, Patrick Erbacher, Jean-Paul Behr, *Proc. Natl. Acad. Sci.* **2007**, *104*, 16050.

[184] Michael Neu, Oliver Germershaus, Martin Behe, Thomas Kissel, *J. Contr. Release.* **2007**, *124*, 69.

[185] Nathan D. Donahue, Handan Acar, Stefan Wilhelm, *Adv. Drug Deliv. Rev.* **2019**, *143*, 68.

[186] N. P. Gabrielson, D. W. Pack, *Biomacromolecules* **2006**, *7*, 2427.

[187] W. X. Siow, Y.-T. Chang, M. Babič, Y.-C. Lu, D. Horák, Y.-H. Ma, *Int. J. Nanomedicine* **2018**, *13*, 1693.

[188] T. Bus, A. Traeger, U. S. Schubert, *J. Mater. Chem. B* **2018**, *6*, 6904.

[189] R. H. Mo, J. L. Zaro, W.-C. Shen, *Mol. Pharm.* **2012**, *9*, 299.

[190] M. Gooding, L. P. Browne, F. M. Quinteiro, D. L. Selwood, *Chem. Biol. Drug Des.* **2012**, *80*, 787.

[191] S. Sandgren, F. Cheng, M. Belting, *J. Biol. Chem.* **2002**, *277*, 38877.

[192] Ü. Langel, *Cell-Penetrating Peptides*, Springer Singapore, Singapore, **2019**.

[193] W. Li, Y. Liu, J. Du, K. Ren, Y. Wang, *Nanoscale* **2015**, *7*, 8476.

[194] Z.-X. Zhao, S.-Y. Gao, J.-C. Wang, C.-J. Chen, E.-Y. Zhao, W.-J. Hou, Q. Feng, L.-Y. Gao, X.-Y. Liu, L.-R. Zhang et al., *Biomaterials* **2012**, *33*, 6793.

[195] B. Ding, Z. Chen, *J. Phys. Chem. B.* **2012**, *116*, 2545.

[196] B. M. deRonde, N. D. Posey, R. Otter, L. M. Caffrey, L. M. Minter, G. N. Tew, *Biomacromolecules* **2016**, *17*, 1969.

[197] H. C. Davis, N. D. Posey, G. N. Tew, *Biomacromolecules* **2022**, *23*, 57.

[198] J. M. Harris, R. B. Chess, *Nat. Rev. Drug Discov.* **2003**, *2*, 214.

[199] M. Katano, H. Yamamoto, E. Kubota, M. Nakamura, T. Matsuo, F. Nagumo, T. Hisatsugu, T. Katsuki, J. Tadano, *Surg Today* **1993**, *23*, 13.

[200] D. Held, P. Kilz in *Monitoring Polymerization Reactions*, John Wiley & Sons, Ltd, **2013**.

[201] F. Koch, M. Müller, F. König, N. Meyer, J. Gattlen, U. Pieles, K. Peters, B. Kreikemeyer, S. Mathes, S. Saxer, *R. Soc. Open Sci.* **2018**, *5*, 171562.

[202] M. L. Obenauer, J. A. Dresel, M. Schweitzer, P. Besenius, F. Schmid, *Macromol. Rapid Commun.* **2024**, *45*, 2400149.

[203] "Cloning vector pGL3-Basic, complete sequence", can be found under https://www.ncbi.nlm.nih.gov/nuccore/U47295.2?report=fasta (08. Feb.2025).

[204] M. Tang, S. Sakasai, H. Onishi, K. Kawano, Y. Hattori, *J. Drug Target.* **2023**, *31*, 74.

[205] D. Dey, S. Kumar, R. Banerjee, S. Maiti, D. Dhara, *J. Phys. Chem. B.* **2014**, *118*, 7012.

[206] S. M. Sarett, T. A. Werfel, I. Chandra, M. A. Jackson, T. E. Kavanaugh, M. E. Hattaway, T. D. Giorgio, C. L. Duvall, *Biomaterials* **2016**, *97*, 122.

[207] L. Soliman, "HEK 293 Cells: Background, Advantages and Applications", can be found under https://www.biospace.com/hek-293 (24.Jan.20205).

[208] Aysun Adan, Günel Alizada, Yağmur Kiraz, Yusuf Baran, Ayten Nalbant, *Crit Rev Biotechnol.* **2017**, *37*, 163.

[209] S. Mishra, P. Webster, M. E. Davis, *Eur. J. Cell Biol.* **2004**, *83*, 97.

[210] M. K. Grun, A. Suberi, K. Shin, T. Lee, V. Gomerdinger, Z. M. Moscato, A. S. Piotrowski-Daspit, W. M. Saltzman, *Biomaterials* **2021**, *272*, 120780.

[211] H. T. T. Do, C. H. Lee, J. Cho, *Cancers* **2020**, *12*.

[212] V. M. Keatings, P. D. Collins, D. M. Scott, P. J. Barnes, *Am. J. Respir. Crit. Care Med.* **1996**, *153*, 530.

[213] Z.-J. Han, Y.-B. Li, L.-X. Yang, H.-J. Cheng, X. Liu, H. Chen, *Molecules* **2021**, *27*.

[214] E. Pauls, J. Senserrich, M. Bofill, B. Clotet, J. A. Esté, *Clin. Exp. Immunol.* **2007**, *147*, 189.

[215] C.-K. Chen, P.-K. Huang, W.-C. Law, C.-H. Chu, N.-T. Chen, L.-W. Lo, *Int. J. Nanomedicine* **2020**, *15*, 2131.

[216] B. Dalby, S. Cates, A. Harris, E. C. Ohki, M. L. Tilkins, P. J. Price, V. C. Ciccarone, *Methods* **2004**, *33*, 95.

[217] N. I. Medeiros, J. A. S. Gomes, *Methods Mol. Biol.* **2019**, *1955*, 309.

[218] A. S. Riching, A. Malloy, E. M. Anderson, J. Sheard, P. Mikkonen, A. van Brabant Smith, Z. Strezoska, J. Levenga, *Curr. Protoc.* **2024**, *4*, 1121.

[219] "ODN D-SL03", can be found under https://www.invivogen.com/odn-dsl03 (08. Feb.2025).

[220] Y. Kumagai, O. Takeuchi, S. Akira, *Adv. Drug Deliv. Rev.* **2008**, *60*, 795.

[221] M. R. Shurin, P. P. Pandharipande, T. D. Zorina, C. Haluszczak, V. M. Subbotin, O. Hunter, A. Brumfield, W. J. Storkus, E. Maraskovsky, M. T. Lotze, *Cell. Immunol.* **1997**, *179*, 174.

[222] E. Koike, H. Takano, K. Inoue, R. Yanagisawa, *Int. Immunopharmacol.* **2008**, *8*, 1737.

[223] M. N'diaye, A. Warnecke, S. Flytzani, N. Abdelmagid, S. Ruhrmann, T. Olsson, M. Jagodic, R. A. Harris, A. O. Guerreiro-Cacais, *J. Leukoc. Biol.* **2015**, *99*, 437.

[224] T. Ito, M. Yang, Y.-H. Wang, R. Lande, J. Gregorio, O. A. Perng, X.-F. Qin, Y.-J. Liu, M. Gilliet, *J Exp Med* **2007**, *204*, 105.

[225] Steven M. Lewis, Adam Williams, Stephanie C. Eisenbarth, *Sci. Immunol.* **2019**, *4*, 6085.

[226] P. Chen, X. He, Y. Hu, X.-L. Tian, X.-Q. Yu, J. Zhang, *ACS Applied Materials & Interfaces* **2023**, *15*, 19937.

[227] A. Kennedy, E. Waters, B. Rowshanravan, C. Hinze, C. Williams, D. Janman, T. A. Fox, C. Booth, A. M. Pesenacker, N. Halliday et al., *Nat. Immunol.* **2022**, *23*, 1365.

[228] C. Volpi, F. Fallarino, M. T. Pallotta, R. Bianchi, C. Vacca, M. L. Belladonna, C. Orabona, A. de Luca, L. Boon, L. Romani et al., *Nat. Commun.* **2013**, *4*, 1852.

[229] I. F. Tannock, D. Rotin, *Canc. Res.* **1989**, *49*, 4373.

[230] "CpG ODNs - TLR9 Agonists", can be found under https://www.invivogen.com/odn2007#details (23. Jan.2025).

9 List of Abbreviations

a.u.	arbitrary units
ACN	Acetonitrile
AcOH	Acetic acid
Act	Activated
Ahx	Hexanoic acid
Ala	Alanine
alt	alterning
APC	Antigen-presenting cells
Asp	Aspartic acid
ATP	Adenosine triphosphate
B-	Base
B cells	B lymphocytes
BMDC	Bone marrow-derived dendritic cells
Boc	*tert*-Butyloxycarbonyl
bp	base pairs
Bzl	Benzoyl
CAC	Critical aggregation concentration
CBA	Cytometric bead arra
CD	Circular dichroism
CD19+	Cluster of differentiation 19+
CD40	Cluster of differentiation 40
CD80	Cluster of differentiation 80
CD86	Cluster of differentiation 86
cDC1	conventional dendritic cell 1
cDC2	conventional dendritic cell 2
CHCA	α-cyano-4-hydroxycinnamic acid
CL	Crosslinker
conc.	concentrated
COO	Carboxyl
COSY	correlation spectroscopy
CP	Cyclopeptide
CpG	Cytosine-phosphate-guanine dinucleotide motif
CPP	cell-penetrating peptides
CPPM	cell-penetrating peptides mimetics
CryoTEM	Cryo-transmission electron microscopy
CuAAC	copper-catalyzed azide-alkyne cycloaddition
CXCL8	chemokine (C-X-C motif) ligand 8, Interleukin-8
Cy3	Cyanine 3
DBU	1,8-diazabicyclo[5,4,0]undec-7-ene
DCC	dicyclohexylcarbodiimide
DCM	Dichlormethane
DCs	dendritic cells
δ	Chemical shift
DEPT	diethylphosphoryl cyanide

DHB	2,4-dihydroxylbenzoeacid
DIC	diisopropylcarbodiimide
DIPEA	N,N-diisopropylethylamine
Dit	dithranol
DMF	N,N-Dimethylformamid
DMSO	Dimethylsulfoxide
DMTMM·BF4	4-(4,6-dimethoxy-[1,3,5]-triazin-2-yl)-4-methylmorpholinium tetrafluoroborate
DNA	Deoxyribonucleic acid
DOPE	1,2-dioleoyl-sn-glycero-3-phosphoethanolamine
DOTAP	1,2-dioleoyl-3-trimethylammonium propane
DPPA	Diphenylphosphoryl azide
e.g.	*exempli gratia* - for example
ECM	extracellular matrix
EDC HCl	1-Ethyl-3-(3-dimethylaminopropyl)carbodiimide hydrochloride
EDT	1,2-ethanedithiol
EGFR	Epidermal growth factor receptor
eq.	equivalent
ER	Endoplasmic riticulum
ESI-MS	Electrospray ionization mass spectrometry
et.al.	*et alii, et aliae, et alia*
FACS	fluorescence-activated cell sorting
FLT3	feline McDonough sarcoma like tyrosine kinase 3
Fmoc	Fluorenylmethyloxycarbonyl
Fmoc-Glu-OtBu	*N*-(9-fluorenylmethoxycarbonyloxy) glutamic acid tert-butyl ester
Fmoc-Osu	*N*-(9-fluorenylmethoxycarbonyloxy)succinimide
FVD	Fixable viability dye
G′	storage modulus
G′′	loss modulus
Gln	Glutamine
Glu	Glutamic acid
Gly	Glycine
GPC	Gel permeation chromatography
H+	Protons
HATU	O-(7-Aza-1H-benzotriazol-1-yl)-*N*,*N*,*N*',*N*'-tetramethyluronium hexafluorophosphate
HB	corresponding acid
HBTU	O-(Benzotriazol-1-yl)-*N*,*N*,*N*',*N*'-tetramethyluronium hexafluorophosphate
HCl	Hydrochloric acid

HEK-293T cells	Human Embryonic Kidney 293T cells, derived from HEK293 cells with stable expression of the SV40 large T antigen
HEPES	2-[4-(2-Hydroxyethyl)piperazin-1-yl]ethane-1-sulfonic acid
HF	Hydrogen fluoride
HFIP	Hexafluoro-2-propanol
His	Histidine
HIV-1 Virus	Human Immunodeficiency Virus Type 1
HOAt	1-hydroxy-7-azabenzotriazole
HOBt	1-hydroxybenzotriazole
HOPO	1-hydroxy-2-pyridone
HPLC	High-performance liquid chromatography
I-effect	electron-withdrawing effect
IL-9	Interleukin 8
in situ	In its original location
in vitro	Outside a living organism
in vivo	Inside a living organism
IRF	interferon regulatory factors
ISRE	Interferon-stimulated response element
LC-MS	Liquid chromatography-mass spectrometry
LDL receptor	low density lipoprotein receptor
Leu	Leucine
LVE	Linear viscoelasticity
Lys	Lysine
M	Molar mass
MACs	Macrophages
MALDI-TOF-MS	Matrix-assisted laser desorption/ionization time-of-flight
MCF-7	Michigan Cancer Foundation-7, a human estrogen receptor-positive breast cancer cell line
MeOH	Methanol
Met(O)	Methionine sulfoxide
MF	Molecular formula
miRNA	Micro ribonucleic acid
mPEG	monomethoxy-polyethylene glycol
MPLC	Medium pressure liquid chromatography
mRNA	messenger ribonucleic acid
MS	Mass spectrometry
MW	Molecular weight
MyD88	Myeloid differentiation primary response 88
N/P	Negative/Positive ratio
NaAsc	Sodium ascorbate
N_{agg}	Extent of aggregation
NF-κB	Nuclear factor kappa-light-chain-enhancer of activated B cells
NHS	*N*-hydroxysuccinimide

NK cells	Natural killer cells
NK1.1+	Natural Killer 1.1 positive, a surface marker expressed on certain NK cells
NMM	*N*-methylmorpholine
NMR	Nuclear magnetic resonance
NPC	Nuclear pore complex
OaAEP1b	asparaginyl endopeptidase
ODN	Oligodeoxynucleotide
Opfp	pentafluorophenol
Oxyma	hydroxyiminocyanoic acid ethyl ester
p50	NF-κB p50 subunit
p65	NF-κB p65 subunit
PBS	phosphate buffered saline
pDC	Plasmacytoid dendritic cells
pDNA	Plasmid deoxyribonucleic acid
PEG	Polyethylene glycol
PEI	Polyethylenimine
Pep-1	A cell-penetrating peptide
PG	Protecting group
PII	polyproline-II
pKa	Acid dissociation constant
PLA	Poly(D,L-lactide)
PLL	Poly-L-lysine
PMN	Polymorphonuclear neutrophils
pos.	positive
pPEGA	Polyethylene glycol acrylate brush chains
ppm	parts per million
PSar	polysarcosine
PyBOP	Benzotriazol-1-yloxytripyrrolidinophosphonium hexafluorophosphate
R	Residue
R15	Polyarginine
reagent L	TFA/TIPS/H2O/EDT
RedOx	Reduction-Oxidation
RES	Reticuloendothelial System
RI signal	Refractive Index Signal
RISC Complex	RNA-induced silencing complex
RNA	Ribonucleic acid
RNAi	Ribonucleic acid interference
ROS	Reactive oxygen species
RP-HPLC	Reversed-Phase High-Performance Liquid Chromatography
rt	room temperature
SCPN	cyclic peptide nanotubes
SEC	Size exclusion chromatography
Ser	Serine
SIM	Structured illumination microscopy

siRNA	Small interfering RNA
Sn1	Substitution nucleophilic unimolecular
Sn2	Substitution nucleophilic bimolecular
sp2	sp^2 Hybridization
SPPS	Solid-phase peptide synthesis
t	time
T cells	T lymphocyte
TAT-protein	Trans-Activator of Transcription, a regulatory protein essential for HIV-1 gene expression and viral replication
TBEC	2-(1H-Benzotriazol-1-yl)-1,1,3,3-tetramethyluronium-3-ethoxycarbonyl-3-oxo-1-propen-1-ylester
TBTA	tris(benzyltriazoylmethyl)amine
tBu	tert-butyl
TEGOMe	tetraethyleneglycol monomethyl ether
TEM	Transmission electron microscopy
TFA	Trifluoroacetic acid
TFE	2,2,2-Trifluoroethanol
TFMSA	trifluoromethanesulfonic acid
THF	Tetrahydrofuran
ThT	thioflavine-T
TIPS	triisopropylsilane
TLC	thin-layer chromatography
TLR9	Toll-like receptor 9
TNF-α	Tumor necrosis factor
Tris buffer	Tris(hydroxymethyl)aminomethane buffer
Trt	Triphenylmethyl-based protecting group
Trp	Tryptophan
Upy	ureidopyrimidinone
UV	Ultraviolet
via	By way of
vice versa	In reverse order
w/o	without
w/v	weight/volume percentage
w/w	weight/weight percentage
wt%	weight prozent
Xxx	Unspecified amino acid
ζ	mass ratio

10 Appendix

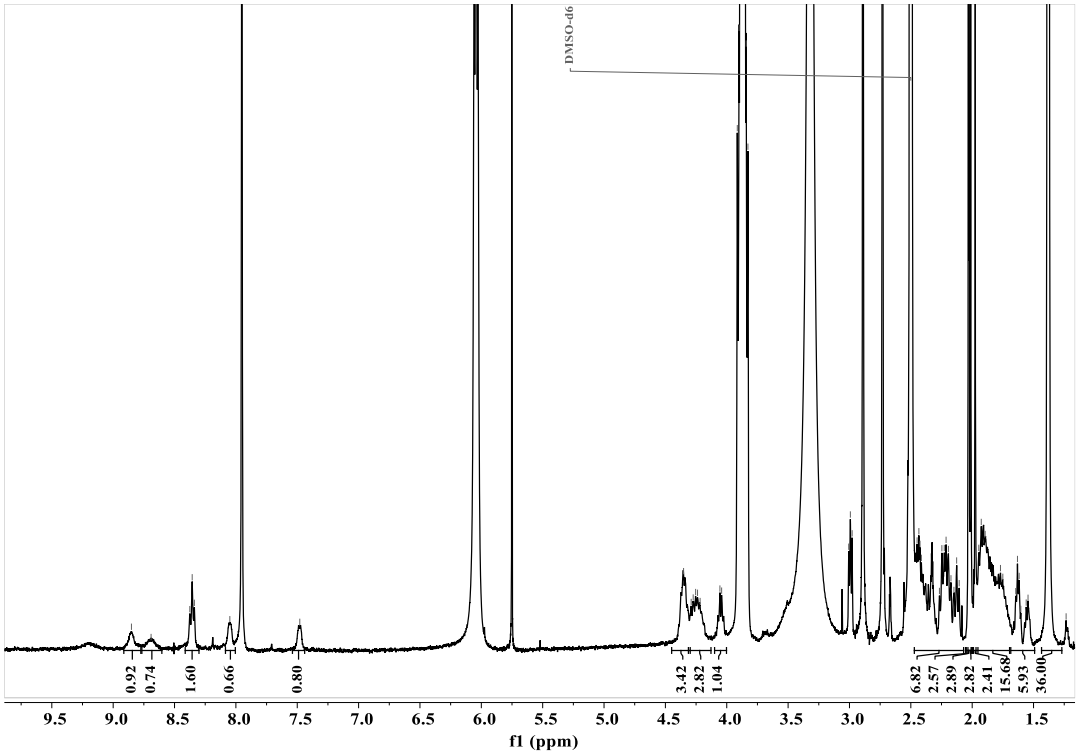

Figure 10.1: *^{1}H NMR spectrum of **III-1** in DMSO-d6.*

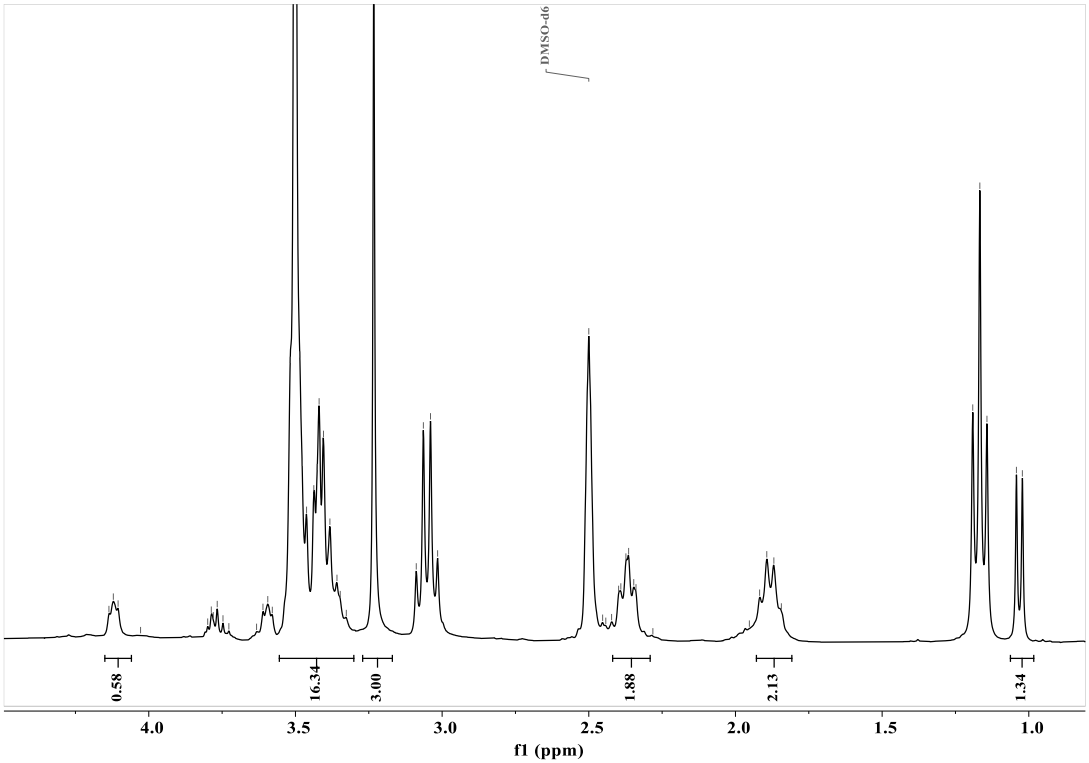

Figure 10.2: *^{1}H NMR spectrum of **III-4** in DMSO-d6.*

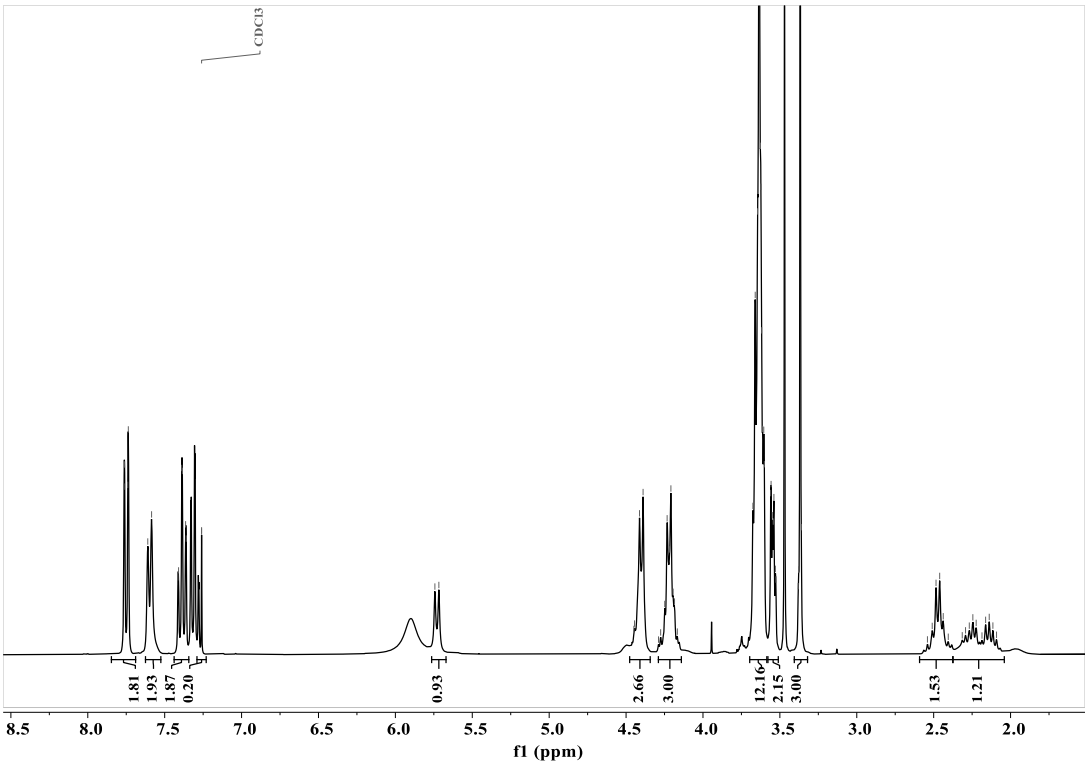

Figure 10.3: *^{1}H NMR spectrum of* ***III-5*** *in $CDCl_3$.*

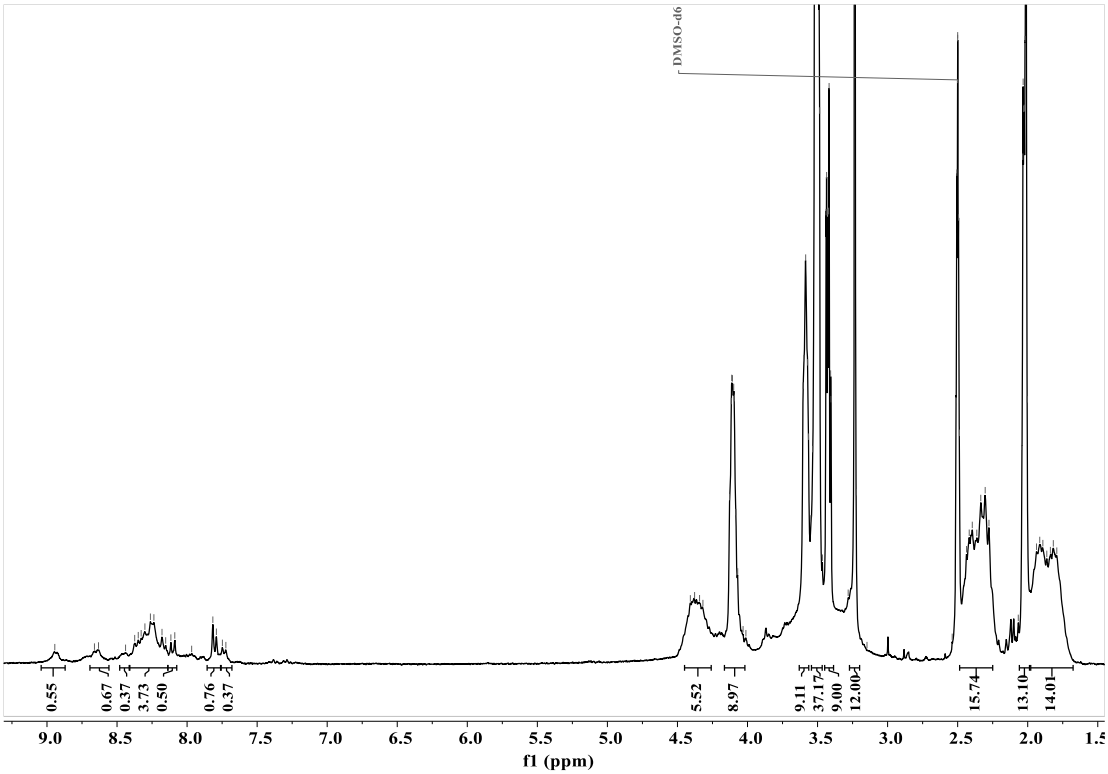

Figure 10.4: *^{1}H NMR spectrum of* ***III-6*** *in DMSO-d6.*

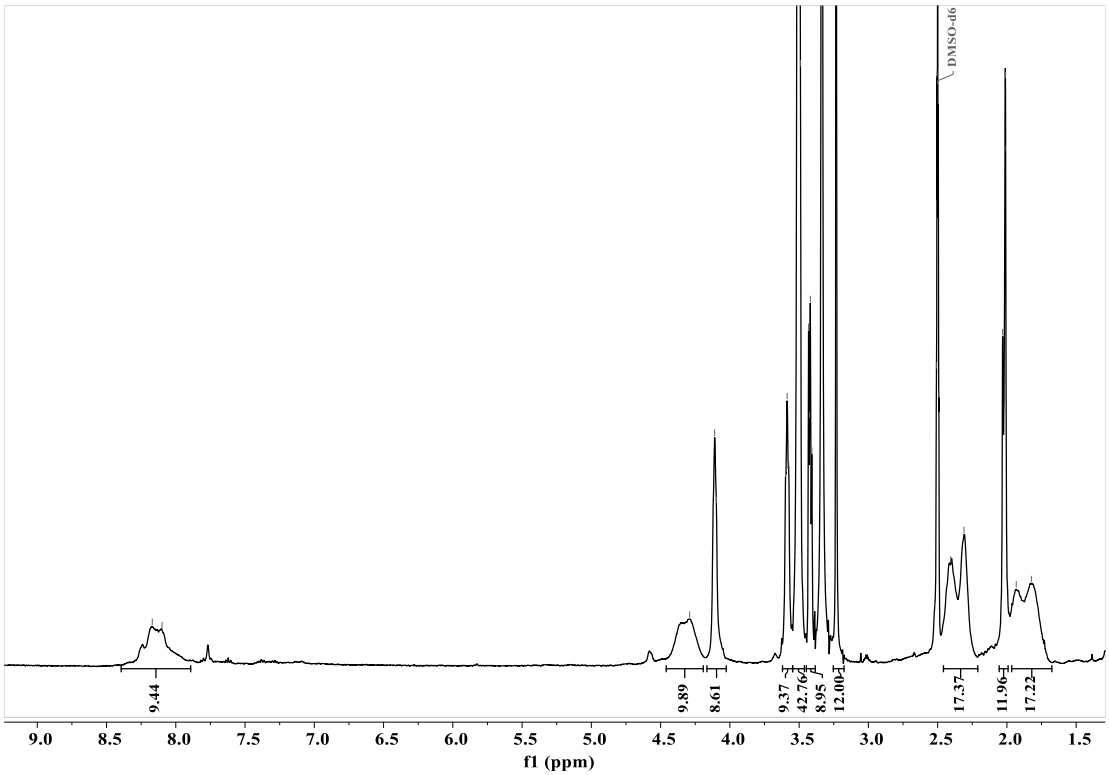

Figure 10.5: *^{1}H NMR spectrum of* ***CP1*** *in DMSO-d6.*

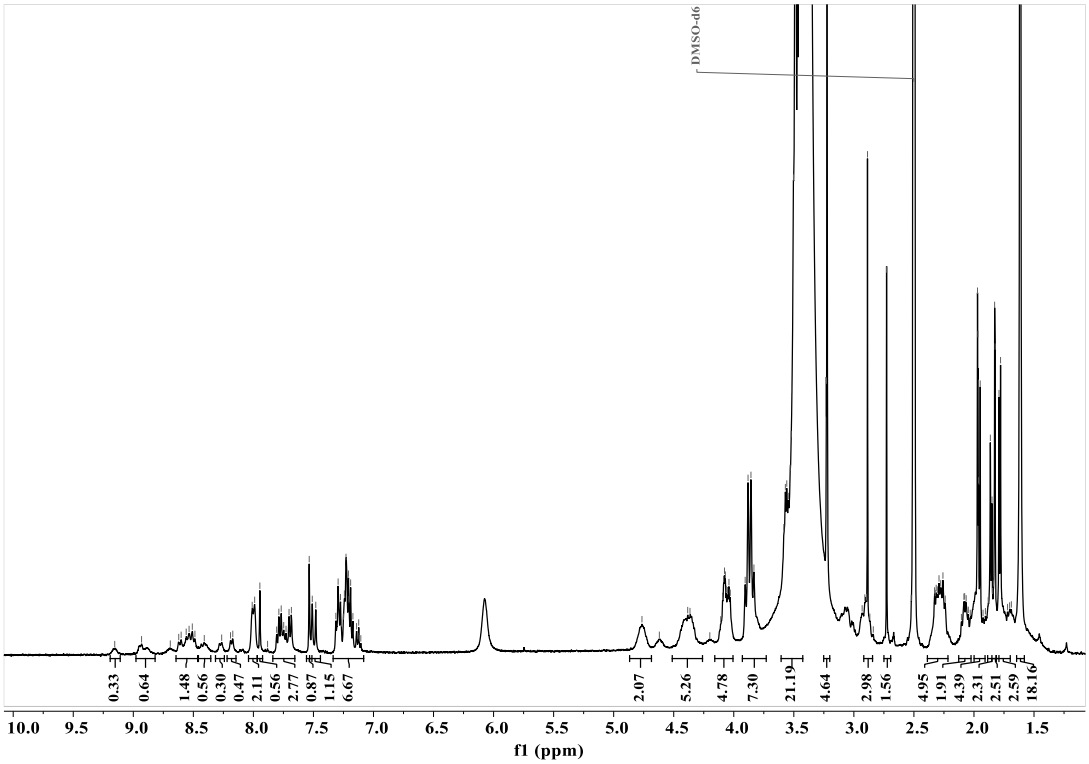

Figure 10.6: *^{1}H NMR spectrum of* ***III-7*** *in DMSO-d6.*

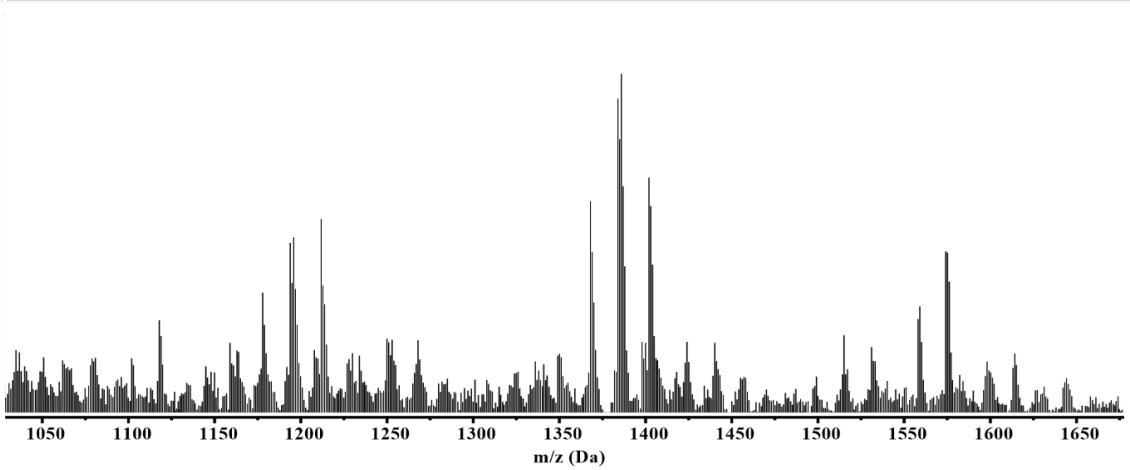

Figure 10.7: *MALD-TOF-MS (CHCA, pos. DMF) of* ***CP2*** *synthesis.*

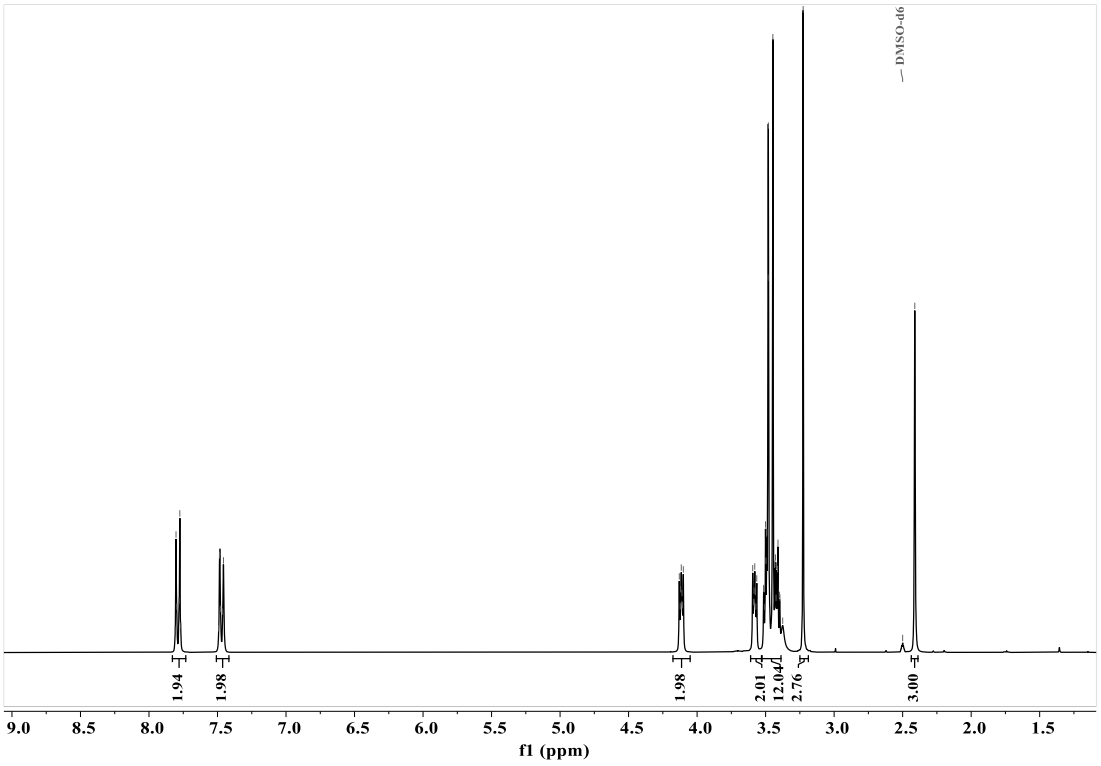

Figure 10.8: *^{1}H NMR spectrum of* ***III-9*** *in DMSO-d6.*

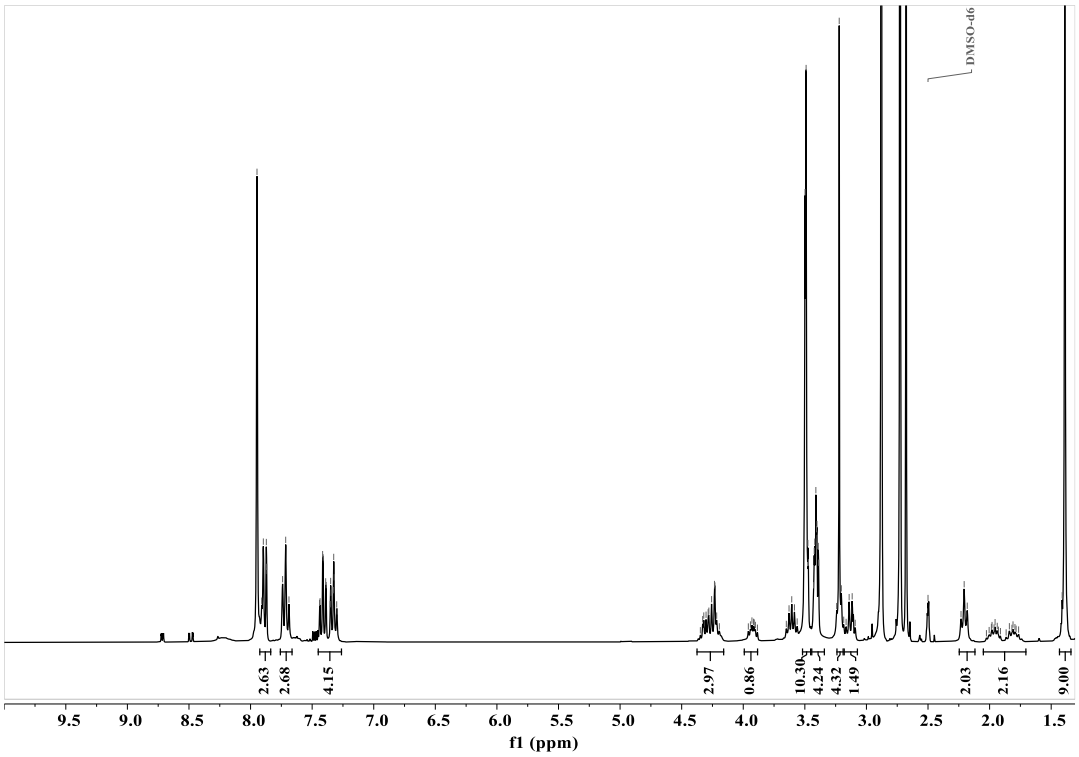

Figure 10.9: *^{1}H NMR spectrum of* ***III-12*** *in DMSO-d6.*

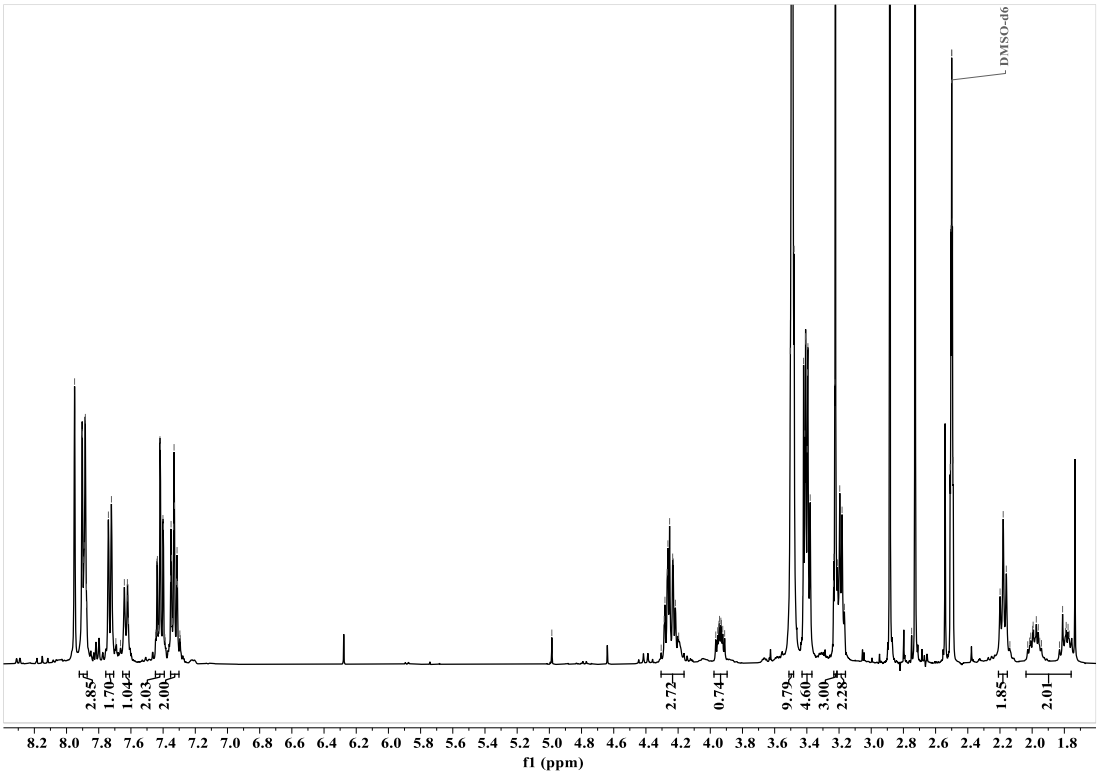

Figure 10.10: *^{1}H NMR spectrum of* ***III-13*** *in DMSO-d6.*

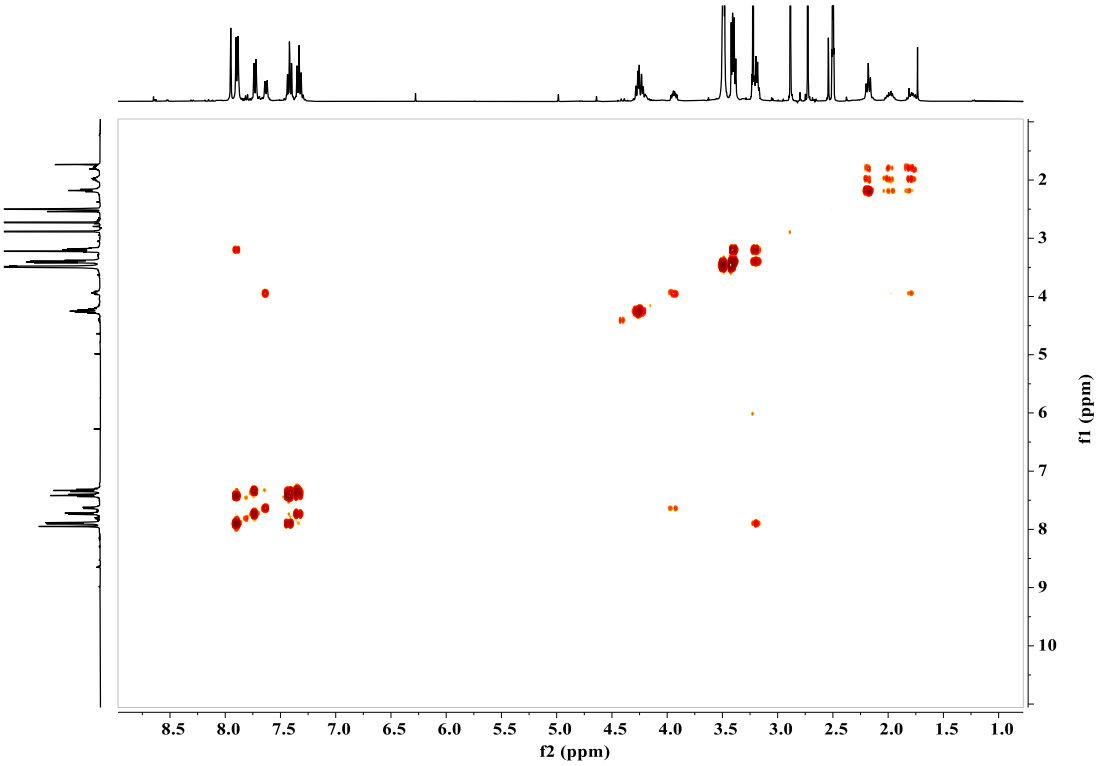

Figure 10.11: *2D-COSY-NMR spectrum of* ***III-13*** *in DMSO-d6.*

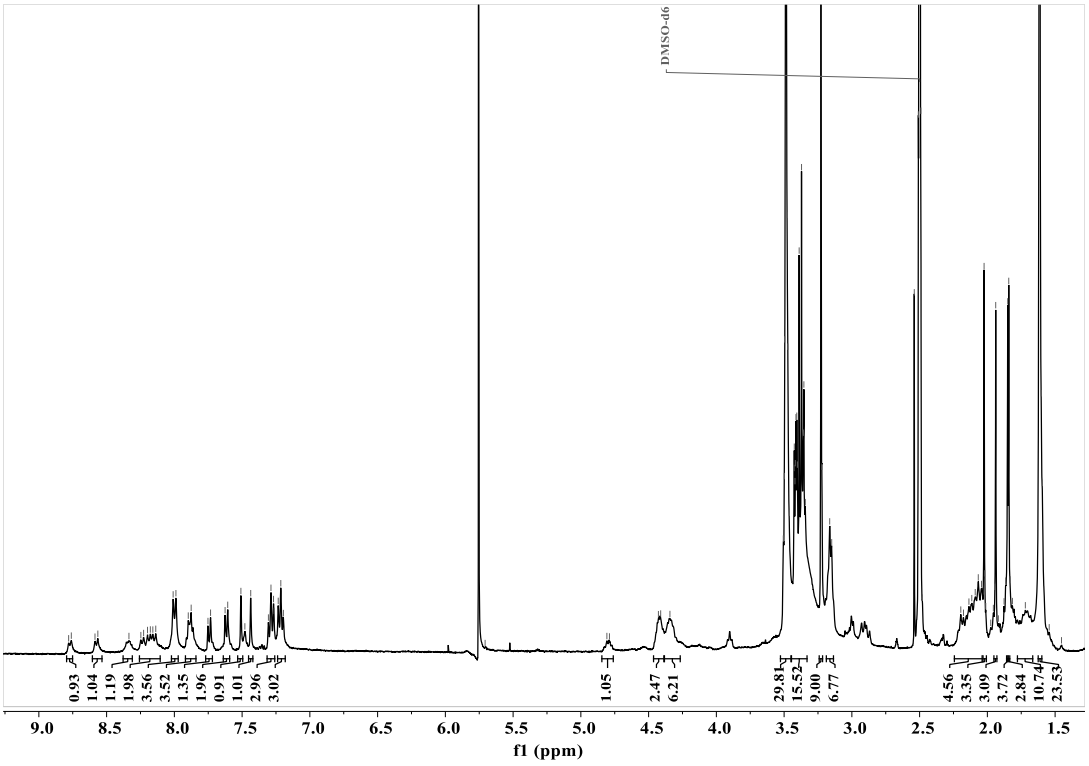

Figure 10.12: *^{1}H NMR spectrum of* ***III-14*** *in DMSO-d6.*

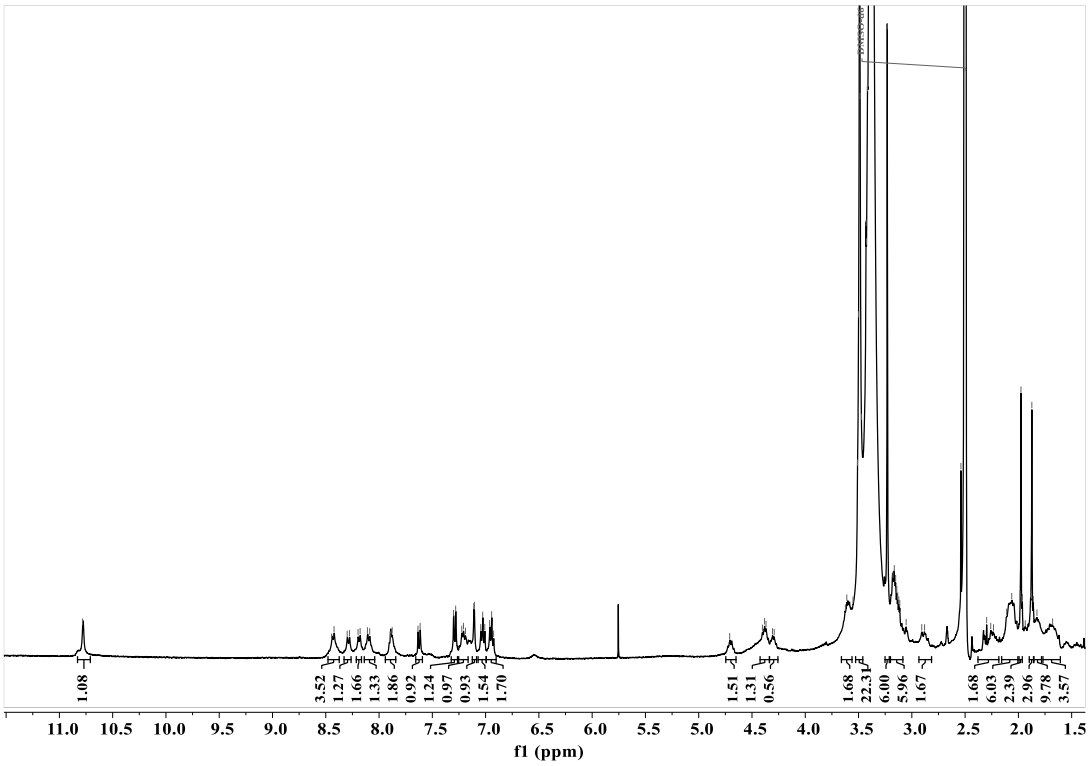

Figure 10.13: *^{1}H NMR spectrum of **CP3** in DMSO-d6.*

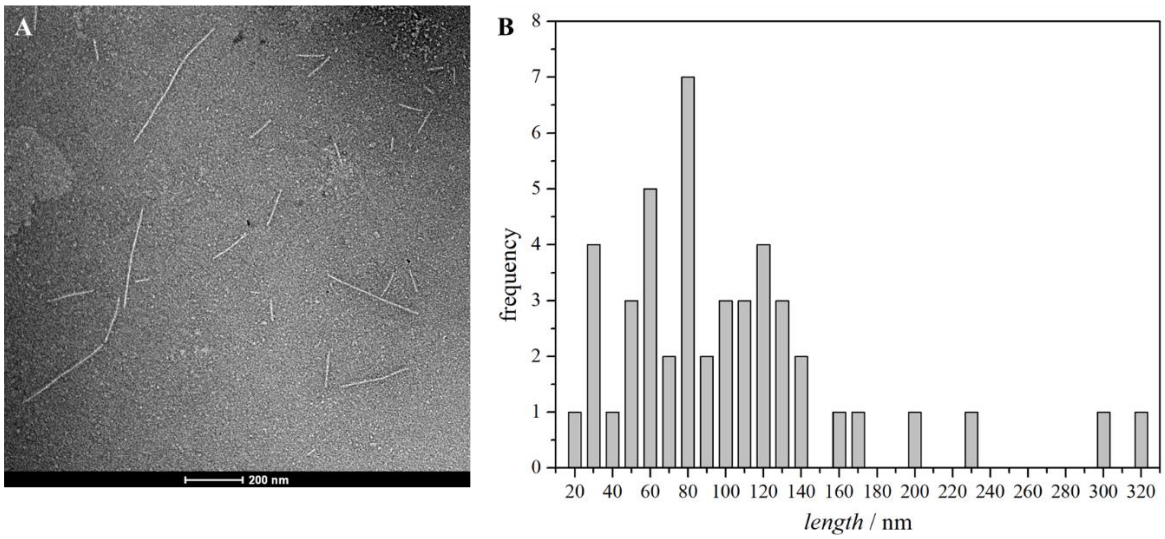

Figure 10.14: ***A*** *TEM images of **CP3** 100 μM in TRIS (negative stain);* ***B*** *Frequency of nanorod length from TEM image (n=44).*

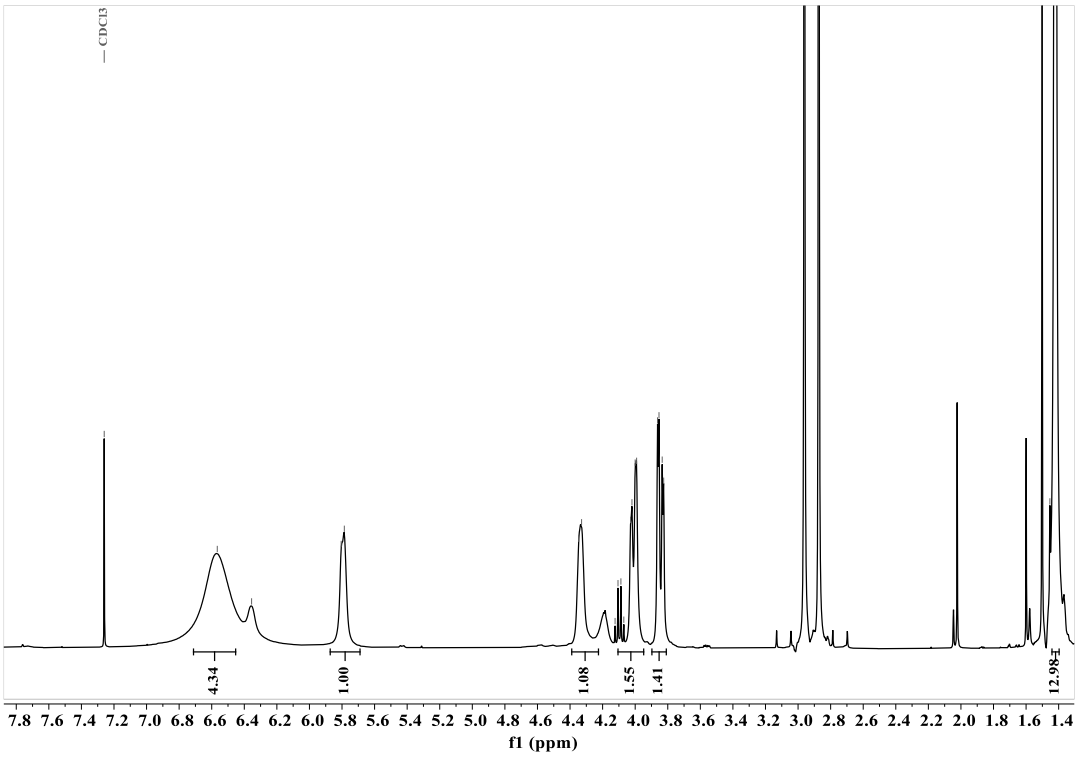

Figure 10.15: *^{1}H NMR spectrum of* ***IV-1*** *in $CDCl_3$.*

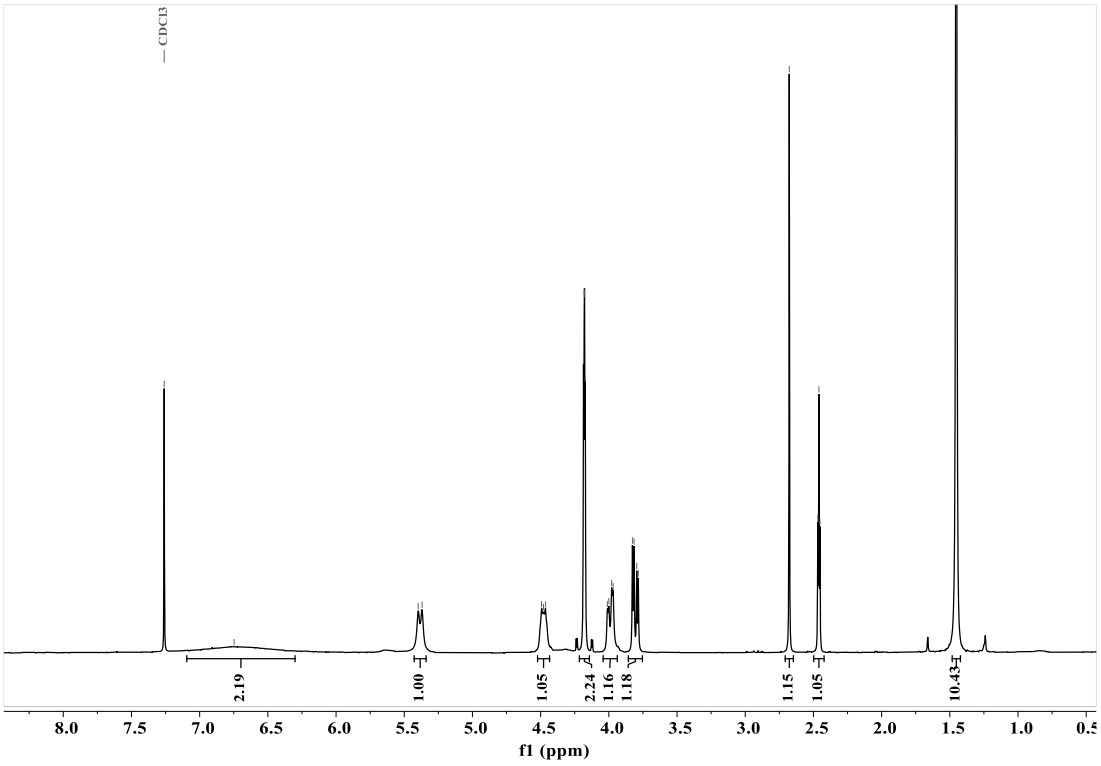

Figure10.16: *^{1}H NMR spectrum of* ***IV-2*** *in $CDCl_3$.*

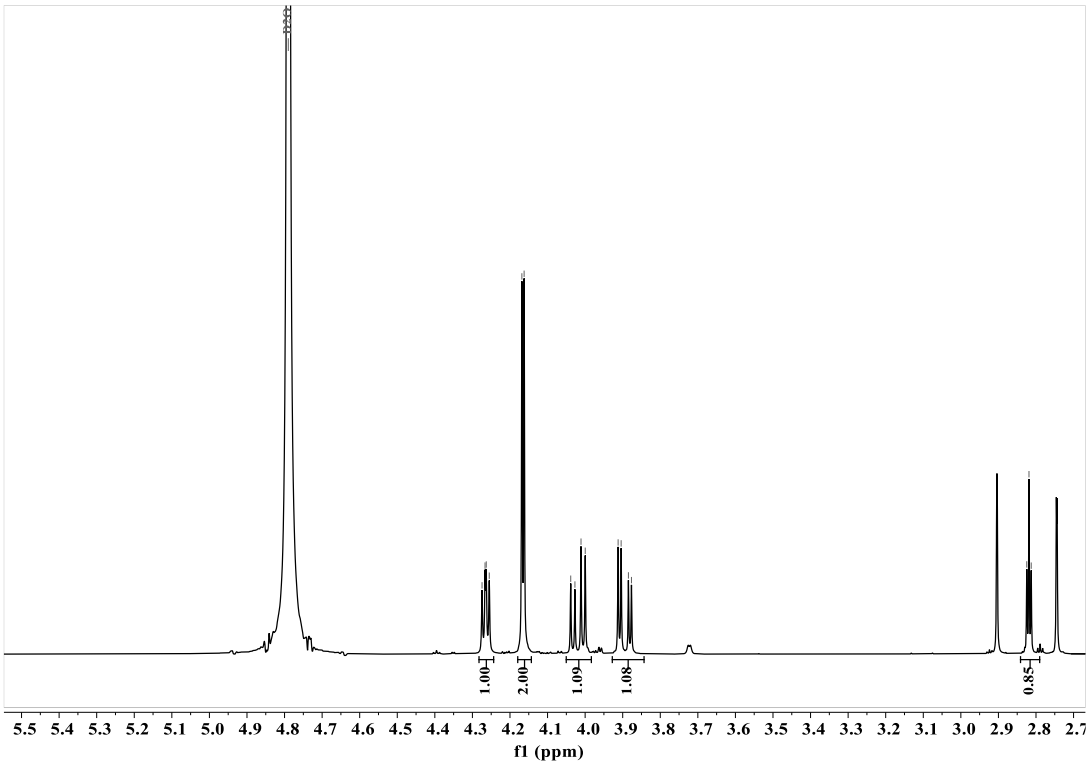

Figure 10.17: *^{1}H NMR spectrum of* ***IV-3*** *in D_2O.*

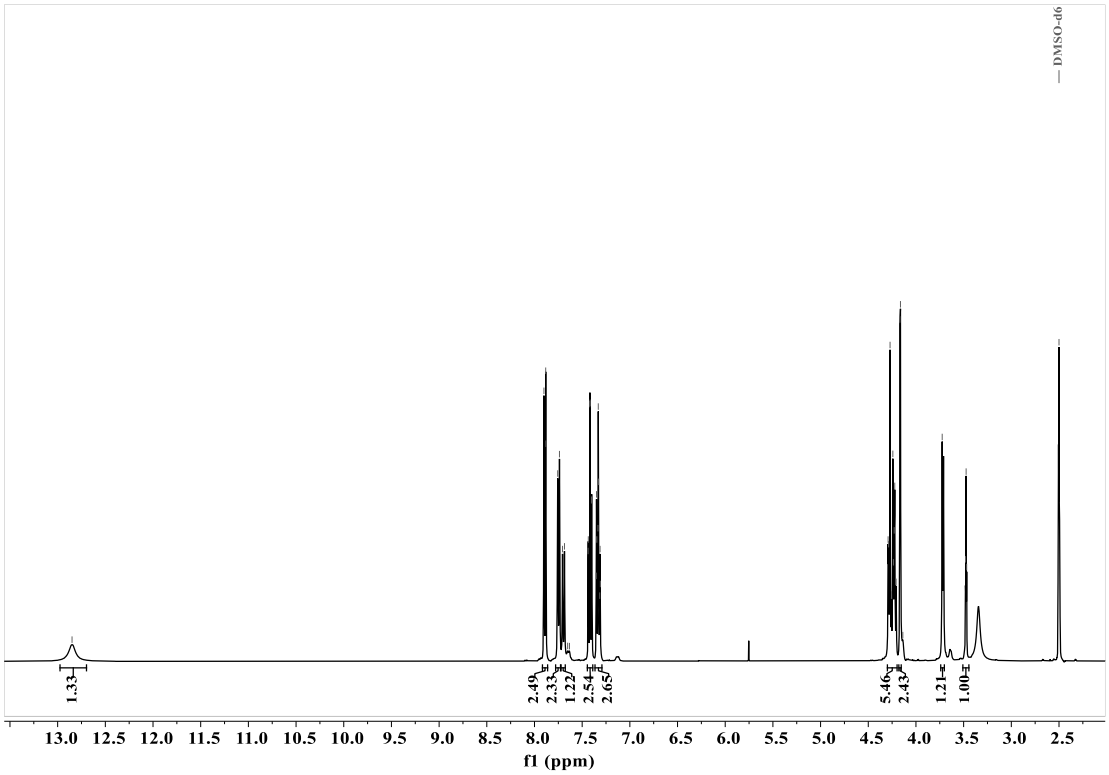

Figure10.18: *^{1}H NMR spectrum of* ***IV-4*** *in DMSO-d6.*

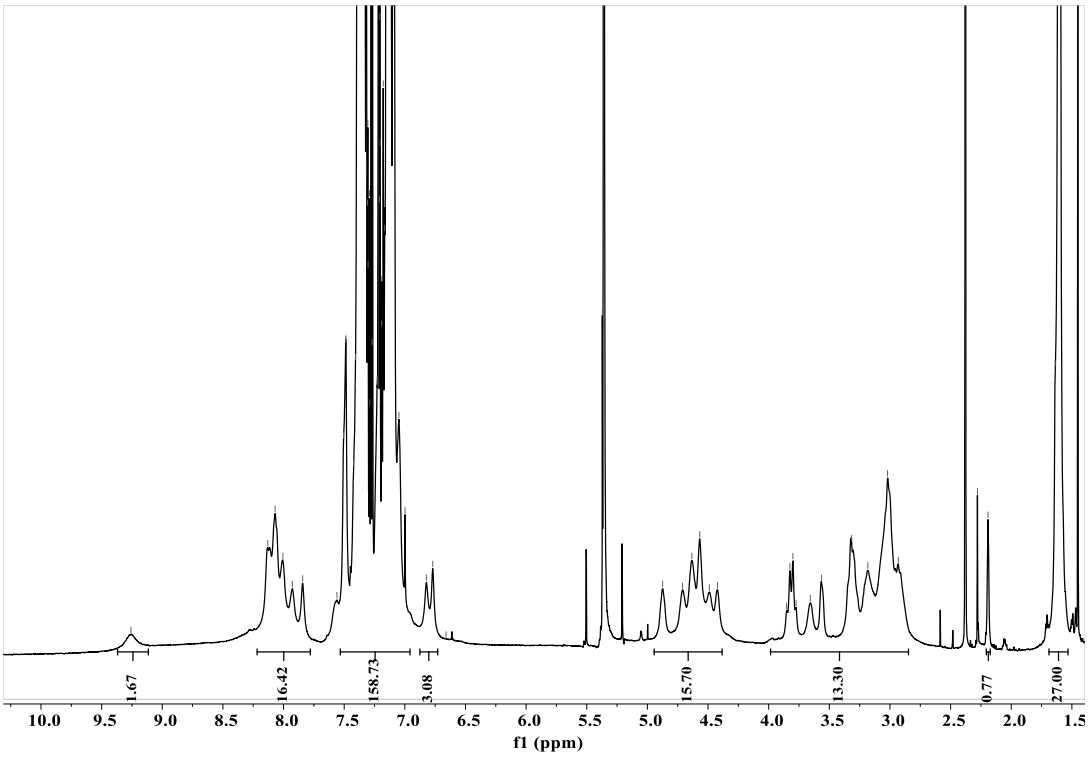

Figure 10.19: *^{1}H NMR spectrum of **IV-5** in $CDCl_3$.*

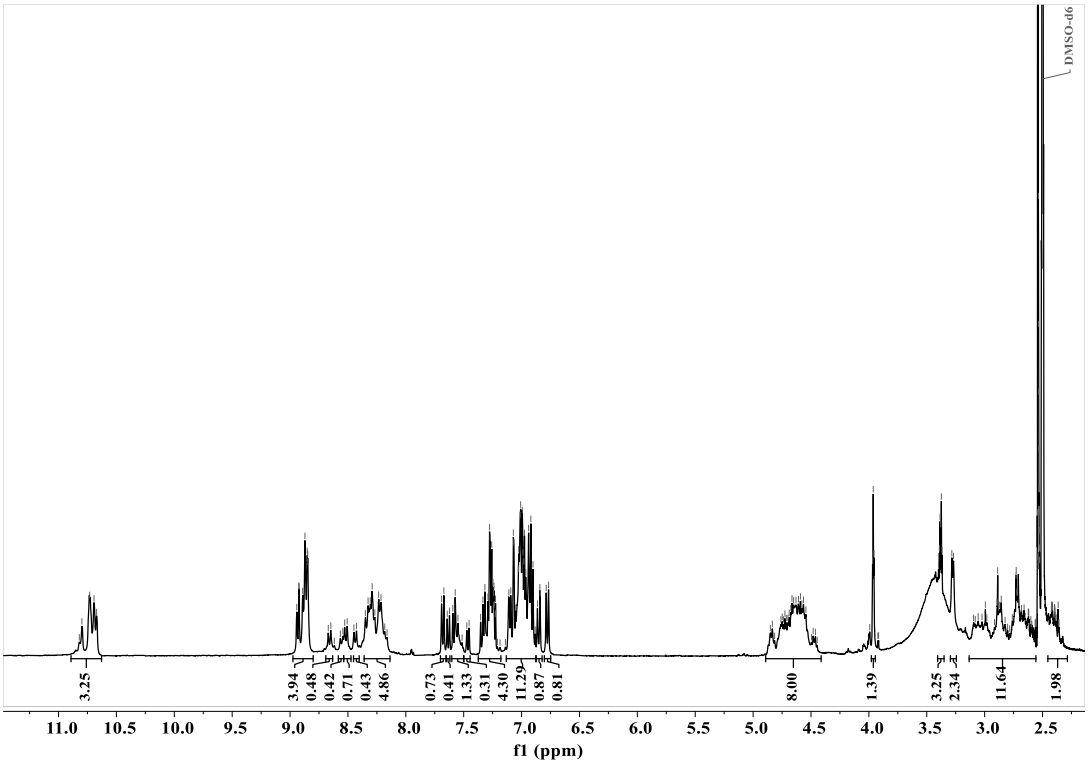

Figure 10.20: *^{1}H NMR spectrum of **CP4** in DMSO-d6.*

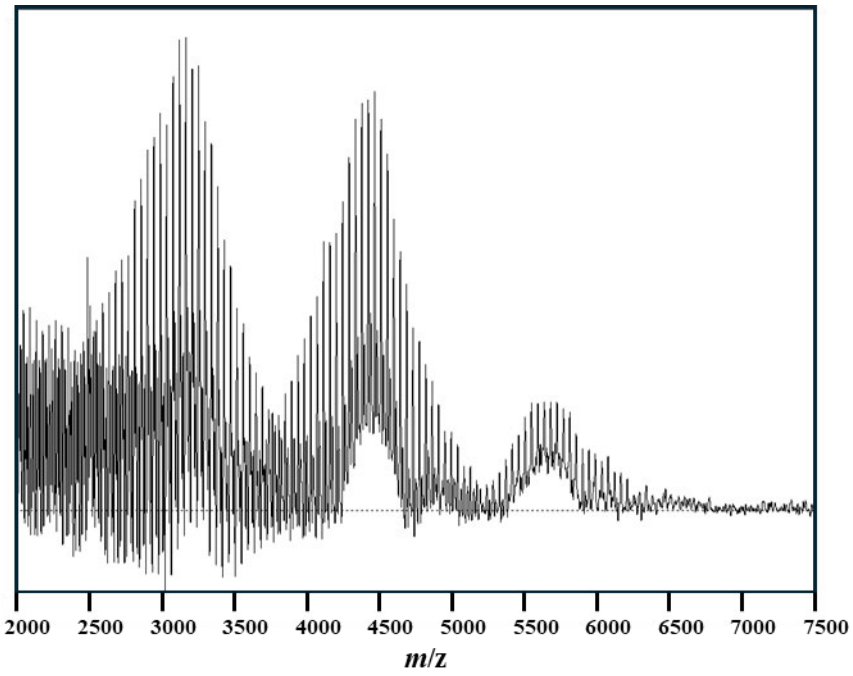

Figure 10.21: *MALD-TOF-MS (CHCA+KTFA, pos. DMF) of* ***CP4$_2$PEG3000*** *synthesis (Synthesis 2).*

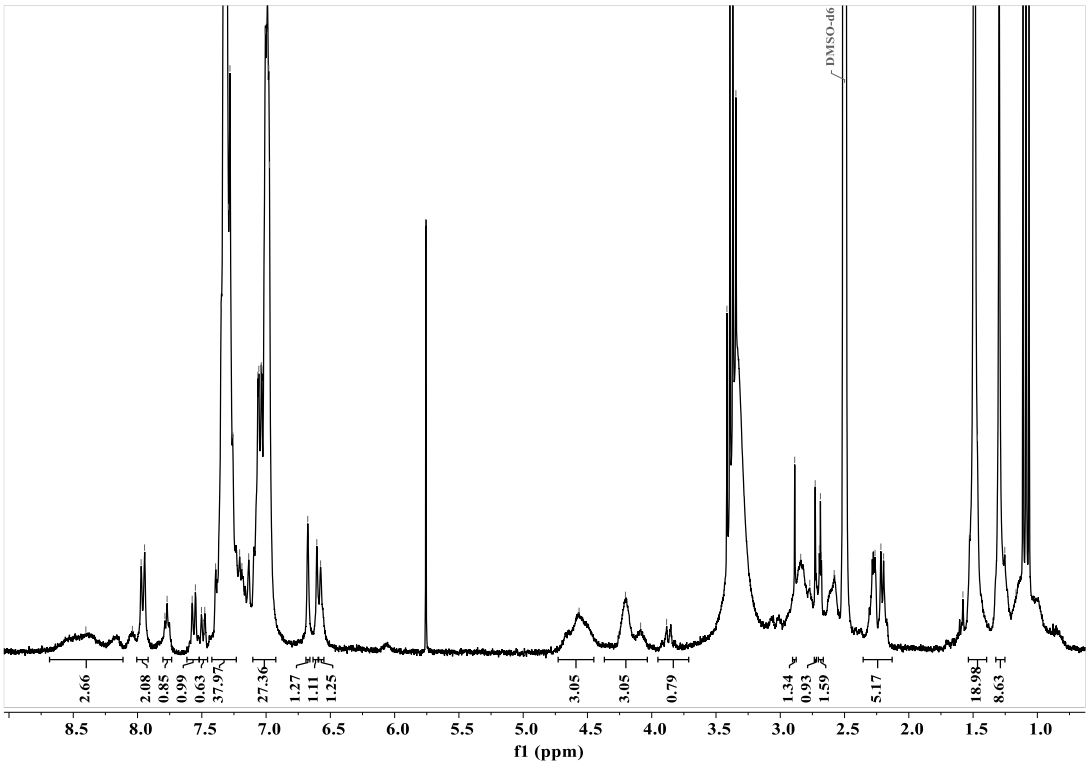

Figure 10.22: *^{1}H NMR spectrum of* ***IV-7*** *in DMSO-d6.*

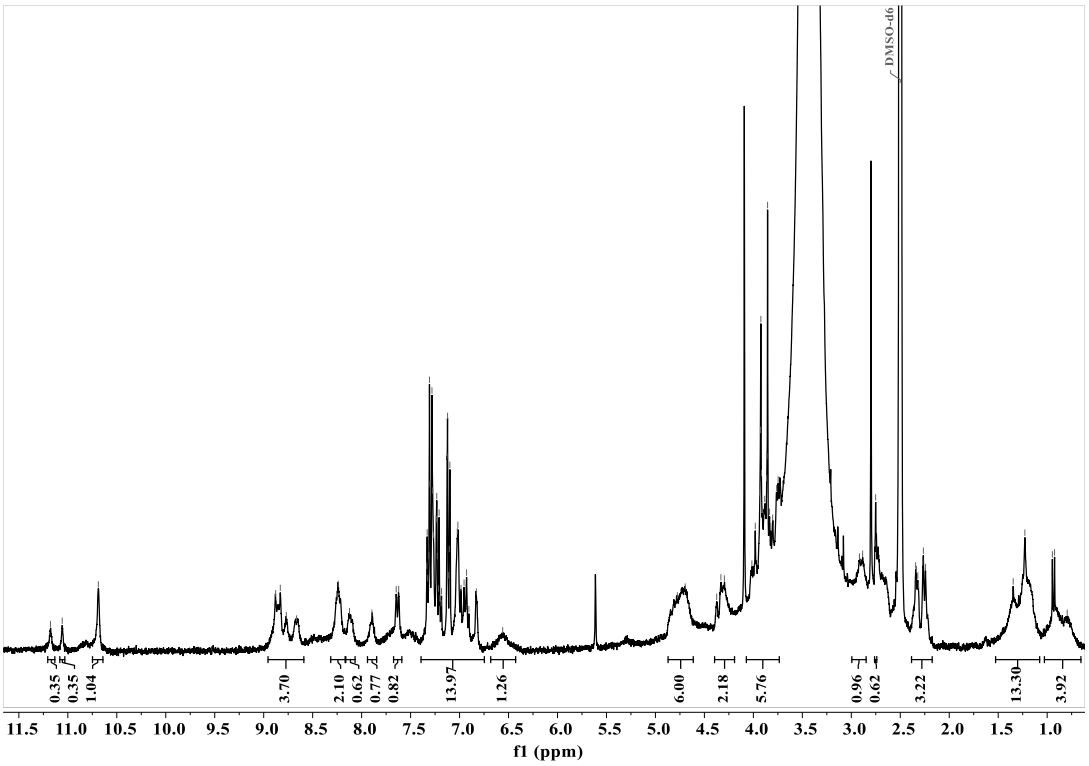

Figure 10.23: *^{1}H NMR spectrum of* ***CP5*** *in DMSO-d6.*

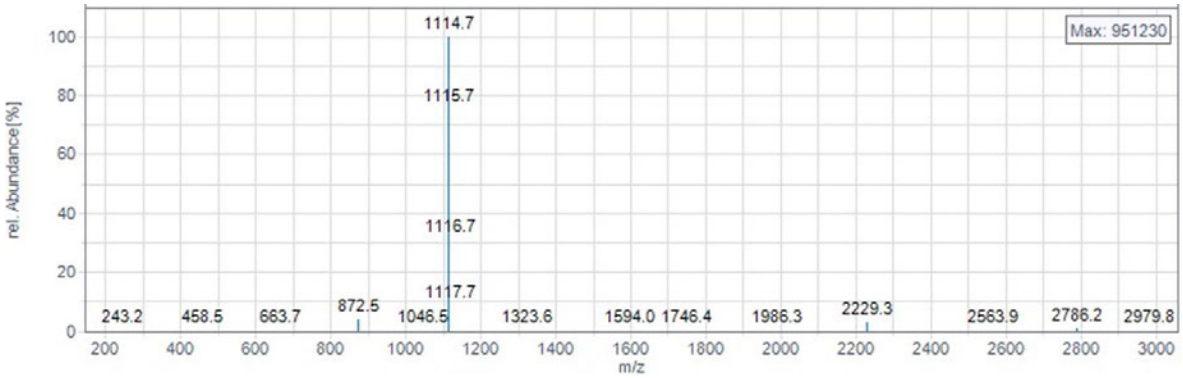

Figure 10.24: *Mass spectrum (LC-MS, Method F, figure 4.9) of Synthesis of H-L-Lys(pentynoyl)-D-His(Trt)-L-Trp(Boc)-OH.*

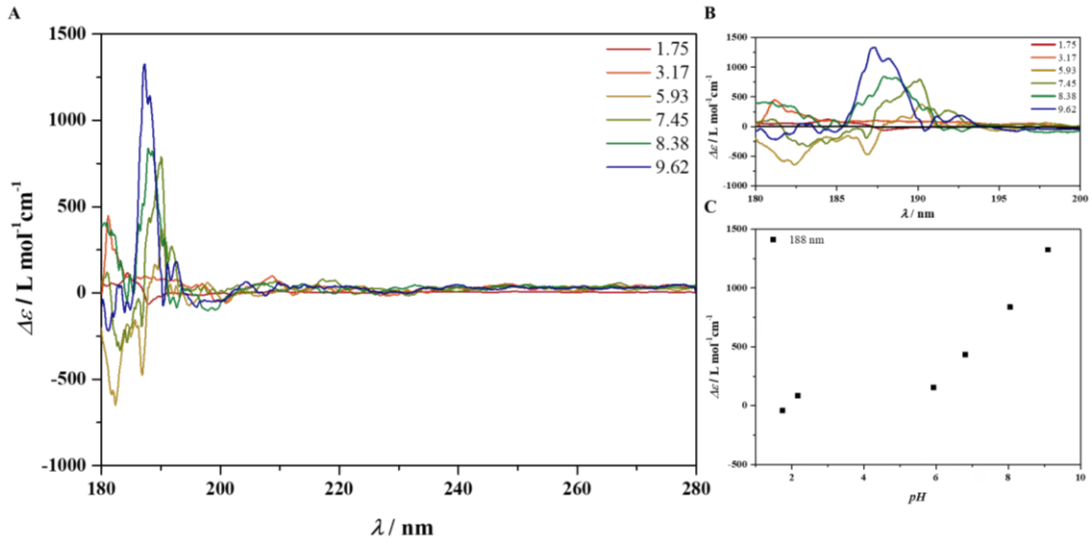

Figure 10.25: A *CD spectrum of solutions of* ***CP5*** *in milliq-H_2O (pH = 6.4) at different pH;* ***B*** *CD spectra zoomed into the wavelength range of 180 nm-200 nm,* ***C*** *CD signal at 188 nm depending on pH.*

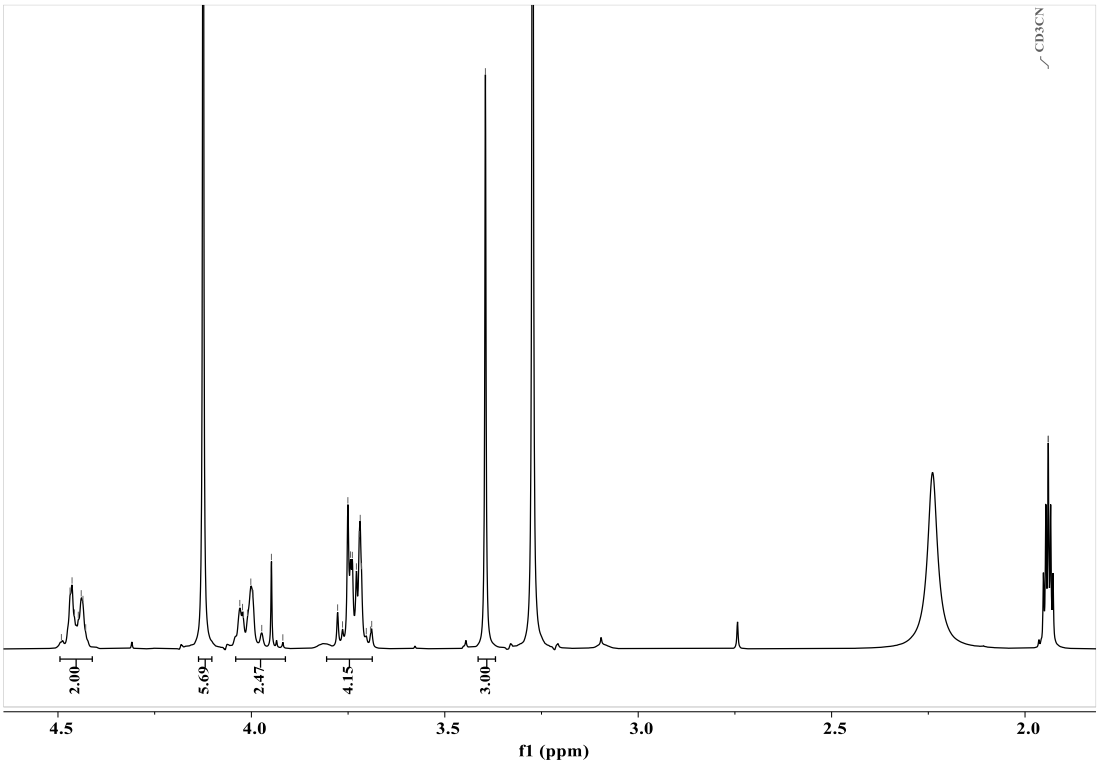

Figure 10.26: *^{1}H NMR spectrum of* ***IV-12*** *in MeCN-d3.*

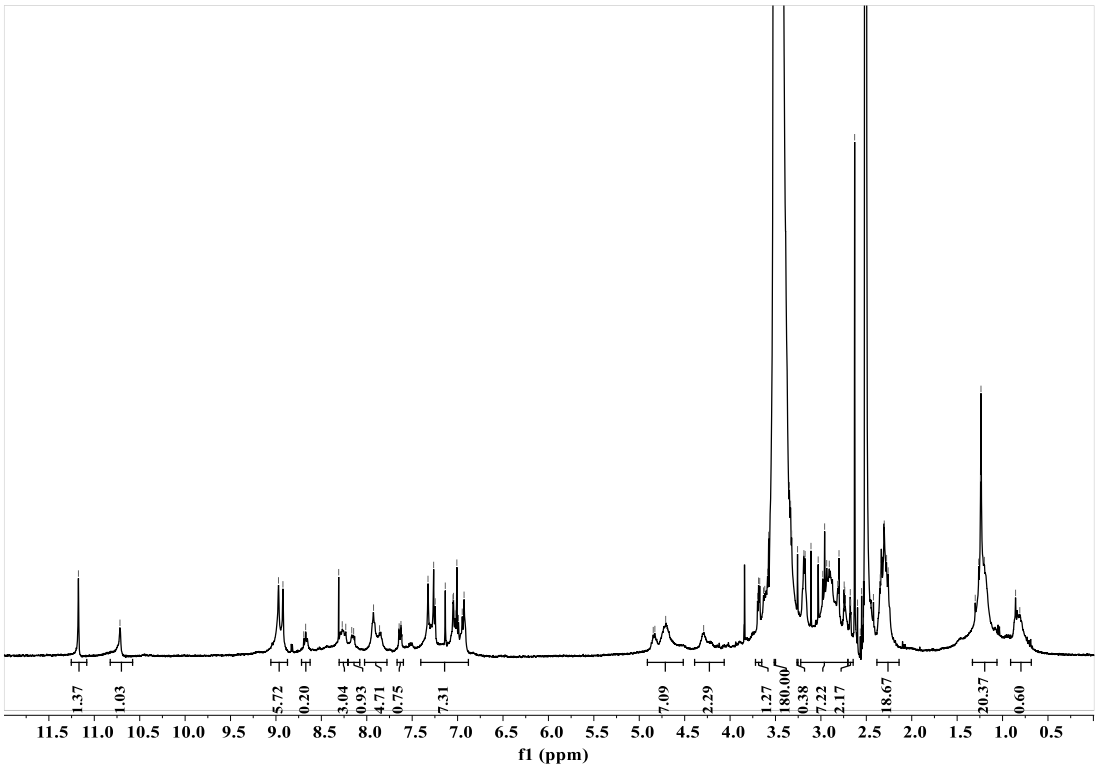

Figure 10.27: *^{1}H NMR spectrum of* ***CL2000*** *in DMSO-d6.*

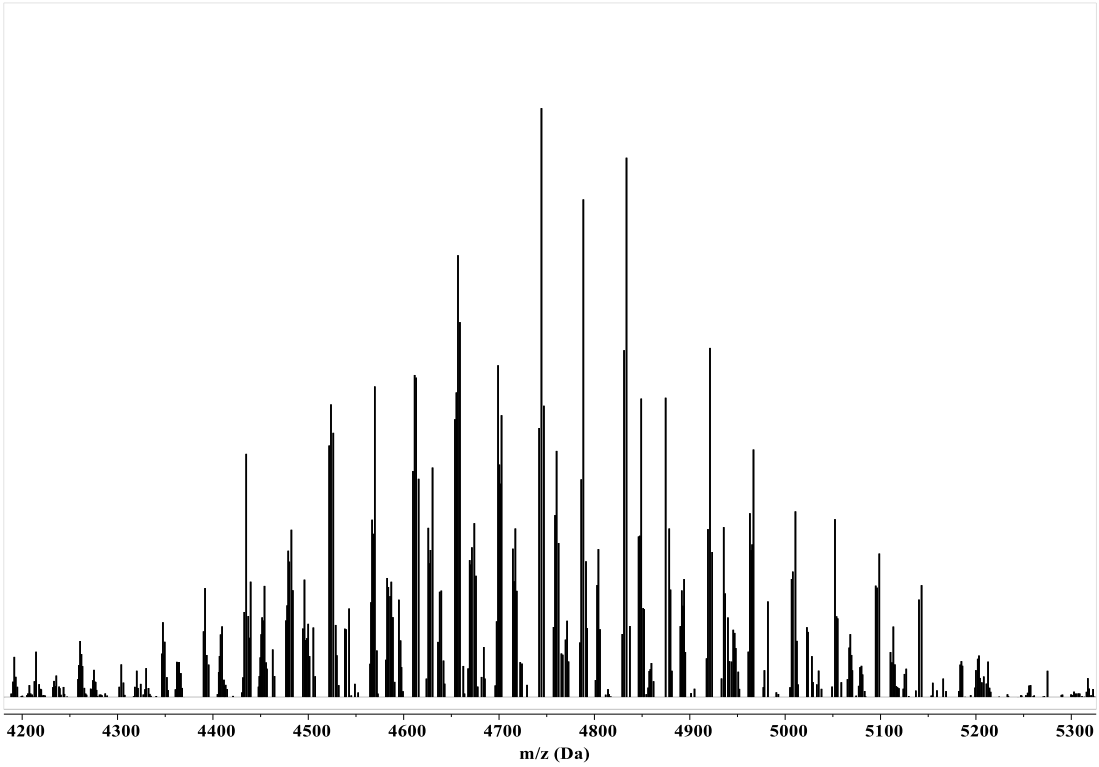

Figure 10.28: *MALD-TOF-MS (DHB+KTFA, pos. DMF) of* ***CL2000****.*

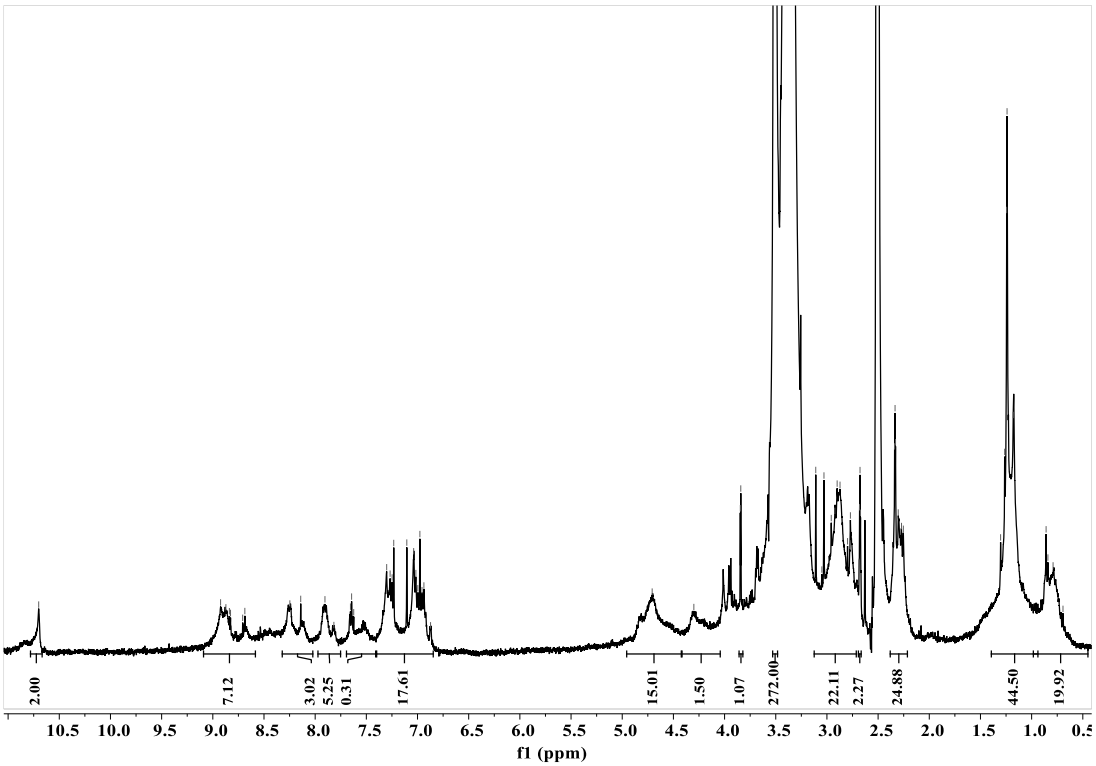

Figure 10.29: *^{1}H NMR spectrum of* ***CL3000*** *in DMSO-d6.*

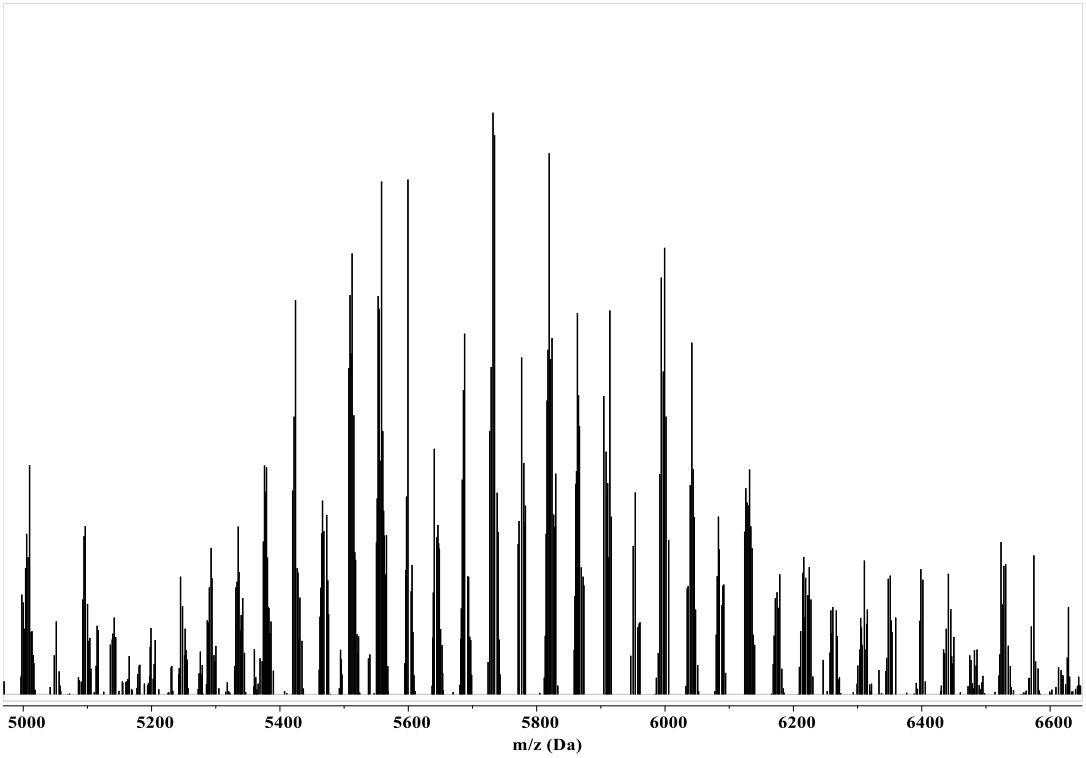

Figure 10.30: *MALD-TOF-MS (DHB+KTFA, pos. DMF) of* ***CL3000****.*

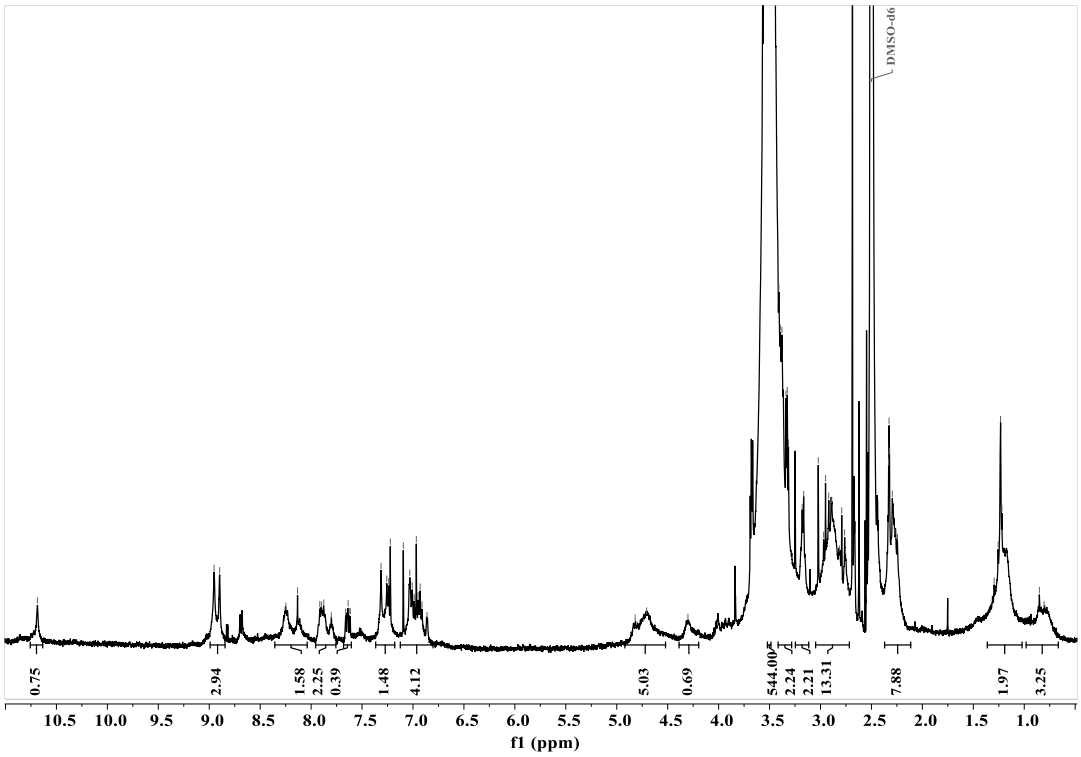

Figure 10.31: *^{1}H NMR spectrum of* ***CL6000*** *in DMSO-d6.*

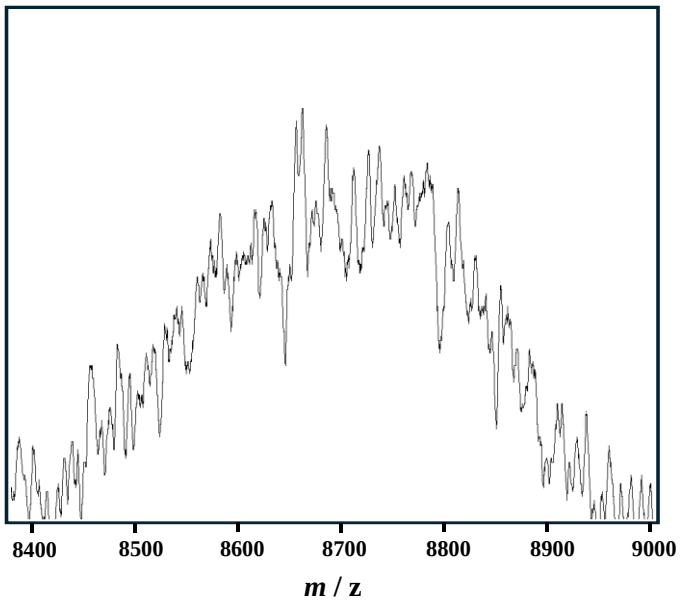

Figure 10.32: *MALD-TOF-MS (DHB+KTFA, pos. DMF) of* ***CL6000****.*

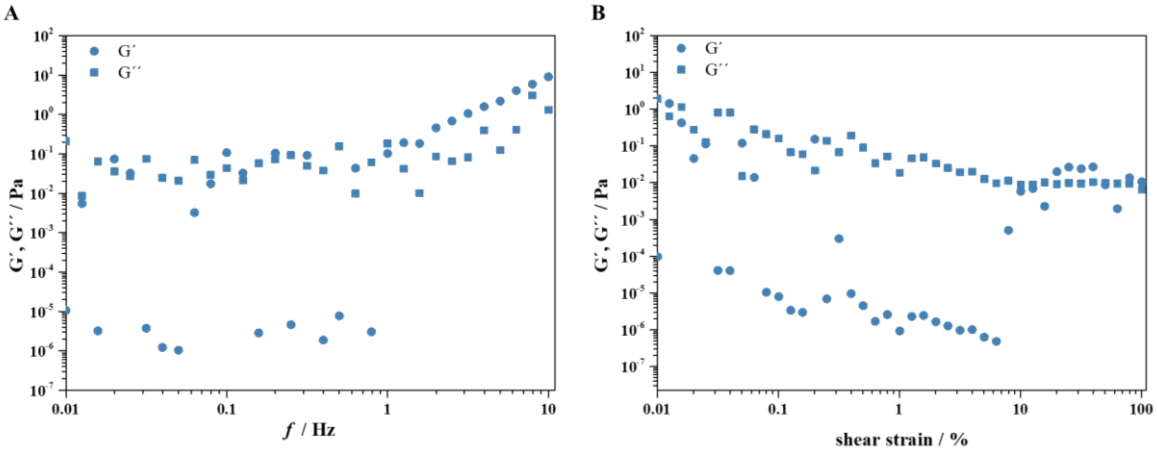

***Figure 10.33: A** Frequency sweep (0.1% strain, 0.01- 10 Hz) and **B** shear strain sweep (1 Hz, 0.01 – 100% strain) of a mixture of **CP5:CL300 (80:20)** (1 wt% in phosphate-buffered saline, pH = 7.4) with storage (G') and loss moduli (G") at constant 20 °C.*

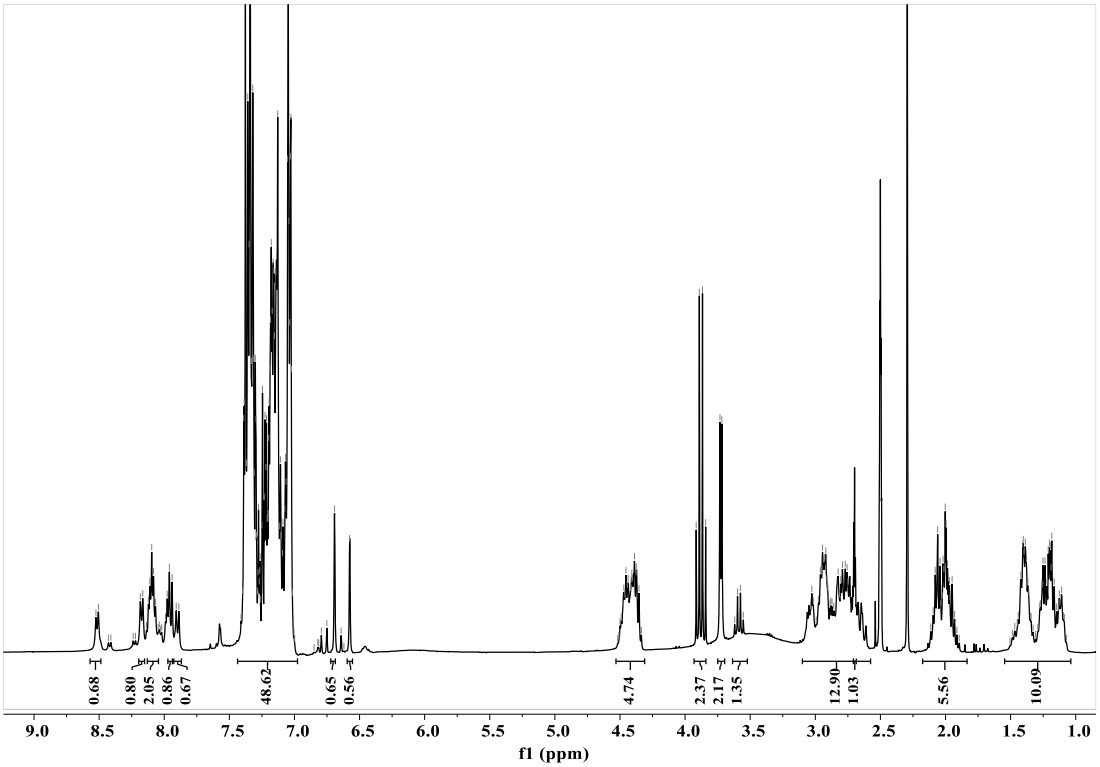

***Figure 10.34:** ^{1}H NMR spectrum of **V-1** in DMSO-d6.*

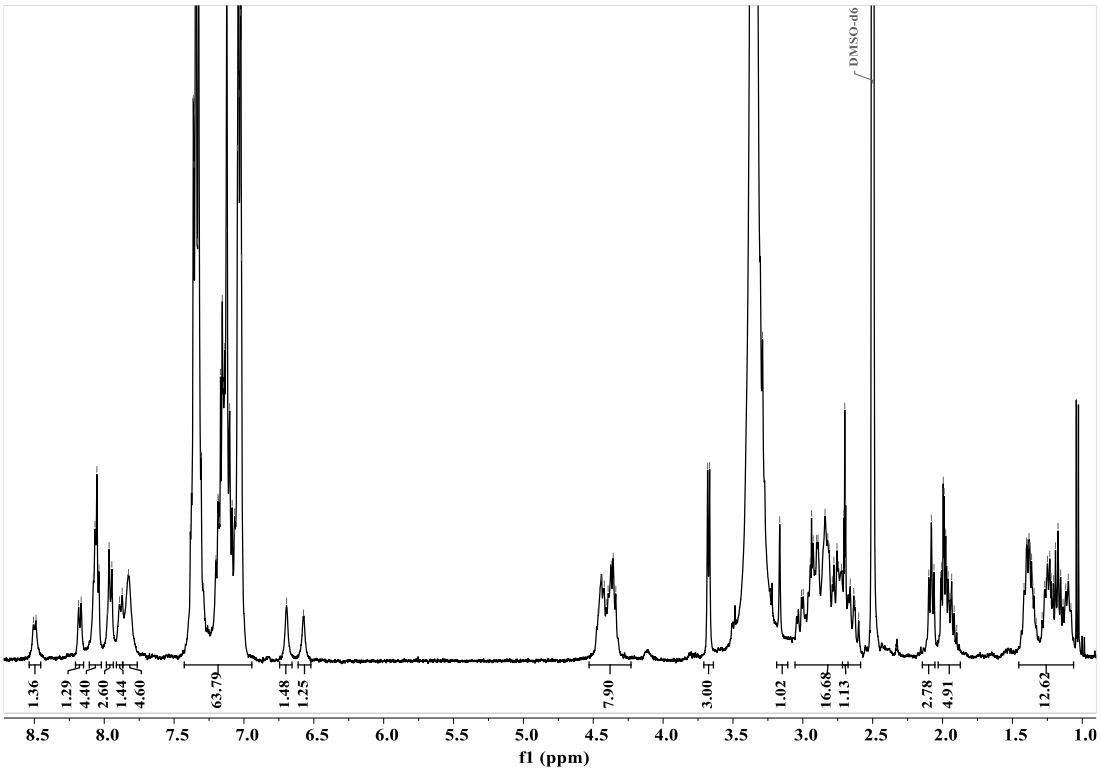

Figure 10.35: *^{1}H NMR spectrum of **V-3** in DMSO-d6.*

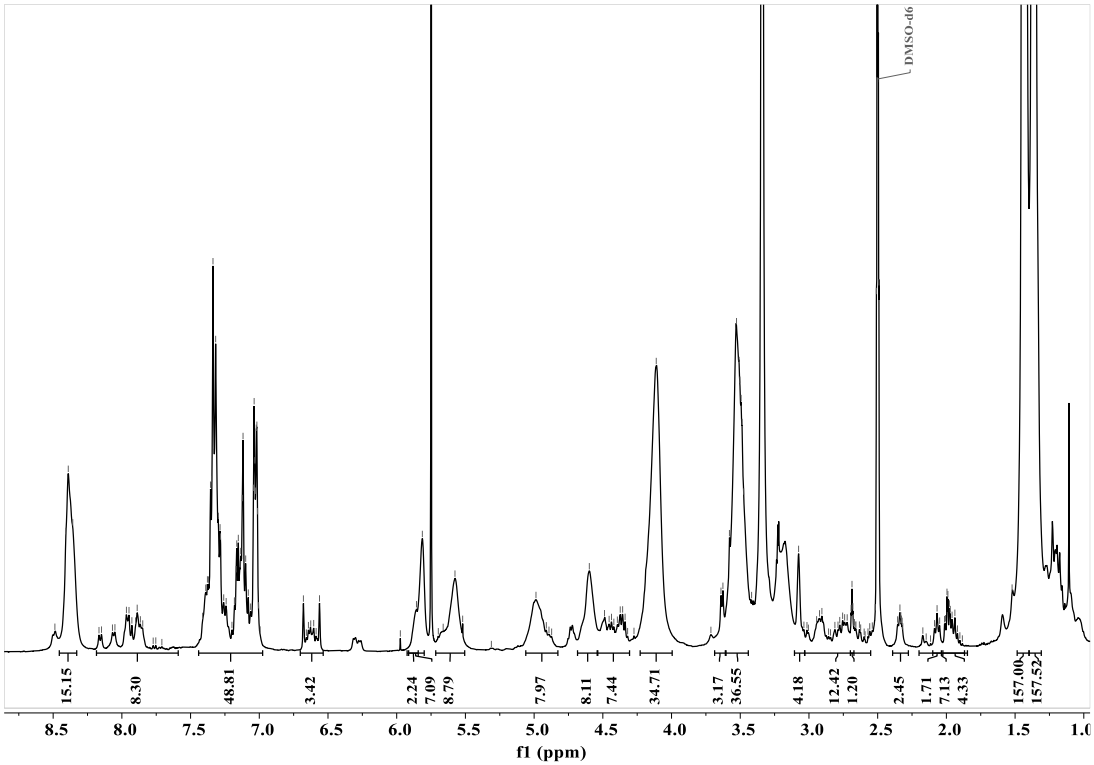

Figure 10.36: *^{1}H NMR spectrum of **V-4(PG5)** in DMSO-d6.*

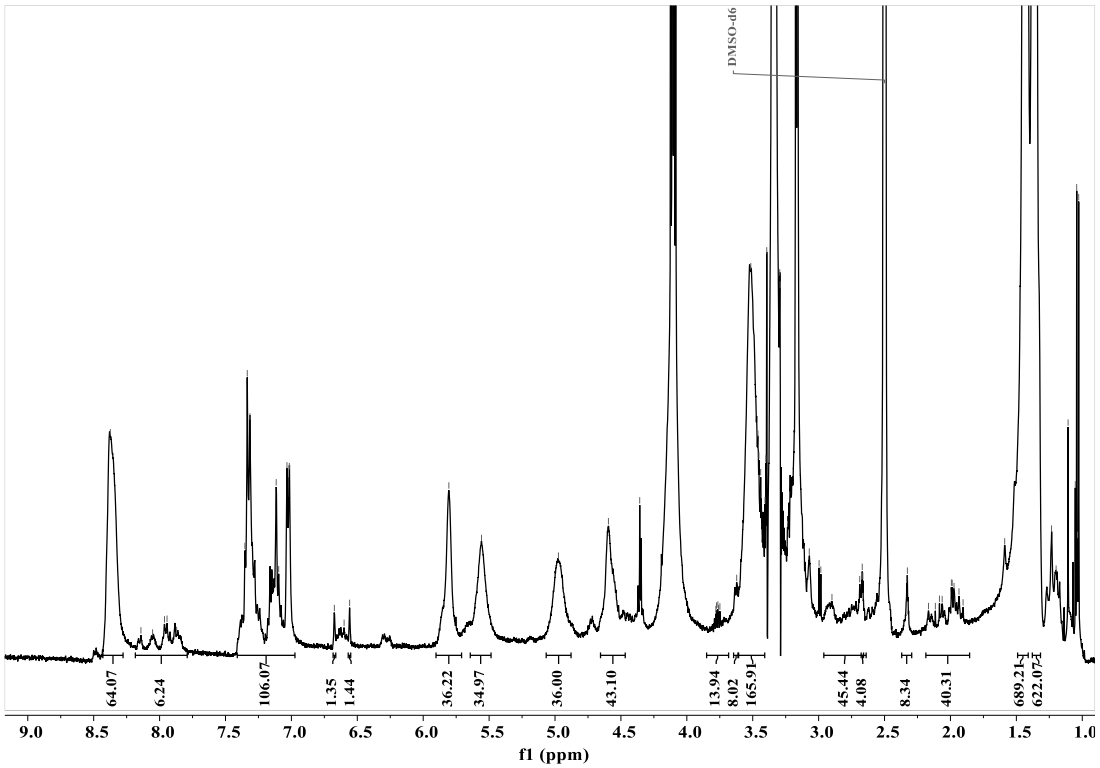

Figure 10.37: *^{1}H NMR spectrum of* ***V-4(PG9)*** *in DMSO-d6.*

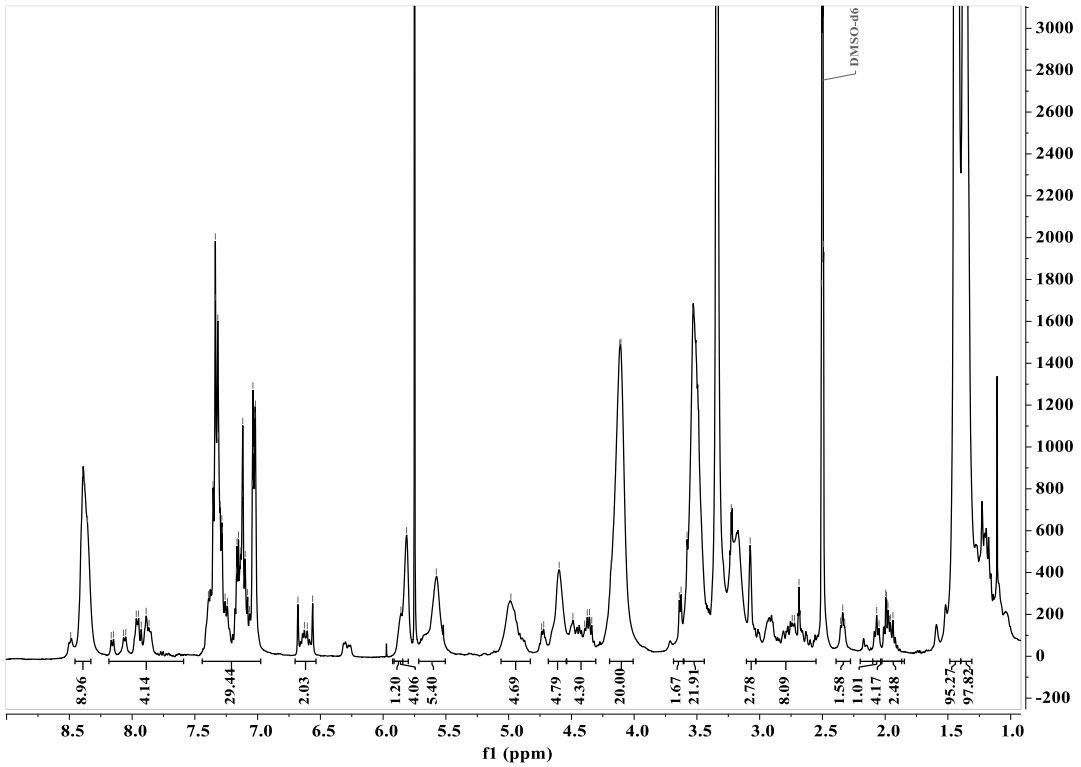

Figure 10.38: *^{1}H NMR spectrum of* ***V-5(PG5)*** *in DMSO-d6.*

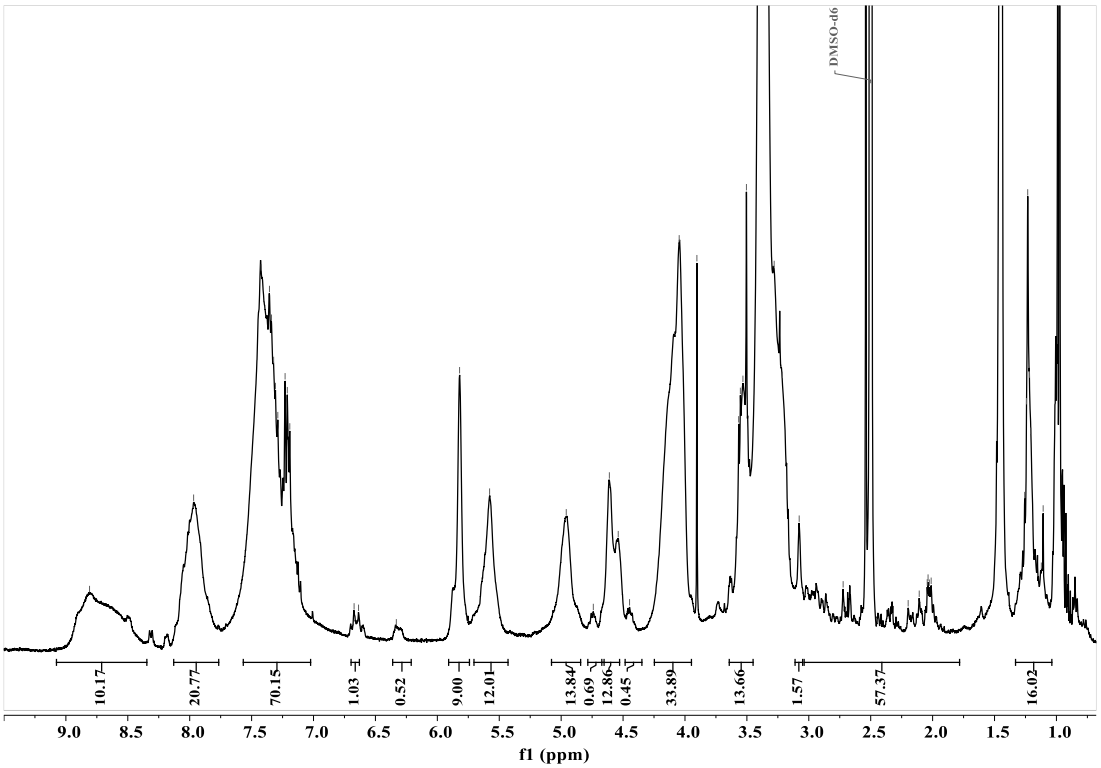

Figure 10.39: *^{1}H NMR spectrum of* ***V-5(PG9)*** *in DMSO-d6.*

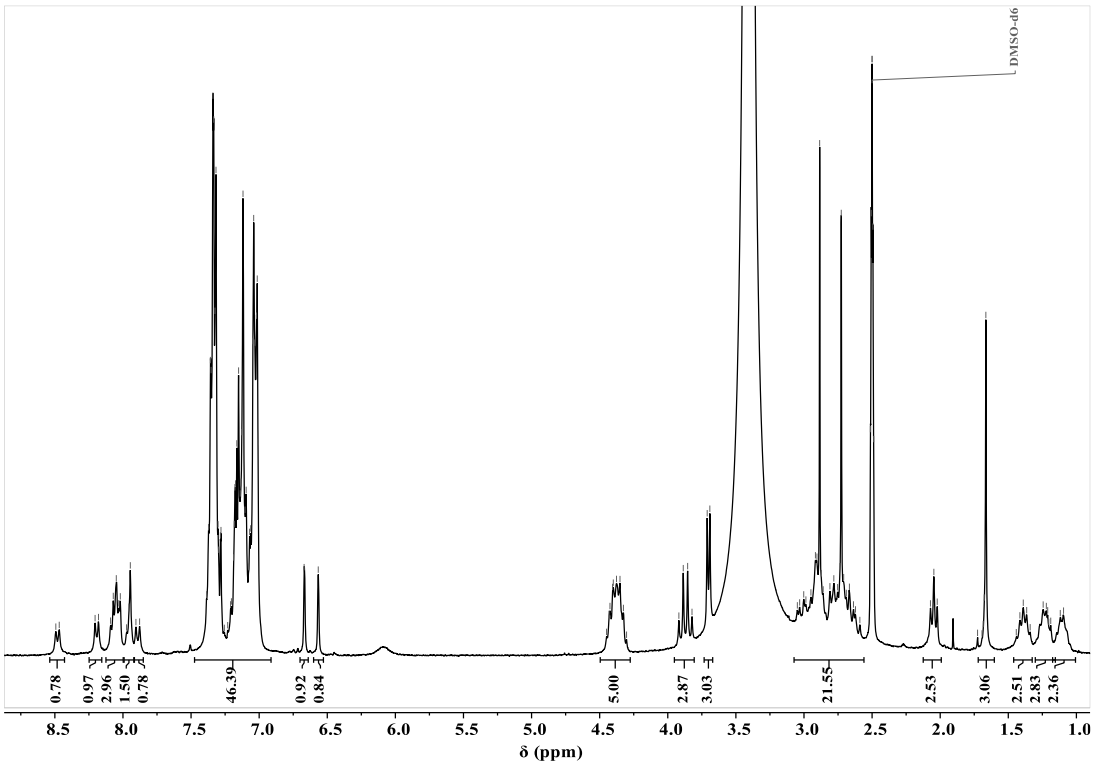

Figure 10.40: *^{1}H NMR spectrum of* ***V-6*** *in DMSO-d6.*

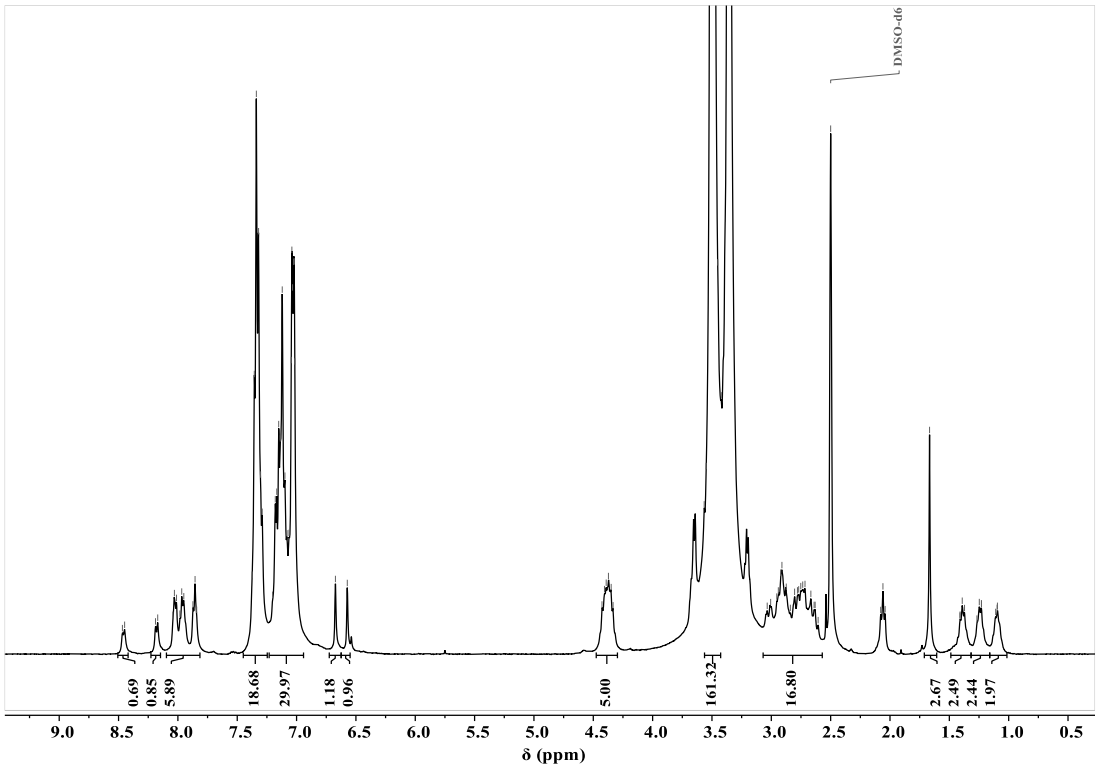

Figure 10.41: *^{1}H NMR spectrum of **V-7** in DMSO-d6.*

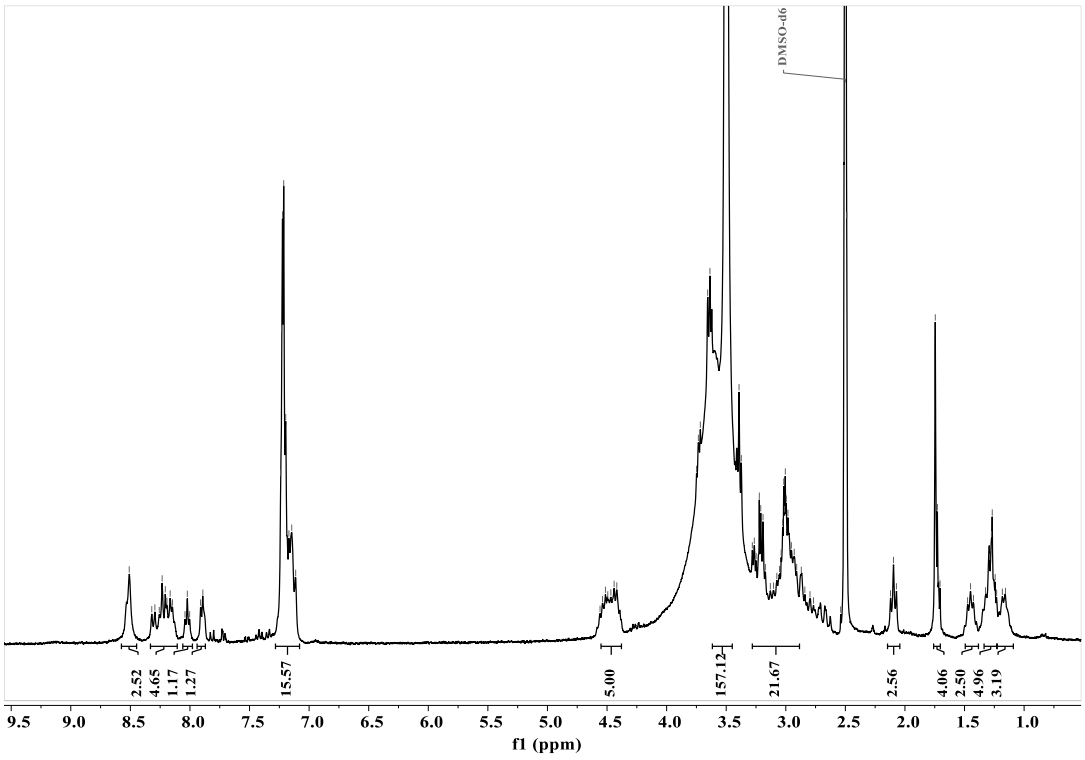

Figure 10.42: *^{1}H NMR spectrum of **V-8** in DMSO-d6.*

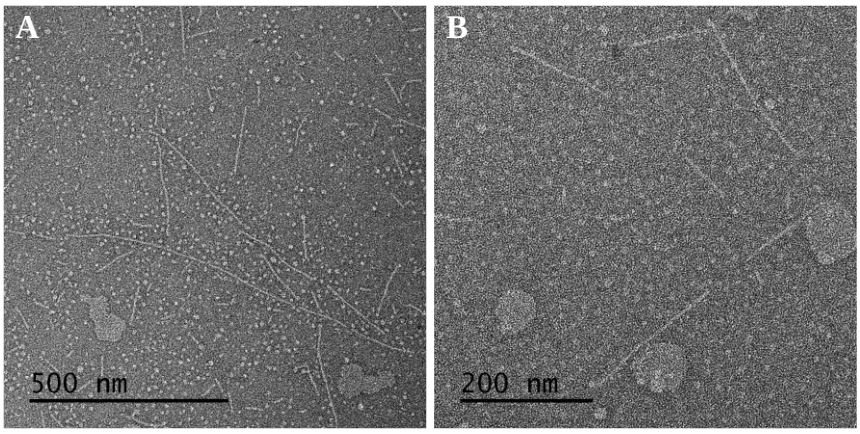

Figure 10.43: *TEM images of 200 µM TRIS buffer at pH 7.6 (negative stain) of* ***A V-5(PG5)****;* ***B Copolymer*** *(5:1* ***V-8/V-5(PG5))***

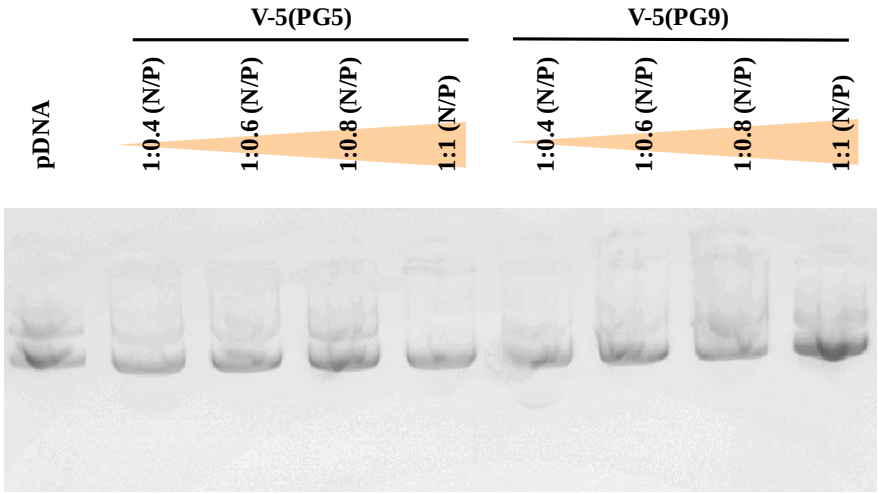

Figure 10.44: *Gel electrophoresis results for the polyplex formation between pDNA (0.4 µM) and* ***V-5(PG5)*** *and* ***V-5(PG9)*** *at different charge ratios (N/P) with an incubation time of 20 min and the free uncomplexed pDNA, visualized under UV light after gel staining with GelRed®, 2.0 % agarose gel, 100 V, 117 mA, 12 W for 30 min.*

Eigenständigkeitserklärung

Eidesstattliche Erklärung gemäß § 10 Abs. 3d der Promotionsordnung des Fachbereichs 09 Chemie, Pharmazie und Geowissenschaften der Johannes Gutenberg-Universität Mainz vom 24. Juli 2007 in der Fassung vom 22. August 2012

Hiermit versichere ich, dass ich die vorliegende Dissertation selbstständig und unter ausschließlicher Verwendung der in der Arbeit angegebenen Hilfsmittel (table 10.1)sup angefertigt habe. Ich habe die Dissertation weder vollständig noch in Teilen als Prüfungsarbeit für eine andere Prüfung eingereicht. Ebenso wurde die vorliegende oder eine inhaltlich identische bzw. teilweise identische Arbeit nicht als Dissertation bei einer anderen Fakultät oder einem anderen Fachbereich vorgelegt.

Mainz, 21.05.2025

[redacted]

Nicole Martina Hutter

Table 10.1: *Use of AI tools.*

KI-Tool	Genutzt für	Warum	Wann
DeepL Translate	Übersetzung einzelner Wörter und Textabschnitte in die englische Sprache	Übersetzung und Hilfe für grammatikalische Korrektur	über die gesamte Arbeit hinweg
DeepL Write	Umformulierung Textentwürfe	bessere Lesbarkeit	über die gesamte Arbeit hinweg
ChatGPT	Umformulierung Textentwürfe und Literaturrecherche	bessere Lesbarkeit und relevante Paper finden	über die gesamte Arbeit hinweg